# DNA Origami Templated Plasmonic Nanostructures

**Eva-Maria Roller**

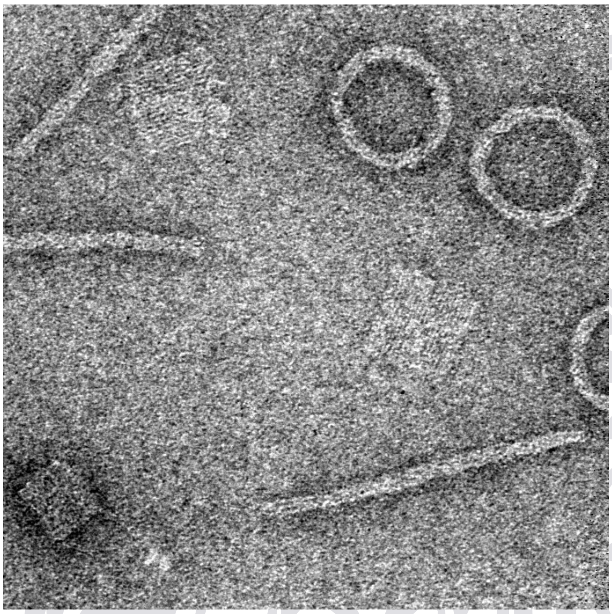

München 2016

# DNA Origami Templated Plasmonic Nanostructures

**Eva-Maria Roller**

SIGILL. UNIVERSITAT. LUDOVIC. MAXIM.

München 2016

# DNA Origami Templated Plasmonic Nanostructures

**Eva-Maria Roller**

Dissertation
an der Fakultät für Physik
der Ludwig-Maximilians-Universität
München

vorgelegt von
Eva-Maria Roller
aus Calw

München
4. November 2016

| | |
|---|---|
| Erstgutachter: | Prof. Dr. Tim Liedl |
| Zweitgutachter: | Prof. Dr. Alexander Högele |
| Tag der Verteidigung: | 21. Dezember 2016 |

Titelbild: DNA origami template structures designed within this thesis.

# Publications

Publications based on the results of this thesis:

- *DNA-Assembled Nanoparticle Rings Exhibit Electric and Magnetic Resonances at Visible Frequencies.*
  E.-M. Roller, L. Khosravi Khorashad, M. Fedoruk, R. Schreiber, A. O. Govorov, and T. Liedl
  **Nano Letters**, 15, 1368 - 1373 (2015).
- *Plasmon-Exciton Coupling Using DNA Templates.*
  E.-M. Roller, C. Argyropoulos, A. Högele, T. Liedl, and M. Pilo-Pais
  **Nano Letters**, 16, 5962 - 5966 (2016).
- *Quantitative single molecule surface-enhanced Raman Scattering by optothermal tuning of DNA origami assembled pasmonic nanoantennas.*
  S. Simoncelli*, E.-M. Roller*, P. Urban, R. Schreiber, A. J. Turberfield, T. Liedl, and T. Lohmüller
  **ACS Nano**, 10, 9809 - 9815 (2016). *equal contribution
- *Hot spot-mediated non-dissipative and ultrafast plasmon passage.*
  E.-M. Roller, L. V. Besteiro, C. Pupp, L. Khosravi Khorashad, A. O. Govorov, and T. Liedl
  Submitted.

Manuscript based on the results of this thesis:

- *Plasmonic Focus Point Analysis of Chiral Molecules.*
  L. M. Kneer*, E.-M. Roller*, R. Schreiber, A. O. Govorov, and T. Liedl
  Manuscript in preparation. *equal contribution

Further publications:

- *Alignment and Graphene-Assisted Decoration of Lyotropic Chromonic Liquid Crystals Containing DNA Origami Nanostructures.*
  K. Martens, T. Funck, S. Kempter, E.-M. Roller, T. Liedl, B. M. Blaschke, P. Knecht, J. A. Garrido, B. Zhang, and H. Kitzerow
  **Small** 12, 1658 - 1666 (2016).
- *Plasmonic DNA-Origami Nanoantennas for Surface-Enhanced Raman Spectroscopy.*
  P. Kühler, E.-M. Roller, R. Schreiber, T. Liedl, T. Lohmüller, and J. Feldmann
  **Nano Letters**, 14, 2914 - 2919 (2014).

- *Hierarchical assembly of metal nanoparticles, quantum dots and organic dyes using DNA origami scaffolds.*
  R. Schreiber*, J. Do*, E.-M. Roller, T. Zhang, V. J. Schüller, P. C. Nickels, J. Feldmann, and T. Liedl
  **Nature Nanotechnology** 9, 74 - 78 (2014). *equal contribution
- *DNA-based self-assembly of chiral plasmonic nanostructures with tailored optical response.*
  A. Kuzyk*, R. Schreiber*, Z. Fan, G. Pardatscher, E.-M. Roller, A. Högele, F. C. Simmel, A. O. Govorov, and T. Liedl
  **Nature** 483, 311 - 314 (2012). *equal contribution

## Contributions to conferences and workshops

- *Nanoscale DNA origami based plasmonic metal nanoparticle rings*
  E.-M. Roller, R. Schreiber, and T. Liedl
  **Programmable Self-Assembly of Matter**, New York, United States, 2013.
- *Nanoscale DNA origami based plasmonic ring structures*
  E.-M. Roller, L. Khosravi Khorashad, M. Fedoruk, R. Schreiber, A. O. Govorov, and T. Liedl
  **CeNS Workshop 2014 - Walk and Talk at the Nanoscale**, Venice, Italy, 2014.
- *DNA-assembled Nanoparticle Rings with Electric and Magnetic Resonances at Visible Frequencies*
  E.-M. Roller, L. Khosravi Khorashad, M. Fedoruk, R. Schreiber, A. O. Govorov, and T. Liedl
  **Metamaterials'2015 - The 9th International Congress on Advanced Electromagnetic Materials in Microwaves and Optics**, Oxford, United Kingdom, 2015.
- *Nanoscale DNA origami based plasmonic structures*
  E.-M. Roller, L. M. Kneer, L. Khosravi Khorashad, M. Fedoruk, R. Schreiber, A. O. Govorov, and T. Liedl
  **DNA Nanotechnology meets Plasmonics**, Bad Honnef, Germany, 2015.
- *Nanoscale DNA origami based plasmonic structures*
  E.-M. Roller, M. Pilo-Pais, and T. Liedl
  **Statussymposium on Functional Macroscopic Systems**, Hanover, Germany, 2016.

# Kurzfassung

Die Beeinflussung, Konzentrierung und Steuerung von Licht durch nanoskopische Materialien ist auf Grund der vielfältigen Anwendungsgebiete in Bereichen wie der Optoelektronik, der Metamaterialforschung und im Feld hoch sensitiver optischer Detektion von großem Interesse. Strukturen aus Metallnanopartikeln sind bekannt für ihre Eigenschaften der plasmonischen Kopplung und Feldverstärkung auf einer Größenskala wesentlich kleiner als der Lichtwellenlänge. Entscheidend für die optische und sensorische Funktion plasmonischer Strukturen ist die exakte räumliche Anordnung der metallischen Nanokomponenten sowie der zu detektierenden Moleküle. Ziel dieser Arbeit war es, mittels der DNA Origami Methode plasmonische Nanostrukturen mit maßgeschneiderten optischen Eigenschaften herzustellen und zu charakterisieren. Hierfür wurde die sich selbst organisierende DNA Origami Technik verwendet, um nanoskopische Trägerstrukturen zur Positionierung von Nanopartikeln und (Farbstoff-) Molekülen zu erzeugen.

Im ersten Teil dieser Arbeit wurde eine ringförmige Anordnung aus Goldnanopartikeln hinsichtlich ihrer elektrischen und magnetischen Resonanzen mittels Einzelstruktur-Dunkelfeldspektroskopie untersucht. Das Vorhandensein magnetischer Resonanzen im sichtbaren Wellenlängenbereich konnte nachgewiesen werden. Solche Resonanzen sind eine der Grundvoraussetzungen für optische Metamaterialien. Im zweiten Teil wurde die Wechselwirkung von Plasmonen und Exzitonen untersucht. Hierzu wurde die Kopplung eines Systems bestehend aus einem Nanopartikel Dimer und einem Farbstoff durch Untersuchung der Fernfeld-Streueigenschaften charakterisiert. Der dritte Teil dieser Arbeit bezieht sich auf plasmonische Sensoren für chirale Moleküle. Dabei wurde das im ultravioletten Bereich liegende Zirkulardichroismus-Signal chiraler Moleküle, die sich im plasmonischen Heißpunkt zweier Goldnanopartikel befinden, auf den sichtbaren Wellenlängenbereich übertragen und verstärkt. Im vierten Teil wurde die Energieübertragung in heterogenen Trimerstrukturen bestehend aus Gold- und Silbernanopartikeln analysiert. Es konnte gezeigt werden, dass die Übertragung zwischen den zwei äußeren Partikeln ohne nennenswerten Energieverlust im zentralen Nanopartikel stattfindet. Somit konnte ein plasmonisches Transfersystem realisiert werden. Im letzten Teil dieser Arbeit wurde ein Farbstoffmolekül zentral im plasmonischen Heißpunkt aus zwei Goldnanopartikeln mittels einer DNA Origami Struktur platziert. Durch nachfolgendes Aufheizen der Struktur konnte der Abstand zwischen den zwei Goldnanopartikeln reduziert werden. Dies ermöglichte oberflächenverstärkte Raman Messungen des Farbstoffes auf der Einzelmolekülebene. Die DNA Origami basierte Vorgehensweise diente somit zur Charakterisierung verschiedenster plasmonischer Systeme.

# Abstract

Nanoscale materials for the manipulation, concentration and guidance of light are of great interest due to their potential applications in signal modulation, metamaterials research and sensitive optical detection. Metallic nanostructures are known for their plasmonic coupling, strong field confinement and enhancement properties in subwavelength regions. The precise spatial and geometrical arrangement of the nanocomponents with respect to the molecules to be detected is crucial for the optical and sensory properties of plasmonic structures. The scope of this thesis was to create and characterize plasmonic DNA origami based nanostructures with tailored optical properties. For this purpose, the DNA origami technique was used to create artificial self-assembled templating structures for the precise geometrical and spatial arrangement of metal nanoparticles and (dye) molecules.

In the first part of this work, the optical response of ring shaped arrangements of gold nanoparticles was measured by single structure dark-field scattering spectroscopy. It was shown that the ring shaped arrangement support electric and artificial magnetic resonances in the visible frequency domain, which is a prerequisite for the development of plasmonic metamaterials. In the second part of this thesis, the interaction of plasmons and excitons was studied. For this, a system consisting of a gold nanoparticle dimer and a dye was characterized by far field scattering spectroscopy. The plasmon-exciton coupling interaction displayed itself in distinct hybrid states. The third part of the thesis covers plasmonic sensors for chiral molecules. Chiral molecules were placed in a plasmonic hot spot, which resulted in the enhancement and transfer of the molecular circular dichroism signal to the plasmon resonance wavelength. In the fourth part of the thesis, the coherent energy transfer in heterogeneous trimer structures consisting of gold and silver nanoparticles was analysed. It was shown, that the energy is transferred between the two outer particles via the third intermediate particle without energy dissipation. Thus, a plasmonic passage system was realized. In the last part of this thesis, a single dye molecule was placed precisely within a plasmonic hot spot of two gold nanoparticles using a DNA origami structure. It was possible to subsequently reduce the gap size by heating the structure. This allowed for the analysis of the dye, on a single molecule level, by surface enhanced Raman spectroscopy. Overall, the DNA origami templating approach allowed for the characterization and investigation of various different plasmonic systems.

# Contents

# 1. Introduction

Nanotechnology deals with the control, manipulation, study and application of matter at the atomic or molecular scale (nanoscale). It is widely interdisciplinary as it involves multiple disciplines such as physics, chemistry, biology, material science and engineering. The initial suggestion to engineering matter at the nanoscale was given in 1959 at the annual American Physical Society meeting at Caltech by the physicist Richard Feynman in his famous talk "There's Plenty of Room at the Bottom". Nowadays, the impact of nanotechnology research has reached everyday life, from antibacterial agents based on silver nanoparticles to sunscreens based on zinc oxide nanoparticles.

Due to their increased surface to volume ratio, the physical, chemical and biological properties of nanoscale materials are often distinctly different from their bulk material counterparts. Examples of these new properties include enhanced chemical reactivity, increased mechanical stability and unique optical features [1, 2]. The latter point is of particular relevance for noble metals if the size reaches the nanoscale regime and thus the structure's size is smaller than the wavelength of visible light. Metal nanoparticles have a large effective scattering and absorption cross sections and their resonance frequency strongly depends on their size, shape and surroundings. Moreover, they enhance the field in their vicinity when subjected to incident light. The scattering of an electromagnetic wave by a spherical metal nanoparticle was described analytically by Mie and Lorenz at the beginning of the 20th century [3, 4]. The unique optical properties of metal nanoparticles are caused by collective oscillations of their free electrons. The corresponding quasiparticle is called *localized surface plasmon* [5]. Today, metal nanoparticles of different types can be synthesized in various sizes and shapes with resulting predefined optical properties [6, 7]. Moreover, they can be functionalized with various chemical groups [8]. As a result, metal nanoparticles have received much attention as functional components of nanotechnological devices, covering a wide range of diverse applications such as sensing, drug delivery and imaging [9].

Despite the current advances and commercialization, in order to produce new devices possessing features on the nanometer scale, reliable manufacturing methods with precise nanoscale arrangement of components and structural control are needed. The existing nano-manufacturing methods can be classified into two major approaches: *top-down* and *bottom-up* fabrication [10].

In the top-down methods, nanoscale structures are achieved by reducing, cutting or shaping large, bulk pieces of materials to nanoscale dimensions or by directly writing nanoscale features on top of a bulk solid support layer. Well known top-down methods are photo- and electron beam lithography [11, 12]. Top-down constructed metal nanostructures have reached high precision over macroscopic length scales [13, 14]. However, photo-lithographical techniques are currently limited in the minimum feature size while electron beam lithography is not suitable for high throughput manufacturing due to its direct writing nature. Moreover, metal nanostructures fabricated by lithography suffer from high surface roughness and inherent grain boundaries compared to colloidal synthesized metal nanostructures, which is unfavourable for plasmonic applications.

In contrast, the bottom-up approach relies on the arrangement of small components such as individual atoms or molecules with respect to each other to create nanoscale objects and complex systems. In bottom-up self-assembling methods, the individual components organize themselves into two or three dimensional nanoscale structures. In general, the bottom-up self-assembling approach is fast and cost efficient. Self-assembled metal nanostructure complexes such as chain structures are reached either directly by interparticle forces between the particles or indirectly by using functional modifications of the metal nanocomponents [15, 16]. However, advanced complex metal nanostructures require the controlled placement and arrangement at the single component level. For this purpose, DNA nanotechnology has already demonstrated a significant impact in the field of metal nanostructure assembly.

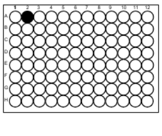

DNA nanotechnology offers a self-assembly methodology which is based on the intrinsic molecular recognition of DNA, permitting its use as a pre-programmable templating material. As such, it allows the artificial and complex arrangement of nanocomponents with novel properties. In recent years, the DNA origami technique developed in 2006 by Paul W. K. Rothemund [17], has emerged as a bottom-up approach to create complex and addressable nanoscale objects. A two or three dimensional DNA origami structure consists of a $\sim 7$-kilobase long single-stranded scaffold which is folded with the help of hundreds of shorter synthetic staple strands into the desired pre-programmed nanoscale shape [17–19]. The resulting objects are fully addressable since the exact spatial position of each DNA sequence is known by design. Other DNA functionalized nanocomponents such as metal nanoparticles and dyes can then be specifically attached to the DNA origmi structure via DNA base pairing. Thus, DNA origami objects serve as template structures for the subsequent spatial arrangement of nanocomponents. Thus, the technique allows to build complex, functional nanoscale objects from the bottom-up [20, 21].

### Content of this work

The scope of this thesis is to employ the DNA origami technique as a versatile templating method to create nanoscale, addressable and plasmonic active structures. For this, five different metal nanoparticle arrangements are investigated and the different interaction effects of plasmons, excitons and chiral molecules are studied.

The work is structured as follows: Chapter 2 introduces the theoretical background to DNA nanotechnology and how DNA is used as a nanoscale building material. Also, the optical properties of metal nanoparticle systems are shortly reviewed. Chapters 3 to 7 discuss optically active nanoscale systems in detail. Each of these chapters starts with a short overview of the respective theoretical and experimental background of the system under investigation, followed by a description of the analysed structure and its optical behaviour. Specifically, chapter 3 discusses ring shaped arrangements of metal nanoparticles which are able to support magnetic resonances in the visible frequency range. Chapter 4

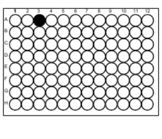

studies plasmon-exciton interactions of a dimer arrangement of gold nanoparticles and a dye molecule. Chapter 5 analyses the signal detection of a chiral molecule placed in between two gold nanoparticles. Chapter 6 investigates plasmonic passage systems in a heterogeneous trimer metal nanoparticle geometry. Chapter 7 deals with dye molecules placed in between two gold nanoparticles and studies the resulting surface enhanced Raman signal. The last chapter 8 summarizes all results and gives an outlook for future applications.

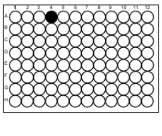

# 2. Theoretical Background

## 2.1. DNA Nanotechnology

Nanoscience and nanotechnology deal with the manipulation of matter on dimensions ranging from 1 nm to 100 nm. The control of individual atoms and molecules is crucial to fabricate defined nanoscale and macroscale structures with engineered properties such as stability, weight, chemical reactivity, electronic properties and interaction with light. The great challenge in this field is to develop arrangement techniques and strategies for the precise three dimensional organization of individual atoms, molecules, and nanoscale components to create functional nanoscale objects. Over the last decades, DNA nanotechnology has emerged as a method able to fulfill such organizational demand. In comparison to lithographical top-down approaches, DNA nanotechnology is part of bottom-up self-assembling methodologies. Here, single components are arranged into larger complexes via molecular recognition driven by the Watson-Crick base pairing.

### 2.1.1. Basic Properties of Deoxyribonucleic Acid

Nucleic acids, proteins, carbon hydrates and lipids are the required molecules for living organisms. Whereas the large biopolymer nucleic acid, categorized into deoxyribonucleic acid (DNA) or ribonucleic acid (RNA), stores the genetic information. In 1869, DNA was first isolated by the Swiss physician Friedrich Miescher [22]. In the following years, progress in DNA isolation as well as in revealing its chemical composition [23] took place. In 1943 Oswald Avery and colleagues demonstrated the function of DNA as the carrier of genetic information which was later on confirmed by the Hershey-Chase experiment [24]. Based on X-ray diffraction patterns produced by Rosalind Franklin and Maurice Wilkins the DNA double helical structure was firstly described by James Watson and Francis Crick in 1953 [25]. For this breakthrough discovery James Watson, Francis Crick and Maurice Wilkins were honoured with the Nobel Prize in Physiology or Medicine in 1962.

The biopolymer DNA consists of repeating units called *nucleotides*. Each nucleotide itself is composed of a sugar (2-deoxyribose), a phosphate group and one out of four different nitrogen-containing *nucleobases*. The four nucleobases are cytosine (C), guanine (G), adenine (A) and thymine (T), whereas A and G are purine bases and T and C are pyrimidine bases. In a single stranded DNA (ssDNA) chain the nucleotides are covalently linked together by phosphodiester bonds between the 5'-phosphate and the 3'-hydroxyl group of two neighbouring pentose sugars. This linking of nucleotides results in a directional phosphate-deoxyribose backbone strand with a 5' phosphate end and a 3' hydroxyl end. In neutral pH, DNA is negatively charged because of the deprotonation of each phosphate group on the backbone [26].

In a double stranded DNA (dsDNA) helix, two single strands hybridize in antiparallel manner. The planar bases are pointing inside, the backbones are facing outwards of the double helix centre. That structure guarantees that in buffer conditions, the hydrophilic ionic backbones are pointing toward the surrounding medium while the hydrophobic bases are inside. Salt in the buffer solution compensates for the equal charging of the backbones and prevents dsDNA from denaturation into two ssDNA strands due to electrostatic repulsion forces. In a dsDNA helix the preferred base hybridization occurs between the complementary Watson-Crick basepairs A and T as well as the pair G and C (see figure 2.1). The numberless possible combinations of base sequences in a DNA chain allows to encode genetic information. The Watson-Crick basepairs differ in the amount of hydrogen bonds formed between complementary bases. For CG combination three hydrogen bonds are formed while for AT pairs only two hydrogen bonds are possible. The result of this asymmetry is that dsDNA with a higher CG content is slightly more stable than one with a lower CG content [27, 28].

The stability of dsDNA arises mainly from the attractive forces of the hydrogen bonds between each paired bases as well as from the *stacking interactions* between

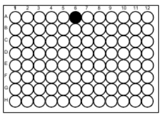

adjacent bases. The base stacking results from overlapping of delocalized $\pi$-electron systems. Both interactions are responsible for the double helix formation and both are relatively weak compared to other chemical binding mechanism such as covalent bonds. Therefore it is important to look at the thermal stability of dsDNA. A parameter for that is the *melting temperature* $T_m$ of double stranded DNA, which is defined as the temperature at which half of the DNA strands in solution are in a double stranded configuration while the other strands are denatured.

Experimentally the melting temperature is determined by measuring the absorption at $\lambda = 260\,\mathrm{nm}$ while heating the DNA in solution. At $\lambda = 260\,\mathrm{nm}$ the DNA bases have an absorption maximum for light. The amount of absorption depends on the base pairing. Double stranded DNA has a smaller molar absorption coefficient as the sum out of the molar absorption coefficients of the single nucleobases. Therefore, the absorption increases with dissociation of the hydrogen bonds or in other words with higher temperature. The typical DNA melting curve has a sigmoidal shape. Alternatively, the DNA melting temperature can be calculated using the following equation which includes the nearest neighbour model for Watson-Crick base pairs [27]:

$$T_m[^\circ\mathrm{C}] = \frac{\Delta H^0 \cdot 1000}{\Delta S^0 + R \cdot ln(\frac{C_T}{4})} - 273.15 \tag{2.1}$$

$\Delta H^0$ is the change in enthalpy in [kcal/mol], $\Delta S^0$ is the change in entropy in [cal/mol·K], $C_T$ is the total molar strand concentration in [M], $R$ is the gas constant in [cal/mol·K].

The geometrical parameters of the dsDNA helix depend on the DNA conformation. The so called B-DNA form is most common found under physiological conditions. B-DNA has a right handed double helix structure with a distance of 0.34 nm between adjacent nucleotides, a helical pitch of 10.5 nucleotides, and a diameter of 2.0 nm. Moreover, a DNA double helix offers alternating a major and a minor groove with widths of 2.2 nm and 1.2 nm, respectively. The grooves are caused by the two different glycosidic bond angles. The obtuse angle forms the major groove, the acute angle the minor groove [29, 30]. Depending on the

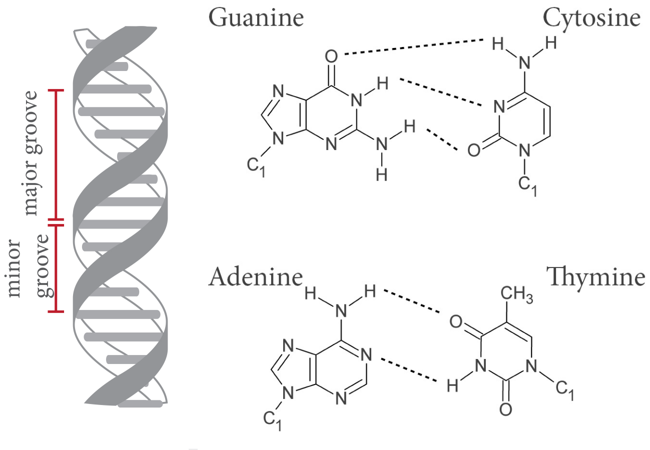

(a) (b)

Figure 2.1.: Structure of DNA. **(a)** Schematic illustration of B-form DNA double helix with major and minor grooves. **(b)** DNA base pairs with the hydrogen bonds illustrated as dashed lines.

sequence, environmental parameters such as pH-value, hydration level, salt concentration etc. [31] other double helix conformations such as the right handed A-form or the left handed Z-form are possible.

### 2.1.2. DNA as a Building Material

Ever since the double helical structure of dsDNA was predicted in 1953 by Watson and Crick and the final confirmation of the importance of its structure for replication by the Meselson-Stahl experiment, the progress and research activity in the field of molecular biology and genetics was immense. In 1982, another field of DNA research was started by Nadrian Seeman - the field of structural DNA nanotechnology where DNA is not used in its biological context but as a building material. Nadrian Seeman proposed to use branched DNA junctions to create lattices and not only linear duplexes [32]. Three decades later this field of structural DNA nanotechnology has grown tremendously and has proven its potential to control matter on the nanoscale [33, 34].

The next section will give a short overview how the intrinsic material properties of the DNA molecule enable and promote nanoscale engineering. A more detailed description can be found in reference [35].

### Nanoscale dimensions

With its inherently nanoscale dimensions of 2 nm in diameter, 0.34 nm separation distance between adjacent bases and a pitch of 10.5 base pairs per turn, the DNA double helix lends itself to be a building material for nanoscale objects. The rigid geometry of the DNA double helix with a persistence length of $\sim 50\,\mathrm{nm}$ [36–38], makes it furthermore possible to design and construct complex three dimensional geometries on the nanoscale.

### Programmable self assembling

The geometry of a DNA based nanoconstruct is programmable and formed by hybridization of complementary strands. Whereas the exact DNA sequence of those strands is artificially designed to produce individual motifs as soon as they build Watson-Crick base pairs. The basic motif used in programmed DNA nanostructures is the *Holliday junction* [39] which is displayed in figure 2.2(a). The designed highly specific and energetically favoured hybridization of the complementary bases A and T, as well as G and C is the underlying crucial principle of self-assembled DNA nanoconstructs. Additional two double stranded helices can cohere over *sticky end* hydrogen bonding. A sticky end is a single stranded elongation of a double stranded helix, which can bind to a complementary single stranded overhang of a second double stranded helix (see figure 2.2(b)). It is worth to note that the resulting structure, an elongated Watson-Crick double helix, is a priori known and that there is no other technique such as crystalline analysis needed to predict the relative three dimensional orientation of cohered DNA double helices.

### Stable branched DNA constructs

To create arbitrary shaped DNA constructs, it is important that other motifs than a straight DNA double helix are stable. The availability of DNA motifs with branched helical axis is crucial for DNA nanotechnology. Such branched motifs occur in nature, one example been the four-arm branched Holliday junction. Four DNA strands are linked together to four double helices in such a way that they form the shape of a cross. In biology, Holliday junctions usually have a symmetric sequence and play a key role in genetic recombination processes [39, 40]. This symmetry in the sequence leads to a not fixed junction. The four branches can migrate through the crossing point. In contrast, artificially designed Holliday junctions can have asymmetric sequences close to the crossing point, which prevents the branch migration. With that the Holliday junction is a stable immobile construction to achieve four branched junctions. Also multiple branched junctions can be achieved by designing the DNA sequences accordingly. Two and three dimensional lattices are formed if multiple Holliday junctions are linked together via sticky ends.

### Producibility and Integrability

The basic components of stable, custom shaped, pre-programmable DNA nanoconstructs are the individual single DNA strands with. Their sequences determine the shape of the hybridized structure. Whereas each of the individual single DNA strands must have its specific sequence. Therefore the availability of single stranded DNA of any sequence is crucial and a pre-requirement for programmable DNA nanoconstructs. Nowadays synthetic DNA strands can be industrially produced in almost every sequence and with different oligonucleotide functionalizations such as thiol modifications and fluorescent tags. These custom oligonucleotides are commercially available with high yield up to $\sim 60$ bases long.

All these different characteristics of DNA can result in self organized, predictable, chemically and physically relative stable nanoscale constructs which consist not only of linear chains but also of branched junctions. In 1991 the first artificial nanoscale DNA construct - a cube - was realized by the group of Nadrian Seeman [41]. The cube structure contains twelve double stranded edges having the same length and eight junctions at the cube corners. To reach this geometry six single stranded DNA molecules are used, each of them surrounding one cube

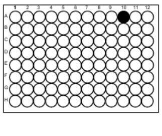

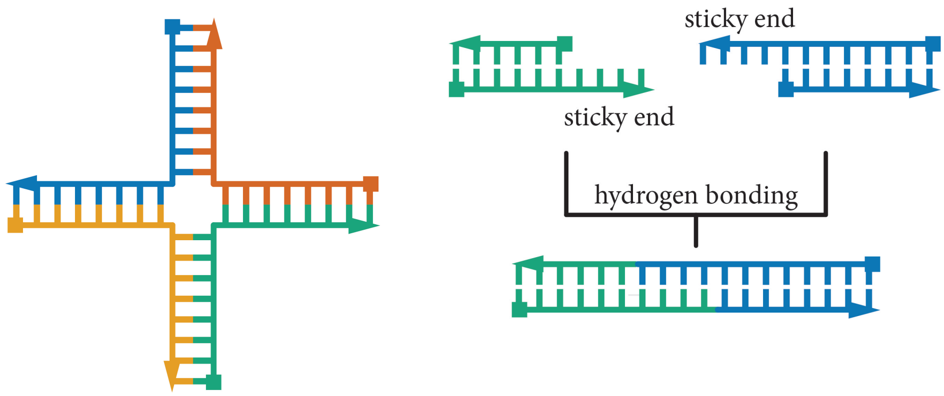

(a) (b)

Figure 2.2.: DNA Motifs. **(a)** Schematic illustration of a Holliday junction formed by four DNA strands. **(b)** Illustration of sticky end binding over short single stranded overhangs.

face. Each of this single strand is hybridized to four neighbouring strands. In the following years other geometries such as octahedrons and 2D crystals were realized [42, 43]. Additional types of junctions were established. One of them is the DNA double crossover junction where two single strands of different directionality are linked together by the crossover of an additional single DNA strand. The double cross over motif is used to link DNA helices together.

### 2.1.3. DNA origami method

In 2006, the field of structural DNA nanotechnology received an additional impulse through the invention of the so called 'DNA origami' method. This method was first proposed and implemented by Paul Rothemund [17] and raised the complexity and size of DNA nanoconstructs to the next level. The term origami refers to the Japanese folk art of folding paper into desired shapes. The same is done on the nanoscale level with a long viral single stranded DNA strand, called scaffold strand, which is folded into the desired shape by the help of hundreds of short synthetic oligonucleotides, called staple strands. Usually the scaffold strand has a length of around $7-8$ kBases and is derived from the bacteriophage M13. The staple stands are 20 to 60 nucleotides long.

The technique proposed by Rothemund is a one pot self-assembling method where the scaffold strand and the staple strands are mixed together in salt containing buffer. Firstly, the solution is heated up to $\sim 65°C$ to denature all dsDNA and then slowly cooled down over the course of a couple of hours so that the staple strands can bind to their corresponding scaffold segment. During the cooling down step, the staples strands are hybridizing to their complementary positions on the scaffold strand. Since one staple stand is complementary at least to two distinct segments on the scaffold strand, the long scaffold is forced to fold into the predesigned shape. Shapes realized by Rothemund are two dimensional squares, stars, disks and triangles. Their dimensions are around 100 nm x 100 nm and fold with high yields up to 90 %.

A huge advantage of the DNA origami method in comparison to single stranded DNA assemblies is, that the quality and purity of the staple stands is not crucial to reach high yields of correctly folded structures and that time consuming DNA sequence design with stoichiometry studies is not required. Moreover, the structures are highly addressable since the exact spatial position of every single staple strand is known. Rothemund also showed that by elongation of distinct staple strands at predefined positions on the surface of the DNA origami structures with hairpins. With that, patterns such as a world map or words were visible via atomic force microscopy. Additionally, larger DNA origami patterns can be reached by multimerization of several single DNA origami structures. The origami technique allows constructing nanoscale objects with robust, designed geometrical features.

In 2009, the field of DNA-origami received its next boost by the invention of three dimensional DNA origami structures [18, 44, 45]. The group of Douglas *et al.* [18] extended Rothemund's two dimensional technique to the third dimension by stacking multiple sheets of DNA double helices. To achieve this, the helices were interconnected to their neighbours by staple and scaffold crossovers. A scaffold or staple crossover between two parallel double helices is possible at positions were the corresponding bases are pointing towards each other. Taking

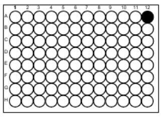

the intrinsic rotation of B-DNA with a pitch of 21 bases per two full turns into account, after 7 bases the spatial orientation of a possible crossover point is rotated exactly by 240°, after 14 bases by 480° and after 21 bases 720°. Thus, a double helix can be connected to three neighbours via crossover points at those in multiple of 7 bases repeating positions. With that, the spatial orientation of the helices results in a *honeycomb lattice* with an 120° angle between the helices.

Another arrangement method for three dimensional DNA-origami structures is based on a *square lattice*. Here, each double helix can have four neighbours with an angle of 90° between the helices. DNA-origami structures designed with a square lattice are more dense and offer flatter surfaces than those designed with the honeycomb lattice. The crossover points for those structures are multiple of 8 bases apart of each other. Since the square lattice geometry with its 90° angles is not exactly matching the intrinsic rotational properties of B-DNA, structures based on this lattice suffer from a general twist. The twist can be corrected by additional insert or delete base pairs in between crossover points to counteract the general twist. The same principle is used to create twisted and curved DNA-origami structures [19]. For example, a curved structure is achieved by insert additional base pairs at the outer helices to get a larger diameter and delete base pairs at the inner helices to bend the structure.

Overall, the DNA origami method allows to design and to construct two and three dimensional nanostructures of almost arbitrary shapes as shown in figure 2.3. Importantly, the exact spatial location within the nano-structure of every single staple strand and its corresponding sequence is known - each staple strand is addressable. Thus, another intrinsic property of DNA - the base pairing - can be used to functionalize the nanoconstructs. For that, two basic approaches are used. Either specific staple strands are directly modified with chemical linkers such as dyes or staple strands are extended with a specific sequence. Those staple strands are called *handles*. Components such as metal nanoparticles functionalized with the complementary handle sequence can thus be attached to the DNA-origami structure [46] as illustrated in figure 2.4. The use of a predefined amount of handles at predefined positions opens the doors to not only structure materials on the nanoscale but also to give the nanoconstructs functionality.

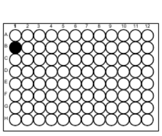

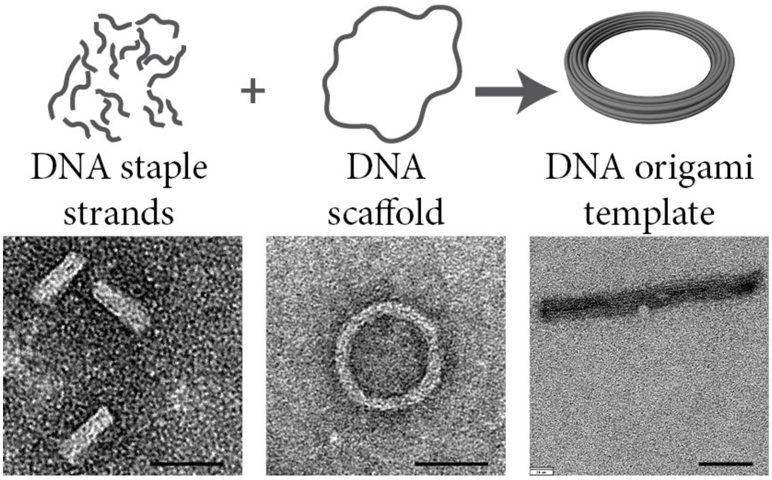

Figure 2.3.: Scheme of DNA origami folding and TEM images of DNA origami structures. Left panel: A long viral scaffold strand is folded with the help of short synthetic staple strands in the predefined, designed shape. Right panel: TEM images and 3D illustration of different realized structures. From left to right: a four layer sheet, a donut shape structure and two bridged cylindrical 14 helix bundles. Scale bar 50 nm.

With that, the field of DNA-origami nanotechnology was extended from structural to functional orientated materials. Within the last years the DNA-origami method was proofed to be a viable tool to design nanoscale objects with broadband functionality ranging from biosensing and nanomedicine to superresolution microscopy [47–52]. DNA-origami constructs can be used as template materials to organize metal nanoparticles, dyes and quantum dots with nanometer precise accuracy [21, 46, 53–56]. In the field of plasmonics, the use of such template structures to organize metal nanoparticles with high accuracy allowed to gain new insights into optical effects arising from the spatial arrangement of nanoparticles [20, 57].

## 2.2. Metal nanoparticle systems

Systems consisting of noble metal nanoparticles are highly interesting since they interact with the visible light. Long before the optical properties of metal nanopar-

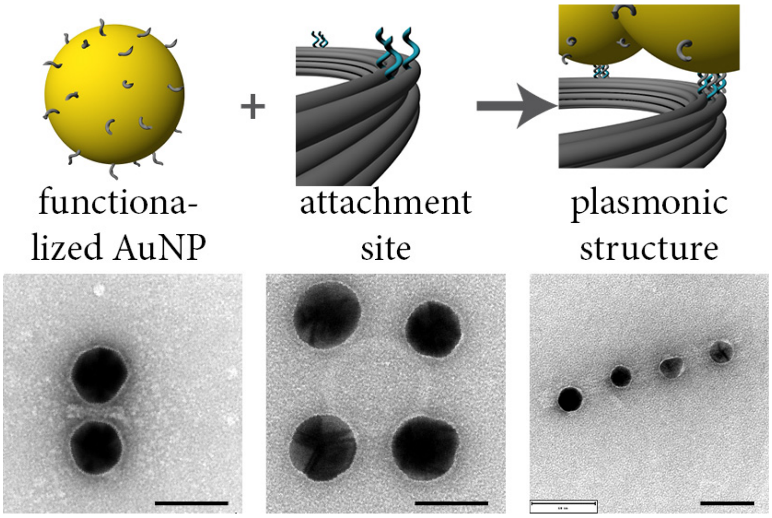

Figure 2.4.: Functionalization of a DNA origami template structure. Left panel: A DNA functionalized nanoparticle is attached to a DNA origami template structure via complementary base pairing. Right panel: Spatial organized gold nanoparticle by attachment to DNA origami structures illustrating the versatility of the DNA origami template approach for plasmonic nanoparticle organizations. Scale bar 50 nm.

ticle systems were investigated, they have been used in staining glass. One of the first known metal nanoparticles containing object is the Lycurgus Cup, a Roman glass cage cup, from the 4th-century. Due to the containing gold and silver nanoparticles, this cup shows a dichroic optical behaviour; its colour appears to be different depending on the observation of light in transmission or reflection. Another example are medieval church windows, where metal nanoparticles of different material and sizes were used to achieve the brilliant colours. However the underlying chemical and optical properties were not yet understood.

The first synthesis of pure colloidal gold nanoparticles (AuNPs) was achieved by Michael Faraday in 1856. The systematic studies to electromagnetic properties of noble metal nanoparticles started in the early 1900 with the works of Gustav Mie and Rufus Ritchie with the theoretical description of the absorption and scattering properties. Nowadays, the field of plasmonics is boosted by the development of better and better nano fabrication techniques such as electron beam lithography and self-assembling approaches. Today, metal nanoparticle systems can be found in different applications such as sensor systems, waveguides and solar cells [58–60].

The following sections will give a basic overview about optical properties of noble metal nanoparticles, the underlying concepts to describe them and how they interact. The sections are mainly written according to the book of Maier [61]. Further reading and detailed derivations can also be found in the books of Barnes [62] and Kreibig [63].

### 2.2.1. Fundamentals of Plasmonics - particle plasmon excitation

The typical size of metal nanoparticles ranges from 5 nm to 100 nm, which is in the range of the penetration depth of electromagnetic waves at visible frequencies [64] (e.g. for AuNPs up to 40 nm). For nanoparticles much smaller than the wavelength of light, the electromagnetic wave fully penetrates the particles without changing its phase. Metal nanoparticles already exhibit a band structure with *quasi free* electrons in the conduction band. Those electrons that are loosely bound to the nuclei cause the unique optical and physical properties of metals. If an electromagnetic wave interacts with a metal (nanoparticle), the *quasi free electron gas* of the conduction band is deflected in phase with respect to the fixed positively charged remaining atomic core. This charge distribution causes due to Coulomb's law a restoring force. The electrons oscillate back and forth with the frequency of the external electromagnetic wave. This process can be described with a classical driven harmonic oscillator model with a damping constant. The corresponding quasi particle for this collective oscillations of the free electron gas density is called *plasmon*.

Due to the acceleration of the electrons out of their equilibrium, an electromagnetic wave - the scattered light of the particle - is radiated. The intensity of the scattered light for a nanoparticle is frequency dependent. In the scattering spectrum of a metal nanoparticle a resonance frequency is observed, which occurs for gold and silver nanoparticles in the visible frequency range. The exact spectral position and intensity of the plasmon resonance frequency depends on the material, geometrical shape and size of the nanoparticle as well as on the sur-

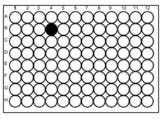

rounding medium. After introducing the concept behind plasmons, the following section describes light matter interaction and the plasmon resonance of spherical metal nanoparticles in greater detail.

### 2.2.2. Dielectric Function of the Free Electron Gas

The optical and electrical properties of metals are described in their dielectric response function $\epsilon_r$. The dielectric response expresses how strong a material is reacting to an external electric field. For metals such as gold and silver the dielectric function is dominated by the conduction band electrons in the visible frequency range. A classical description is the free electron model, also known as *Drude-Sommerfeld model.* In this model, the electrons are considered as an ideal gas of free electrons, meaning that electron-electron interactions, as well as details of the lattice potential are completely neglected.

The electrons respond with coherent oscillations to an applied electromagnetic field, whereas their motion is damped via collisions having a characteristic collision frequency $\gamma = 1/\tau$, with $\tau$ the relaxation time of the free electron gas. The equation of motion for an electron of mass $m_e$ of the free electron gas which is subjected to an external electric field $\vec{E}(t) = \vec{E}_0 e^{(-\mathrm{i}\omega t)}$ can be written as:

$$m_e \ddot{\vec{x}} + m_e \gamma \dot{\vec{x}} = -e\vec{E}(t) \tag{2.2}$$

A particular solution to this equation 2.2 is $\vec{x}(t) = \vec{x}_0 \vec{E}(t)$ with the complex amplitude $\vec{x}_0 = e/(m_e(\omega^2 + \mathrm{i}\gamma\omega))$. The displacement of the electron gas of density $n$ with respect to the fixed core causes a macroscopic polarization $\vec{P} = -ne\vec{x}$. Due to equation 3.2 $\vec{D} = \epsilon_0 \vec{E} + \vec{P}$ this results in a dielectric displacement:

$$\vec{D} = \epsilon_0 \left(1 - \frac{\omega_p^2}{\omega^2 + \mathrm{i}\gamma\omega}\right) \vec{E} \tag{2.3}$$

Whereas $\omega_p = \sqrt{\frac{ne^2}{\epsilon_0 m_e}}$ is the *plasma frequency* of the free electron gas with the electron density $n_e$, the elementary charge $e$, the permittivity of the vacuum $\epsilon_0$ and the electron mass $m_e$. The plasma frequency of gold is $\hbar\omega_p = 8.89\,\mathrm{eV}$ while the plasma frequency of silver is $\hbar\omega_p = 9.04\,\mathrm{eV}$ [65].

The complex dielectric function $\epsilon(\omega) = \epsilon_1(\omega) + \mathrm{i}\epsilon_2(\omega)$ of the free electron gas corresponds to

$$\epsilon(\omega) = 1 - \frac{\omega_p^2}{\omega^2 + \mathrm{i}\gamma\omega} \tag{2.4}$$

with the real part given as

$$\epsilon_1(\omega) = 1 - \frac{\omega_p^2}{\omega^2 + \gamma^2} \tag{2.5}$$

and the imaginary part

$$\epsilon_2(\omega) = \frac{\gamma\omega_p^2}{\omega(\omega^2 + \gamma^2)} \tag{2.6}$$

This model is valid for an ideal free-electron gas where $\epsilon \to 1$ at $\omega \gg \omega_p$. For noble metals, such as gold and silver, the model needs to be modified for $\omega > \omega_p$ due to a remaining polarization arising from the static background charging of the positive core ions. The polarization is extended to $\vec{P}_\infty = \epsilon_0(\epsilon_\infty - 1)\vec{E}$ with a dielectric constant $\epsilon_\infty$. With that, the dielectric function of noble metals is described as:

$$\epsilon(\omega) = \epsilon_\infty - \frac{\omega_p^2}{\omega + \mathrm{i}\gamma\omega} \tag{2.7}$$

More modifications in the Drude model such as coupling between the electrons and lattice atoms can be incorporated. For example, one can use the effective mass $m_{eff}$ instead of $m_e$ in the plasma frequency. However, the dielectric function is also influenced by the d-band electrons, which can be excited to the sp-conduction band at wavelength around 660 nm and lower. For that, a linear restoring force can be introduced as approximation in the equation of motion. In practical use, one usually resorts numerical simulations, and it is customary to use experimental frequency dependent dielectric functions. Common values to fit the dielectric function for gold and silver are taken from Johnson and Christy [66] and Palik [67]. The interaction of a nanoparticle with an external applied electromagnetic field and the simulated electric near field distribution of a 40 nm gold nanoparticle is shown in figure 2.5. Local regions of higher field enhancement - so called *hot spots* - around the nanoparticle are visible.

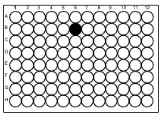

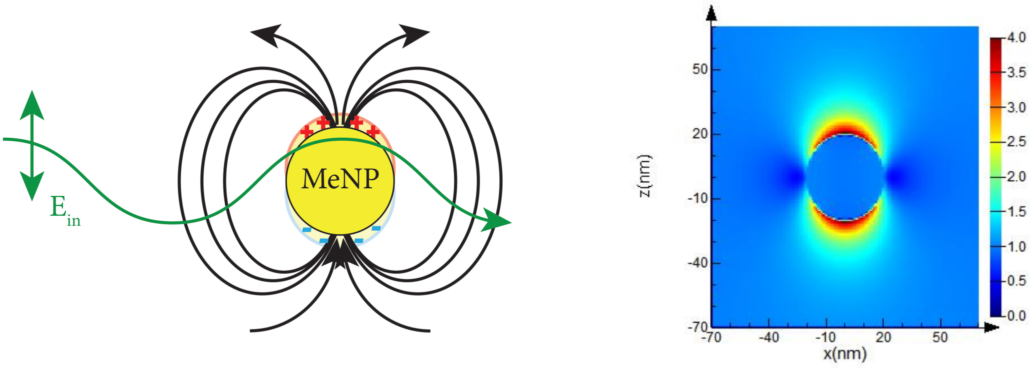

(a) (b)

Figure 2.5.: **(a)** Schematic illustration of the coherent oscillations of the free electrons in a metal nanoparticle due to interaction with an incoming electromagnetic field. **(b)** Simulation of the intensity distribuation of the electric near-field of a 40 nm gold nanoparticle in air at resonance.

### 2.2.3. Single Spherical Nanoparticle

For an exact solution of the absorption and scattering of a nanoparticle by light it would be necessary to solve Maxwell's equation with corresponding boundary conditions. To analyse the plasmonic properties of a metal nanoparticle of diameter $d$ and its interaction with the surrounding, it is necessary to know the electromagnetic field distribution inside and outside of the nanoparticle. The knowledge of the field distributions allows to calculate the scattering and absorption cross section of the nanoparticle. For spherical particles this is analytical exactly solvable as shown by Mie [3]. However, the approximation used for that in the following section, is the *quasi-static approximation* which is only valid for particles which are much smaller than the wavelength of the incident light ($d \ll \lambda$). Which means that the phase of the oscillating electromagnetic field is considered to be constant over the whole particle volume. A uniform, isotropic spherical nanoparticle with radius $r_p$, dielectric $\epsilon_p$, located in a surrounding medium with dielectric constant $\epsilon_m$ is placed in a constant static electric field $\vec{E}_{in} = E_0 \cdot \hat{e}_z$. The electric field causes an overall polarization of the nanoparticle. The solution of the *Laplace equation* $\nabla^2\Phi = 0$ allows to calculate the electric field $\vec{E} = -\nabla\Phi$.

With the boundary conditions

$$\Phi_{in}(r_p) = \Phi_{out}(r_p) \quad , \quad \epsilon_p \frac{\partial \Phi_{in}}{\partial r} = \epsilon_m \frac{\partial \Phi_{out}}{\partial r} \tag{2.8}$$

and the condition that the electric field at large distances from the nanoparticle is not influenced, the electrostatic potentials inside $\Phi_{in}$ and outside $\Phi_{out}$ of the nanoparticle sphere are calculated to be [68]:

$$\begin{aligned} \Phi_{in} &= -E_0 \frac{3\epsilon_m}{\epsilon_p + 2\epsilon_m} r cos(\Theta) \\ \Phi_{out} &= -E_0 r cos(\Theta) + E_0 {r_p}^3 \frac{\epsilon_p - \epsilon_m}{\epsilon_p + 2\epsilon_m} \frac{cos(\Theta)}{r^2} \end{aligned} \tag{2.9}$$

Equation 2.9 is similar to the potential of an ideal dipole [69] given as:

$$\Phi_{Dipol} = \frac{1}{4\pi\epsilon_m} \frac{p \cdot cos(\Theta)}{r^2} \tag{2.10}$$

Hence, the potential outside of the particle $\Phi_{out}$ is interpreted as the superposition of the applied field and an induced dipole with the dipole moment $\vec{p} = \epsilon_0 \epsilon_m \alpha \vec{E}_0$, where $\alpha$ the polarizability is:

$$\alpha = 4\pi {r_p}^3 \frac{\epsilon_p - \epsilon_m}{\epsilon_p + 2\epsilon_m} \tag{2.11}$$

This equation has the same functional form as the Clausius-Mossotti relation [68]. The complex polarizability $\alpha$ of a small sphere with subwavelength diameter is maximal amplified if the denominator of equation 2.11 $|\epsilon_p(\omega) + 2\epsilon_m| = min$ turns minimal. Since the imaginary part of the dielectric function $\epsilon_p(\omega) = \epsilon_{p1}(\omega) + \mathrm{i}\epsilon_{p2}(\omega)$ can be neglected, as the losses of metal nanoparticles are small, the condition simplifies to:

$$\epsilon_{p1}(\omega) = -2\epsilon_m \tag{2.12}$$

Equation 2.12 is the condition for the dipole *plasmon resonance* of a metal nanoparticle and its associated mode in an oscillating field is the *dipole plasmon* of the nanoparticle. The *plasmon resonance* is the resonant, coherent oscillation of the free conduction electrons with the applied electromagnetic field. The scattering of the nanoparticle is maximal at that frequency. For a Drude like particle the resonance frequency is due to equation 2.5 in combination with equation 2.12 and with the condition $\omega \gg \gamma$ given by:

$$\omega_{res} = \frac{\omega_p}{\sqrt{2\epsilon_m + 1}} \tag{2.13}$$

The resonance frequency is strongly dependant on the dielectric surrounding. If $\epsilon_m$ increases the resonance red-shifts. The distribution of the electric field $\vec{E} = -\nabla\Phi$ of a spherical nanoparticle in the near field can be calculated from the potentials given in equation 2.9 to:

$$\begin{aligned} \vec{E}_{in} &= \frac{3\epsilon_m}{\epsilon_p + 2\epsilon_m}\vec{E}_0 \\ \vec{E}_{out} &= \vec{E}_0 + \frac{1}{r_p^3}\frac{3\vec{n}(\vec{n}\cdot\vec{p}) - \vec{p}}{4\pi\epsilon_0\epsilon_m} \end{aligned} \tag{2.14}$$

with $\vec{n} = \frac{\vec{r}}{r}$. The field at the plasmon resonance is enhanced ($|\vec{E}|^2/|\vec{E}_0|^2$), but rapidly decreases with increasing distance from the nanoparticle ($E_{out} \propto \frac{1}{r_p^3}$).

The efficiency with which a nanoparticle scatters and absorbs light is also related to the polarizability. However the polarizability as in equation 2.11 varies only in the amplitude by changing the size of the metal nanoparticle, but not with respect to the wavelength of the light. The corresponding scattering, extinction and absorption cross sections of metal nanoparticles can be calculated out of the dipole radiation of the particle [70] to:

$$\begin{aligned} \sigma_{sca} &= \frac{k^4}{6\pi}|\alpha|^2 \\ \sigma_{abs} &= k\mathrm{Im}(\alpha) \\ \sigma_{ext} &= \sigma_{abs} + \sigma_{sca} \end{aligned} \tag{2.15}$$

with the wave number $k = 2\pi/\lambda$. The scattering cross section scales for small particles ($r_p \ll \lambda$) with $\sigma_{sca} \propto r_p^6$. In measured extinction cross sections of nanoparticles the peak shifts to a higher wavelength with increasing nanoparticle diameter. The quasi-static-approximation is no longer valid for larger particles, since the phase of the driving field changes over the particles volume; an electrodynamic approach is needed. In the *Mie theory* the scattered field for nanoparticle with sizes larger than $\lambda/10$ [3] is described by taking higher order multipole terms and not only the dipole term into account.

### 2.2.4. Plasmonic Coupling

If two plasmonic nanoparticles are in such close proximity that their near fields are overlapping, the electric field felt by each of these particles is the sum of the external applied field $E_0$ and the near field of the neighbouring particle. Thus their plasmon oscillations interact. A new plasmon mode exhibiting an energy different from the modes of the two single particles, arises. This interaction is called *plasmonic coupling* between the nanoparticles. Hereafter, the concept of plasmonic coupling will be shortly introduced by the example of a dimer geometry consisting of two closely spaced, identical, spherical metal nanoparticles. The coupling is seen as coupling of two dipoles. Two general coupled plasmon modes can be distinguished - a *bright mode* and a *dark mode*. In the dark mode, the induced dipoles cancel out in the far field, as the single particle plasmons are oscillating out of phase. It is worth to note that in the hetero-dimer case (two not identical particles) the dipoles don't cancel out and the dark mode gets visible in the far field. In addition, the dark mode is hard to stimulate optically. Whereas the bright mode has a non zero total dipole moment since the plasmons are oscillating in phase. The optical excitation of the bright mode is easily achievable [71, 72].

The coupling strength is dependent not only on the gap size between the nanoparticles and their size, but also on the orientation of the dimer axis with respect to the external applied electromagnetic field. The polarizability of the dimer structure is directional. For an incident plane wave polarized along the dimer axis the corresponding coupled plasmon mode is called *longitudinal mode*, for an incident wave polarized vertical to the dimer axis the mode is called *transversal mode*. The difference between those to modes can be explained by the induced dipoles. For the longitudinal mode, they are oriented parallel to the dimer axis, resulting in a stronger coupling, the incident field is increased by the induced dipoles. For the transversal mode the induced dipoles are vertical oriented, so that the cou-

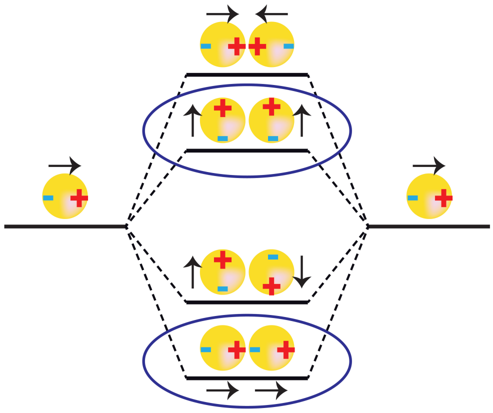

Figure 2.6.: Illustration of the energy diagram of two metal nanoparticles and its coupled modes. The energy level of the hybrid mode depends on the relative dipole orientation. The bright modes - the modes which can be excited optically - are marked with circles.

pling strength is reduced. A common model to visualize the plasmon coupling interaction is - in analogy to the hybridization of atomic orbitals in molecules - the plasmon hybridization picture. Figure 2.6 shows the above discussed modes for bonding (lower energy, red shifted) and for anti bonding (higher energy, blue shifted), the dark and bright modes are marked as well.

In close analogy to exciton coupling, where the field $E$ each dipole experiences is the sum of the incident field $E_0$ and the field of the neighbouring dipole, the plasmon hybridization can be modelled in the same way. The resulting dipole-dipole interaction energy is given by [68, 73, 74]:

$$U = -\frac{\zeta|\mu|^2}{4\pi\epsilon_0 r^3} \tag{2.16}$$

where $r$ is the distance between the dipoles and the orientation is given by the parameter $\zeta$. For polarizations along the axis $\zeta = 2$ the interaction energy is negative, the resonance is red shifted. For transversal polarization $\zeta = -1$ the interaction energy is positive, the dipole interaction is repulsive, resulting in a blue shift of in the spectrum. As smaller the distance between the particles is, as larger is the coupling strength. Most of the spectral features of plasmon coupling are represented in the dipole-dipole interaction picture, however it neglects higher order multipole terms and retardation effects of the electromagnetic field due to the size of the nanoparticles. Electrodynamic simulation methods such as finite-difference-time-domain (FDTD) and discrete dipole approximation (DDA) account for that. Figure 2.7 illustrates the interaction of two closely spaced gold nanoparticles with an electromagnetic wave as well as corresponding simulation of the electric near-field distribution done with Lumerical FDTD.

### 2.2.5. Plasmonic Heating

Metal nanoparticles are not only good light scatterers, but they can also be used to generate heat. Light absorbed by metal nanoparticles induces plasmon resonances. The scattered light, which arises from coherent electron oscillations, is the result of radiative decay process of the plasmons. A non-radiative decay channel arises from incoherent electron oscillations. The electrons undergo electron-electron or electron-phonon collisions, the kinetic energy is transformed into thermal energy resulting in heat generation [75], which is subsequently transferred to the surrounding medium. Under continuous light illumination the temperature equilibrium is reached as soon as the generated and dissipated thermal energy are balanced. The steady state temperature around a single, spherical nanoparticle can be calculated out of the heat transfer equation to be:

$$\Delta T(r) = \frac{V_{NP} Q}{4\pi k_0 r} \tag{2.17}$$

with $r$ the distance from the nanoparticle centre ($r > R_0$, $R_0$ nanoparticle radius), $k_0$ the thermal conductivity of the surrounding medium, $V_{NP}$ the volume of the nanoparticle and $Q$ the heat source of the system. It can be shown that the temperature increase is proportional to the nanoparticle radius ($\Delta T \propto r_{NP}^2$) and depend on the material properties [75].

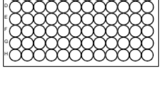

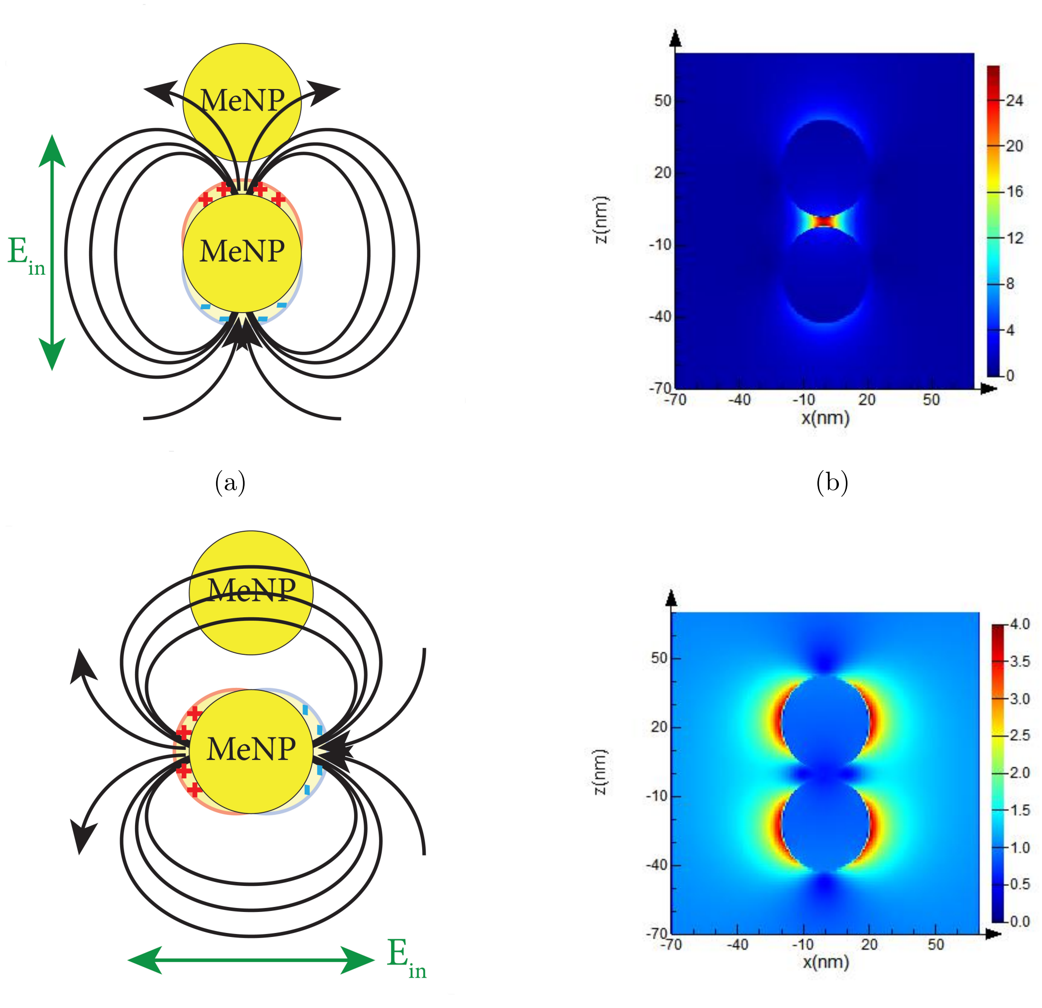

(a) (b)

(c) (d)

Figure 2.7.: Plasmonic coupling of two metal nanoparticles. **(a)** Schematic illustration of the longitudinal mode. The incoming electromagnetic field is polarized parallel to the dimer axis and **(b)** corresponding intensity distribution of the electric near-field at the resonance case of two 40 nm gold nanoparticle with an interparticle gap of 4 nm in air. **(c)** Schematic illustration of the transversal mode. The incoming electromagnetic field is polarized perpendicular to the dimer axis and **(d)** corresponding intensity distribuation of the electric near-field at the resonance case of two 40 nm gold nanoparticle with an interparticle gap of 4 nm in air.

# 3. Plasmonic Metamaterials

*Metamaterials* are artificial engineered materials which have designed properties to interact with and to influence electromagnetic radiation in a non conventional manner that does not exist in nature. The word meta comes from the Greek $\mu\epsilon\tau'\alpha$ which means beyond. As seen above, the optical properties of metals are mainly originating from the conduction electrons and therefore from the underlying atomic lattice structure.

In analogy to that metamaterials are also comprised of subunits. In order to influence light, these subunits must exhibit dimensions which are much smaller than the wavelength of the incident electromagnetic wave. If this requirement is met, the effective optical material parameters ($\mu_{eff}$ and $\epsilon_{eff}$) are defined by those subunits, hence they are called metaatoms [76]. To obtain a solid metamaterial, also the distance between the metaatoms has to be smaller than the wavelength [77]. For isotropic metamaterials the metaatoms need to be organized in all three dimensions or dispersed in solution.

## 3.1. Introduction to Metamaterials

When considering the interaction of light with matter, the properties of the material are important. *Maxwell's equations* describe the relation between an applied electromagnetic field and the resulting response of the matter by an induced electromagnetic field [78].

This response is described by Maxwell's equations in matter (Maxwell's equations of macroscopic electromagnetism):

$$\begin{aligned}
\nabla \cdot \vec{D} &= \rho_{ext} \\
\nabla \cdot \vec{B} &= 0 \\
\nabla \times \vec{E} &= -\frac{\partial \vec{B}}{\partial t} \\
\nabla \times \vec{H} &= \frac{\partial \vec{D}}{\partial t} + \vec{J}_{ext}
\end{aligned} \tag{3.1}$$

with the fields $\vec{D}$ (dielectric displacement), $\vec{B}$ (magnetic induction), $\vec{E}$ (electric field), $\vec{H}$ (magnetic field) and the external charge ($\rho_{ext}$) and current ($\vec{J}_{ext}$) densities. The Maxwell's equations are linked via the magnetization $\vec{M}$ and the polarization $\vec{P}$:

$$\begin{aligned}
\vec{D} &= \epsilon_0 \vec{E} + \vec{P} \\
\vec{H} &= \frac{1}{\mu_0}\vec{B} - \vec{M}
\end{aligned} \tag{3.2}$$

where $\epsilon_0$ and $\mu_0$ are the electric permittivity and magnetic permeability constants in vacuum, respectively. In linear, isotropic and nonmagnetic media the constitution relations turn to:

$$\begin{aligned}
\vec{D} &= \epsilon_0 \epsilon \vec{E} \\
\vec{B} &= \mu_0 \mu \vec{H}
\end{aligned} \tag{3.3}$$

with the material dependent permittivity $\epsilon$ and permeability $\mu$. If an electromagnetic wave with an electric part of $\vec{E} = \vec{E}_0 \cdot e^{\mathrm{i}(\vec{k}\vec{r}-\omega t)}$ and a magnetic part $\vec{H} = \vec{H}_0 \cdot e^{\mathrm{i}(\vec{k}\vec{r}-\omega t)}$ with wave vector $\vec{k}$ and frequency $\omega$ interacts with matter, for the electric and magnetic field follows with equation 3.1:

$$\begin{aligned}
\vec{k} \times \vec{E} &= \omega \mu_0 \mu \vec{H} \\
\vec{k} \times \vec{H} &= -\omega \epsilon_0 \epsilon \vec{E}
\end{aligned} \tag{3.4}$$

Thus, in order for matter to influence the electromagnetic wave, microscopic building blocks of an artificial material have to be designed so that they can reach the desired values of the effective permittivity $\epsilon(\omega)$ and permeability $\mu(\omega)$ values. The complex refractive index $\tilde{n}(\omega) = n(\omega) + \mathrm{i}\kappa(\omega)$, with $\kappa$ the extinction

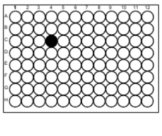

coefficient, is linked to $\epsilon$ and $\mu$ via:

$$\tilde{n} = \sqrt{\epsilon\mu} \tag{3.5}$$

For 'common' materials, both $\epsilon$ and $\mu$ are positive and hence $n$ is positive. If either $\epsilon$ or $\mu$ is negative, the propagation of electromagnetic wave is exponentially damped - only an evanescent wave propagates, the refractive index is imaginary. If both values are negative an electromagnetic wave can propagate, the refractive index is negative. Due to the sign of equation 3.4 the *Poynting vector* $\vec{S} = \vec{E} \times \vec{H}$, which gives the directional energy flux density of an electromagnetic field, and the wave vector $\vec{k}$ are pointing in opposite directions. The theoretical possibility to achieve a negative refractive index by negative effective $\epsilon_{eff}$ and negative $\mu_{eff}$ was shown for the first time in 1999 by Pendry *et al.* [77].

For the visible frequency range the focus lies on achieving a negative effective permeability. If damping is neglected, the dielectric function of metals with plasma frequency (plasmon resonance frequency) $\omega_p$ (undamped free electron plasma) follows from equation 2.4 to be:

$$\epsilon(\omega) = 1 - \frac{\omega_p^2}{\omega^2} \tag{3.6}$$

Hence, for $\omega_p > \omega$ a negative permittivity can be achieved - for noble metals this is the case in the visible frequency range.

The following section will give a short overview about the different concepts to reach plasmonic metamaterials and metaatoms mainly focused to the visible frequency range.

## 3.2. State of the Art

Since the first realized material with negative refractive index in the GHz frequency range in 2001 [79], the operation frequency has been constantly shifted to higher frequencies by design optimizations.

One widely used design to reach a negative refraction index is the split ring resonator concept. Split ring structures are made of a metallic conductor and are U-shaped. Thus, a LC circuit with a conductive and a capacitive element is obtained. If an electromagnetic wave is applied, an induced magnetic field arises due to the conduction current, influencing the permeability of the material. A negative effective permeability at a wavelength as small as $1.2\,\mu$M was achieved by gold split ring resonators [80]. Such split ring resonators are fabricated using electron beam lithography to reach small structural sizes in the range of 100 nm. It has been shown, that the resonance frequency of split ring resonators scales inverse to the structural dimensions [81–83]. Nowadays, metamaterials reached near infrared (NIR) frequencies [84, 85].

With that the field of metamaterial research started to merge with the field of plasmonics. However, just scaling down the structural dimensions of split ring resonators to reach higher resonance frequencies is no longer possible, since the metals start loosing their perfect metal character with infinite carrier density and zero carrier velocity. The kinetic energy of the electrons can no longer be neglected and losses have to be taken into account. As a result, the intensity of the split ring resonance frequency decreases and is no longer strong enough to reach the desired negative effective permeability. The resonance frequency of split ring resonators saturates at about a few hundred THz [81] and at optical frequencies the scaling law breaks down [81].

To achieve metamaterials at optical frequencies, new plasmonic based / inspired concepts needed to be developed. One concept is the so called metal-dielectric-metal fishnet structure [86, 87] consisting of two meshed metal layers with a dielectric layer in between. A 3D fishnet metamaterial was lithographically realized by Valentine et al. [88]. Another method to influence the propagation of light is to realize a surface which can continuously shift the phase of the light. Metasurfaces with lithographically arranged V-shaped plasmonic nanoantennas were realized by Ni et al. [89].

Approaches to construct metaatoms with colloidal nanoparticles and nanorods include cut-wire pair structures [90] and chiral structures [20, 57]. The mentioned cut wire pair structure consists of two parallel aligned nanorods, which are slightly longitudinally shifted with respect to each other. This shift introduces a symmetry break and can lead to an isotropic negative index [91]. Chiral metaatoms consist of molecules that cannot be superimposed on their mirror images. It has

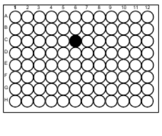

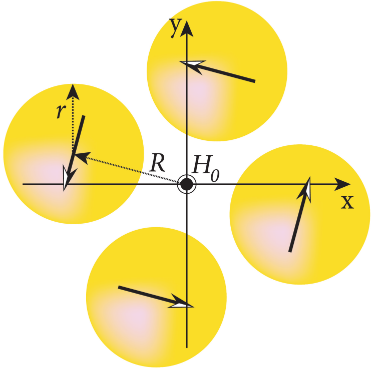

Figure 3.1.: Ring geometry out of four metal nanoparticles. An incoming electromagnetic wave induces electric dipoles (black arrows). A resonant displacement current is supported by the ring of plasmonic particles leading to an induced magnetic response.

been shown by Pendry et al. [92] that it is possible to achieve negative refraction with materials exhibiting chiral properties. Another concept for plasmonic based metamolecules is to arrange metal nanoparticles in a planar ring shaped geometry [93–95]. In this geometry, a resonant circulating *displacement current* introduces a magnetic response as illustrated in figure 3.1. So far, this concept was realized by pushing four single gold nanoparticles (AuNPs) with an AFM tip into a single ring shaped arrangement [96].

## 3.3. DNA origami to create plasmonic ring shaped metaatoms

The DNA origami technique as described in section 2.1 allows to construct DNA based nanoscale objects of arbitrary shapes in large quantities ($\sim 10^8$ identical structures). Since these objects are precisely addressable, they can be used as templates to precisely position metal nanoparticles and hence to create plasmonic active materials.

In publication A.1 [97], a doughnut shaped DNA origami consisting of a bundle with fourteen bended double helices (bended 14hB) was constructed. The origami

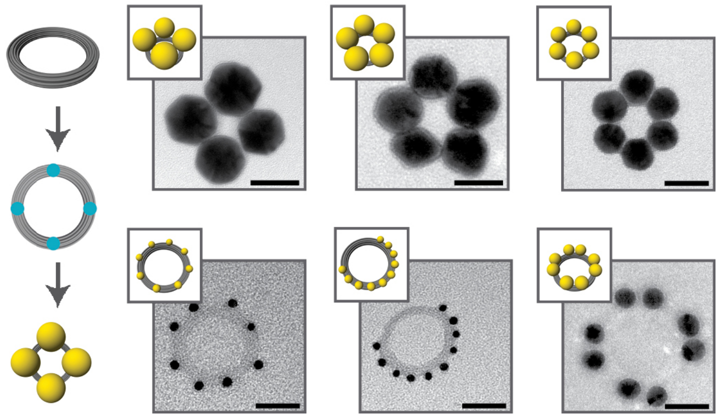

Figure 3.2.: A ring shaped 14hB DNA origami structure with predefined metal nanoparticle attachment sites serves as a template geometry. The number and location of the attachment points on the template structure defines the final ring shaped organization of metal nanoparticles. Geometries shown here consists of AuNPs ranging from 10 nm to 40 nm diameter and four to ten particles per ring. Scale bar 40 nm.

structure, having a diameter of 62 nm and a cross-section of ~ 10 nm, offers 27 repeating, evenly spaced (21 bases (~ 7.1 nm)) attachment sites for nanoparticle docking. As a result, the bended 14hB serves as perfect template structure to spatially arrange versatile nanoparticles in a ring shaped geometry (see figure 3.2). Thus, the DNA origami approach offers the possibility to realize metaatoms based on a circulating displacement current. Several such plasmonic ring shaped structures were realized in publication A.1.

Rings containing four 40 nm AuNPs were characterized using single molecule dark-field scattering spectroscopy. The resulting spectra were compared to corresponding theoretical simulations (see figure 3.3). Indeed, it was possible to observe a magnetic resonance mode at 720 nm. This finding shows, that the DNA origami template approach allows to produce metamolecules with an artificial magnetic response at optical frequencies in a self-assembled parallel way at high quantities. Next to its templating properties, the DNA origami approach benefits from the fact that it is a solution based process. Thus, all DNA based plasmonic structures are directly available in solution which opens the doors for a new class of metafluids.

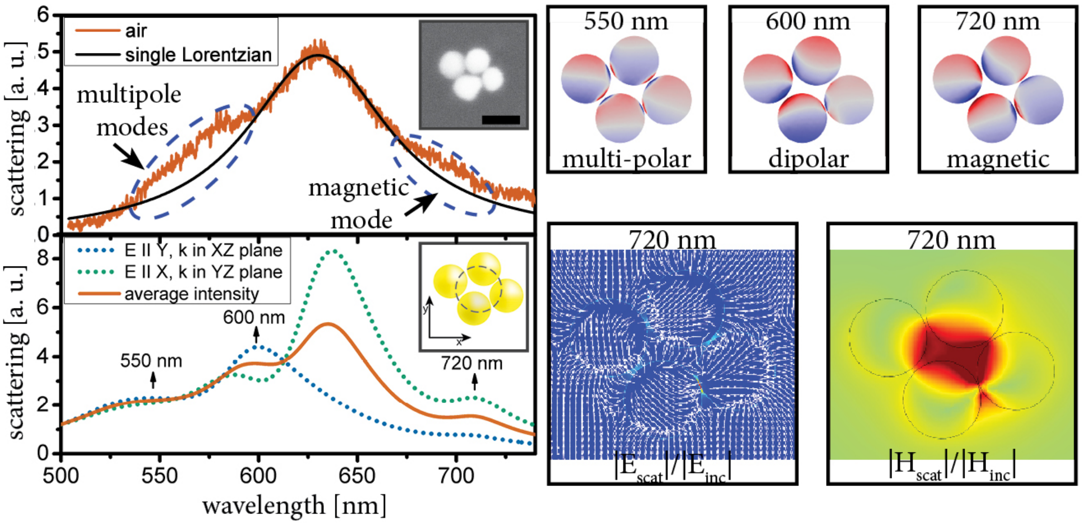

(a) (b)

Figure 3.3.: Analysis of a four particle ring on the single structure level. **(a)** Multiple resonance peaks are visible in the dark field scattering spectrum (upper panel). Inset: SEM image of the measured structure. Scale bar 50 nm and corresponding polarization resolved numerical simulations (lower panel). **(b)** Simulations of the surface charge distributions of the peaks and the electric and magnetic field at the 720 nm peak.

To summarize, in the associated publication A.1 it was possible to create DNA origami based ring shaped plasmonic materials with electric and magnetic resonances in the visible frequency range. The analysis was performed via single structure dark-field scattering spectroscopy of dried plasmonic rings in combination with corresponding numerical simulations. Moreover the DNA origami templating approach is a solution based method, which enabled to study the optical properties of a bulk solution of ring structures. The availability of ring shaped structures with defined electric and magnetic responses dispersed in a solution can trigger new applications such as metasprays.

The concept of using DNA origami templates to create artificial plasmonic metamolecules was recently extended to metasurfaces [98]. It was shown by Wang *et al.* that two dimensional DNA origami tiles can be used to construct lattices of arranged AuNPs with pre-programmed patterns. By incorporation of

AuNPs into a hexagonal DNA origami tile structure, a ring shaped AuNP hexamer was realized. The characterization of that single AuNP hexamer revealed also a magnetic dipolar resonance mode. Two dimensional lattice structures of multiple hexagonal tiles displayed enhanced interparticle coupling [98].

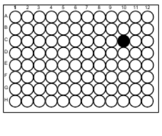

## 3.4. Associated Publication P1

### DNA-Assembled Nanoparticle Rings Exhibit Electric and Magnetic Resonances at Visible Frequencies

by

Eva-Maria Roller, Larousse Khosravi Khorashad, Michael Fedoruk, Robert Schreiber, Alexander O. Govorov, and Tim Liedl

published in Nano Letters, 15, 1368 - 1373 (2015)

see Appendix A.1

# 4. Plasmon-Exciton Systems

*Hybrid systems*, made out of at least two different types of materials, combine the intrinsic properties of each material to gain new characteristics. Systems exhibiting strong light-matter interactions are candidates to study fundamental quantum phenomena such as cavity quantum electrodynamics [99] but they are also relevant for new applications such as in the area of light harvesting complexes [100], optically active devices [101] and quantum information processes [102]. The underlying principle of the examples is the strong coupling between a quantum emitter and a resonant cavity. The coherent energy exchange between the emitter and the cavity leads to a mode hybridization, known as *vacuum Rabi splitting* [103]. Such quantum optical systems have been widely studied in solid state systems [104, 105].

## 4.1. Introduction to Plasmon-Exciton Systems

If a quantum emitter is placed within an optical cavity, they can both interact. In the weak coupling regime the spontaneous emission rate from the emitter is enhanced or diminished [106, 107]. In the strong coupling regime, the optical modes of the cavity and the emitter in resonance interact strongly and mixed states are produced. This leads to two hybrid modes separated by the Rabi frequency $\Omega$ [99, 103]. The interaction strength of the quantum emitter with the resonant cavity depends on the ratio between the cavity quality factor $Q$ to the mode volume $V$. Thus, to reach strong coupling, it is crucial to either achieve high $Q$ values or small mode volumes $V$. High $Q$ values are for example reached with low temperature experiments. For optical cavities, the extend to which light can be focused in a specific volume is diffraction limited. To overcome this limitation, plasmonic nanocavities can be used [108]. They offer the great advantage that, due to plasmonic effects, the enhanced electromagnetic field is focused in very small, not diffraction limited volumes. Hybrid systems of nanoparticles in close proximity to quantum emitters are possible candidates for strong light-matter interaction at ambient temperatures. Under light illumination, the plasmons of the nanoparticles can couple to the excitons of quantum emitters resulting in *plasmon-exciton coupling* (see figure 4.1). The degree of interaction between plasmons and excitons in a hybrid metal nanostructure and quantum emitter systems can be described by the coupling energy $g$ and can be divided in three regimes: enhanced absorption, Fano resonance (induced transparency) and Rabi splitting (strong coupling) [109]. The three regimes are displayed in the absorption and scattering characteristics of the hybrid system. In strongly coupled plasmon-exciton systems the energy exchange results in the formation of hybrid modes, called *plexcitons*. The observed *normal mode splitting* can be described by the model of two coupled harmonic oscillators [102] with Hamiltonian

$$\hat{\mathcal{H}} = \begin{pmatrix} \tilde{\omega}_p & g \\ g & \tilde{\omega}_{qe} \end{pmatrix} \tag{4.1}$$

with complex eigenvalues [110]

$$\tilde{\omega}_{\pm} = \frac{\tilde{\omega}_p + \tilde{\omega}_{qe}}{2} \pm \sqrt{g^2 + \frac{(\tilde{\omega}_p - \tilde{\omega}_{qe})^2}{4}}, \tag{4.2}$$

Here, $\tilde{\omega}_p$ and $\tilde{\omega}_{qe}$ are the complex frequencies of the plasmon and quantum emitter ($\tilde{\omega} = \omega + i\Gamma/2$), $g$ is the coupling constant and $\Gamma$ is the dissipation term extracted from the FWHM linewidth. If the plasmon resonance frequency $\omega_p$ is equal to the resonance frequency of the quantum emitter $\omega_{qe}$ the difference of the real components of the eigenvalues of equation 4.2 is the *Rabi splitting* $\Omega$ given by [110]

$$\Omega = \Delta\omega = 2\sqrt{g^2 - \frac{1}{16}(\Gamma_p - \Gamma_{qe})^2} \tag{4.3}$$

By varying the plasmon resonance with respect to the quantum emitter resonance the evolution of the upper $\omega_+$ and lower $\omega_-$ hybrid state as a function of the

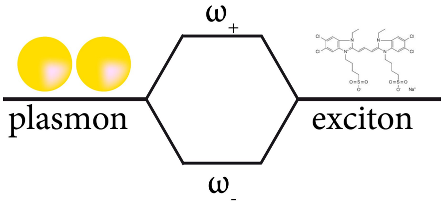

Figure 4.1.: Hybridization energy states diagram for a plasmon-exciton system.

plasmon mode can be observed. For strong coupling the energy positions display an anti-crossing behaviour [102].

## 4.2. State of the Art

Plasmon-exciton coupled systems have been experimentally realized with dyes deposited on top of thin silver films [111] and on a lithographic produced array of metallic nanodiscs [112]. Also, individual gold nanorods covered with a dye shell have been shown to display plasmon-exciton interaction [113]. Since it takes less time for the photons to return to the same quantum emitter in smaller cavities, the coupling is increased. The coupling energy $g \propto 1/\sqrt{V_{eff}}$ scales with $V_{eff}$ the effective mode volume [102]. Therefore, further reduction of the effective mode volume is crucial to reach the strong coupling regime at room temperatures.

This can be achieved by making use of the electromagnetic field confined within the plasmonic 'hot spot'. The combination of lithographical constructed gold dimers with a J-aggregated dye placed in the hot spot region was shown to reach the strong coupling regime in the NIR [114]. However, lithographic produced structures exhibit larger surface roughness than colloidal metal nanoparticles. Thus, colloidal gold shell structures [115] and triangular shaped nanoparticles [116, 117] have been used to promote plasmon-exciton interactions.

Even smaller volumes and higher field enhancement can be achieved by a dimer metal nanoparticle conformation with (sub)nanometer gaps between the plasmonic particles. Very recently, single molecule strong coupling of a dye molecule placed in a plasmonic nanocavity was shown [118]. Therefore, a nanoparticle was deposited onto a thin gold film separated by a sub-nanometer thin molecular

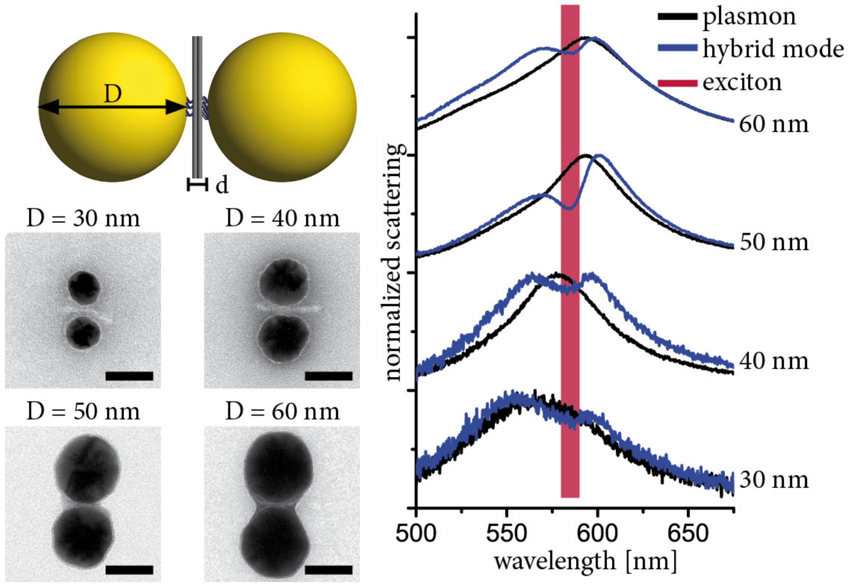

(a) (b)

Figure 4.2.: DNA origami as template for plasmon-excition coupling studies. **(a)** Schematic design and TEM image of gold nanoparticle dimer structures templated by a two-layer DNA origami sheet. The diameter of the gold nanoparticles ranges from 30 nm to 60 nm. Scale bar 40 nm. **(b)** Normalized single structure dark field scattering spectra of dimer structures with different nanoparticle diameters before (dark-blue) and after (black) photobleaching of the J-aggregated dye.

spacer [118], which results in a so-called 'nanoparticle-on-mirror geometry' for the plasmonic nanocavity. Another recent demonstration of strong coupling was achieved between single colloidal quantum dots placed between lithographic produced bow-tie silver antennas [119]. These two recent examples take advantage of plasmonic field confinement.

## 4.3. DNA origami to study Plasmon-Exciton Interaction

The DNA origami technique offers an unique methodology to tune the plasmon resonance frequency by varying the interparticle gap size or the nanoparticle

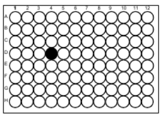

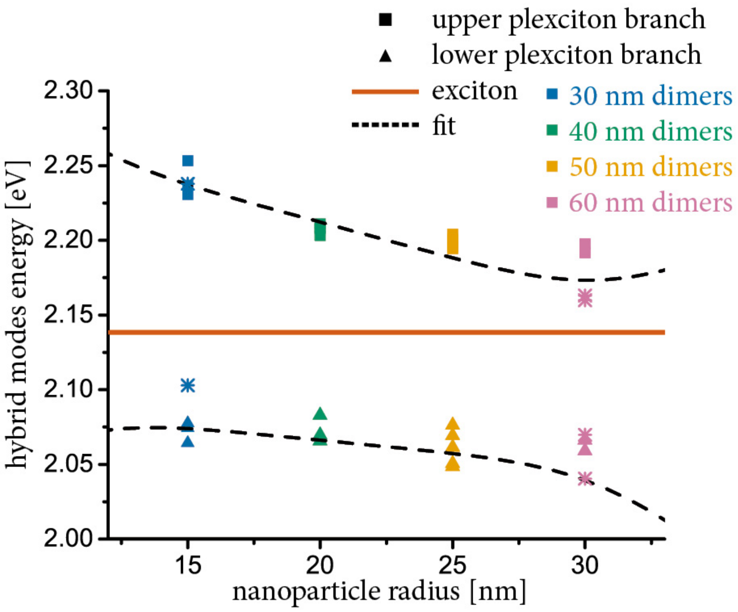

Figure 4.3.: Hybrid plasmon-exciton energies for several dimer structures plotted as a function of the nanoparticle radius. The dashed line is the fit of the eigenvalues of a two-coupled harmonic oscillator model.

diameter. With that, this technique offers the advantage to create plasmonic hot spots and to tune the plasmon resonance frequency with respect to the quantum emitter frequency.

The system realized in publication A.2 [120] consists of a DNA origami two layer sheet which serves as a spacer between two gold nanoparticles. The size of the gold nanoparticles was varied from a diameter of 30 nm to a diameter of 60 nm while the gap size between the particles was kept constant due to the DNA origami spacer. The DNA based plasmonic dimer structures were then immobilized on a glass substrate and incubated with a Cyanine based J-aggregate dye (TDBC). Most of the dye was then flushed away except at the locations of the dimers. The TDBC dye is considered to adsorb on the AuNP surface during the incubation [121].

The characterization on the single structure level was performed with dark field scattering spectroscopy. The data in figure 4.2 show the spectral response of the hybrid structures. The plasmon resonance of the dimer consisting of two 40 nm

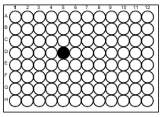

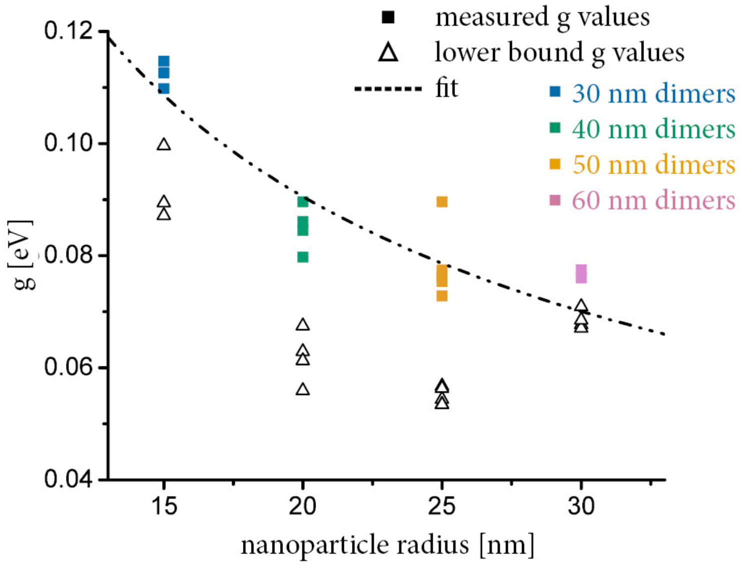

Figure 4.4.: Experimental obtained coupling values (g) for individual dimer structures (squares) and the lower bound g values for the strong coupling regime (triangles).

gold nanoparticles was designed to perfectly overlap with the resonance for the chosen J-aggregate. By decreasing and increasing the nanoparticle diameter from 30 nm to 60 nm, the plasmon resonance was moved across the dye resonance.

The analysis of the hybrid energy levels with respect to the plasmon energy level of several individual dimer structures revealed the expected anti-crossing behaviour with a coupling constant $g$ of 90 meV (see figure 4.3). A Rabi splitting of $\Omega \approx 150\,\text{meV}$ was observed. Additionally, it was possible to show how the coupling strength varies with the change of the effective mode volume of the different nanoparticle dimer constructs.

Nanoparticle dimers with smaller nanoparticle radius $R$ displayed a stronger coupling, which is in agreement with the theoretical expectations. In a nanoparticle dimer system, the effective mode volume $V_{eff}$ can be approximated to be a cylinder. In detail, the base of the cylinder with diameter $\sqrt{Rd}$ represents the width of the induced surface charge and the height of the cylinder is the gap size between the two nanoparticles ($d$) [122]. This results in the expected scaling of the the coupling energy of $g \propto 1/\sqrt{V_{eff}} \propto 1/\sqrt{Rd^2} \sim 1/R^{0.5}$. Figure 4.4 displays

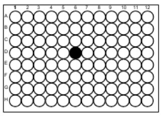

a fit with scaling $g \propto 1/R^n$ with $n = 0.63 \pm 0.08$ which is in very good agreement with the expected scaling.

Overall, the DNA origami templating approach allowed to engineer tunable plexcitonic systems that operate at room temperatures and optical frequencies. Gold nanoparticles of different diameters were organized in a dimer conformation with fixed gap size by the solution based DNA template method resulting in small plasmonic cavities. With that, the DNA origami technique proofed to be a viable tool to study fundamental plasmon-exciton interactions. Moreover the addressability of the DNA origami template structure has the potential to directly place individual emitters in a plasmonic cavity with very a very confined mode volume and strong field enhancement.

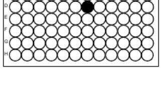

## 4.4. Associated Publication P2

### Plasmon-Exciton Coupling Using DNA Templates

by

Eva-Maria Roller, Christos Argyropoulos, Alexander Högele, Tim Liedl, and
Mauricio Pilo-Pais

published in Nano Letters, 16, 5962 - 5966 (2016)

see Appendix A.2

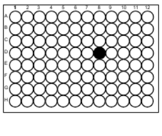

# 5. Circular Dichroism based Sensors

*Circular Dichroism* (CD) arises when matter absorbs left (L) and right (R) handed circular polarized light in different intensities. It can be measured by the absorption difference via CD spectroscopy.

$$\Delta A = A_L - A_R \tag{5.1}$$

Optical active chiral molecules such as proteins and DNA offer a CD signal in the ultraviolet frequency range, as well as in the infrared regime [123, 124]. The CD signal of DNA arises due to its chiral secondary structure [125, 126]. In general, a molecule is chiral if it can not be superimposed on its mirror image. Enantiomers are the mirror images of a chiral molecule. In nature, the chiral state of biomolecules plays an important role in recognition processes and biochemical reactions. CD spectroscopy is used to gain information about conformational states of chiral active molecules, their ratio of enantiomers and to monitor chemical reactions by observation of conformational changes [127, 128]. Thus, to detect the CD signal in a reliable and sensitive manner it is crucial to gain new insights into reaction processes and structural conformations, which could promote for example the development of new drugs.

## 5.1. Introduction to Circular Dichroism Enhancement and Transfer

Most natural occurring biomolecules possess their absorption and their circular dichroism in the ultraviolet range. At the same time, they are rather weak absorbers, thus to detect their UV CD signal a high concentration of the molecule of interest is needed.

On the other hand, plasmonic nanoparticles are known to strongly enhance electromagnetic fields, turning them into a powerful tool for advanced spectroscopy methods of molecules such as SERS [129]. Along these lines, plasmon enhanced sensing of chiral molecules could be a viable method to analyse the chirality at low molecular concentrations.

Plasmon resonances of metal nanoparticles such as gold and silver are in the visible frequency range, which is not in CD resonance with most chiral biomolecules. However, it was shown theoretically that the off resonant plasmon bands can interact with the dipoles of chiral molecules [130].

The chiral property of a molecule in vicinity to a non chiral metal nanoparticle can be enhanced and transferred to the plasmon resonance frequency of the metal nanoparticle. The occurrence of an additional plasmon induced CD line at the plasmon resonance of the metal nanoparticle is based on an enhanced electric field which also enhances the Coulombic interaction between the chiral molecule and the non-chiral metal nanoparticle. Due to the non-vanishing optical rotatory dispersion (ORD) in the visible frequency range of a chiral molecule with intrinsic CD resonance in the UV range, off resonant interaction between the molecular dipole and the plasmon is still expected. The *optical rotatory dispersion* is a non-absorbing response of chiral materials and defines the frequency dependent specific rotation of light passing through the chiral material. The CD and the ORD are related to each other via the Kramers-Kronig transformation and come along with each other as 'normal' absorption and dispersion [131].

An isolated chiral molecule has a CD which is described by [125, 132]

$$CD_{molecule} \propto Im(\vec{\mu}_{12} \cdot \vec{m}_{21}) \tag{5.2}$$

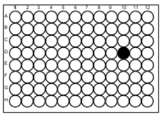

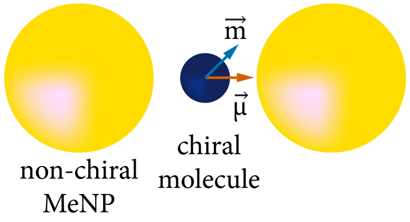

Figure 5.1.: Schematic illustration of a system composed of two non-chiral metal nanoparticles and a chiral molecule with electric and magnetic dipole moments $\vec{\mu}$ and $\vec{m}$ placed in the plasmonic hot spot.

with the electric $\vec{\mu}_{12}$ and magnetic $\vec{m}_{21}$ dipole moment. For a chiral molecule in close proximity to a metal nanoparticle this equation has to be modified along reference [130] to

$$CD_{molecule-NP} \propto a \cdot Im[(\hat{P} \cdot \vec{\mu}_{12}) \cdot \vec{m}_{21}] + b \cdot F(\vec{\mu}_{12}, \vec{m}_{21}) \tag{5.3}$$

where $a$, $b$ are coefficients depending on the material, geometry and the incident light frequency and $\hat{P}$ is the electric field enhancement matrix which takes account for the influence of the nanoparticle to the optical electric field inside the molecule. The second term $F(\vec{\mu}_{12}, \vec{m}_{21})$ describes the arising CD signal at the plasmon frequency due to the dipole-plasmon complex. For a molecule placed in between a plasmonic hot spot as illustrated in figure 5.1, this is the main term contributing to the plasmonic CD effect. The $CD_{dipole-field}$ term has its origin in interference of the incident field and the induced field inside the nanoparticle due to the chiral molecular dipole [133]. The plasmonic CD signal is proportional to the ORD of the molecule [133]

$$CD_{dipole-field} \propto f(\omega) \times ORD_{mol,0} \propto f(\omega) \frac{m_{12}\mu_{21}}{\omega_0 - \omega_{plasmon}} \tag{5.4}$$

with the complex function $f(\omega)$ for the energy dissipation inside the metal.

Thus the enhanced plasmonic CD arises from two main effects - the non vanishing ORD response of the chiral molecule at the plasmon resonance and the plasmonic hot spot effect.

## 5.2. State of the Art

Complexes consisting of achiral metal nanoparticles and chiral molecules which show a non zero CD signal at the plasmon frequency have been realized experimentally [134–137].

Aggregates of gold nanoparticles with oligonucleotides showed an additional CD band at visible frequencies, which was only observable for the aggregated forms and not for non-aggregated CD-chiral molecules [134]. This is an indication that the field enhancement in between aggregated gold nanoparticles is needed to observe the new CD band. To prove that the CD originates from the transfer effect of the oligonucleotides situated between the aggregated gold nanoparticles and not from a possible chiral aggregation of the gold nanopartilces, controls of only gold clusters without chiral components were performed. The controls did not show a CD signal proofing the initial hypothesis.

Other heterocomplexes of chiral molecules and achiral metal structures are realizations of the chiral molecule riboflavin on top of gold islands deposited on a glass substrate [135], peptide coated gold nanoparticles [136], cysteine modified nanoparticles [137, 138] and silver synthesised on DNA [139].

The effect of the spatial orientation of the chiral molecular dipole with respect to plasmonic particles, as well as the inter-component gap distances was analysed by a gold nanorod (AuNR) DNA complex system [140]. In this system, two AuNRs were attached in multiple orientations using a DNA origami one layer sheet. The two AuNRs were either aligned parallel to the axis of the double stranded DNA helices of the DNA origami sheet or perpendicular to it (see figure 5.2). It was shown, that the chirality of the resulting bisignate CD signals depends on the orientation of the AuNRs with respect to the orientation of the dsDNA helices (parallel or perpendicular) [140]. Thus, the opposite chiral response of the AuNRs-DNA origami complex resulted from the specific dipole-dipole orientations of the double stranded DNA helices and the AuNRs [140].

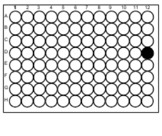

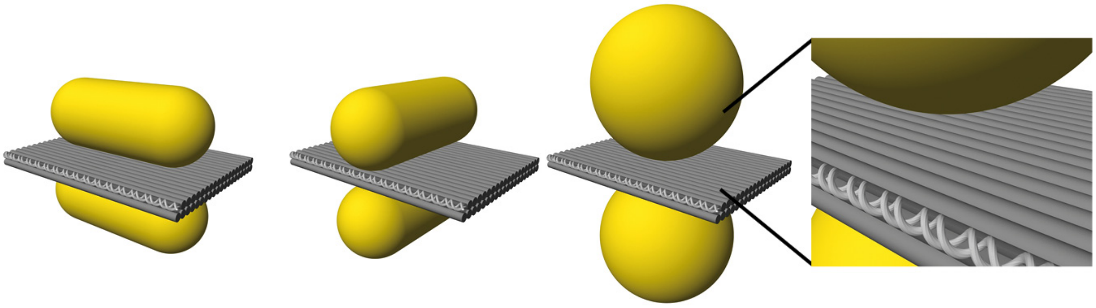

(a) (b)

Figure 5.2.: Orientation of the dsDNA helices of a DNA origami structure with respect to plasmonic nanocomponents. **(a)** Two AuNRs are organized on opposite sides of a DNA origami structure. The longitudinal axis of the AuNRs is either parallel (left panel) or perpendicular (right panel) aligned with respect to the dsDNA helices of the DNA origami structure. The geometries are similar to reference [140]. **(b)** Two AuNPs are organized on opposite sides of a two layer sheet DNA origami structure. Zoom in: the dsDNA helices of the origami structure are oriented perpendicular with respect to the electric field of the plasmonic hot spot formed by the dimer AuNP configuration.

## 5.3. DNA origami to detect CD signals

The plasmonic CD with its CD transfer effect to the plasmon resonance frequency range of the metal offers the possibility to detect the molecular CD signal at visible frequencies. Moreover, the CD signal can be enhanced by the metal nanoparticle arrangement as for example if the chiral molecule is placed in a plasmonic hot spot. As a result of this, it is possible to realize plasmonic-enhanced CD sensors which work at visible frequencies with very low molecular concentrations.

In this work (see also A.3) plasmonic CD sensors, owning a plasmonic hot spot conformation, were realized. The hot spot was realized by a dimer gold nanoparticle geometry as well as by two gold nanorods facing towards each other. In between the achiral metal nanoparticles and nanorods the chiral molecules are located. Here, we used a DNA origami structure and its oligonucleotides as chiral molecules. The DNA origami structure allows the nanoscale dimer geometry to be realized in solution and guarantees that the chiral analyte molecules - here

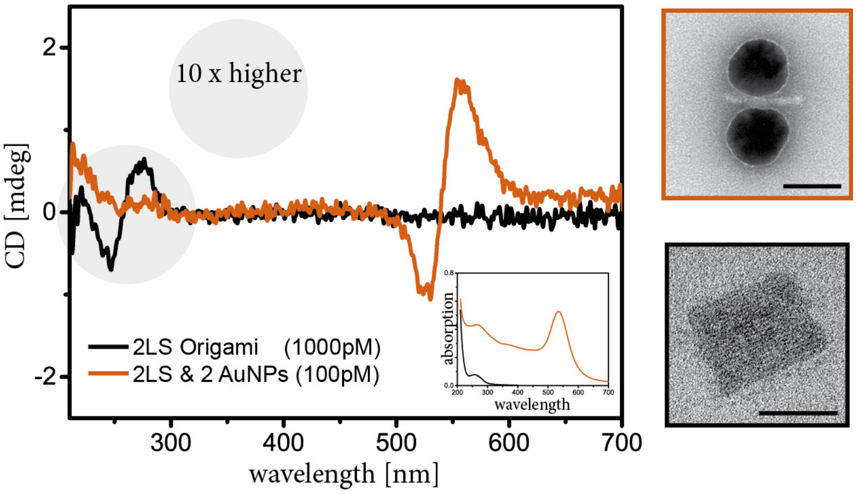

Figure 5.3.: CD spectra of DNA origami 2 layer sheet (2LS) structure and of a plasmonic dimer structure consisting of two 40 nm AuNPs and the 2LS placed in the hot spot. For the dimer structure a new CD mode at the plasmon resonance frequency of the AuNPs appears, which is an indication for the CD transfer effect. Right panel: corresponding TEM images. Scale bar 40 nm. Inset: corresponding absorption spectra.

oligonucleotides - are located in the centre of the hot spot. In this case, the double stranded DNA helices of the DNA origami structure are oriented perpendicular to the dimer nanoparticle axis (to the electric field of the hot spot) as illustrated in figure 5.2.

The variation of the plasmonic particles by the use of gold nanoparticles, nanorods and gold nanoparticles with an additional silver shell allows to tune the plasmon resonance wavelength of the dimer structure. As a result, also the transferred CD signal from the chiral molecules was tuned to the desired wavelength. Additionally, rectangular DNA origami structures with different amount of layers were used to trigger the gap size distance between the particles and thus to vary the hot spot intensity. The influence of the hot spot intensity to the CD signal was investigated by the use of DNA origami structures with a one layer sheet (1LS), two layers (2LS) and four layers (4LS) in between the dimer nanoparticle geometry. However, not only the hot spot intensity but also the amount of chiral molecules in between the plasmonic hot spot changed by using different amount of DNA origami layers.

The 2LS origami structure with two attached 40 nm AuNPs on opposite sites of the rectangular sheet turned out to give a good CD signal at the plasmon resonance wavelength and showed a high AuNP dimer structure yield of $\sim 75\%$. Hence, this configuration was further characterized as a promising candidate for a sensitive chiral molecule sensor structure. It was possible to detect a CD signal from the 2LS metal-chiral molecule dimer structures at a concentration of 100 pM in the visible frequency range. This measurement sensitivity enables to detect the CD signal from DNA (the chiral molecule) at a 10x lower concentration as needed without the plasmonic transfer and enhancement geometry (see figure 5.3).

Since the intensity of the detected transferred CD signal depends on the field enhancement at the chiral molecule position, which is shown in figure 5.4, this aspect was further investigated by changing the AuNPs positions with respect to the DNA origami 2LS structure. Figure 5.4 shows the analysed conformations, the CD spectra are normalized to the dimer structure concentration. Shifting the two AuNPs apart from each other or using only one AuNP decreases the hot spot intensity at the chiral molecule (DNA origami) position, which resulted in a lower detected CD signal. Also placing the AuNPs on one side of the DNA origami structure influences the detectable CD signal. As a control, it was not possible to measure a CD signal from single, DNA modified AuNPs at the used low concentrations. As a result, the heterocomplex approach with its arrangement of chiral molecule and metal nanoparticles in a hot spot conformation is crucial to study the plasmonic CD transfer and enhancement in a controlled manner at low concentrations of 100 pM.

To conclude, the CD signal of a chiral molecule placed in a plasmonic hot spot was observed at the plasmon resonance wavelength. The intensity of the transferred CD signal for multiple geometrical conformations was studied. The linear gold nanoparticle dimer geometry with its strong field confinement and chiral molecule placement in the centre was essential to detect the transferred CD signal of low DNA origami concentrations of 100 pM. Consequently, a chiral molecule sensor based on the CD transfer effect to the plasmon resonance

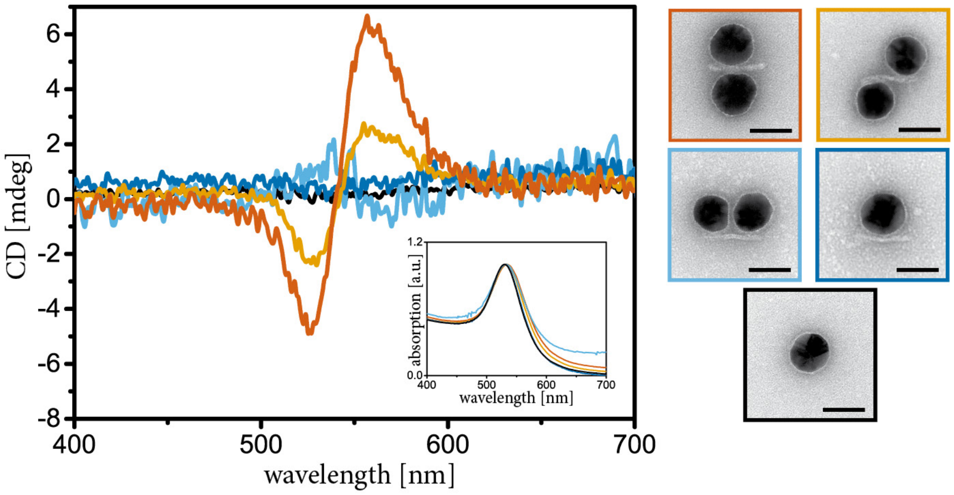

Figure 5.4.: Dependence of the CD transfer signal from the field enhancement intensity. The plasmonic hot spot intensity at the position of the chiral molecule is reduced by shifting the two AuNPs apart from each other (orange), placing them on the same side of the origami structure (blue) and by using only one AuNP (light blue). Single DNA modified AuNPs are not showing a transferred CD signal at the used concentrations of 100 pM (black). Right panel: corresponding TEM images. Scale bar 40 nm.

wavelength was realized and characterized. This is the first step towards a more general chiral molecule sensors scheme in the visible frequency range. With its inherent addressability, in future work the DNA origami can be modified so that a specific chiral molecules is placed in the center of the plasmonic hot spot and detected by the field enhancement and CD transfer process.

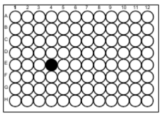

## 5.4. Associated Manuscript P3

### Plasmonic Focus Point Analysis of Chiral Molecules

by

Luisa M. Kneer*, Eva-Maria Roller*, Robert Schreiber, Alexander O. Govorov,
and Tim Liedl
*equal contribution

Manuscript in preparation (2016)

see Appendix A.3

# 6. Plasmonic Passage using Heterogeneous Systems

Efficient ways to transfer energy over short and long distances is crucial for future devices to process optical information, in the field of energy harvesting and in information technologies. Energy transfer plays an important role in biological photosynthesis processes [141] as well as in industrial solar-energy conversion [142]. However, the diffusion of excitons in solar cells, Förster energy transfer [143, 144] in biomolecular systems and information transfer in computer technology are incoherent processes and dissipative. In optics, coherence is crucial to achieve for example interference of electromagnetic waves as used in the creation of holograms. In nanoscale metal systems, information can be transported coherently by plasmons, however such systems are usually dissipative due to the high scattering probability of the electrons. In quantum mechanics, coherent transfer processes are realized for example by stimulated Raman adiabatic passage (STIRAP) and *coherent tunnelling by adiabatic passage* (CTAP) where population transfer between an initial and final state is achieved via a third state in optical trap and triple well systems [145, 146]. In such processes no heat is dissipated during the transfer process.

## 6.1. Introduction to Passage Systems and Heterogeneous Systems

Processes which enable effective transfer of energy or population are known from techniques to manipulate the state of a quantum system. In that field, mainly two methods - non-adiabatic and adiabatic - are used for coherent population transfer. Non-adiabatic transitions are fast but sensitive to noise, whereas adiabatic transitions offer high fidelity, but are slow. The ideal method to transfer populations is a combination, robust and fast.

Originally, adiabatic passage techniques were developed for optical applications and NMR (nuclear magnetic resonance) spectroscopy. The optical Stimulated Raman adiabatic passage (STIRAP) is a technique to manipulate the population distribution over the quantum states of an object. In this laser based method, the complete population transfer from an initial to a final state is achieved by a third intermediate state which is coupled to the initial and final state by a radiation field [147]. The Coherent Tunnelling by Adiabatic Passage (CTAP) is similar to STIRAP technique but it relies on complete coherent electronic transport. In a triple well CTAP system, the coherent population transfer between two long living, spatially separated levels is done via a third intermediate level. During the CTAP process the energy is not changed, no heat is dissipated. To realize CTAP system electrons in a quantum dot system [148] or neutral atoms in optical traps [149] are proposed. Other systems analogous to the STIRAP scheme can be used for any objects with an appropriate quantum structure. Such analogous systems have been experimentally realized e.g. with coherent transfer of light by adiabatic passage in an optical waveguide system [150] and in classical systems such as photonic structures to manipulate light propagation [151, 152]. Information transport on the nanoscale can also be mediated by plasmonic structures.

As seen in chapter 2 Plasmons are coherent oscillations of the free electron gas in metal nanoparticles, but they are dissipative which is displayed in high scattering and local heating properties of metal nanoparticles. To achieve an efficient use of plasmonic waveguides and transfer information over larger distances, this dissipative losses have to be overcome. In analogy to the above described quantum mechanical mechanism, one can think about a plasmon based passage system for fast, coherent and low dissipative transport of information on the nanoscale. In the nanoparticle trimer system proposed here, energy transfer between two spatially separated plasmonic particles is realized by the use of a third intermediate plasmonic particle of different type and energetic level. An schematic illustration of such a plasmonic coherent bus system is shown in figure 6.1.

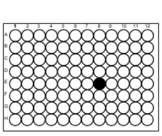

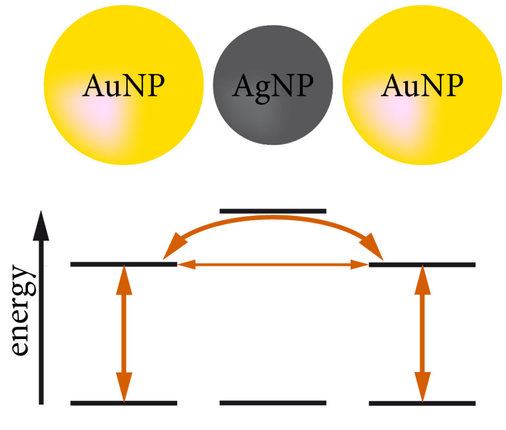

Figure 6.1.: Schematic illustration of a coherent plasmonic bus system. The energy is transfered between the two outer AuNPs via the central AgNP. Light induced transitions are represented via the solid vertical arrows.

## 6.2. State of the Art

One experimental realization of an optical analogy to the CTAP process was demonstrated with light transfer in a triple-welled optical waveguide structure [150]. The structure consists of three waveguides, a left (L), a right (R) and a central (C) one (see figure 6.2). The central waveguide is straight, the two others are curved with opposite curvature sign . With that geometry there is a minimal distance point between the central waveguide and its left, respectively right neighbour. The tunnelling rate of light coupled into one waveguide to the other depends on the distance between the waveguides. By design the distance between the left and right waveguide is too large so that the tunnelling rate between them can be neglected, so that the function of the central waveguide is to enable light to tunnel from the left to the right waveguide. Therefore the coupling rate between neighbouring waveguides is tuned by the geometrical design, making the triple waveguide geometry an optical analogy to the CTAP system.

To realize a non-dissipative plasmon based passage system, plasmonic particle with different energetic levels are needed. A requirement for heterogeneous plasmonic architectures is precise control over shapes, distances and materials

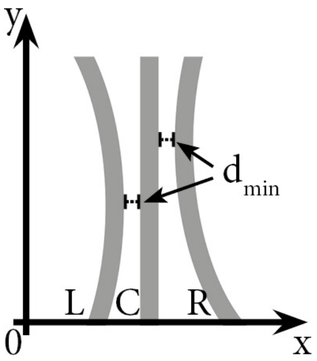

Figure 6.2.: Schematic design to the three-waveguide structure used by Longhi *et al.* in reference [150].

of the nanoscale components. Lithographic approaches for heterogeneous plasmonic constructs consists of bimetallic dimers of gold and silver disks [153] as well as nanodot arrays [154]. Heterogeneous nanoparticle assemblies consisting of colloidal nanoparticles were realized with DNA modified AuNPs, which were subsequently in an asymmetric way covered with a silver shell by adding Ag precursors. The asymmetric silver growth on top of the AuNP surface to form heterogeneous dimer structures was triggered by the salt concentration during the growth process [155, 156]. Heterodimers of gold and silver nanoparticles were formed by the use of DNA linkers [72]. Another method to create heterogeneous dimer structures is the DNA origami method. In a few experimental realizations, it has been shown that silver and gold nanoparticles can be organized on the same DNA origami template. This was achieved either by a two step process [53] or by using different DNA linker sequences [97, 157]. Such realized structures are gold-silver dimer nanostructures or ring shaped structures.

## 6.3. DNA origami for Heterogeneous Plasmonic Passage Systems

The organisation of metal nanoparticles by the DNA origami method has already been discussed. Nevertheless, most of the so far produced nano-architectures

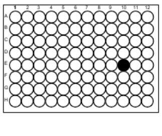

consist of only one type of material (mainly AuNPs). The method itself, however, allows in principle to organize different types of nanocomponents in a specific way.

With the goal to reach coherent coupling and ultrafast energy transfer between two nanoparticles via a third intermediate state, a heterogeneous trimer chain like plasmonic system was built in the associated publication. A 14 helix bundle (14hB) DNA origami structure was used to organize three nanoparticles in a chain-like geometry. The 14hB structure is a 200 nm long cylinder and offers, by design, 27 attachment sites for nanocomponents along its longitudinal axis. With that the 14hB provides a rigid template structure for the realization of various chain-like nanoparticle geometries.

Here, two gold nanoparticles (diameter 40 nm) and one silver nanoparticle (diameter 30 nm) were attached to the structure in such a way, that the silver nanoparticle is specifically placed in between the two gold nanoparticles (see figure 6.3). This was achieved by using two sets of handles and corresponding anchors - one for the AuNPs and the other one for the AgNP. The gap size between the nanoparticles was tuned to be $\sim 4$ nm by appropriate choice of the corresponding attachment sites. The resulting interparticle distance between the two outer AuNPs is 38 nm. Conceptually, the two AuNPs without the intermediate AgNP are too far apart from each other to support a strong coupled plasmonic mode, thus no energy transfer is expected. With the central AgNP, the distance between the AuNPs is bridged and therefore plasmonic coupling and coherent energy transfer between the outer AuNPs becomes possible. Hence, the central AgNP fulfils the function as loss-less virtual transmitting state.

In this work (see also A.4) the non-dissipative passage in the heterogeneous nanoparticle trimer chain was demonstrated by optical characterization via single structure dark-field scattering spectroscopy as well as by corresponding theoretical simulations. Figure 6.4 shows the measured spectral shift between the scattering spectrum of a homo AuNP dimer structure and the spectrum of a hetero AuNP/AgNP trimer structure. The spectral shift of $\sim 40$ nm implies the connecting ability of the central AgNP. Heat dissipation simulations of trimer geometry confirm that the AgNP is not dissipating energy at the longitudinal resonance frequency proving that the energy is coherently transferred between the two outer AuNPs with the help of the central AgNP.

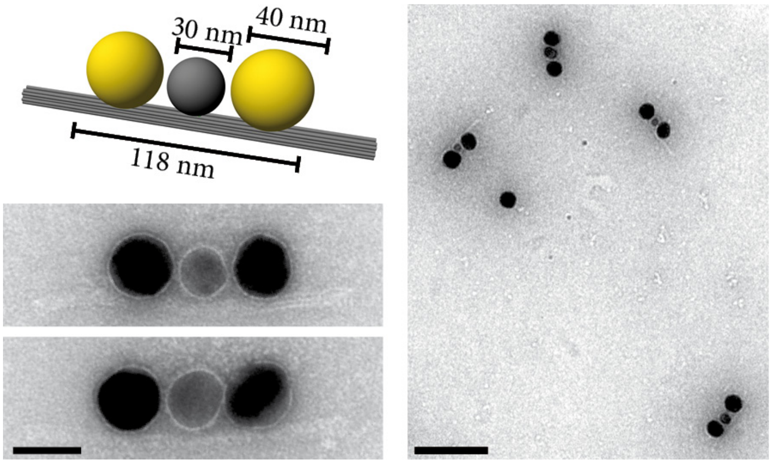

Figure 6.3.: Schematic design of the DNA origami templated heterogeneous trimer system consisting of two AuNPs and one central AgNP and representative close-up and wide field TEM images. Scale bar 40 nm, respectively 200 nm.

Hence, the DNA origami based hetero trimer structure is a realization of a non-dissipative passage system which transfers energy between two spatially separated plasmonic nanoparticles via a third intermediate particle.

In summary, the assembly of a plasmon based passage system was achieved by the DNA origami technique. It was demonstrated both, experimentally and theoretically that the construct is able to transfer energy in a coherent, non-dissipative way between two remote nanoparticles via a third transmitting element. This device could find future applications in the field of information transfer over large distances via plasmonic waveguides. Future work could on one hand focus on such transfer processes over larger distances e.g. using multiple intermediate AgNPs. On the other hand, transfer processes in nanoparticle chains of homogeneous materials could be investigated. In this case, first investigations showed a prominent peak shift of $\sim 70$ nm in the longitudinal mode of a $40-30-40$ nm trimer AuNP configuration compared to the longitudinal mode of the corresponding dimer without an intermediate particle (see figure 6.5).

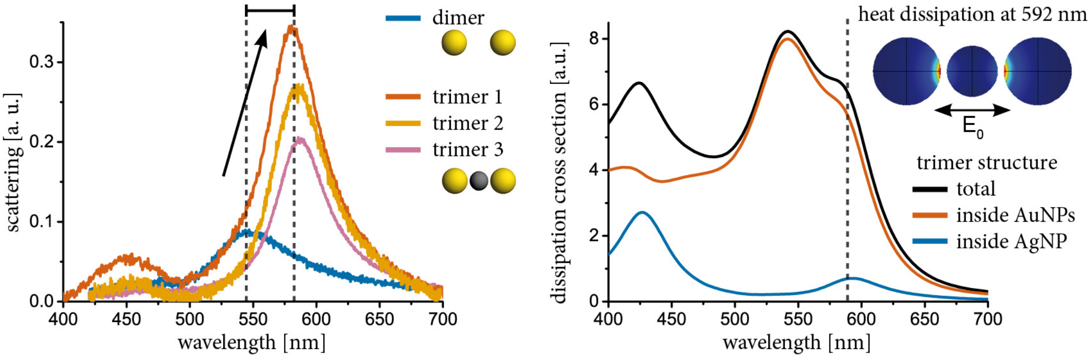

(a)

(b)

Figure 6.4.: Characterisation of the plasmonic transfer system. **(a)** Single structure dark field scattering spectroscopy of a dimer structure with only AuNPs and a corresponding trimer structure with a central AgNP in between the two AuNPs. The observed plasmon resonance shift is $\sim 40\,\text{nm}$. **(b)** Heat dissipation cross section simulation to the trimer geometry depict that the AgNP is not dissipative at the resonance wavelength of $\lambda = 592\,\text{nm}$.

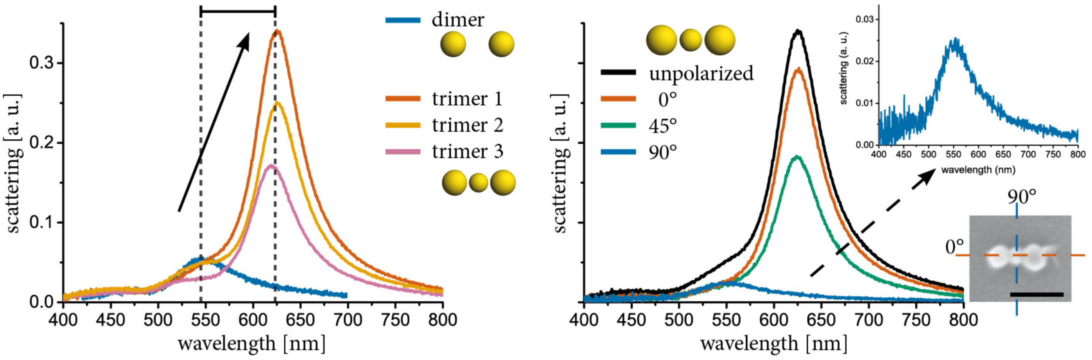

(a)

(b)

Figure 6.5.: Characterisation of chain like structures based on DNA origami. **(a)** Single structure dark field scattering spectroscopy of a dimer structure with only AuNPs and a corresponding trimer structure with two 40 nm AuNPs and one central 30 nm AuNP. The observed plasmon resonance shift between the dimer and trimer strucutres is $\sim 70\,\text{nm}$. **(b)** Corresponding polarization resolved scattering spectra to the AuNP trimer structure.

## 6.4. Associated Publication P4

### Hot spot-mediated non-dissipative and ultrafast plasmon passage

by

Eva-Maria Roller, Lucas V. Besteiro, Claudia Pupp, Alexander O. Govorov, and Tim Liedl

submitted (2016)

see Appendix A.4

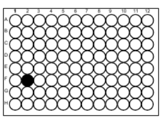

# 7. Single Molecule Surface Enhanced Raman Scattering

When light is interacting with matter, photons can be scattered either elastically (Rayleigh scattering) or inelastically. The inelastic scattering between a photon and a molecule is called *Raman scattering* which was first experimentally observed in 1928 for liquids by C. V. Raman and his student K. S. [158] as well as in crystals by G. Landsberg and L. Mandelstam [159]. This effect was theoretically predicted in 1923 by A. Smekal [160].

Spontaneous Raman scattering is mediated by rotational and vibrational modes of the molecule, which is considered to be a short time in a virtual excited level. The Raman scattered photons can have both, higher (Anti-Stokes Raman scattering, $AS$) or lower frequency (Stokes Raman scattering, $S$) than the incident photons. The corresponding frequencies of the Stokes and Anti-Stokes bands are

$$\begin{aligned} \nu_S &= \nu_{exc} - \nu_M \\ \nu_{AS} &= \nu_{exc} + \nu_M \end{aligned} \tag{7.1}$$

with $\nu_M$ being the molecular vibrational frequency and $\nu_{exc}$ being the incident light frequency (see figure 7.1). The difference in frequency from incident light to scattered light is specific for the molecule and originates from the effect that the molecule changes its vibrational and rotational oscillation. Since the distinctive Raman transitions of a molecule corresponds to the molecular electron bondings and symmetries, Raman scattering can be used to gain structural information and to detect conformational changes of the molecule [161, 162].

## 7.1. Introduction to Surface Enhanced Raman Scattering

Since the Raman scattering cross sections of $(10^{-31} - 10^{-29})$ cm$^2$ per molecule are two to three times smaller than Rayleigh scattering cross sections and ten times smaller than those of fluorescent processes, the signal must be enhanced to get a reasonable signal to noise ratio. One method to enhance the signal is called *surface enhanced Raman scattering* (SERS). The power of the spontaneous Raman scattered signal is linear dependent to the incoming excitation power. Thus, SERS signals can for example be observed if a molecule is placed in close proximity (in the near field) of a plasmonic nanoparticle.

The Raman scattering power for e.g. a stokes process is:

$$P_S(\nu_S) = N\sigma_{RS}I(\nu_{exc}) \tag{7.2}$$

with $N$ the number of molecules, $\sigma_{RS}$ the Raman scattering cross section and $I(\nu_{exc})$ the excitation intensity. The underlying principles of SERS can be explained by two contributing effects. First, excitation of localized surface plasmons and hence increased electromagnetic field in the proximity of the nanoparticle gives *electromagnetic enhancement* ($I(\nu_{exc})$) and second, changes in the rotational and vibrational modes of the molecule in the proximity of the metal nanoparticle give *chemical enhancement* ($\sigma_{SERS} > \sigma_{RS}$).

Here, we focus on the electromagnetic enhancement which has a much larger influence onto the total SERS intensity [163]. The proximity of the Raman analyte to a metal nanoparticle leads to twofold enhancement. First, the intensity of the incoming light ($exc$), which excites the Raman modes in the molecule is higher. Second, emitted light field of the Raman signal ($S$ or $AS$) gets also enhanced. This results in a huge increase of the total enhancement of the Raman signal. The SERS power (Stokes) turns to

$$P_S = N\sigma_{SERS}\frac{|\vec{E}_{loc}(\nu_{exc})|^2}{|\vec{E}_0|^2}\frac{|\vec{E}_{loc}(\nu_S)|^2}{|\vec{E}_0|^2} \tag{7.3}$$

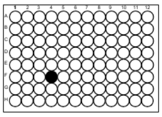

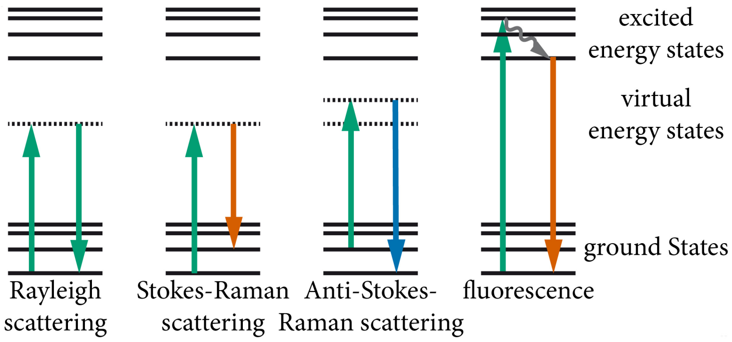

Figure 7.1.: Jablonski diagram showing energy transitions of different optical scattering processes on a molecule.

with $|\vec{E}_{loc}|$ is the local field at the Raman analyte. For Raman scattering the frequency of the scattered light is only slightly shifted from the incident light frequency compared to the plasmon linewidth. Therefore they can be approximated to have the same frequencies.This results in an overall electromagnetic enhancement factor ($EF$) to the total SERS:

$$EF = \frac{|\vec{E}_{loc}(\nu_{exc})|^2}{|\vec{E}_0|^2} \frac{|\vec{E}_{loc}(\nu_S)|^2}{|\vec{E}_0|^2} \approx \frac{|\vec{E}_{loc}(\nu_{exc}|^4}{|\vec{E}_0|^4} \tag{7.4}$$

As one can see, the SERS signal depends on the fourth power of the field. Thus organizing metal nanoparticles in such a way that the electromagnetic field gets strongly enhanced and placing the Raman analyte directly at the position of the highest field enhancement is a way to reach high Raman scattering intensity which are needed for single molecule Raman spectroscopy. The maximum $E^4$ enhancement is achieved when both, the excitation and emission enhancement processes, are the highest. It has been shown, that this is the case if the excitation frequency (laser) is slightly shifted to the blue with respect to the plasmon resonance frequency [164].

## 7.2. State of the Art

Since SERS was discovered in 1977 [165], the interest in this non-destructive technique for determining chemical components and structural information in-

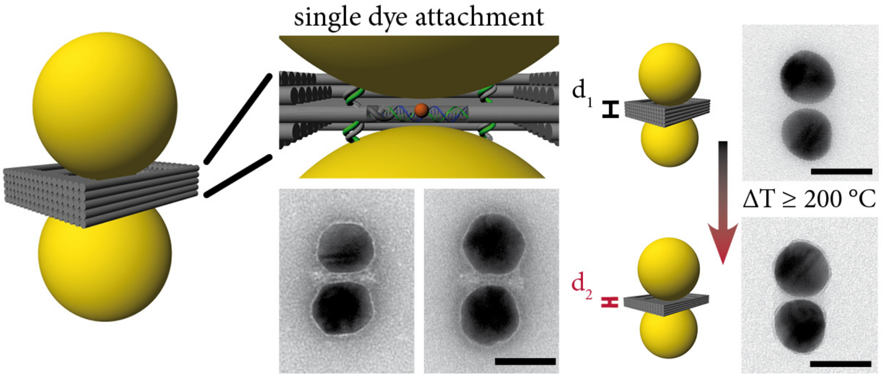

(a) (b)

Figure 7.2.: **(a)** Schematic illustration of the DNA origami based plasmonic antenna structure with single dye molecule placement and corresponding TEM images. Scale bar 40 nm. **(b)** Thermal heating of the plasmonic antenna structures induces a reduction of the interparticle gap size due to thermal shrinking of the DNA origami template as observed by TEM imaging. Scale bar 40 nm.

creased constantly. The SERS substrates were constantly improved to reach higher enhancement factors by optimizing their shapes, material coatings and plasmonic particle arrangement [166–169]. Also plasmonic nanoparticles brought into close proximity by the help of DNA linkers were shown to be good SERS substrates [170, 171]. Recently DNA origami based plasmonic nanoantenna structures were used for SERS detection of molecules [172–175]. Hereby the DNA origami structures served as a template to organize the nanoparticles in a hot spot conformation. Dyes, intercalating with DNA and Raman active were then used to detect SERS. However, those DNA origami based structures did not yet achieve the single molecule Raman detection level.

## 7.3. DNA origami for Single Molecule Raman Scattering

The DNA origami technique showed to be a viable method to organize metal nanoparticles in ’hot spot’ conformations [172, 173]. At the same time they

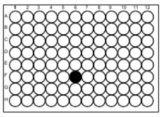

are well suited to place dye molecules with high precision at predefined spatial positions [176]. Thus, DNA origami based dimer structures having a target dye molecule precisely positioned in the region of the strongest field enhancement are perfect candidates for single molecule SERS detection. The 'hot spot' intensity for such structures crucially depends on the particle size as well as on the gap size between the particles [73, 177].

So far, single molecule SERS detection with nanoparticle Dimer structures was achieved for structures having a gap size smaller than 2 nm [156, 171, 178, 179]. However, the technique used to create such a small gap size was overgrowing of the nanoparticles with an additional silver shell, which involves an additional, unwanted chemical treatment. In this publication A.5 [180] it is shown, how to overcome this limitation.

The SERS substrate consists of a funnel formed DNA origami structure which is designed to accommodate two 40 nm goldnanoparticles. One to four Raman active dye molecules (here: Cy3 and Cy3.5) are directly bound to staple strands by click chemistry (see section A.5). This guarantees the incorporation of the the dye molecule into the DNA origami structure. The dye label staple strands are located directly in the geometrical centre of the dimer structure. Figure 7.2 illustrates this. After immobilizing the dimer structures on a glass substrate the average gap size was determined to be in average 2.8 nm. However, with this conformation no single molecule SERS signal was detectable. For that, an increase of the field enhancement is needed, which can be achieved by using larger gold nanoparticles or by reducing the gap size.

It is known [181, 182], that temperatures above 200 °C cause shrinking of dried DNA origami structures. This effect was used in the associated publication to reach gap sizes below 2 nm. Both, thermal heating of the substrate as well as optothermal heating via laser irradiation onto the dimer structures resulted in reduction of the gap size (see figure 7.2. Such dimer structures allowed the detection of single molecule SERS.

Moreover, it was possible to map SERS intensity with respect to plasmonic field enhancement. Therefore SERS intensities of multiple dimer structures of a specific Raman vibrational mode of the dye located at the hot spot was plotted versus the corresponding longitudinal plasmonic mode of the dimer structure

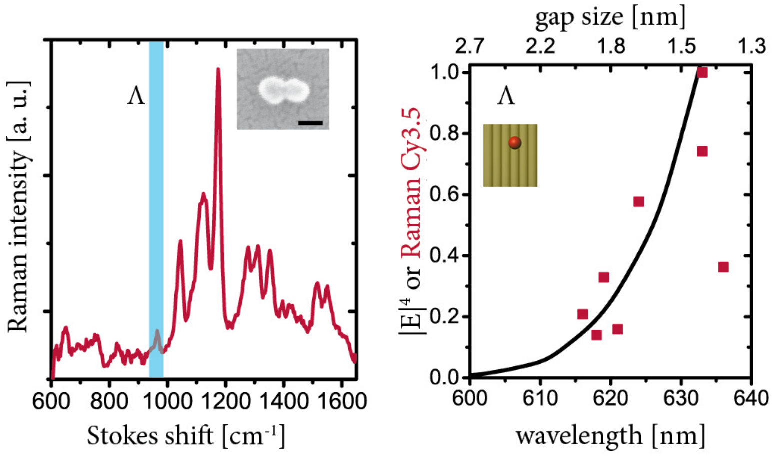

(a) (b)

Figure 7.3.: **(a)** Single molecule SERS data after optothermal shrinking of the dimer gap size. Inset: Corresponding SEM image of the antenna structure. Scale bar 40 nm. **(b)** Mapping of the SERS intensity as a function of the dimer gap size for a specific vibrational mode of the Cy3.5 (red squares) and the theoretical Raman scattering enhancement (black line).

and compared to theoretical simulations of the enhancement factor. The expected $|E^4|$ enhancement was in good agreement as shown in figure 7.3.

In short, the presented DNA origami based dimer structures with a specific amount of dye allowed quantitative single molecule SERS. The gap size reduction of DNA origami based metal nanoparticle structures by plasmonic or purely thermal heating is a general effect. Thus, it can be applied to various DNA templated plasmonic structures. Moreover, mapping the effect of the near field enhancement in the plasmonic hot spot to the SERS signal intensity was achieved and compared with theory. Overall, a general approach for single molecule SERS by DNA origami templating method was shown, which can be transferred to several different SERS reporter molecules. Since the DNA origami technique is a solution based process, the DNA origami templated SERS structures are directly available in a bulk solution. Along these lines, one can envision a sensor based on SERS detection e.g. of DNA bases, which works in solution.

## 7.4. Associated Publication P5

### Quantitative single molecule surface-enhanced Raman Scattering by optothermal tuning of DNA origami assembled pasmonic nanoantennas

by

Sabrina Simoncelli*, Eva-Maria Roller*, Patrick Urban, Robert Schreiber,
Andrew J. Turberfield, Tim Liedl, and Theobald Lohmüller
*equal contribution

published in ACS Nano, 10, 9809 - 9815 (2016).

see Appendix A.5

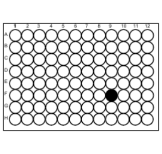

# 8. Conclusion and Outlook

In this thesis, I demonstrated the versatile application spectrum of the DNA origami technique in the field of plasmonic nanostructures. The precise spatial arrangement of metal nanoparticles with the help of DNA origami template structures allowed to study light-matter interactions of nanoscale objects. The DNA origami template structures with their well-defined size and shape enabled it to control the metal nanoparticle arrangement with nanometer precision. Additional to their templating function they served as addressable sites for dye molecules.

The first part, covered the field of *metamaterials*. A doughnut-like DNA origami structure provided a tool to create ring shaped metal nanoparticle arrangements with different numbers (four to eight) and sizes (10 nm to 40 nm) of the nanoparticles. Single structure dark-field scattering spectroscopy was used to show that a four gold nanoparticle ring geometry can support magnetic resonances in the visible frequency domain - a first step towards negative refraction. Moreover the DNA origami template approach is a solution based approach, resulting directly in a bulk liquid of the plasmonic ring structures, which opens the doors for new materials such as metasprays.

The second part discussed *plasmon-exciton interactions*. Here, the DNA origami template allowed the organization of gold nanoparticles with diameters from 30 nm to 60 nm in a plasmonic dimer antenna conformation, whereas the gap size between the particles was kept fixed by the template structure. This allowed to tune the longitudinal plasmon resonance frequency from $\sim 560$ nm to $\sim 600$ nm. The spatial overlap of such plasmonic antennas with an organic dye having a resonance frequency in-between this range allowed to study plasmon-exciton interactions. The tuning across or even matching of the longitudinal plasmon mode with respect to the exciton was displayed in the observation of hybrid plasmon-exciton modes in the far field scattering spectra. For future work, hybrid DNA based plasmon-exciton systems provide the possibility to study the energy exchange between plasmon and exciton in detail.

A third application of DNA origami templates was in the field of *sensors.* The sensor studied in this thesis was a chiral molecule sensor. As most biological molecules are chiral molecules, their sensitive detection is of interest. However, their circular dichroism signal is in the UV frequency. Here, it was possible to measure and enhance the CD signal in the visible frequency domain. This was achieved by placing a DNA origami template structure directly in the hot spot between two metal nanoparticles. In this way, the molecular CD signal was picked up to the resonance frequency of the plasmon and enhanced at the same time. It was possible to detect a CD signal at a low DNA origami structure concentration of $\sim 100\,\mathrm{pM}$. In the future, a DNA origami template can serve as a binding site for chiral molecules of interest, which opens the doors for sensitive chiral molecule sensors.

The fourth example demonstrating the versatility of the DNA origami template approach in plasmonics was a *heterogeneous plasmonic passage system.* The cylinder-like DNA origami template was designed to accommodate three metal nanoparticles, whereas the outer two were gold nanoparticles and the central one was a silver nanoparticle. With far field scattering spectra of the trimer structure and corresponding numerical simulations it was shown, that energy is coherently transferred between the two outer gold nanoparticles with the help of the central silver nanoparticles, whereas the silver nanoparticle did not dissipate energy. Henceforth, a non dissipative plasmon based coherent passage system was established. In future applications, plasmonic nanostructures can be elements for coherent transfer and processing of information.

The last example of DNA origami templated plasmonic systems was in the field of *single molecule Raman spectroscopy.* The employed DNA origami template structure did not only serve as building block to create a plasmonic hot spot dimer nanoparticle conformation. At the same time a single DNA functionalized dye molecule was incorporated into the DNA origami structure, resulting in a dye placement directly at the highest field enhancement. Plasmonic heating was used for shrinking of the dimer gap size to reach even higher field enhancements. Hence, it was possible to acquire single dye surface enhanced Raman scattering data without further chemical treatment such by an additional silver shell. Moreover, mapping of the plasmonic hot spot and its corresponding field enhancement was possible. DNA based Raman detection can be used to analyse very small concentrations of molecules.

To summarize, the design flexibility of DNA template structures offer a great tool to study various functional plasmonic systems dried on a surface or in solution. All structures analysed in this thesis were static. In future, the formation of dynamic, functional plasmonic devices will be a consequent next step. Such structures could be plasmonic sensors, which change their conformation upon detection of a target molecule which will then be displayed in a detectable signal change. Detection methods for this could be circular dichroism, single structure spectroscopy or even just a colour change. Additionally, plasmonic nanoparticles are also good local heaters. Therefore, arranged metal nanoparticles could be used to reach a precise and local temperature increase.

# A. Appendix

## A.1. Associated Publication P1

### DNA-Assembled Nanoparticle Rings Exhibit Electric and Magnetic Resonances at Visible Frequencies

by

Eva-Maria Roller, Larousse Khosravi Khorashad, Michael Fedoruk, Robert Schreiber, Alexander O. Govorov, and Tim Liedl

published in Nano Letters, 15, 1368 - 1373 (2015).

NANO LETTERS
Letter
pubs.acs.org/NanoLett

# DNA-Assembled Nanoparticle Rings Exhibit Electric and Magnetic Resonances at Visible Frequencies

Eva-Maria Roller,[†] Larousse Khosravi Khorashad,[‡] Michael Fedoruk,[†] Robert Schreiber,[§] Alexander O. Govorov,[‡] and Tim Liedl*,[†]

[†]Fakultät für Physik and Center for Nanoscience, Ludwig-Maximilians-Universität München, Geschwister-Scholl-Platz 1, 80539 Munich, Germany

[‡]Department of Physics and Astronomy, Ohio University, Athens, Ohio 45701, United States

[§]Clarendon Laboratory, Department of Physics, University of Oxford, Parks Road, Oxford OX1 3PU, United Kingdom

*Supporting Information*

**ABSTRACT:** Metallic nanostructures can be used to manipulate light on the subwavelength scale to create tailored optical material properties. Next to electric responses, artificial optical magnetism is of particular interest but difficult to achieve at visible wavelengths. DNA-self-assembly has proved to serve as a viable method to template plasmonic materials with nanometer precision and to produce large quantities of metallic objects with high yields. We present here the fabrication of self-assembled ring-shaped plasmonic metamolecules that are composed of four to eight single metal nanoparticles with full stoichiometric and geometric control. Scattering spectra of single rings as well as absorption spectra of solutions containing the metamolecules are used to examine the unique plasmonic features, which are compared to computational simulations. We demonstrate that the electric and magnetic plasmon resonance modes strongly correlate with the exact shape of the structures. In particular, our computations reveal the magnetic plasmons only for particle rings of broken symmetries, which is consistent with our experimental data. We stress the feasibility of DNA self-assembly as a method to create bulk plasmonic materials and metamolecules that may be applied as building blocks in plasmonic devices.

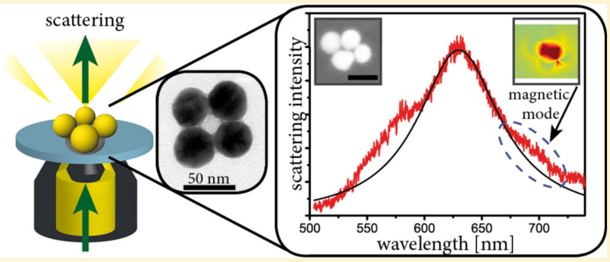

**KEYWORDS:** *DNA origami, nanoparticles, plasmonic metamaterials, self-assembly*

A negative refractive index metamaterial requires both electric permittivity and magnetic permeability to be negative. While metals naturally exhibit negative real values for their permittivity at visible frequencies, negative permeability has to be created through an "artificial magnetic" response.[1,2] The well-known concept to achieve this goal in the THz domain is to create electric and magnetic resonances in split ring resonators,[3] which has been realized in many examples and led to the development of gradient index lenses[4,5] and switching devices for terahertz radiation.[6] This and similar approaches that are based on electric leads, however, are hard to transfer into the visible frequency domain due to the changing conduction properties of metals at high frequencies and the resulting saturation effect of the magnetic response.[7] As an alternative route to artificial magnetic responses, it has been proposed that metal nanoparticles that are brought together in a ring geometry can support a circulating displacement current induced by plasmonic resonances.[8−10] Similar to the conduction current within split ring resonators the plasmonic interaction can lead to the emergence of magnetic resonances at visible or near-infrared frequencies. Recent implementations of such ring resonators also experimentally demonstrated the appearance of magnetic resonances and even magnetic-based optical Fano resonance.[11] Studies that investigated size- and shape-controlled nanoscale ring arrangements of plasmonic particles used either atomic force microscope nanomanipulation[11] or lithography[12,13] to achieve their goal. Other approaches are based on the use of dielectric spheres as substrates for the random attachment or growth of plasmonic nanoparticles[14−16] or nanoshell clusters.[17,18] To take advantage of the intriguing concept to use plasmonic particle devices as building blocks for large scale metamaterials it is necessary to reach full control over design and manufacturing of subwavelength structures as well as to be able to produce large numbers of plasmonic structures in a parallel manner.

Here we report a strategy to overcome these challenges by using the DNA origami method[19−21] to fabricate versatile templates for metamolecules on a length scale much smaller than the wavelength of visible light. Structural DNA nanotechnology allows the assembly of trillions of identical nanoscale three-dimensional objects at once in a simple, solution-based reaction.[22,23] A DNA origami structure is built

**Received:** December 3, 2014
**Revised:** January 16, 2015
**Published:** January 22, 2015

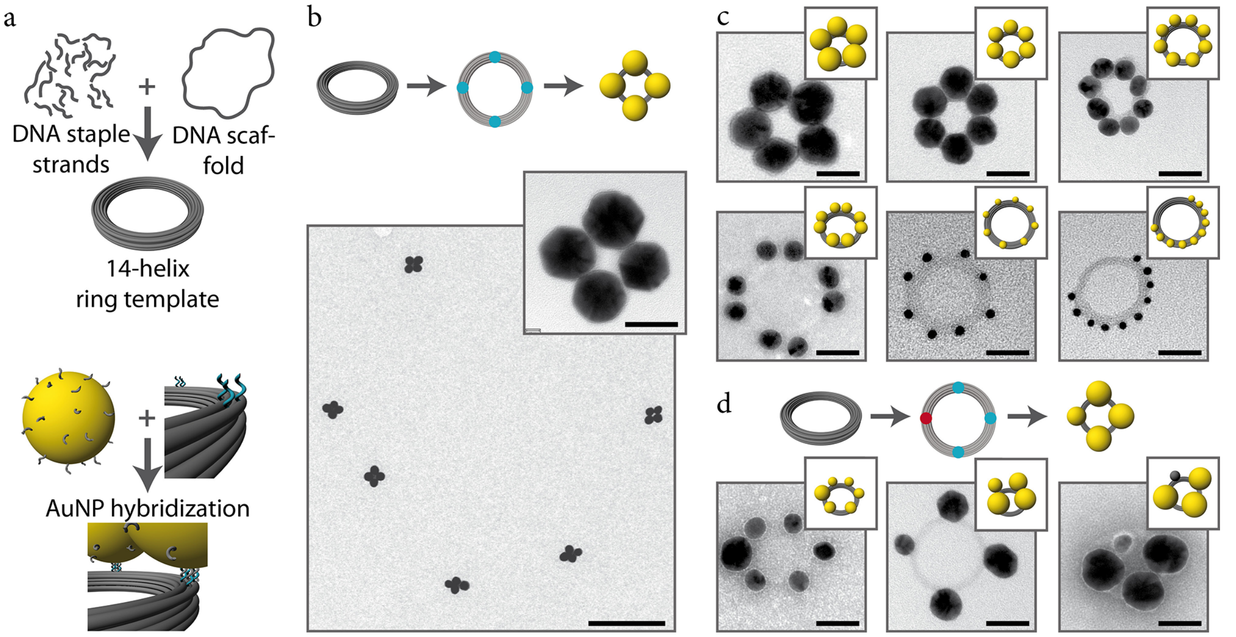

**Figure 1.** DNA origami–nanoparticle ring structures. Plasmonic rings were built by arranging nanoparticles on ring-shaped DNA origami structures. (a) Self-assembly of DNA origami nanoparticle rings: an 8 kb-long DNA scaffold was annealed with ∼250 synthetic staple strands (each ∼40 bases long) to create a ring-shaped 14-helix bundle template structure (14HB-template). In the next step, DNA-functionalized AuNPs were attached to defined positions on the 14HB-template via hybridization of the handle sequences protruding from the origami ring and the complementary DNA strands on the AuNPs. (b) Upper panel: schematic illustration of the 14HB-template with four identical attachment sites to create a symmetric four particle ring. Lower panel: Wide-field transmission electron microscopy (TEM) micrograph of plasmonic ring structures consisting of four 40 nm AuNPs. Scale bar: 400 nm. Inset: Zoom-in. Scale bar: 40 nm. (c) Upper panels: Schematic illustration and TEM images of 14HB-templates with five 40 nm AuNPs (left), six 30 nm AuNPs (middle), and eight 20 nm AuNPs (right) attached. Scale bars: 40 nm. Lower panels: Eight 20 nm AuNPs attached in a ring of dimers (left), eight 10 nm AuNPs attached in a ring of equal spacing (middle), and ten 10 nm AuNPs in a C-shaped geometry. Scale bars: 40 nm. (d) Schematic illustration and TEM images of asymmetric ring structure assembly where the attachment sites offer two different sequences (illustrated as red and blue dots). Six (left) and four (middle) AuNPs with two different diameters (30 and 20 nm, and 40 and 20 nm, respectively) are shown, as well as three AuNP and one AgNP (right) with diameters of 40 and 20 nm, respectively.

from one long scaffolding DNA single-strand (here: 8634 nucleotides) that is assembled into the desired two- or three-dimensional shape via the annealing with ∼250 short "staple" oligonucleotides. Because of their inherent and defined sequence addressability, DNA structures allow nanometer precise positioning of objects such as metallic nanoparticles through the incorporation of DNA handle sequences at virtually any site on the structures.[24−29]

For our goal to create nanoparticle ring resonators of defined geometries, this bottom-up fabrication method was employed to assemble several nanoring geometries consisting of a defined number of metal nanoparticles that were all equal or of various sizes and materials. Using the software cadnano (cadnano.org)[30] and CanDo[31,32] we designed a ring-shaped DNA-origami structure of 14 parallelly arranged DNA double-helices of 200 nm length that were bent by design[33] into a full circle by insertion and deletion of bases at selected sites (see Supporting Information for design details and experimental protocols S1−S4). The resulting structure has a diameter of 62 nm and a ring cross-section of ∼10 nm. To serve as a versatile template for all desirable ring-shaped particle geometries, the DNA origami structure offers repeating units of DNA handles that can act as specific attachment sites for DNA-functionalized nanoparticles, overall 27 evenly spaced sites. It is thus possible to create a large diversity of particle ring geometries. Figure 1 illustrates the self-assembling process and a variety of implemented particle arrangements, including symmetric and asymmetric site-specific organization of particles of different sizes and materials. In the first experimental step, the DNA origami template is annealed by heating up and slowly cooling down a solution containing the scaffold strand and a set of staple oligonucleotides including all sequences that are needed to form the desired attachment sites for particle binding. After purification of the folded DNA origami template via gel electrophoresis, DNA-functionalized gold (AuNP) and silver (AgNP) nanoparticles of the desired size were hybridized to the attachment sites. Here particles of 10−40 nm in diameter were used but in principle also larger and smaller particles could be employed.[26] The AuNPs are covered with 15 nucleotide (nt) long single-stranded DNA (ssDNA) sequences to bind them to the origami template as well as to stabilize them against high salt concentrations that are needed during the annealing process. A second gel electrophoresis step is performed to purify the now assembled metamolecules from the excess of unbound AuNPs and little amounts of aggregated structures (Supporting Information Figure S5). Note that the presence of an excess of nanoparticles during the assembly largely inhibits the aggregation of the metamolecules. We achieved yields of correctly arranged particle rings of up to 73%, (statistics and additional TEM images can be found in the Supporting Information Figures S6−S9). By choosing unique handle sequences at specific attachment sites and by introducing the complementary functionalized particle species, various particle types can be attached at defined positions in one step (Figure 1d) (see Supporting Information for particle functionalization and purification).

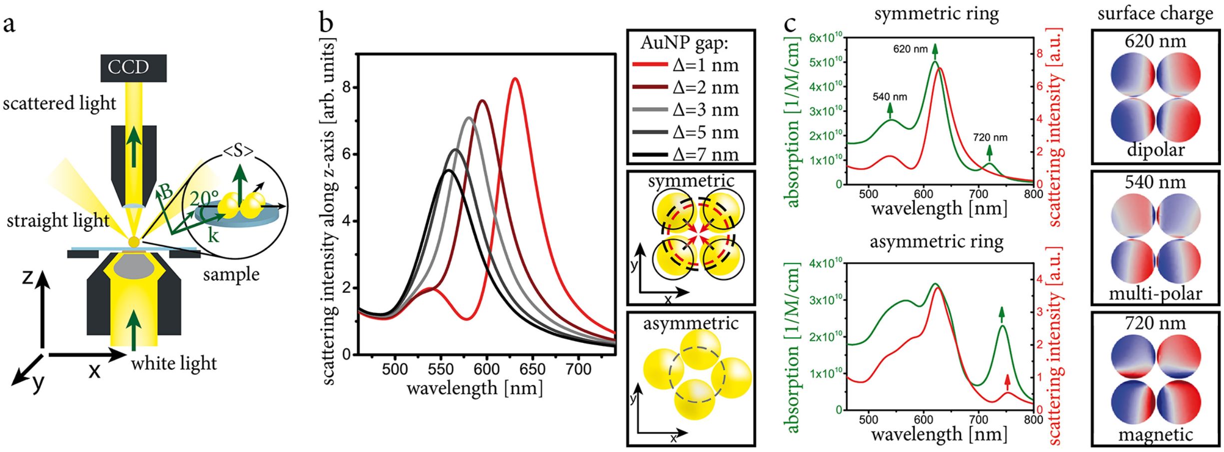

**Figure 2.** Experimental setup and simulated scattering and absorption spectra of symmetric and asymmetric four-particle ring structures. (a) Experimental dark-field setup and the corresponding model for the numerical simulations (inset). (b) The scattering spectrum of a symmetric ring structure consisting of four 40 nm AuNPs strongly depends on the gap size Δ between the particles. For distances smaller than 4 nm a second resonance peak appears in the scattering spectra. (c) The symmetric ring with a gap size of 1 nm shows two peaks in the scattering simulation but three peaks in the absorption whereas the asymmetric ring shows three peaks both in scattering and absorption. The origins of these peaks are dipolar, multipolar, and magnetic interactions.

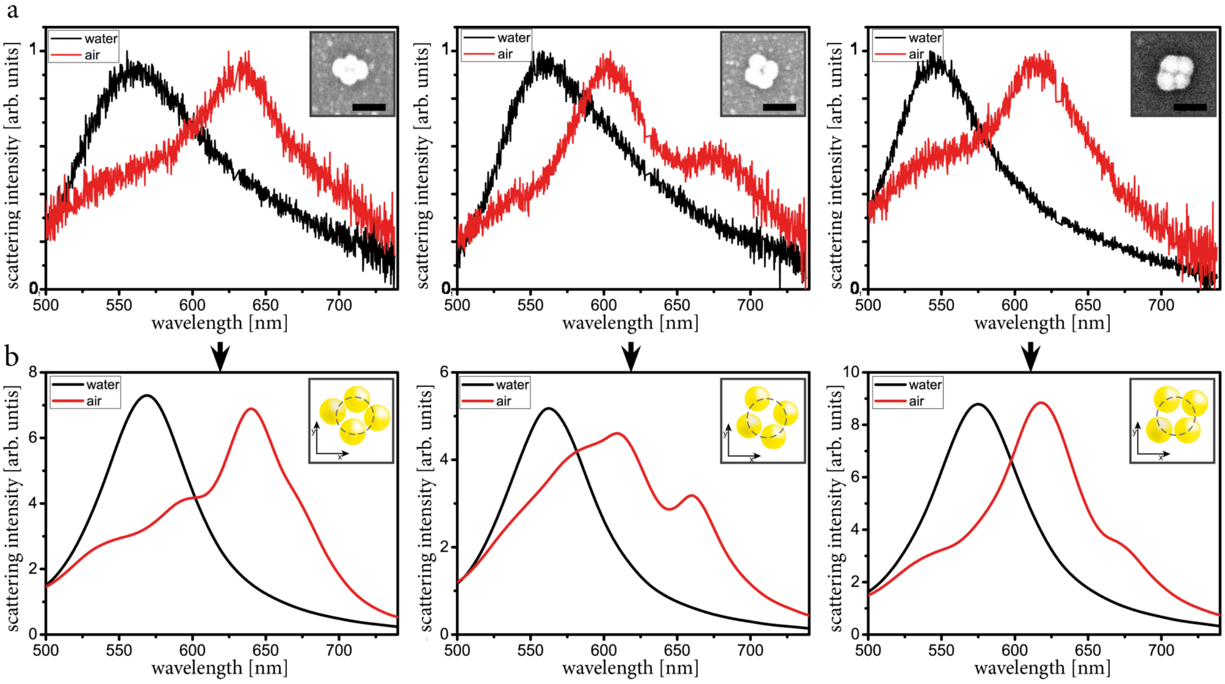

**Figure 3.** Scattering spectra of individual ring structures immobilized on glass substrates. The spectral shape is strongly dependent on the exact particle ring geometry. (a) Each two scattering spectra were collected from the same structures immersed in buffer (black curves) and after drying in air (red curves). Insets: corresponding SEM images of each ring structure. Scale bar: 100 nm. (b) The spectra in air were simulated with the AuNP positions as determined from SEM data. The spectra in water were then fitted by moving the positions of each AuNP 4 nm radially outward.

Obviously, also smaller and larger ring diameters could be implemented by varying the template DNA structure. The origami template chosen in this study provides a good balance between structural stiffness (cross section) of the ring template and large enough diameter to accommodate the attachment of four or more 30 and 40 nm AuNPs with small gaps between the particles. Importantly, we found in our experiments that small interparticle distances are essential to support circulating current modes along the rings. Because of their comparatively simple spectra, we focus in the following on four-particle metamolecules.

The plasmonic properties of the assembled individual ring structures were characterized by dark-field scattering spectroscopy. In our experimental setup the unpolarized incident light hits the glass substrate at ~23° from all sides and the scattered light is collected above the sample and perpendicular to the glass surface (Figure 2a). First, numerical COMSOL simulations conforming to our experimental geometry were performed to understand the scattering behavior of the particle

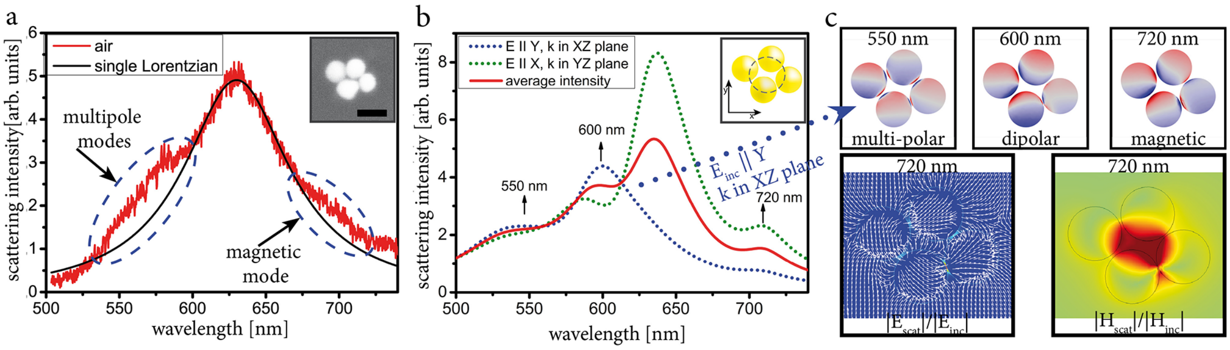

**Figure 4.** Analysis of single scattering spectrum. (a) Scattering spectra of a structure exhibiting multiple modes. Inset: corresponding SEM image. Scale bar: 50 nm. (b) Simulation of the scattering spectra for different polarizations of the incident light corresponding to the particle ring presented in panel a. Three distinguishable peaks are visible. (c) Simulation of the surface charge distribution for all peaks as well as the electric and magnetic field corresponding to the peak at 720 nm.

rings. In our simulations, we used the empirical dielectric constant of gold taken from Johnson and Christy.[34] Figure 2b shows the simulated scattering spectra for symmetric planar rings consisting of four 40 nm AuNPs. The gap size between the particles was varied between 7 and 1 nm. As observed in previous studies,[35−37] the peak position of the plasmonic resonance shifts to longer wavelengths for smaller gap sizes. Additionally, at gap sizes smaller than 4 nm a second peak becomes distinguishable in the scattering spectra whereas the absorption simulation shows three peaks. We analyzed the three modes in a surface charge intensity plot for the case of 1 nm gaps and found them to originate from dipolar, multipolar, and magnetic interactions (Figure 2c). Interestingly, the rings with perfect symmetry exhibit three modes in the computed absorption spectra, whereas the computed scattering spectra show two modes only and do not show the magnetic mode. However, the simulations executed with slightly asymmetric rings (Figure 2b) do show three distinguishable peaks in both absorption and scattering as here the symmetry breaking induces coupling between the far-field scattered light and the magnetic modes.

To investigate the scattering spectra of the plasmonic ring structures experimentally they were immobilized on a substrate, analyzed with a dark-field spectrometer, and then imaged with scanning electron microscopy (SEM) to determine the exact position of every single AuNP in each ring. For the measurements a droplet of solution containing the ring structures was deposited on a plasma-cleaned quartz glass. After 10 min, the droplet was flushed away by water and the surface was quickly dried with nitrogen. As the particle rings are slightly distorted during the adsorption and the subsequent drying process, small deviations from the designed particle geometries are observed in the SEM images and these spatial variations are in turn reflected in the disparity of the recorded spectra (Figure 3a). To further investigate the influence of the surrounding medium we performed scattering measurements of ring structures in air (red lines in Figure 3a) but also immersed in a buffered solution (1× TBE, 11 mM $MgCl_2$, black lines in Figure 3a).

For structures immersed in solution only one dominant broad resonance at around 560 nm is observed while the spectra taken in air exhibit multiple distinct peaks, as well as a red shift of the dominant resonances. The change of the effective permittivity could explain this red shift[38,39] but not the appearance of the additional resonances. These peaks are a strong indication of a reduction of the interparticle distance,[35,37] which is expected to occur during the drying process, as dehydration will reduce the electrostatic and steric repulsion between the ssDNAs that coat the AuNPs.[38] To study this conformational change of only a few nanometers and to support the experimental observations we performed numerical simulations. The positions of all AuNPs in the dried rings were determined from the SEM images with an accuracy of 1 nm and served as precondition for the simulations. We found an average surface-to-surface distance of 2.4 nm ±1.9 nm (Supporting Information Figure S7) and strikingly, the simulated scattering spectra match the measured spectra of the individual dried structures remarkably well (red lines in Figure 3b). It was also possible to simulate the shape of the experimental spectra collected from the structures immersed in buffer. Therefore, not only the effective permittivity was adapted but also the position of each AuNP had to be moved 4 nm radially outward, which validates the assumption of a shift in the position of the AuNPs during the drying process.

Generally, already small deviations in the positions of the AuNPs compared to a perfect symmetric ring structure cause shifts in the occurring resonant peaks and the emergence of new resonances (cf. simulated spectra in Figure 2b,c and observed and simulated spectra in Figure 3a,b). To analyze the origin of the measured resonances additional numerical simulations were performed for the ring structure shown in Figure 4a. The simulations show three distinguishable peaks in the scattering spectra (Figure 4b). Two peaks (at 550 and 600 nm) were already visible in the symmetric ring case (Figure 2c) and belong to the multipolar and dipolar resonances. The third peak appearing in the computed scattering spectra at 720 nm has its origin in a magnetic plasmon resonance and appears in the scattering configuration only for four-particle rings with broken symmetry. In such asymmetric rings, the magnetic plasmons become active in the scattering because the broken symmetry opens a coupling channel between the magnetic mode and the far-field photons propagating along the *z*-axis. Figure 4c shows the surface charge distributions for all peaks as well as the electric and magnetic field map corresponding to the magnetic resonance at 720 nm. Importantly, the experiments confirm that the response of plasmonic ring structures is very sensitive to their exact geometries and that electric and magnetic resonances can be supported at optical frequencies in our DNA-assembled nanoparticle ring resonators (additional spectra can be found in the Supporting Information Figures S10 and S11).

One of the great advantages of DNA-based self-assembly is the possibility to manufacture large numbers of identical objects dispersed in solution, which gives access to the use of the DNA-assembled metamolecules as building blocks in metafluids and to scale up the production.[21,25] To demonstrate that our DNA origami ring structures also perform in liquids, we carried out absorption measurement of bulk solutions containing plasmonic rings with four 40 nm AuNPs. Indeed, the observed spectral peak is shifted from 530 nm for freely dispersed and DNA-coated 40 nm gold nanoparticles to 540 nm for the DNA-assembled particle rings (Figure 5a). The experimental result is in agreement with simulations, which assume an interparticle distance of 10 nm and predict a shift from 530 to 542 nm (Figure 5b).

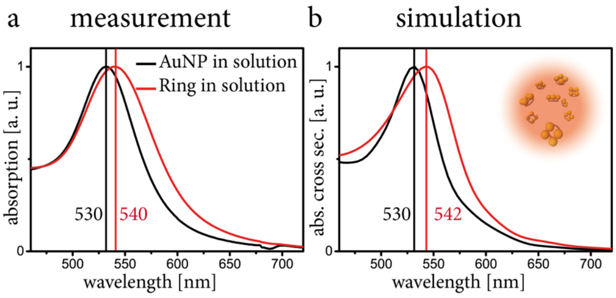

**Figure 5.** Optical characterization of the bulk plasmonic ring structures in solution. The absorption spectrum of plasmonic ring structures consisting of four 40 nm AuNPs was measured in bulk solution. (a) Measured absorption spectra of 40 nm AuNPs covered with ssDNA (black curve) and the ring structure with four attached 40 nm AuNPs in solution (red curve). (b) Corresponding finite difference time domain (FDTD) simulations of 40 nm AuNP in solution (black curve) and a symmetric ring structure (red curve) with a gap of 10 nm between the AuNP.

Overall, we successfully implemented DNA origami structures as templates for the synthesis of a wide variety of ring geometries containing nanoparticles of selectable size and type. We were able to construct various light-manipulating ring structures with interparticle gaps of only a few nanometers and we demonstrated their ability to support strong plasmonic resonances in the visible frequency domain both attached to a substrate and dispersed in solution. These resonances include dipolar, multipolar, and magnetic modes and are very sensitive to the ring symmetry. Our DNA-based self-assembly approach offers the opportunity to build metamolecules in large numbers with nanometer resolution and dispersed in solutions. This opens the route to a new class of material such as metasprays or metamolecules incorporated in a solid host, which could then be used in nanophotonic and sensing applications.

## ■ ASSOCIATED CONTENT

### Supporting Information

Materials and methods, DNA origami gold nanoparticle attachment, and additional data. This material is available free of charge via the Internet at http://pubs.acs.org.

## ■ AUTHOR INFORMATION

### Corresponding Author

*E-mail: tim.liedl@lmu.de.

### Author Contributions

E.M.R., A.O.G., and T.L. designed the research. E.M.R. and R.S. designed the nanostructures. E.M.R. and M.F. performed experiments. E.M.R., L.K., and A.O.G. performed simulations and E.M.R., A.O.G., and T.L. wrote the manuscript.

### Notes

The authors declare no competing financial interest.

## ■ ACKNOWLEDGMENTS

This work was funded by the Volkswagen Foundation, the DFG through the Nanosystems Initiative Munich (NIM), the ERC through the Starting Grant ORCA and the U.S. Army Research Office under Grant W911NF-12-1-0407.

## ■ REFERENCES

(1) Shalaev, V. M. *Nat. Photonics* **2007**, *1*, 41−48.

(2) Smith, D. R.; Pendry, J. B.; Wiltshire, M. C. K. *Science* **2004**, *305*, 788−792.

(3) Smith, D. R.; Padilla, W. J.; Vier, D. C.; Nemat-Nasser, S. C.; Schultz, S. *Phys. Rev. Lett.* **2000**, *84*, 4184−4187.

(4) Smith, D. R.; Mock, J. J.; Starr, A. F.; Schurig, D. *Phys. Rev. E: Stat., Nonlinear, Soft Matter Phys.* **2005**, *71*, 036609.

(5) Greegor, R. B.; Parazzoli, C. G.; Nielsen, J. A.; Thompson, M. A.; Tanielian, M. H.; Smith, D. R. *Appl. Phys. Lett.* **2005**, *87*, 091114.

(6) Chen, H. T.; Padilla, W. J.; Zide, J. M.; Gossard, A. C.; Taylor, A. J.; Averitt, R. D. *Nature* **2006**, *444*, 597−600.

(7) Zhou, J.; Koschny, T.; Kafesaki, M.; Economou, E. N.; Pendry, J. B.; Soukoulis, C. M. *Phys. Rev. Lett.* **2005**, *95*, 223902.

(8) Alù, A.; Engheta, N. *Phys. Rev. B* **2008**, *78*, 085112.

(9) Alù, A.; Salandrino, A.; Engheta, N. *Opt. Express* **2006**, *14*, 1557−1567.

(10) Campione, S.; Guclu, C.; Ragan, R.; Capolino, F. *ACS Photonics* **2014**, *1*, 254−260.

(11) Shafiei, F.; Monticone, F.; Le, K. Q.; Liu, X.-X.; Hartsfield, T.; Alù, A.; Li, X. *Nat. Nanotechnol.* **2013**, *8*, 95−99.

(12) Nazir, A.; Panaro, S.; Proietti Zaccaria, R.; Liberale, C.; De Angelis, F.; Toma, A. *Nano Lett.* **2014**, *14*, 3166−3171.

(13) Lassiter, J. B.; Sobhani, H.; Fan, J. A.; Kundu, J.; Capasso, F.; Nordlander, P.; Halas, N. J. *Nano Lett.* **2010**, *10*, 3184−3189.

(14) Sheikholeslami, S. N.; Alaeian, H.; Koh, A. L.; Dionne, J. A. *Nano Lett.* **2013**, *13*, 4137−4141.

(15) Sheikholeslami, S. N.; Garcia-Etxarri, A.; Dionne, J. A. *Nano Lett.* **2011**, *11*, 3927−34.

(16) Mühlig, S.; Cunningham, A.; Scheeler, S.; Pacholski, C.; Bürgi, T.; Rockstuhl, C.; Lederer, F. *ACS Nano* **2011**, *5*, 6586−6592.

(17) Fan, J. A.; Bao, K.; Wu, C.; Bao, J.; Bardhan, R.; Halas, N. J.; Manoharan, V. N.; Shvets, G.; Nordlander, P.; Capasso, F. *Nano Lett.* **2010**, *10*, 4680−4685.

(18) Fan, J. A.; Wu, C.; Bao, K.; Bao, J.; Bardhan, R.; Halas, N. J.; Manoharan, V. N.; Nordlander, P.; Shvets, G.; Capasso, F. *Science* **2010**, *328*, 1135−1138.

(19) Rothemund, P. W. K. *Nature* **2006**, *440*, 297−302.

(20) Douglas, S. M.; Dietz, H.; Liedl, T.; Hogberg, B.; Graf, F.; Shih, W. M. *Nature* **2009**, *459*, 414−418.

(21) Kuzyk, A.; Schreiber, R.; Zhang, H.; Govorov, A. O.; Liedl, T.; Liu, N. *Nat. Mater.* **2014**, *13*, 862−866.

(22) Zhang, F.; Nangreave, J.; Liu, Y.; Yan, H. *J. Am. Chem. Soc.* **2014**, *136*, 11198−11211.

(23) Seeman, N. C. *Annu. Rev. Biochem.* **2010**, *79*, 65−87.

(24) Ding, B.; Deng, Z.; Yan, H.; Cabrini, S.; Zuckermann, R. N.; Bokor, J. *J. Am. Chem. Soc.* **2010**, *132*, 3248−3249.

(25) Kuzyk, A.; Schreiber, R.; Fan, Z.; Pardatscher, G.; Roller, E.-M.; Högele, A.; Simmel, F. C.; Govorov, A. O.; Liedl, T. *Nature* **2012**, *483*, 311−314.

(26) Schreiber, R.; Do, J.; Roller, E.-M.; Zhang, T.; Schuller, V. J.; Nickels, P. C.; Feldmann, J.; Liedl, T. *Nat. Nanotechnol.* **2014**, *9*, 74−78.

(27) Tan, S. J.; Campolongo, M. J.; Luo, D.; Cheng, W. *Nat. Nanotechnol.* **2011**, *6*, 268−276.

(28) Tan, L. H.; Xing, H.; Lu, Y. *Acc. Chem. Res.* **2014**, *47*, 1881−1890.

(29) Zheng, J.; Constantinou, P. E.; Micheel, C.; Alivisatos, A. P.; Kiehl, R. A.; Seeman, N. C. *Nano Lett.* **2006**, *6*, 1502−1504.

(30) Douglas, S. M.; Marblestone, A. H.; Teerapittayanon, S.; Vazquez, A.; Church, G. M.; Shih, W. M. *Nucleic Acids Res.* **2009**, *37*, 5001−5006.

(31) Castro, C. E.; Kilchherr, F.; Kim, D.-N.; Shiao, E. L.; Wauer, T.; Wortmann, P.; Bathe, M.; Dietz, H. *Nat. Methods* **2011**, *8*, 221−229.

(32) Kim, D.-N.; Kilchherr, F.; Dietz, H.; Bathe, M. *Nucleic Acids Res.* **2012**, *40*, 2862−2868.

(33) Dietz, H.; Douglas, S. M.; Shih, W. M. *Science* **2009**, *325*, 725−730.

(34) Johnson, P. B.; Christy, R. W. *Phys. Rev. B* **1972**, *6*, 4370−4379.

(35) Su, K. H.; Wei, Q. H.; Zhang, X.; Mock, J. J.; Smith, D. R.; Schultz, S. *Nano Lett.* **2003**, *3*, 1087−1090.

(36) Jain, P. K.; El-Sayed, M. A. *Chem. Phys. Lett.* **2010**, *487*, 153−164.

(37) Yu, X.; Lei, D. Y.; Amin, F.; Hartmann, R.; Acuna, G. P.; Guerrero-Martínez, A.; Maier, S. A.; Tinnefeld, P.; Carregal-Romero, S.; Parak, W. J. *Nano Today* **2013**, *8*, 480−493.

(38) Thacker, V. V.; Herrmann, L. O.; Sigle, D. O.; Zhang, T.; Liedl, T.; Baumberg, J. J.; Keyser, U. F. *Nat. Commun.* **2014**, *5*, 3448.

(39) Kühler, P.; Roller, E.-M.; Schreiber, R.; Liedl, T.; Lohmüller, T.; Feldmann, J. *Nano Lett.* **2014**, *14*, 2914−2919.

## A.2. Associated Publication P2

### Plasmon-Exciton Coupling Using DNA Templates

by

Eva-Maria Roller, Christos Argyropoulos, Alexander Högele, Tim Liedl, and
Mauricio Pilo-Pais

published in Nano Letters, 16, 5962 - 5966 (2016).

NANO LETTERS

Letter

pubs.acs.org/NanoLett

# Plasmon–Exciton Coupling Using DNA Templates

Eva-Maria Roller,[†] Christos Argyropoulos,[‡] Alexander Högele,[†] Tim Liedl,[†] and Mauricio Pilo-Pais*,[†]

[†]Faculty of Physics and Center for NanoScience (CeNS), Ludwig-Maximilians-Universität (LMU) München, Geschwister-Scholl-Platz 1, 80539 Munich, Germany

[‡]Department of Electrical and Computer Engineering, University of Nebraska-Lincoln, Lincoln, Nebraska 68588, United States

Ⓢ *Supporting Information*

**ABSTRACT:** Coherent energy exchange between plasmons and excitons is a phenomenon that arises in the strong coupling regime resulting in distinct hybrid states. The DNA-origami technique provides an ideal framework to custom-tune plasmon–exciton nanostructures. By employing this well controlled self-assembly process, we realized hybrid states by precisely positioning metallic nanoparticles in a defined spatial arrangement with fixed nanometer-sized interparticle spacing. Varying the nanoparticle diameter between 30 nm and 60 nm while keeping their separation distance constant allowed us to precisely adjust the plasmon resonance of the structure to accurately match the energy frequency of a J-aggregate exciton. With this system we obtained strong plasmon–exciton coupling and studied far-field scattering at the single-structure level. The individual structures displayed normal mode splitting up to 170 meV. The plasmon tunability and the strong field confinement attained with nanodimers on DNA-origami renders an ideal tool to bottom-up assembly plasmon–exciton systems operating at room temperature.

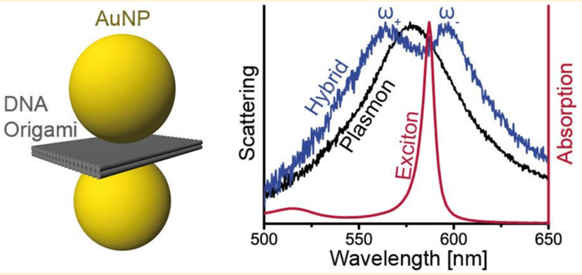

**KEYWORDS:** *DNA origami, plexcitons, excitons, plasmons, J-aggregates, Rabi splitting*

Nanoparticles (NPs) subjected to light excitation exhibit collective oscillations of electrons (*plasmons*), which in turn can greatly affect the behavior of quantum emitters positioned in nearby locations. The resulting plasmon–exciton coupling is of interest as it may facilitate studies of fundamental quantum phenomena such as coherent energy exchange, entanglement, and cavity quantum electrodynamics.[1] Potential applications of strongly coupled-exciton systems include artificial light harvesting,[2] threshold-less lasing, or their use in quantum information processing.[3] The degree of interaction between plasmons and quantum emitters can be classified based on their coupling strength ($g$), displaying different signatures in the far-field scattering spectra, such as enhanced absorption dip, Fano resonance, or Rabi splitting.[3] Although these effects are usually associated with quantum-mechanical phenomena, they can be qualitatively described by classical electrodynamics.[3−5] Plasmon frequencies can be tuned by varying the metallic NP size, geometry, interparticle separation, and their two- or three-dimensional arrangement. Moreover, near-field enhancement can be obtained using small gaps among metallic NPs or using structures with sharp morphology.[6] If an exciton is placed in regions with enough field confinement, it is possible to achieve the necessary coupling strength to reach the regime of strong coupling, which results in a normal mode splitting, in close analogy to a coupled harmonic oscillator.[3] Our focus is on the strong coupling regime where the energy exchange between the plasmon and the exciton results in distinct hybrid modes, the so-called *plexciton* states.

Experimental realizations of plasmon-exciton coupling include work on metallic films,[7] lithographic constructs,[8,9] and individual colloids.[10] Even though complex structures can be fabricated using lithographic techniques and have already been used to promote plasmon-exciton coupling,[8,9] this methodology is limited in the minimum feature size. In addition, metallic structures produced by lithography exhibit greater plasmon damping due to their surface roughness and inherent grain boundaries. All of these aspects lower the quality factor ($Q$) and the near-field enhancement, decreasing the interaction strength one could potentially achieve with top-down fabricated structures. To circumvent these limitations, one can resort to colloidal NPs, which are routinely synthesized in well-defined sizes and feature less ohmic losses due to their higher crystallinity as compared to top-down structures. Consequently, individual nanocrystals such as gold shells,[11] silver rods,[10] and silver triangles[12−14] have already been reported to display plexcitonic signatures in the presence of J-aggregates. These unmodified colloids, however, lack the ability to assemble into complex plasmonic designs that are required for specific applications.[2] More importantly, individual colloids do not take advantage of the additional field confinement that results from bringing together two or more closely spaced NPs. In addition, silver colloids are known to

**Received:** July 20, 2016
**Revised:** August 16, 2016
**Published:** August 17, 2016

DOI: 10.1021/acs.nanolett.6b03015
*Nano Lett.* 2016, 16, 5962−5966

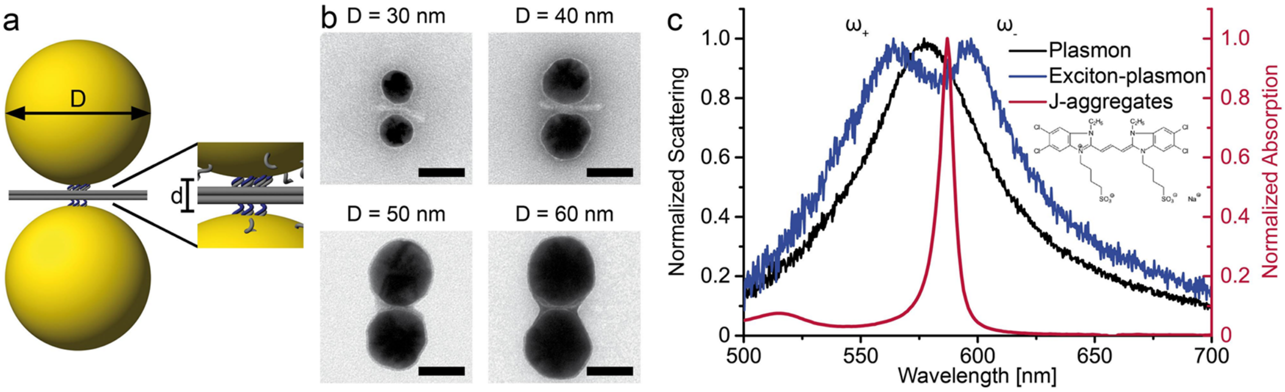

**Figure 1.** (a) Schematic of a two-layer DNA-origami sheet templating a gold nanoparticle dimer with a designed separation of ~5 nm. (b) TEM images of DNA sheets accommodating NPs of different diameters ranging from 30 to 60 nm. Scale bars are 40 nm. (c) Typical spectra of 40 nm dimer with (dark blue) and without (black) J-aggregates. J-aggregate absorption is depicted in red. Inset shows the chemical structure of the molecular exciton used in this work.

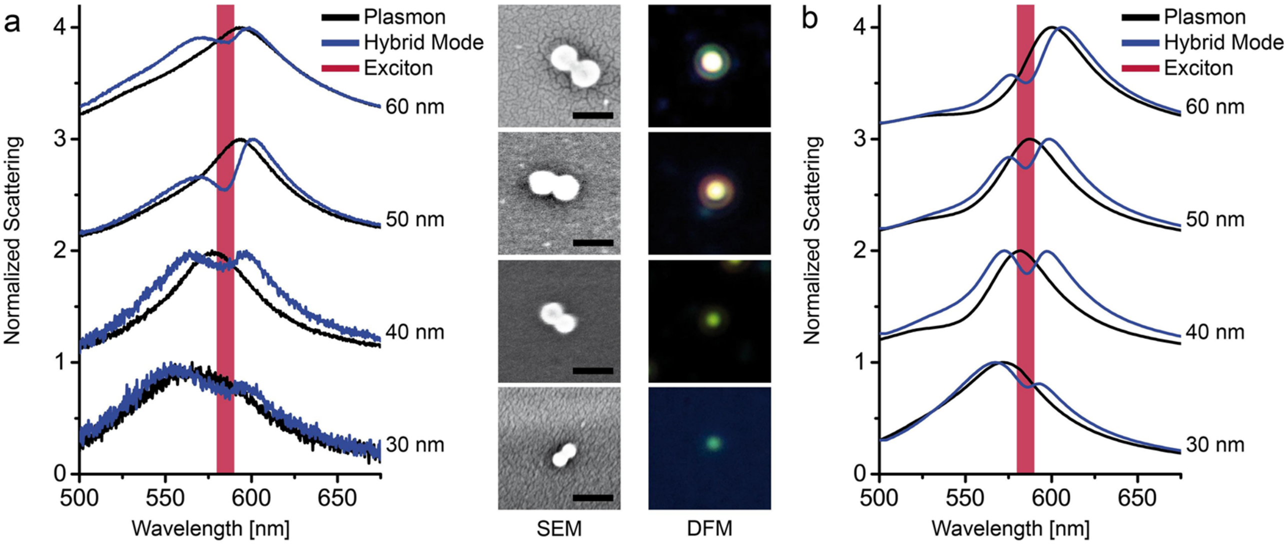

**Figure 2.** (a) Normalized scattering spectra before (dark-blue) and after (black) photobleaching the J-aggregate for 30, 40, 50, and 60 nm NPs dimers. The spectral region shaded in red covers the energy resonance of the J-aggregate. The right panels show the structures corresponding to each spectrum under SEM and darkfield microscopy. Scale bars: 100 nm. (b) Numerical simulations show excellent agreement with the experimental data.

oxidize, making the use of colloidal gold the preferred choice for plasmon−exciton systems. Very recently, plasmon−exciton coupling using individual molecules in combination with a nanoparticle-on-mirror (NPoM) configuration,[15] as well as coupling between individual colloidal QDs with lithographically produced silver bow-tie antennas[16] have been reported, highlighting plasmonic cavities as promoters of strong light-matter interactions.

DNA-origami is a technique routinely used to fabricate structures with nanoscale dimensions (~100 nm) and programmable designs.[17,18] In a one-pot reaction, a long viral single-stranded DNA (ssDNA) scaffold (~7k bases) is folded by the help of ~200 complementary short synthetic ssDNA oligonucleotides. These structures can be used as templates with sequence-specific DNA binding sites, where nano-components functionalized with complementary DNA sequences can be attached to the binding sites (Figure 1a).[19,20] DNA-templated metallic structures have already been tailored to affect the optical properties of nearby components such as custom-tuned “hot spots” for surface-enhanced Raman scattering (SERS),[21−24] enhancement and quenching of fluorophores,[25,26] and colloidal quantum dots.[27,28] In addition, the DNA-origami technique has been successfully used to tailor light, displaying strong circular dichroism[29] as well as magnetic resonances.[30]

Here, we demonstrate strong coupling between plasmons and excitons (J-aggregates) at room temperature and optical frequencies by exploiting the position accuracy that is achievable with the DNA-origami technique. This technique provides unprecedented control in the design of plexcitonic systems, bringing this technology one step closer to practical applications as compared to all previously proposed plexcitonic designs. By attaching pairs of colloidal gold nanocrystals to a DNA origami template, we fabricated a nanoantenna configuration with a fixed intergap distance of ~5 nm. The resonance frequency of the longitudinal plasmon mode of our constructs scales with the NP size and thus can be tuned across and even matched with the resonance of the desired exciton. This allowed us to observe normal mode splitting in the far-field scattering of individual constructs.

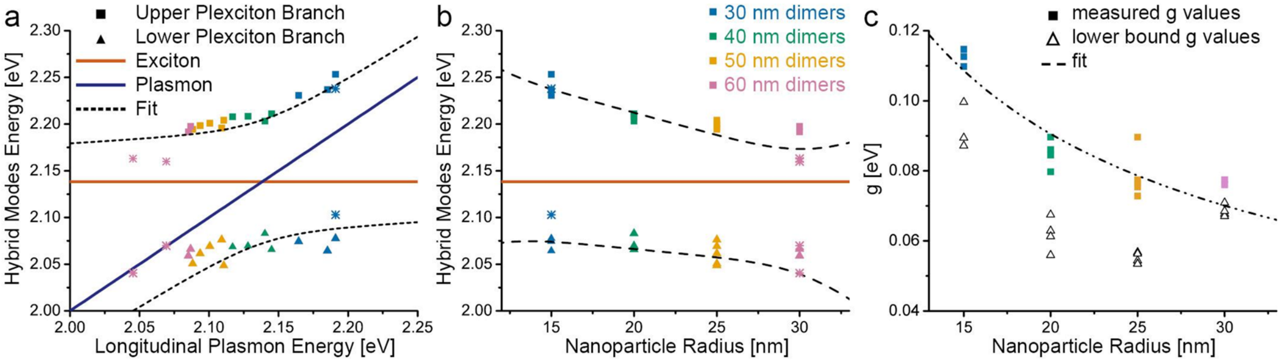

**Figure 3.** (a) Hybrid plasmon−exciton state energies are plotted as a function of their corresponding plasmon resonance and (b) as a function of the NP radius, showing the anticrossing behavior. Dashed lines are fits of the eigenvalues of a two-coupled harmonic oscillator with complex frequencies. Stars represent structures that do not fulfill the strong coupling condition and were not used in the fitting procedure. Both fittings (a and b) yield a Rabi splitting of $\Omega \sim 150$ meV. (c) Coupling constant ($g$) values obtained for individual structures reveal a scaling of $g \propto 1/R^n$, $n = 0.63 \pm 0.08$ in very good agreement with the expected $g \propto 1/\sqrt{V_{\text{eff}}} = 1/R^{0.5}$. Dimers composed of smaller NP sizes display a larger coupling constant $g$. Triangles depict the lower bound for the strong coupling given by $g^2 > (\Gamma_p^2 + \Gamma_{qe}^2)/16$.

Our DNA-templated nanodimer assemblies were fabricated using pairs of 30, 40, 50, or 60 nm diameter gold NPs functionalized with DNA linkers complementary to specific binding sites on a two-layered DNA-origami sheet (Figure 1a). Transmission electron microscopy (TEM) images of gel-purified structures reveal high yields (Supporting Figures S1−S3) of correctly assembled particle dimers with designed interparticle gap of 5 nm. For this particular gap size we find that dimers built from 40 nm NPs are in closest spectral resonance with the exciton frequency of the cyanine-based dye used in this work (CAS No. 18462-64-1, FEW Chemicals GmbH). This methanol soluble dye readily stacks to form J-aggregates when dissolved in water. When absorbed to glass substrates, we find thin layers of J-aggregates to exhibit a scattering peak at 580 nm (2.14 eV) and a narrow fwhm line width of 30 meV (Supporting Figure S5b). For our measurements of combined plasmon-exciton systems, the assembled structures were deposited on a glass substrate and then immersed in a J-aggregate water bath solution (50 $\mu$M). After overnight incubation, the samples were blown with nitrogen, flushing out most of the J-aggregate excess except at the location of the NP dimers. Far-field scattering measurements on individual structures were then performed using a home-built darkfield microscope (Supporting Figure S4 and Note 2). After recording the spectral response of the hybrid structures, the samples were exposed for 1 h to continuous white light illumination under a 100× objective to completely photobleach the J-aggregates.[12] This permitted us to additionally record the plasmon resonance of the structures without the contribution of the excitons. Figure 1c shows the far-field scattering spectra of a single AuNP dimer assembled using DNA-origami with J-aggregates before (dark-blue line) and after (black line) photobleaching the excitons.

Spectral red-shifts are more pronounced on dimers with bigger NP sizes due to stronger interparticle coupling. Thus, detuning of the plasmon mode with respect to the exciton resonance was achieved by building dimers with NPs sizes ranging from 30 to 60 nm (Figure 2a), while using the same origami design and thus a constant interparticle gap. This allowed us to tune the plasmon resonance wavelength between 2.05 and 2.20 eV across the exciton resonance at 2.14 eV. As a result of the coupling, the scattering spectrum splits into hybrid states of lower ($\omega_-$) and higher ($\omega_+$) energies. Polarization-resolved measurements show that only the longitudinal mode couples, as only this mode matches the exciton resonance (Supporting Figure S5b). For each particle size, we measured the scattering spectra of several individual structures and present exemplary spectra for all sizes in Figure 2a. Numerical simulations show excellent agreement with the experimental data (Figure 2b, Supporting Note 4). Using the data collected for Figure 2a, we followed the position evolution of the upper $\omega_+$ and the lower $\omega_-$ hybrid states as a function of the longitudinal plasmon mode and NP radius ($R$). As expected, the energy positions display a pronounced avoided crossing, characteristic of strong coupling (Figure 3).[3]

The Rabi frequency ($\Omega$) corresponds to the spectral separation of the normal modes ($\Delta\omega$) when the plasmon and the exciton are at perfect resonance. To extract its value, we modeled the system as a two coupled harmonic oscillators with complex frequencies $\tilde{\omega} = \omega + i\Gamma/2$. The resulting complex eigenvalues are[31]

$$\tilde{\omega}_{\pm} = \frac{\tilde{\omega}_p + \tilde{\omega}_{qe}}{2} \pm \sqrt{g^2 + \frac{(\tilde{\omega}_p - \tilde{\omega}_{qe})^2}{4}} \qquad (1)$$

where $\tilde{\omega}_p$ and $\tilde{\omega}_{qe}$ are the complex frequencies of the plasmon and quantum emitter (J-aggregate), respectively, and $g$ is the coupling constant. The position of the hybrid modes ($\omega_{\pm}$) as well as the fwhm line-widths of the exciton ($\Gamma_{qe}$) and the plasmon ($\Gamma_p$) were extracted by Lorentzian fitting of the corresponding scattering spectra, as described in Supporting Note 3. The spectral separation between the upper and lower modes resonances, $\Delta\omega$, is then given by (Supporting Note 3):

$$(\Delta\omega)^2 = \sqrt{(\omega_p - \omega_{qe})^2(\Gamma_p - \Gamma_{qe})^2 + \left(4g^2 + (\omega_p - \omega_{qe})^2 - \frac{(\Gamma_p - \Gamma_{qe})^2}{4}\right)^2} \qquad (2)$$

eq 2 reduces to the commonly used Rabi splitting $\Omega = 2\sqrt{g^2 - (\Gamma_p - \Gamma_{qe})^2/16}$ when $\omega_p = \omega_{qe}$, which sets a threshold of $g^2 > (\Gamma_p - \Gamma_{qe})^2/16$ to ensure the splitting is real valued. An indication that the strong coupling regime has been reached[3] is given by $g^2 > (\Gamma_p^2 + \Gamma_{qe}^2)/16$, which shows that the

DOI: 10.1021/acs.nanolett.6b03015
Nano Lett. 2016, 16, 5962−5966

splitting between the new modes is greater than their line width. This sets a lower bound value of $g > 60$ meV for the structures in resonance with the exciton ($\Gamma_{p,r=20nm} = 240$ meV). To extract the coupling constant $g$ of our system, we first performed a fitting on the upper $\omega_+$ and lower $\omega_-$ modes as a function of the plasmon frequency $\omega_p$ (Figure 3a). This procedure assumes a constant $g$ for all particle sizes. The extracted exciton−plasmon coupling $g_{fit}$ is ~90 meV, which results in a Rabi splitting of $\Omega \sim 150$ meV.

To account for the varying $g(R)$ as the NP radius is changed, we then fitted the exponential function $g = aR^n$ (Figure 3c) using radial-dependent parameters ($\Gamma_{p(R)}$, $\omega_{p(R)}$) extracted from the recorded data (Supporting Figure S6). Here, $a$ and $n$ are fitting parameters. This analysis revealed a coupling constant which scales with the NP radius as $g \sim 1/R^n$, $n = 0.63 \pm 0.08$, showing that higher coupling constants are obtained for smaller NP sizes. At the expected anticrossing position ($R = 20$ nm), both fitting procedures provide an equal value of $g \sim 90$ meV. Note that in our analyses only those spectra with a real valued coupling constant were taken into account when considering eq 2. Structures with values far from resonance (depicted with asterisks in Figure 3) only exhibited a Fano-like signature or absorbance dip enhancement. Figure 3c displays the $g$ dependence on the radius and clearly shows that dimers with reduced NP size exhibit larger coupling constants. The $g$ values were extracted by replacing the individual $R$, $\omega_p$, $\Delta\omega$, and $\Gamma_p$ parameters in eq 2 for each measured NP dimer. Following ref 32, we approximated the effective mode volume of two closely spaced NPs to be a cylinder with a circular base of diameter $\sqrt{Rd}$ (width of the induced surface charge) and height $d$ (gap distance), $V_{eff} \propto Rd^2$.[32] The measured $g \sim 1/R^n$ with $n = 0.63 \pm 0.08$ is in very good agreement with the expected scaling of $g \propto 1/\sqrt{V_{eff}} \sim 1/R^{0.5}$. In summary, we observe that smaller particles exhibit the strongest coupling. However, the steep decrease in scattering of smaller NP systems makes the study of individual structures below 30 nm in size challenging. Moreover, we also expect that as the NP size is further reduced, surface scattering damping would start to dominate. Thus, there is an ideal NP size where the coupling strength is maximal. This regime was not accessible with our current experimental setup.

We have successfully demonstrated that DNA templates can be used to rationally engineer plexcitonic systems that display hybridized modes between plasmons and molecular excitons (J-aggregates) at room temperature. Our structures are programmed to self-assemble in solution and take full advantage of the field confinement produced by closely spaced metallic colloidal nanocrystals. The coupled plasmon mode can be custom-tuned to be in resonance with the exciton of interest by setting the desired interparticle separation and nanoparticle size. Moreover, one could further exploit the full addressability of the DNA-origami technique to incorporate and precisely position additional nanocomponents, such as individual dyes or quantum dots. As such, the DNA-origami technique provides an unparalleled control in the fabrication of plexcitonic systems and represents a promising platform to achieve fully integrated nanobreadboards and quantum nanocircuits. In future work, we will further investigate the coherent energy exchange between the plasmon and the exciton of our hybrid systems via second-order photon correlation spectroscopy. The design flexibility and the parallel assembly formation of DNA templates are ideally suited to study plasmon−exciton coupling and to fabricate complex structures for optical applications.

## ■ ASSOCIATED CONTENT

### Ⓢ Supporting Information

The Supporting Information is available free of charge on the ACS Publications website at DOI: 10.1021/acs.nanolett.6b03015.

Materials, detailed experimental methods, data analysis, and numerical calculation procedures (PDF)

## ■ AUTHOR INFORMATION

### Corresponding Author

*E-mail: m.pilopais@lmu.de.

### Author Contributions

E.M.R., A.H., T.L., and M.P. conceived the experiment. E.M.R. and M.P. conducted the experiments and analyzed the results. C.A. performed the numerical calculations. All authors interpreted the data and reviewed the manuscript.

### Notes

The authors declare no competing financial interest.

## ■ ACKNOWLEDGMENTS

This work was funded by the Volkswagen Foundation, the DFG through the Nanosystems Initiative Munich (NIM) and the ERC through the Starting Grant ORCA. A.H. acknowledges funding by the ERC starting grant No. 336749. C.A. would like to acknowledge support by the Office of Research and Economic Development at University of Nebraska Lincoln and the NSF Nebraska MRSEC.

## ■ REFERENCES

(1) Tame, M. S.; McEnery, K. R.; Özdemir, K.; Lee, J.; Maier, S. A.; Kim, M. S. *Nat. Phys.* **2013**, *9*, 329−340.
(2) Gonzalez-Ballestero, C.; Feist, J.; Moreno, E.; Garcia-Vidal, F. J. *Phys. Rev. B: Condens. Matter Mater. Phys.* **2015**, *92*, 121402.
(3) Törmä, P.; Barnes, W. L. *Rep. Prog. Phys.* **2015**, *78*, 013901.
(4) Savasta, S.; Saija, R.; Ridolfo, A.; Di Stefano, O.; Denti, P.; Borghese, F. *ACS Nano* **2010**, *4*, 6369−6376.
(5) Faucheaux, J. A.; Fu, J.; Jain, P. K. *J. Phys. Chem. C* **2014**, *118*, 2710−2717.
(6) Novotny, L.; van Hulst, N. *Nat. Photonics* **2011**, *5*, 83−90.
(7) Bellessa, J.; Bonnand, C.; Plenet, J. C.; Mugnier, J. *Phys. Rev. Lett.* **2004**, *93*, 036404.
(8) Bellessa, J.; Symonds, C.; Vynck, K.; Lemaitre, A.; Brioude, A.; Beaur, L.; Plenet, J. C.; Viste, P.; Felbacq, D.; Cambril, E.; Valvin, P. *Phys. Rev. B: Condens. Matter Mater. Phys.* **2009**, *80*, 033303.
(9) Schlather, A. E.; Large, N.; Urban, A. S.; Nordlander, P.; Halas, N. J. *Nano Lett.* **2013**, *13*, 3281−3286.
(10) Zengin, G.; Johansson, G.; Johansson, P.; Antosiewicz, T. J.; Käll, M.; Shegai, T. *Sci. Rep.* **2013**, *3*, 3074.
(11) Fofang, N. T.; Grady, N. K.; Fan, Z.; Govorov, A. O.; Halas, N. J. *Nano Lett.* **2011**, *11*, 1556−1560.
(12) Zengin, G.; Wersäll, M.; Nilsson, S.; Antosiewicz, T. J.; Käll, M.; Shegai, T. *Phys. Rev. Lett.* **2015**, *114*, 157401.
(13) Balci, S. *Opt. Lett.* **2013**, *38*, 4498.
(14) DeLacy, B. G.; Miller, O. D.; Hsu, C. W.; Zander, Z.; Lacey, S.; Yagloski, R.; Fountain, A. W.; Valdes, E.; Anquillare, E.; Soljačić, M.; Johnson, S. G.; Joannopoulos, J. D. *Nano Lett.* **2015**, *15*, 2588−2593.
(15) Chikkaraddy, R.; de Nijs, B.; Benz, F.; Barrow, S. J.; Scherman, O. A.; Rosta, E.; Demetriadou, A.; Fox, P.; Hess, O.; Baumberg, J. J. *Nature* **2016**, *535*, 127−130.
(16) Santhosh, K.; Bitton, O.; Chuntonov, L.; Haran, G. *Nat. Commun.* **2016**, *7*, ncomms11823.

(17) Rothemund, P. W. K. *Nature* **2006**, *440*, 297−302.

(18) Douglas, S. M.; Marblestone, A. H.; Teerapittayanon, S.; Vazquez, A.; Church, G. M.; Shih, W. M. *Nucleic Acids Res.* **2009**, *37*, 5001−6.

(19) Schreiber, R.; Do, J.; Roller, E.-M.; Zhang, T.; Schüller, V. J.; Nickels, P. C.; Feldmann, J.; Liedl, T. *Nat. Nanotechnol.* **2013**, *9*, 74−8.

(20) Zhang, T.; Neumann, A.; Lindlau, J.; Wu, Y.; Pramanik, G.; Naydenov, B.; Jelezko, F.; Schüder, F.; Huber, S.; Huber, M.; Stehr, F.; Högele, A.; Weil, T.; Liedl, T. *J. Am. Chem. Soc.* **2015**, *137*, 9776−9779.

(21) Prinz, J.; Schreiber, B.; Olejko, L.; Oertel, J.; Rackwitz, J.; Keller, A.; Bald, I. *J. Phys. Chem. Lett.* **2013**, *4*, 4140−4145.

(22) Kühler, P.; Roller, E.-M.; Schreiber, R.; Liedl, T.; Lohmüller, T.; Feldmann, J. *Nano Lett.* **2014**, *14*, 2914−9.

(23) Thacker, V. V.; Herrmann, L. O.; Sigle, D. O.; Zhang, T.; Liedl, T.; Baumberg, J. J.; Keyser, U. F. *Nat. Commun.* **2014**, *5*, 3448.

(24) Pilo-Pais, M.; Watson, A.; Demers, S.; LaBean, T. H.; Finkelstein, G. *Nano Lett.* **2014**, *14*, 2099−104.

(25) Acuna, G. P.; Bucher, M.; Stein, I. H.; Steinhauer, C.; Kuzyk, A.; Holzmeister, P.; Schreiber, R.; Moroz, A.; Stefani, F. D.; Liedl, T.; Simmel, F. C.; Tinnefeld, P. *ACS Nano* **2012**, *6*, 3189−3195.

(26) Acuna, G. P.; Möller, F. M.; Holzmeister, P.; Beater, S.; Lalkens, B.; Tinnefeld, P. *Science (Washington, DC, U. S.)* **2012**, *338*, 506−10.

(27) Ko, S. H.; Du, K.; Liddle, J. A. *Angew. Chem., Int. Ed.* **2013**, *52*, 1193−1197.

(28) Samanta, A.; Zhou, Y.; Zou, S.; Yan, H.; Liu, Y. *Nano Lett.* **2014**, *14*, 5052−7.

(29) Kuzyk, A.; Schreiber, R.; Fan, Z.; Pardatscher, G.; Roller, E.-M.; Högele, A.; Simmel, F. C.; Govorov, A. O.; Liedl, T. *Nature* **2012**, *483*, 311−4.

(30) Roller, E.-M.; Khorashad, L. K.; Fedoruk, M.; Schreiber, R.; Govorov, A. O.; Liedl, T. *Nano Lett.* **2015**, *15*, 1368−1373.

(31) Gómez, D. E.; Giessen, H.; Davis, T. J. *J. Phys. Chem. C* **2014**, *118*, 23963−23969.

(32) Savage, K. J.; Hawkeye, M. M.; Esteban, R.; Borisov, A. G.; Aizpurua, J.; Baumberg, J. J. *Nature* **2012**, *491*, 574−7.

## A.3. Associated Manuscript P3

### Plasmonic Focus Point Analysis of Chiral Molecules

by

Luisa M. Kneer*, Eva-Maria Roller*, Robert Schreiber, Alexander O. Govorov,
and Tim Liedl
*equal contribution

Manuscript in preparation (2016).

# Plasmonic Focus Point Analysis of Chiral Molecules

*Luisa M. Kneer[1†], Eva-Maria Roller[1†], Robert Schreiber[2], Alexander O. Govorov[3] and Tim Liedl[1*]*

[1]Fakultät für Physik and Center for Nanoscience, Ludwig-Maximilians-Universität München, Geschwister-Scholl-Platz 1, 80539 Munich, Germany

[2]Clarendon Laboratory, Department of Physics, University of Oxford, Parks Road, Oxford OX1 3PU, UK

[3]Department of Physics and Astronomy, Ohio University, Athens, Ohio 45701, USA

†These authors contributed equally to this work.

**The chiral state of a molecule plays a crucial role in molecular recognition processes and biochemical reactions. Because of this and owing to the fact that most modern drugs are chiral, the sensitive and reliable detection of the chirality of molecules is of great interest during the development of drugs and the studies of their function. The majority of naturally occurring biomolecules exhibit spectral absorption and thus circular dichroism (CD) in the UV-range [citations].[1] Theoretical studies[2-3] [citations] and several experiments [citations][4-5] have demonstrated that this UV-CD can be transferred into the plasmonic frequency domain if metal surfaces or particles are in close proximity to chiral biomolecules. We here demonstrate that the CD transfer effect can be drastically enhanced by placing the chiral molecule of interest precisely inside a plasmonic hotspot that can be created between gold nanoparticles or nanorods assembled on a DNA origami scaffold. For this purpose the antenna nanorods were intentionally placed upright on the DNA origami sheets, centering the molecule of interest in the plasmonic hotspot. While the CD signal of pure B-form DNA is usually only detectable in the UV, we here detect characteristic DNA CD spectra in the plasmonic frequency domain originating from DNA molecules inside the hotspot.**

Circular dichroism (CD) arises if light is absorbed by a chiral arrangement of entities that interact with the incoming light. While standard optical absorption spectra are used to determine the identity or the mere concentration of a certain molecule, the analysis of the chirality of a molecular species gives a deeper insight into its conformational states, ratios of enantiomers and allows monitoring conformational changes during ongoing chemical reactions. As biomolecules absorb mostly in the UV, their CD characterization is performed in that frequency range, e.g. for DNA the CD response has mainly been studied in the range of 180-300 nm[6] at concentrations as low as 25 µg/ml.[7] However, theoretically and experimentally it was shown that chiral molecules brought into close contact with non-chiral (also: achiral) metal nanoparticles can induce an additional CD signal at the plasmonic resonance of the nanoparticles in the visible frequency domain.[2, 8] This type of chirality transfer is based on the non-zero optical rotatory dispersion (ORD) that biomolecules exhibit in the visible. Implementations of this effect have been realized with biomolecule-nanoparticle heterocomplexes consisting of gold nanoparticles decorated with peptides,[5] cysteine-modified nanoparticles[9], silver nanoparticles synthesized on DNA[10] and polyfluorenes doped with gold nanoparticles.[11] Such nanoscale heterostructues of chiral and achiral components work as surprisingly efficient CD sensors in the visible frequency range. Moreover, the variation of the sizes and shapes of the achiral metal particles allows exploiting a range of beneficial optical properties of plasmonic nanoparticles such as a variety of plasmon resonances and in particular the local field enhancement inside the assembled hotspots.[12-15] The versatility of plasmonic behavior can be applied to tune the CD sensor with respect to the desired detection wavelength as well as to amplify even weak chiral signals of low concentrated (bio)molecules. To not only impart the chirality from chiral molecules onto achiral nanoparticles but also take full advantage of the optical properties of metal nanoparticles, well-defined and precisely arranged nanoscale heterostructures are needed.

We here report on the sensing of chiral B-form DNA molecules at visible frequencies with the help of an optically active antenna consisting of two plasmonic metal nanoparticles arranged with nanometer-precision on a DNA origami structure.[16-17] This way we created plasmonic hotspots[14, 18] that bear chiral molecules in a defined position and orientation. The DNA origami structures here fulfill a dual purpose, first as the scaffold arranging the antenna particles and second as the chiral molecules under investigation. The chiral analyte molecule, *i.e.* the DNA origami structure, is thus placed exactly inside the plasmonic hotspot between the two gold nanoparticles/ nanorods.[19] This new approach of combining CD transfer with a strong electromagnetic field enhancement[20] allows to detect even very low concentrations of chiral molecules.

Structural DNA nanotechnology enables the assembly of trillions of identical nanoscale three-dimensional structures in a one-pot thermal annealing process. During that reaction, the desired object is obtained by folding a long single-stranded scaffold DNA molecule (here of 7560 nucleotides length) into shape with ~ 200 short synthetic oligonucleotides, so-called staple strands.[16-17] Due to the inherent sequence addressability of the DNA origami structures, it is possible to attach metallic nanoparticles through DNA linkers with nanometer precision and yields up to 99% to these structures.[21] Here, we designed several DNA origami sheets in square lattice configuration[22] with thicknesses of one, two and four dsDNA layers. Spherical gold nanoparticles (AuNPs) with 40 nm diameter or 50 nm long goldnanorods (AuNRs) with 20 nm diameter were attached on the two opposite faces of the DNA rectangle as depicted in Figure 1a-c (see supporting information for detailed experimental protocols). Due to this construction, the chiral target molecule (here the B-form DNA of the origami) is placed in the hotspot of the nanoantenna (Figure 1d). To achieve optimum field enhancement in the AuNR-created hotspots it is essential to orientate the tips towards each other as it is shown in Figure 1c. To attach AuNRs in such an upright conformation (standing AuNRs) to a DNA origami structure and not in the so far used horizontal (lying) orientation[23-24] a special attachment method was developed. A thiol-DNA functionalized AuNR is anchored to the origami structure by elongating DNA strands of the origami structure with the complementary sequence (handles).[25] Here, one AuNR was attached with 12 DNA handles of the same sequence (15xT). The exact handle placement on the DNA origami structure was altered from an elongated array into a more compact pattern as shown in Figure 1e,g. By that, the AuNRs were forced to attach upright on the origami instead of lying parallel to it, as they would do preferentially with the elongated pattern (compare Figure 1e&f). The final compact pattern for the 12 handles per attachment point covers an area of about 13 nm x 16 nm. It is known that during AuNR functionalization the thiolated oligos preferentially conjugate to the ends of the AuNR[26] and, further, that these thiolated oligos are negatively charged as well as the origami itself. A combination of two effects, the electrostatic charge repulsion and the larger number of available oligos at the ends, presumably forced the AuNRs to stand perpendicular to the surface of the origami. This method enabled us to build an AuNR dimer with a B-form DNA in the electromagnetic hotspot.

These nanoantennas were characterized by circular dichroism spectroscopy (CD spectroscopy). Therefore, the CD signal of a bulk solution of nanoantennas consisting either of AuNPs or AuNRs with a 2 layered sheet-like DNA origami structure (2LS) as chiral analyte molecule in the hotspot was recorded in the UV and at visible wavelengths. The measured CD spectra are shown in Figure 2a. They exhibit a very weak, typical bisignated shaped CD signal in the UV range arising from a B-form DNA 2LS structure at 1000pM concentration and larger CD signals in the visible range with similar shape. We associate this CD signature to the CD transfer signal from the chiral DNA molecules placed in the plasmonic hotspot as described in theory by Govorov et al.[2, 8] In short, if the optical rotatory dispersion from a chiral molecule has a non-zero signal in the visible frequency range, which overlaps with the absorption of the plasmonic particles, the CD signal can be transferred and detected at visible wavelengths. Moreover, the high electromagnetic field enhancement allows to detect this signal even at concentrations below 100 pM of the hybrid structure, at which the CD signal in the UV would be hard to detect (compare Figure 2a). The CD signal measured with the AuNP nanoantenna at 100pM is more than 20-fold enhanced compared to the bare 2LS origami. By placing AuNRs instead of AuNPs in the upright manner described above, one can reach a 80-fold enhancement (see Figure 2a). This increased hotspot intensity permits to sense at concentrations of chiral molecules below the UV detection limit.

In order to underline the antenna effect as well as the successful CD transfer, several control measurements with AuNPs were performed (Figure 2b). At first, the 2LS AuNP dimer was altered by shifting the AuNPs from the center of the origami faces to the edges. This mainly decreases the hotspot intensity as can be seen by comparing the green (normal) and the blue (shifted) graph in Figure 2b. When both gold nanoparticles are placed on one side of the 2LS origami, the CD signal no longer reveals the right-handed shape of B-form DNA, but a small left-handed signal (red curve in Figure 2b). Further, the plasmonic hotspot was removed, while leaving the concentration of the DNA origami structure with only one AuNP attached constant compared to the dimer structures (cyan curve and inset in Figure 2b). And finally, only plasmonic particles functionalized with ssDNA oligonucleotides were measured as well with comparable concentration (black curve and inset in Figure 2b). Both did not exhibit any transferred CD signal. Therefore one can conclude, that placing the chiral molecule of interest in a plasmonic hotspot conformation rather than just close to a single plasmonic particle is crucial for the detection sensitivity. This underlines that due to our experimental set-up with the nanoantenna heterostructure and the combination of two effects - the CD transfer and the plasmonic enhancement – it is possible to create a very sensitive detection device at visible wavelengths.

Moreover, the use of different shapes and materials for the plasmonic elements enables to shift the transferred CD signal to a desired wavelength range. The constructional flexibility of our nanoantenna allows using multiplet plasmonic particles for the enhancement and transfer of the CD signal. Here, we demonstrate this by functionalizing the DNA origami 2LS either with two 10 nm AuNPs having a silver shell of 30 nm, two 40 nm AuNPs or two AuNRs owing a longitudinal resonance frequence at 700 nm or 800 nm. Due to the different absorption resonance frequencies of the plasmonic particles also the occurrence of the CD signal is shifted. This again shows the application possibilities of our approach towards chiral molecule sensing at a desired, predefined wavelength.

To conclude, we demonstrated that our nanoantenna heterostructures facilitate the observation of induced chiral transfer of molecular CD signals from the UV to the visible frequency range at very low concentrations. We experimentally proofed the CD transfer of a chiral molecule from the UV to the visible for a broad range of different plasmonic particles up to an 80-fold enhancement. The transfer and pick-up enhancement was studied for different hotspot intensities. A future perspective could be envisioned where the dimer serves as sensing template for various molecules precisely placed in the plasmonic hotspot by the inherent addressability of the DNA origami.

## ASSOCIATED CONTENT

**Supporting Information.** Materials and Protocols

## AUTHOR INFORMATION

### Corresponding Author

*Correspondence and request for materials should be addressed to: tim.liedl@lmu.de

### Author Contributions

TL and RS conceived the research, LK and EMR performed the experiments. AOG contributed the simulations. EMR, LK and TL wrote the manuscript.

The authors declare no competing financial interests.

## ACKNOWLEDGMENT

This work was supported by the Volkswagen Foundation, the DFG through the Nanosystems Initiative Munich (NIM), the European Commission under the Seventh Framework Programme (FP7) as part of the Marie Curie Initial Training Network, EScoDNA (GA no. 317110) and the ERC grant ORCA, agreement n° 336440.

## REFERENCES

1. Fasman, G. D., *Circular Dichroism and the Conformational Analysis of Biomolecules*. Springer Science & Business Media: 2013.
2. Govorov, A. O.; Fan, Z.; Hernandez, P.; Slocik, J. M.; Naik, R. R., Theory of Circular Dichroism of Nanomaterials Comprising Chiral Molecules and Nanocrystals: Plasmon Enhancement, Dipole Interactions, and Dielectric Effects. *Nano Lett.* **2010,** *10*, 1374-1382.
3. Govorov, A. O.; Gun'ko, Y. K.; Slocik, J. M.; Gerard, V. A.; Fan, Z.; Naik, R. R., Chiral Nanoparticle Assemblies: Circular Dichroism, Plasmonic Interactions, and Exciton Effects. *J. Mater. Chem.* **2011,** *21*, 16806-16818.
4. Rao, C.; Wang, Z.-G.; Li, N.; Zhang, W.; Xu, X.; Ding, B., Tunable Optical Activity of Plasmonic Dimers Assembled by DNA Origami. *Nanoscale* **2015,** *7*, 9147-9152.
5. Slocik, J. M.; Govorov, A. O.; Naik, R. R., Plasmonic Circular Dichroism of Peptide-Functionalized Gold Nanoparticles. *Nano Lett.* **2011,** *11*, 701-705.
6. Johnson Jr, W. C., Determination of the Conformation of Nucleic Acids by Electronic Cd. In *Circular Dichroism and the Conformational Analysis of Biomolecules*, Springer: 1996; pp 433-468.
7. Kypr, J.; Kejnovská, I.; Renčiuk, D.; Vorlíčková, M., Circular Dichroism and Conformational Polymorphism of DNA. *Nucleic Acids Res.* **2009,** *37*, 1713-1725.
8. Govorov, A. O., Plasmon-Induced Circular Dichroism of a Chiral Molecule in the Vicinity of Metal Nanocrystals. Application to Various Geometries. *J. Phys. Chem. C* **2011,** *115*, 7914-7923.
9. Shukla, N.; Bartel, M. A.; Gellman, A. J., Enantioselective Separation on Chiral Au Nanoparticles. *J. Am. Chem. Soc.* **2010,** *132*, 8575-8580.
10. Shemer, G.; Krichevski, O.; Markovich, G.; Molotsky, T.; Lubitz, I.; Kotlyar, A. B., Chirality of Silver Nanoparticles Synthesized on DNA. *J. Am. Chem. Soc.* **2006,** *128*, 11006-11007.
11. Oh, H. S.; Liu, S.; Jee, H.; Baev, A.; Swihart, M. T.; Prasad, P. N., Chiral Poly(Fluorene-Alt-Benzothiadiazole) (Pfbt) and Nanocomposites with Gold Nanoparticles: Plasmonically and Structurally Enhanced Chirality. *J. Am. Chem. Soc.* **2010,** *132*, 17346-17348.
12. Kreibig, U.; Vollmer, M., Optical Properties of Metal Clusters. **1995**.
13. Su, K. H.; Wei, Q. H.; Zhang, X.; Mock, J. J.; Smith, D. R.; Schultz, S., Interparticle Coupling Effects on Plasmon Resonances of Nanogold Particles. *Nano Lett.* **2003,** *3*, 1087-1090.
14. Novotny, L.; van Hulst, N., Antennas for Light. *Nat. Photonics* **2011,** *5*, 83-90.
15. Aćimović, S. S.; Kreuzer, M. P.; González, M. U.; Quidant, R., Plasmon near-Field Coupling in Metal Dimers as a Step toward Single-Molecule Sensing. *ACS Nano* **2009,** *3*, 1231-1237.
16. Rothemund, P. W. K., Folding DNA to Create Nanoscale Shapes and Patterns. *Nature* **2006,** *440*, 297-302.
17. Douglas, S. M.; Dietz, H.; Liedl, T.; Hogberg, B.; Graf, F.; Shih, W. M., Self-Assembly of DNA into Nanoscale Three-Dimensional Shapes. *Nature* **2009,** *459*, 414-418.

18. Nordlander, P.; Oubre, C.; Prodan, E.; Li, K.; Stockman, M. I., Plasmon Hybridization in Nanoparticle Dimers. *Nano Lett.* **2004,** *4*, 899-903.

19. Kühler, P.; Roller, E.-M.; Schreiber, R.; Liedl, T.; Lohmüller, T.; Feldmann, J., Plasmonic DNA-Origami Nanoantennas for Surface-Enhanced Raman Spectroscopy. *Nano Lett.* **2014,** *14*, 2914-2919.

20. García de Abajo, F. J., Nonlocal Effects in the Plasmons of Strongly Interacting Nanoparticles, Dimers, and Waveguides. *J. Phys. Chem. C* **2008,** *112*, 17983-17987.

21. Kuzyk, A.; Schreiber, R.; Fan, Z.; Pardatscher, G.; Roller, E.-M.; Hogele, A.; Simmel, F. C.; Govorov, A. O.; Liedl, T., DNA-Based Self-Assembly of Chiral Plasmonic Nanostructures with Tailored Optical Response. *Nature* **2012,** *483*, 311-314.

22. Ke, Y.; Douglas, S. M.; Liu, M.; Sharma, J.; Cheng, A.; Leung, A.; Liu, Y.; Shih, W. M.; Yan, H., Multilayer DNA Origami Packed on a Square Lattice. *J. Am. Chem. Soc.* **2009,** *131*, 15903-15908.

23. Chen, Z.; Lan, X.; Chiu, Y.-C.; Lu, X.; Ni, W.; Gao, H.; Wang, Q., Strong Chiroptical Activities in Gold Nanorod Dimers Assembled Using DNA Origami Templates. *ACS Photonics* **2015,** *2*, 392-397.

24. Lan, X.; Chen, Z.; Dai, G.; Lu, X.; Ni, W.; Wang, Q., Bifacial DNA Origami-Directed Discrete, Three-Dimensional, Anisotropic Plasmonic Nanoarchitectures with Tailored Optical Chirality. *J. Am. Chem. Soc.* **2013,** *135*, 11441-11444.

25. Schreiber, R.; Do, J.; Roller, E.-M.; Zhang, T.; Schuller, V. J.; Nickels, P. C.; Feldmann, J.; Liedl, T., Hierarchical Assembly of Metal Nanoparticles, Quantum Dots and Organic Dyes Using DNA Origami Scaffolds. *Nat. Nanotechnol.* **2014,** *9*, 74-78.

26. Bifeng, P.; Limei, A.; Feng, G.; Hongye, T.; Rong, H.; Daxiang, C., End-to-End Self-Assembly and Colorimetric Characterization of Gold Nanorods and Nanospheres Via Oligonucleotide Hybridization. *Nanotechnol.* **2005,** *16*, 1776.

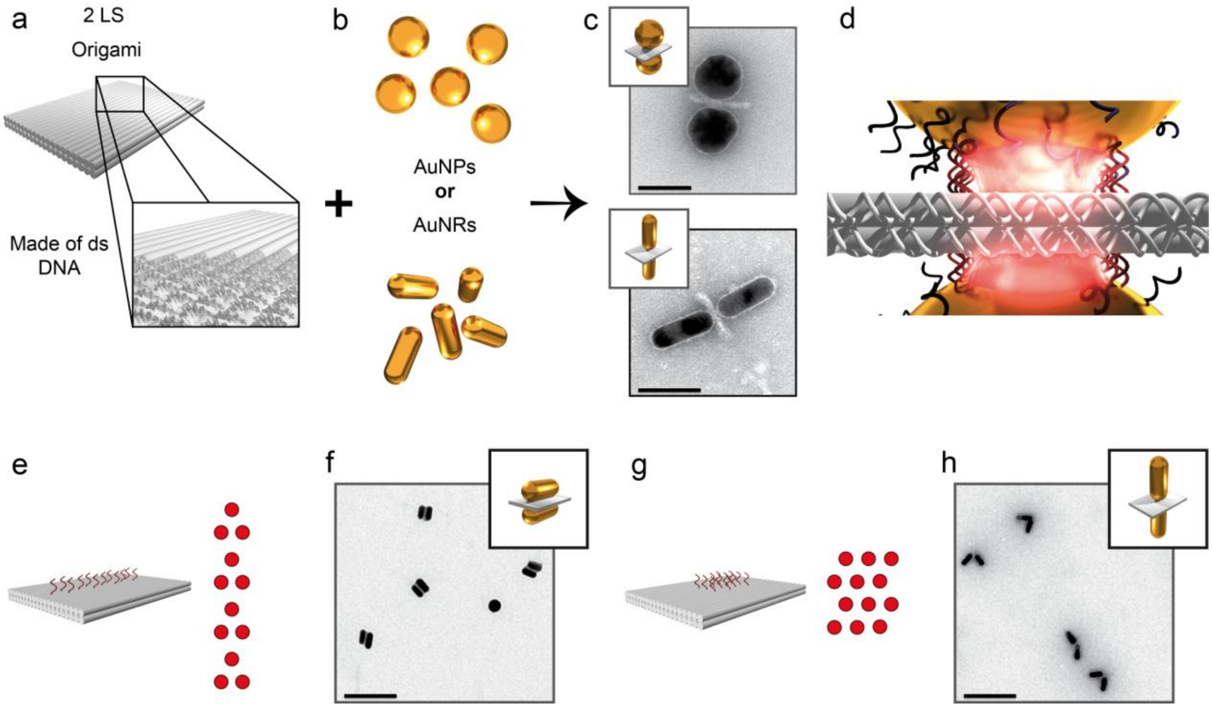

**Figure 1. DNA origami – nanoparticle antennas.** Plasmonic antennas were built by arranging nanoparticles on single- or multi-layered DNA origami structures in square lattice configuration. **a**, This results in parallel B-form DNA helices. **b,** To the self-assembled DNA origami, pre functionalized gold nanoparticles with a diameter of 40 nm or gold nanorods (20 nm x 50 nm) were attached via DNA hybridization. **c,** TEM images of the resulting dimer structures (scale bars: 50 nm). Inset: Illustration of the dimer structures. **d,** The structure made of ds DNA is located in the hot-spot of the gold nanoantenna. **e-h,** The orientation of the AuNRs on the DNA origami structure was determined by selecting the corresponding attachment patterns on the structure. **e,** An elongated shape of the attachment site forces the AuNR to bind in a parallel manner onto the structure. **f,** TEM image of dimer structures with AuNRs bound parallel to the origami surface. **g,** A more compact arrangement of the attachment handles forces the AuNRs to stand perpendicular on the origami structure. **h,** TEM image of structures with AuNRs attached vertical to the origami structure plane. (scale bars: 200 nm)

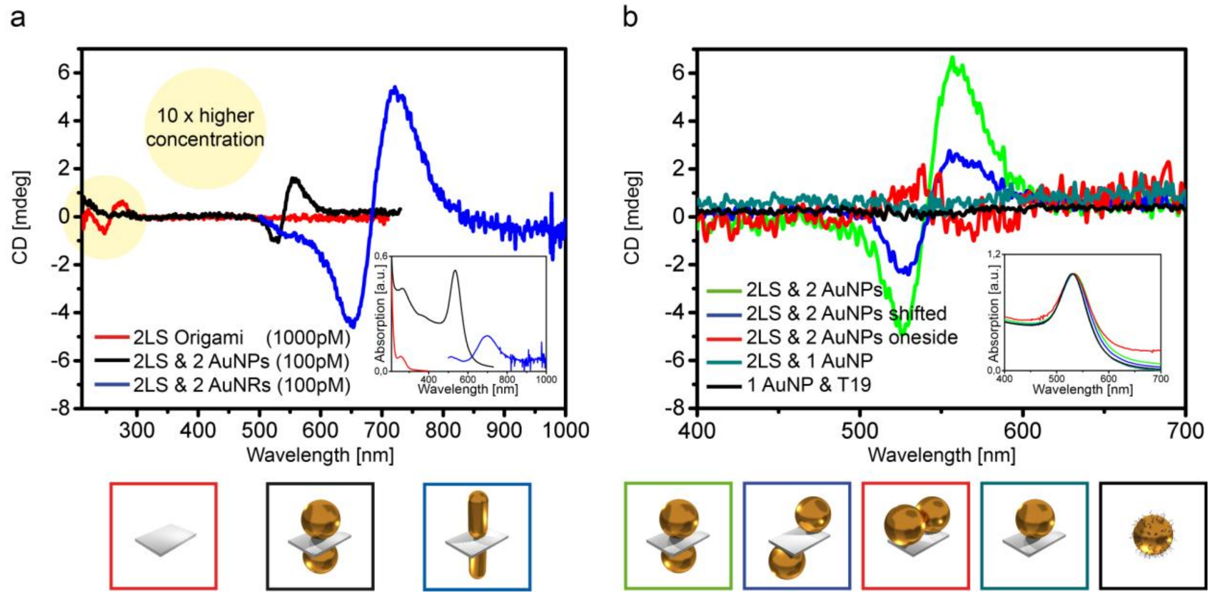

**Figure 2. CD measurements of bulk nanoantenna solution.** The UV-CD of B-form DNA is successfully picked up in the plasmonic frequency range of the nanoantennas. **a**, The characteristic shape of the UV signal (red) of a 2 layered DNA origami in square lattice confirmation (2LS) is maintained while the signal is enhanced by a factor of 20 for AuNPs antenna structures (black) and 80-fold for AuNRs antenna structures (blue). **b**, By comparing the AuNP dimer (green) with similar – yet plasmonically different – dimers, the CD transfer can be proven whilst plasmonic CD can be excluded. For this, we measured a 2LS with shifted AuNPs (blue), as well as a 2LS with both AuNPs on oneside (red). Further, the signal of one AuNP on top of a 2LS is shown in cyan as well as only AuNPs functionalized with ssDNA oligonucleotides are shown in black. The insets depict the corresponding Absoprtion, which is normalized to 1 and thus equal concentration for part b.

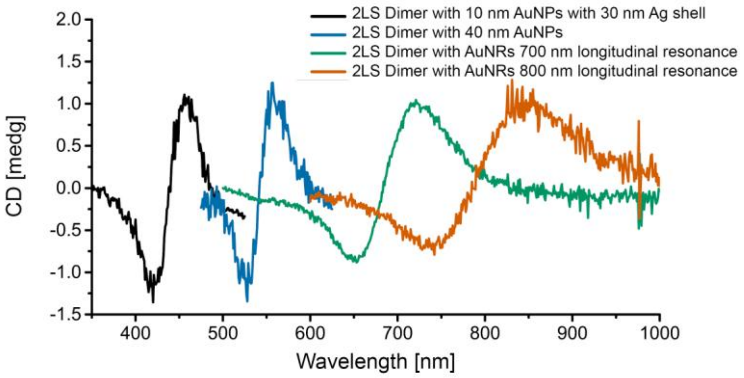

**Figure 3. CD spectra of origami dimer structures with different plasmonic particles attached.** The observed CD signal can be shifted along the whole visible wavelength range by using a variety of nanoparticless. The black curve shows the 2LS with AuNPs with 10 nm diameter attached, which were subsequently enhanced with a 30 nm Ag shell. The 2LS with AuNPS of 40 nm diameter is shown in blue. The green and the orange graph are measured CD signals for the 2LS structure with AuNRs attached in an upright conformation. The AuNRs have a longitudinal resonance frequency of 700 nm and 800 nm respectively.

## A.4. Associated Publication P4

### Hot spot-mediated non-dissipative and ultrafast plasmon passage

by

Eva-Maria Roller, Lucas V. Besteiro, Claudia Pupp, Larousse Khosravi Khorashad, Alexander O. Govorov, and Tim Liedl

submitted (2016).

# Hot spot-mediated non-dissipative and ultrafast plasmon passage

Eva-Maria Roller[1], Lucas V. Besteiro[2], Claudia Pupp[1], Larousse Khosravi Khorashad[2], Alexander O. Govorov[2†], Tim Liedl[1†]

[1]*Physics Department and CeNS, Ludwig-Maximilians-Universität München, 80539 Munich, Germany*
[2]*Department of Physics and Astronomy, Ohio University, Athens, Ohio 45701, USA*

[†] govorov@helios.phy.ohiou.edu; tim.liedl@lmu.de;

**Future computing devices may rely on all-optical components and coherent transfer of energy and information.[1,2] Next to quantum dots or NV-centers that act as photon sources,[3] plasmonic nanoparticles hold great promise as photon handling elements and as transport channels between calculating subunits.[4,5] Energy oscillations between two spatially separated plasmonic entities *via* a virtual middle state are examples of electron-based population transfer, but their realization requires precise control over nanoscale assembly of heterogeneous particles.[6-10] Here, we show the assembly and optical analysis of a triple particle system consisting of a chain of two gold nanoparticles with an inter-spaced silver island. We observe strong plasmonic coupling between the spatially separated gold particles mediated by the connecting silver particle with almost no dissipation of energy. As the excitation energy of the silver island exceeds that of the gold particles, only quasi-occupation of the silver transfer channel is possible. We describe this effect both with exact classical electrodynamic modeling and qualitative quantum-mechanical calculations. We identify the formation of strong hot spots between all particles as the main mechanism for the loss-less coupling between the remote partners. The observed spectra are consistent with a description of coherent ultra-fast energy transfer and could thus prove useful for optical computing applications such as quantum gate operations, but also for classical charge and information transfer processes.**

Low-dissipative transfer of excitations over short and long distances is at the heart of information science as well as energy harvesting. Energy transfer processes, for example, play a key role in highly efficient dipolar interactions in the light harvesting complexes of chloroplasts and low-loss exciton transport is sought after in solar cell development. Both Förster-Resonance Energy transfer (FRET) in biomolecular systems and diffusion of excitons in solar cells are incoherent processes and therefore often dissipative. Also information inside computer chips is, as of today, processed and transferred incoherently. On the other hand, coherence is the key property in glass fibre-based long distance communication; it is a crucial feature in interferometry and indispensable in future quantum computation.

With the goal to achieve fast and coherent transfer between nanoscale components, a variety of quantum approaches emerged. Generally, quantum mechanical tunneling is fast enough to avoid inelastic scattering during the passage, which makes it a low-loss process that is widely used in modern electronic technology. In particular, chains of potential wells were proposed for tunneling by adiabatic passage (CTAP) [1,2] and optical stimulated Raman adiabatic passage (STIRAP) has been realized by transferring spin populations of two long living quantum states *via* an optical third state.[11,12]

Another approach for transport of information at the nanoscale is the use of plasmonic components.[13] Plasmons are coherent, but they are usually dissipative and have only short life times. Both disadvantages are the result of the high scattering probability of electrons in metals. This hampers the use of plasmonic waveguides for transfer applications over distances longer than ~ 1 µm. Inspired by efforts to exploit quantum mechanical mechanisms we now propose a particle trimer system where plasmons are coherently transferred over extended distances. The system consists of two identical but spatially separated nanoparticles of one type and a third intermediate nanoparticle of a different type, the latter exhibiting also a different energetic level. The plasmons are transferred between the identical nanoparticles *via* the third nanoparticle, even with the two identical particles being too far away from each other to couple directly. The experimental realization of such a plasmon-based transfer system requires full control over spatial organization of heterogeneous nanoparticles.

DNA-based self-assembly offers the possibility to fabricate nanoscale objects that can accommodate inorganic particles at extremely well defined positions with high yields.[6-8,14-16] Previous assemblies with DNA-based templates consist of arrays,[8] chain-like,[17,18] helical,[9] or ring shaped[19] arrangements of metal nanoparticles, as well as chains of dyes[20] and quantum dots.[21,22] Owing to the possibility of functionalizing particle species with orthogonal DNA sequences – i.e. sequences that do not interfere with each other – heterogeneous particle architectures have been realized including dimers and trimers,[22,23] lattices,[8] core-satellites[15,24] and rings[19]. Lithographical attempts to build plasmonic devices from heterogenous metals consist of bimetallic nanodot arrays[25] and nanoantenna dimers of gold and silver disks[26]. However, top-down approaches suffer from limited spatial control on the scale below tens of nanometers and generally result in less homogenous crystalline structures made of sputtered or epitaxially deposited materials. Colloidal nanoparticles, in contrast, exhibit high crystalline quality and sharp size-distributions.

To overcome limitations of top-down lithography, we here use a DNA origami structure to spatially arrange gold and silver nanoparticles (AuNPs and AgNPs) in hetero-trimers with nanometer-precision and high assembly yields.[27,28] Our DNA origami template consists of a cylindrical 14-helix bundle (Supplementary Information note S1 and fig. S2), which offers lengthwise three equally spaced sequence-specific attachment sites for DNA functionalized nanoparticles. AuNPs functionalized with a DNA sequence complementary to the outer sites and one AgNP functionalized with a sequence complementary to the middle site were hybridized to each origami template (Fig.1a). The resulting heterogeneous nanoparticle trimer displays a designed interparticle gap of 40 nm between the two outer AuNPs with the AgNP accommodated in between. After assembly, we confirmed this configuration by transmission electron microscopy (TEM) (Fig. 1b and 1c and Supplementary Information note S2, fig. S3). Note that the AgNPs in our experiments are slightly smaller than the AuNPs and exhibit less contrast.

Conceptually, the distance between the AuNPs alone is too large to support plasmonic coupling and thus no transfer of energy is expected. The AgNP bridges this gap and transfers energy coherently between the two outer AuNPs and serves as a loss-less virtual transmitting state (Fig 1d). This can be understood as follows: If we excite our system in the gold plasmon resonance, the two gold plasmons are in resonance, however, at a distance too long to couple. At the same frequency, the silver plasmon is not in resonance but becomes involved as a quasi-resonant virtual state that operates as a transmitter. Since silver has a relatively small Drude dissipation constant, Ag plasmons have a narrow plasmon peak and exhibit a very strong induced dipole moment even for relatively small NP sizes. These important features make AgNPs excellent transmitter elements that allow us to connect the two gold plasmons almost without dissipation as we show in this study using both experiment and theory.

We characterized the plasmonic coherent transfer system with dark-field scattering spectroscopy of individual hetero-trimers and compared the resulting spectra with theoretical calculations. Figure 2a displays the scattering spectra of several AuNP-AgNP-AuNP trimers in comparison to an Au-Au homo dimer, missing the middle AgNP. The dominant resonance wavelength shifts from 549 nm for the AuNP homo dimer to 586 nm for the hetero-trimer structure. At the same time the peak intensity increases by a factor of ~ 4. Apparently, the middle AgNP indeed serves as a connector to enable strong coupling between the two outer AuNPs. The experiments further show that the use of larger AgNPs results in a stronger dominant peak intensity at 586 nm. Concurrently, the resonance level of the AgNP becomes visible as a small peak at 445 nm.

The particle geometries in our numerical simulations were adjusted to the particle positions and sizes as determined from SEM and TEM images. For the simulation of the dimer structure, two 40 nm AuNPs separated by a 38 nm gap were chosen (see also Supplementary Information fig. S4). For the trimer simulations a 30 nm AgNP was placed in the gap. Figure 2b shows that the simulated scattering cross sections are in excellent agreement to the observed spectra. For the hetero-trimer the dominant plasmon resonance peak shifts ~ 40 nm to the red. Furthermore, the peak intensity is increased by a factor of 4 compared to the homo-dimer. Most importantly, the simulations confirm that the AgNP does not dissipate energy at the resonance mode of the hetero-trimer, but instead transfers the energy coherently between the two outer AuNPs (Fig. 2c).

Polarization-resolved scattering measurements give additional insight into this non-dissipative passage. Figure 3a shows such measurements for a single hetero-trimer. For the linear detecting polarizer set to 90° with respect to the long trimer axis only small transversal resonance peaks of the single AgNP and AuNPs are visible at ~ 450 nm and ~ 550 nm, respectively. At parallel (0°) polarization, the coupled, red-shifted mode appears. Our simulations fully reproduce these observations (Fig. 3b).

The charge color maps in Figure 3c display the key feature of the plasmon coupling in our structures: The energy transfer between the Au-NPs occurs *via* the plasmonic hot spots formed in the Au-Ag gaps. These highly localized spots generate surface charges involving high multipole harmonics, which contrasts the standard picture for energy transfer processes between, e.g., dye molecules.

By analyzing the data in Figures 2a and b, we can estimate the lifetime of the plasmon in the trimer and its transfer time between the two Au NPs. From the width of the plasmon peak we obtain a lifetime of ~ 6 fs. From the splitting of the L-plasmon resonances ($\Delta_{splitt}$) we can calculate that $\tau_{transfer} \sim \pi / (2 \cdot \Delta_{splitt}) \sim 4.7\,\mathrm{fs}$ (see Supporting Information note S3 and fig. S1). The observed plasmon lifetime and transfer time are both on the femtosecond time scale indicating efficient and coherent transfer. Due to the strong coupling of the plasmonic dipoles, this process is orders of magnitude faster than FRET, which only achieves ps-times both in plants and between FRET dyes in the lab.[29] In principle, FRET in molecules and semiconductor nanocrystals can be accelerated by plasmons, but only at the cost of high losses in the metal component.[30]

As our structure is describable as a system of coupled oscillators, we can also apply a quantum model of the plasmonic excitations that should yield similar qualitative results. In this model the plasmons in the three NPs are considered as three quantum oscillators that are coupled by Coulomb forces and have each three degrees of freedom (Fig. 4a).[31] To keep the calculations simple, we assume the dipolar limit for the plasmons, which, of course, underestimates the strength of coupling in our real samples. The total number of modes is 9 and the modes can be bright (B) or dark (D) and longitudinal (L) or transverse (T). They further exhibit certain degeneracies (see Supplementary Information note S3 for details and model parameters). The Hamiltonian of the coupled plasmonic oscillators reads

$$\hat{H} = \sum_{\alpha} \hbar\omega_{p,\alpha}\left(\hat{c}_{\alpha}^{+}\hat{c}_{\alpha} + \frac{1}{2}\right) + \sum_{\alpha,\beta} w_{\alpha\beta}\hat{c}_{\alpha}^{+}\hat{c}_{\beta} \ , \qquad (1)$$

where $\alpha(\beta)$ are the indices of all possible plasmonic states of isolated NPs. The quantum index can be represented as $\alpha = (i, \gamma)$, where $i = 1, 2, 3$ is the NP number and $\gamma = x, y, z$ is the direction of oscillation. In Eq. 1, $\omega_{p,\alpha}$ and $w_{\alpha\beta}$ are the plasmon frequencies of isolated NPs and the Coulomb coupling constants, respectively. The Hamiltonian (1) can be easily diagonalized and the spectrum of vibrations can be found. The most interesting modes are the collective longitudinal ones:

$$\omega_{LD,Au-like} = \sqrt{\omega_{p,Au}^{2} + \Delta_{\text{int},Au-Au}^{2}} \ , \ \omega_{LB,Au-like,passage} = \omega_{p,Au}^{2} - \delta_{\text{int}} \ , \ \omega_{LB,Ag-like} = \omega_{p,Au}^{2} + \delta_{LB}$$

(2)

where the parameters $\Delta_{\text{int},Au-Au}$ and $\delta_{\text{int}}$ are the splittings that appear in the spectrum due to the Au-Au and Au-Ag plasmonic interactions.

This relatively simple quantum model reproduces qualitatively the main important features of our experimentally and computationally obtained spectra (Fig. 4b), which makes this an example where classical and quantum pictures are equivalent when considering the coherent properties of coupled plasmons. In particular, the quantum model reproduces the red shift of the main Au-like L-plasmon, the appearance of splittings in the spectra, and a larger splitting for the L-modes as compared to the T-modes. Again, we observe that the Ag-plasmon plays the role of a mediator for the enhanced coupling between the two Au-plasmons. Despite the drastic simplification of our quantum model, which ignores multipolar modes, the formation of hot spots and some other fine details of the system, it helps to understand all plasmonic modes and the characteristic spectral shifts.

To summarize we established a concept for efficient and fast photon transfer where, in contrast to conventional mono-metallic waveguides, a silver nanoparticle is introduced as a transmitter between spatially separated gold nanoparticles. Our plasmon transfer system, based on a DNA origami-supported nanoparticle chain, operates with almost no losses in the transmitting element. This approach allowed us to construct and characterize a coherent, non-dissipative and ultrafast energy passage that outlines the path to an efficient use of plasmonic waveguides for information transfer over larger distances. It opens the doors for future applications of plasmonic nanostructures as elements for coherent transfer and all-optical processing of information.

## References

1 Greentree, A. D., Cole, J. H., Hamilton, A. R. & Hollenberg, L. C. L. Coherent electronic transfer in quantum dot systems using adiabatic passage. *Phys. Rev. B* **70**, 235317 (2004).

2 Rech, J. & Kehrein, S. Effect of Measurement Backaction on Adiabatic Coherent Electron Transport. *Phys. Rev. Lett.* **106**, 136808 (2011).

3 Aharonovich, I., Greentree, A. D. & Prawer, S. Diamond photonics. *Nat Photon* **5**, 397-405 (2011).

4 Ozbay, E. Plasmonics: Merging Photonics and Electronics at Nanoscale Dimensions. *Science* **311**, 189-193 (2006).

5 Akimov, A. V. *et al.* Generation of single optical plasmons in metallic nanowires coupled to quantum dots. *Nature* **450**, 402-406 (2007).

6 Pal, S., Deng, Z., Ding, B., Yan, H. & Liu, Y. DNA-Origami-Directed Self-Assembly of Discrete Silver-Nanoparticle Architectures. *Angew. Chem.* **122**, 2760-2764 (2010).

7 Alivisatos, A. P. *et al.* Organization of 'nanocrystal molecules' using DNA. *Nature* **382**, 609-611 (1996).

8 Zheng, J. *et al.* Two-Dimensional Nanoparticle Arrays Show the Organizational Power of Robust DNA Motifs. *Nano Lett.* **6**, 1502-1504 (2006).

9 Kuzyk, A. *et al.* DNA-based self-assembly of chiral plasmonic nanostructures with tailored optical response. *Nature* **483**, 311-314 (2012).

10 Gopinath, A., Miyazono, E., Faraon, A. & Rothemund, P. W. K. Engineering and mapping nanocavity emission via precision placement of DNA origami. *Nature* **535**, 401-405 (2016).

11 Bergmann, K., Theuer, H. & Shore, B. W. Coherent population transfer among quantum states of atoms and molecules. *Rev. Mod. Phys.* **70**, 1003-1025 (1998).

12 Vitanov, N. V., Halfmann, T., Shore, B. W. & Bergmann, K. Laser-induced population transfer by adiabatic passage techniques. *Annu. Rev. Phys. Chem.* **52**, 763-809 (2001).

13 Maier, S. A. *et al.* Local detection of electromagnetic energy transport below the diffraction limit in metal nanoparticle plasmon waveguides. *Nat. Mater.* **2**, 229-232 (2003).

14 Seeman, N. C. Nanomaterials Based on DNA. *Annu. Rev. Biochem.* **79**, 65-87 (2010).

15 Schreiber, R. *et al.* Hierarchical assembly of metal nanoparticles, quantum dots and organic dyes using DNA origami scaffolds. *Nat. Nano* **9**, 74-78 (2014).

16 Mastroianni, A. J., Claridge, S. A. & Alivisatos, A. P. Pyramidal and Chiral Groupings of Gold Nanocrystals Assembled Using DNA Scaffolds. *J. Am. Chem. Soc.* **131**, 8455-8459 (2009).

17 Klein, W. P. *et al.* Multiscaffold DNA Origami Nanoparticle Waveguides. *Nano Lett.* **13**, 3850-3856 (2013).

18 Ding, B. *et al.* Gold Nanoparticle Self-Similar Chain Structure Organized by DNA Origami. *J. Am. Chem. Soc.* **132**, 3248-3249 (2010).

19 Roller, E.-M. *et al.* DNA-Assembled Nanoparticle Rings Exhibit Electric and Magnetic Resonances at Visible Frequencies. *Nano Lett.* **15**, 1368-1373 (2015).

20 Stein, I. H., Schüller, V., Böhm, P., Tinnefeld, P. & Liedl, T. Single-Molecule FRET Ruler Based on Rigid DNA Origami Blocks. *ChemPhysChem* **12**, 689-695 (2011).

21 Sharma, J. *et al.* DNA-Tile-Directed Self-Assembly of Quantum Dots into Two-Dimensional Nanopatterns. *Angew. Chem., Int. Ed.* **47**, 5157-5159 (2008).

22 Fu, A. *et al.* Discrete Nanostructures of Quantum Dots/Au with DNA. *J. Am. Chem. Soc.* **126**, 10832-10833 (2004).

23 Lee, J.-H., Kim, G.-H. & Nam, J.-M. Directional Synthesis and Assembly of Bimetallic Nanosnowmen with DNA. *J. Am. Chem. Soc.* **134**, 5456-5459 (2012).

24 Pal, S., Sharma, J., Yan, H. & Liu, Y. Stable silver nanoparticle-DNA conjugates for directed self-assembly of core-satellite silver-gold nanoclusters. *Chem. Commun.*, 6059-6061 (2009).

25 Xu, L., Tan, L. S. & Hong, M. H. Tuning of localized surface plasmon resonance of well-ordered Ag/Au bimetallic nanodot arrays by laser interference lithography and thermal annealing. *Appl. Opt.* **50**, G74-G79 (2011).

26 Shegai, T. *et al.* A bimetallic nanoantenna for directional colour routing. *Nat. Commun.* **2**, 481 (2011).

27 Rothemund, P. W. K. Folding DNA to create nanoscale shapes and patterns. *Nature* **440**, 297-302 (2006).

28 Douglas, S. M. *et al.* Self-assembly of DNA into nanoscale three-dimensional shapes. *Nature* **459**, 414-418 (2009).

29 May, V. & Kühn, O. *Charge and energy transfer dynamics in molecular systems*. Vol. 3 (John Wiley & Sons, 2011).

30 Govorov, A. O., Lee, J. & Kotov, N. A. Theory of plasmon-enhanced Förster energy transfer in optically excited semiconductor and metal nanoparticles. *Phys. Rev. B* **76**, 125308 (2007).

31 Otten, M. *et al.* Entanglement of two, three, or four plasmonically coupled quantum dots. *Phys. Rev. B* **92**, 125432 (2015).

**Supplementary Information** containing additional data and protocols is linked to the online version of the paper.

**Acknowledgements:** This work was funded by the Volkswagen Foundation, the DFG through the Nanosystems Initiative Munich (NIM), through the ERC Starting Grant

ORCA (GA N°:336440). A.O.G. and L.V.B acknowledge additional support from the US Army Research Office (W911NF-12-1-0407).

**Author Contributions:** E.M.R., A.O.G. and T.L. conceived the experiments and co-wrote the manuscript. E.M.R. designed the structure and analyzed the data. E.M.R. and C.P. performed the experiments. L.V.B. and L.K.K. performed the simulations, A.O.G developed the quantum model. All authors contributed to the general discussion and reviewed the manuscript.

**Author Information**: The authors declare no competing financial interests. Correspondence and requests for materials should be addressed to TL (tim.liedl@lmu.de).

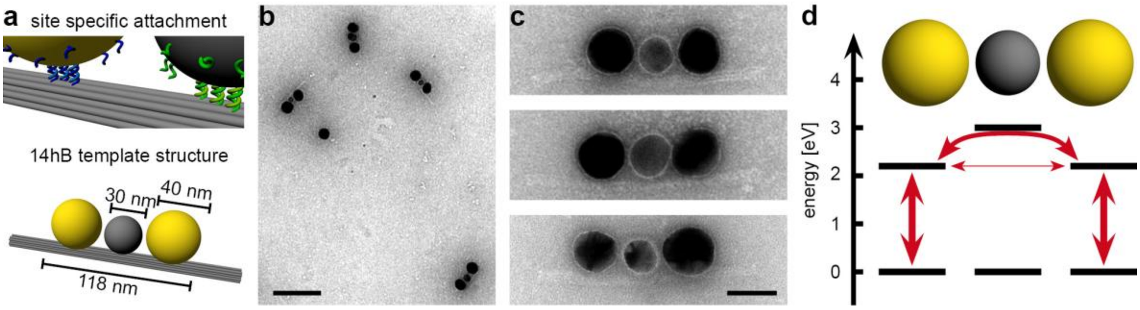

**Figure 1 | Plasmonic transfer system. a,** Design scheme of the DNA origami-templated heterogeneous trimer structure. AuNPs and AgNPs bind *via* specific DNA sequences (shown in blue and green) to designated sites on the DNA origami structure. **b,** Wide field TEM image of the assembled hetero-trimers. Scale bar: 200 nm. **c,** High magnification TEM images reveal the two outer AuNPs, the middle AgNP and the DNA origami scaffold. Scale bar: 40 nm. **d,** Energy scheme and concept of the plasmonic transfer system. The middle Ag particle serves as a virtual transmitter connecting the two separated Au particles.

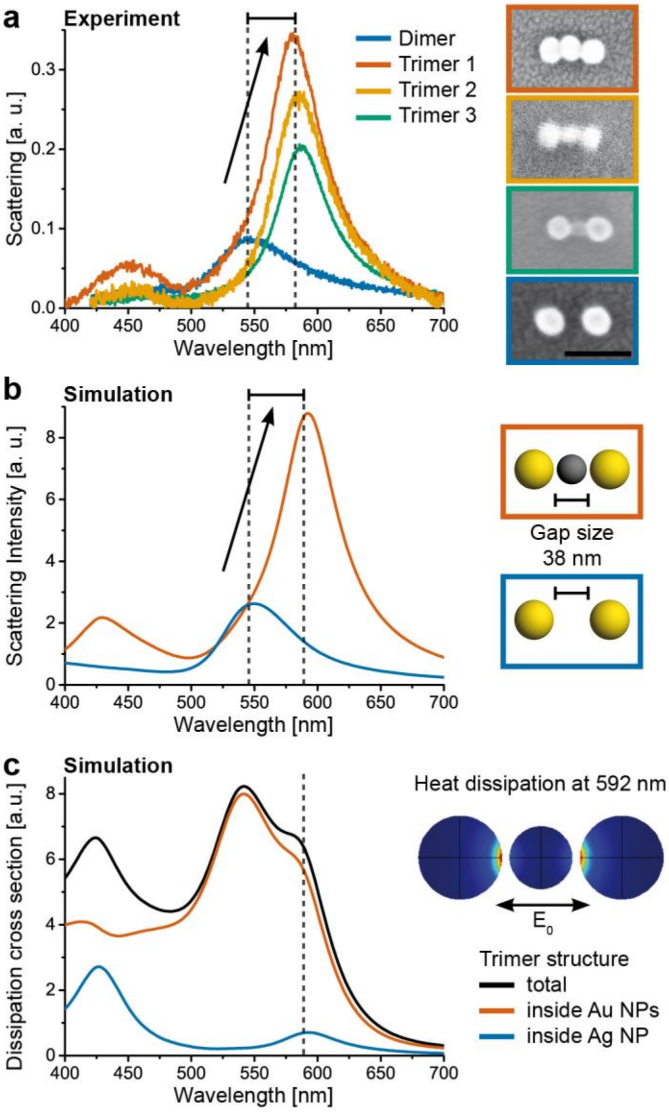

**Figure 2 | Dark-field scattering spectra and simulations of the plasmonic transfer system. a,** Single structure scattering spectra of one homo dimer and three hetero-trimers and SEM images of the corresponding structures. Scale bar: 100 nm. A plasmon resonance shift of ~ 40 nm is observed. **b,** Numerical simulations for a homo dimer structure of two 40 nm AuNPs with a 38 nm gap (blue) and for the same configuration with a 30 nm AgNP placed in the gap (orange). **c,** The simulated heat dissipation cross section of the hetero-trimer reveals that the AuNPs are dissipative at the resonance mode at λ = 592 nm, while the AgNP is not. The color map shows the local heat dissipation in the longitudinal mode. Most of the dissipation appears in the hot spots on the AuNPs.

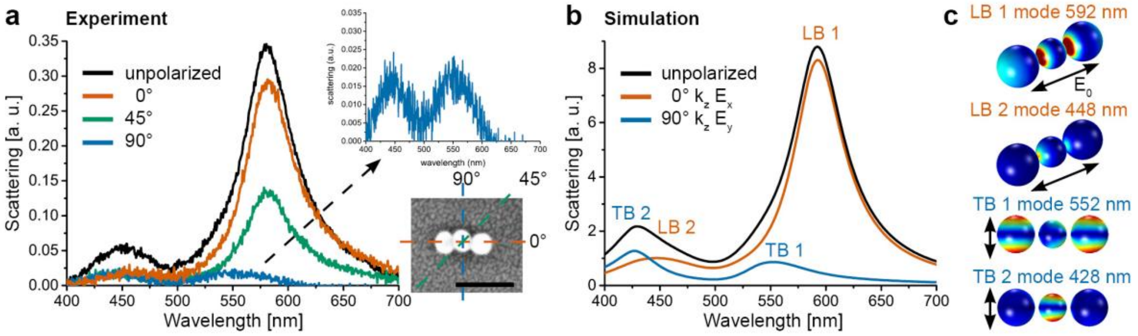

**Figure 3 | Polarization-resolved measurements and calculations. a,** Polarization-resolved scattering spectra of a hetero-trimer structure. Only the resonances of uncoupled AuNPs and single AgNPs are detectable at 90° orientation of the polarizer in the detection path. The resonant mode appears in a parallel orientation of the polarizer. Inset: Orientations of the polarizer are displayed in the SEM image. Scale bar: 100 nm. **b,** Simulated polarization-resolved scattering spectra and **c,** surface charge maps corresponding to the longitudinal and transversal bright modes (LB, TB) are in excellent agreement with the experimental results.

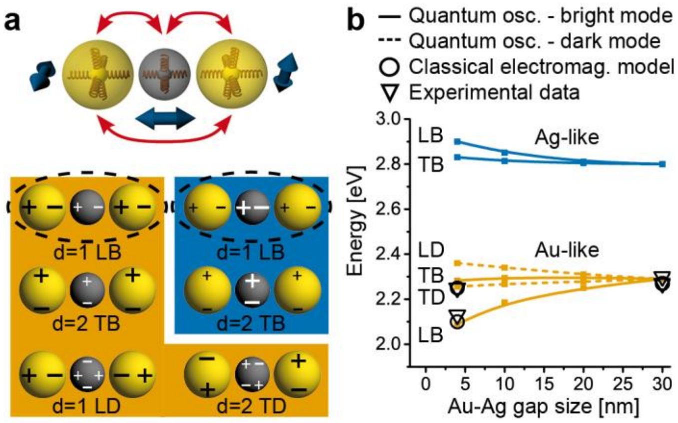

**Figure 4 | Quantum model. a,** Scheme displaying the harmonic-oscillator model of the plasmonic passage (top) and classification of the plasmonic modes (bottom). The main contributing mode to the plasmon passage and the mode assisting the passage of Au plasmons are circled with dashed lines. **b,** Energies of the different plasmonic modes calculated *via* the quantum oscillator model (solid and dashed lines), simulated by the classical electromagnetic model (circles) and experimentally obtained bright modes (triangles).

# A.5. Associated Publication P5

## Quantitative single molecule surface-enhanced Raman Scattering by optothermal tuning of DNA origami assembled pasmonic nanoantennas

by

Sabrina Simoncelli*, Eva-Maria Roller*, Patrick Urban, Robert Schreiber,
Andrew J. Turberfield, Tim Liedl, and Theobald Lohmüller
*equal contribution

published in ACS Nano, 10, 9809 - 9815 (2016).

ACS NANO

www.acsnano.org

# Quantitative Single-Molecule Surface-Enhanced Raman Scattering by Optothermal Tuning of DNA Origami-Assembled Plasmonic Nanoantennas

Sabrina Simoncelli,[†,⊥] Eva-Maria Roller,[‡,⊥] Patrick Urban,[†] Robert Schreiber,[∥] Andrew J. Turberfield,[∥] Tim Liedl,[*,‡,§] and Theobald Lohmüller[*,†,§]

[†]Photonics and Optoelectronics Group, Department of Physics and Center for Nanoscience (CeNS), Ludwig-Maximilians-Universität München, Amalienstraße 54, Munich 80799, Germany

[‡]Department of Physics and Center for Nanoscience (CeNS), Ludwig-Maximilians-Universität München, Geschwister-Scholl-Platz 1, Munich 80539, Germany

[§]Nanosystems Initiative Munich (NIM), Schellingstraße 4, Munich 80539, Germany

[∥]Clarendon Laboratory, Department of Physics, University of Oxford, Parks Road, Oxford OX1 3PU, United Kingdom

Ⓢ *Supporting Information*

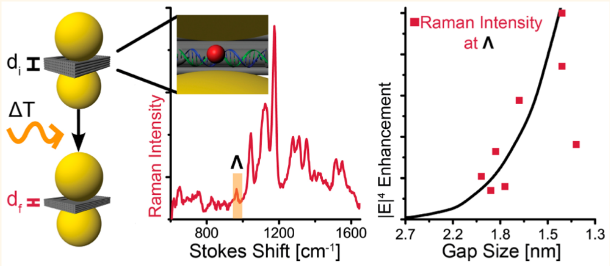

**ABSTRACT:** **DNA origami is a powerful approach for assembling plasmonic nanoparticle dimers and Raman dyes with high yields and excellent positioning control. Here we show how optothermal-induced shrinking of a DNA origami template can be employed to control the gap sizes between two 40 nm gold nanoparticles in a range from 1 to 2 nm. The high field confinement achieved with this optothermal approach was demonstrated by detection of surface-enhanced Raman spectroscopy (SERS) signals from single molecules that are precisely placed within the DNA origami template that spans the nanoparticle gap. By comparing the SERS intensity with respect to the field enhancement in the plasmonic hot-spot region, we found good agreement between measurement and theory. Our straightforward approach for the fabrication of addressable plasmonic nanosensors by DNA origami demonstrates a path toward future sensing applications with single-molecule resolution.**

**KEYWORDS:** *SERS, DNA Origami, single molecule, plasmonic heating*

DNA origami[1,2] allows to design three-dimensional (3D) structures of various materials and functionalities with nanoscale accuracy.[3−7] This broad versatility has been employed in numerous scientific applications in such diverse fields as (bio)sensing,[8−10] catalysis,[11] nanomedicine,[12−15] and super-resolution microscopy.[16,17] In recent years, DNA origami has also been used to assemble complex and multifunctional plasmonic nanostructures such as plasmonic nanoparticle rings,[18] helices,[19] as well as reconfigurable plasmonic metamolecules[20] and for studying enhanced light matter interactions between plasmonic nanoantennas and single molecules.[21]

Plasmonic nanoparticles or nanoantennas are capable of concentrating far-field propagating light into a nanoscale volume.[22] If two gold nanoparticles (AuNPs) are brought into close proximity, the plasmonic coupling between them results in a strong enhancement of the electric field in the nanoparticle gap.[23] The magnitude and spatial distribution of this so-called plasmonic "hot spot" is a consequence of the particle size and separation distance.[24] However, any target molecule must be positioned precisely between the two particles to benefit from the strongest signal enhancement. Controlling these parameters is challenging, but DNA origami has shown to be well suited for addressing this problem. Dimer antennas made of two plasmonically coupled AuNPs that were assembled by DNA origami have been used to significantly enhance fluorescence intensity[21] and the surface-enhanced Raman scattering (SERS) signal from molecules that were located in the nanoparticle gap.[25−28] Particularly SERS substrates often face the problem of poor reproducibility and

**Received:** August 4, 2016
**Accepted:** September 20, 2016
**Published:** September 20, 2016

DOI: 10.1021/acsnano.6b05276

performance since the Raman scattering cross sections of most molecules are orders of magnitude smaller than the cross-section for fluorescence.[29] Detecting Raman signals therefore relies on very high field enhancements, which is associated with an extremely small gap size of only a few nanometers. It has been shown that DNA scaffolds can be employed to align two AuNPs in close proximity by either positioning them on the surface of a DNA sheet[28] or by connecting them on both sides of a DNA stack that spans the nanoparticle gap.[26] For molecules that are embedded in the origami structure, the latter design comes with the benefit that the analyte is located precisely at the area of the largest field enhancement (Figure 1).

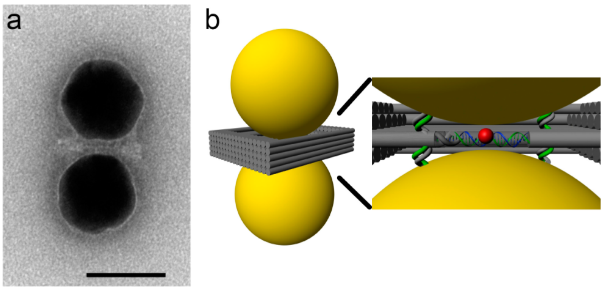

**Figure 1. DNA origami AuNP dimers. (a) Representative TEM image of the plasmonic dimer nanoantenna. Scale bar 40 nm. (b) Schematic diagram of two 40 nm AuNPs hosted on a 3D DNA origami structure of 47 nm × 44 nm lateral dimensions in which one or four DNA staples strands are modified with either a Cy3 or a Cy3.5 molecule.**

DNA origami designs with a nanoparticle gap between 3 and 5 nm have been reported to provide large SERS enhancements of up to 7 orders of magnitude, which was, however, not sufficient to achieve single-molecule sensitivity.[30] Nanoparticle dimer structures with gap sizes <2 nm have shown to be suitable for single-molecule SERS.[31−34] Yet in all cases, the additional growth of a silver layer on top of the AuNP dimers was necessary to reduce the particle spacing, which is a huge disadvantage, particularly for biological applications. In order to avoid any chemical treatment and to boost the field enhancement in the hot spot for quantitative single-molecule detection, it is thus pivotal to reduce the separation distance between two AuNPs in a range between 1 and 2 nm.

An alternative strategy to growing a shell around the particles is to bring them closer together by reducing the thickness of the origami template. Heating of temperature sensitive polymer sheets, for example, has shown to be an effective way to reduce the separation distance between optically printed nanoparticle dimers and tetramers.[35] Pillers *et al.*[36] and Kim *et al.*[37] have reported that heating of DNA origami sheets above 150 °C results in uniform shrinking of the height of the structures by roughly 50%. In a similar way, this temperature-induced shrinking could thus be applied as an experimental strategy to reduce the effective separation distance between two nanoparticles that are aligned by a DNA scaffold.

Heating is in fact a limiting parameter for any SERS measurement that employs plasmonic nanoparticle structures. For Raman measurements, the irradiation with laser light is imperative. Light absorbed by AuNPs, however, is converted into heat.[38,39] Furthermore, the highest SERS enhancement is expected if the laser wavelength is resonant with the nanoparticle plasmons, which is also the regime for most efficient plasmonic heating. Temperatures up to several hundred degrees Kelvin can be reached if the laser power is too high, which can immediately result in the destruction of the sample. Controlled laser illumination, however, can also be employed to deposit a defined amount of heat in a nanoscale region around the particles.

Here, we demonstrate that optothermal-induced shrinking of a DNA origami template in between two AuNPs can be employed to reduce the gap-size to <2 nm and hence increase the field enhancement in the nanoparticle gap. The gap size reduction was investigated by far-field scattering measurements of individual dimer nanoantennas in combination with Raman measurements. With this approach, we were able to quantitatively map the increase of the SERS signal intensity from a single molecule that is placed in the hot spot between both particles as a function of the nanoparticle spacing and found good agreement between experiment and theory.

## RESULTS

### DNA Origami AuNP Dimers Design and Fabrication.

The design of a gold dimer structure assembled on a DNA origami template is shown in Figure 1. Two AuNPs of 40 nm diameter were aligned in close proximity with the help of a stack of five DNA layers with outer dimensions of 47 nm × 44 nm. Out of these five DNA layers, only the middle one forms a complete sheet (see Figure S1). The other layers have a frame-like shape so that the complete DNA origami structure offers two funnel-forming grooves (see Figure 1b). The DNA origami has a two-fold function. On the one hand, each of the grooves is designed to perfectly embed the 40 nm AuNPs, which leads to a rigid AuNP dimer configuration. On the other hand, the one layer of DNA in the middle of the hot spot offers the possibility to have site-specific binding of any molecule of interest. This strategy allows placing a controllable number of Raman reporter molecules precisely in the region of the highest electromagnetic field (for a detailed protocol of the DNA origami dimer self-assembly see the Methods section). Here, we directly modified either one or four DNA staple strands incorporated into this middle DNA layer with a Cy3 or Cy3.5 molecule (see Figure 1b). The different dimer structures with their specific type and number of dye molecules in the hot-spot region were prepared in separate batch reactions. The final structures were subsequently drop-cast on a clean glass coverslide, incubated for 5 min, and dried with nitrogen. Figures 1a, S2, and S3 show representative transmission electron microscopy (TEM) images of the DNA origami AuNP dimer structures. The average gap size of dried DNA origami AuNP dimers was ~2.8 ± 1 nm as verified by Rayleigh scattering spectroscopy.

### Plasmonic Heating and SERS.

A schematic overview of the experimental approach is shown in Figure 2a. The measurement for a single dimer was conducted in a sequence of measurement and heating steps; both Raman scattering and heating were performed with a continuous-wave 612 nm laser. The scattering spectrum of an individual DNA origami dimer modified with only one Cy3.5 molecule placed in the center of the hot spot is shown in Figure 2b. Before laser irradiation, the scattering spectrum of the dimer displayed a resonance at 592 nm (Figure 2b, black line). The corresponding Raman spectra of Cy3.5 did not show any visible peaks (Figure 2c, black line). Raman measurements were carried out at a low excitation intensity of ~14 kW/cm$^2$ to avoid heating of the sample. Control measurements of the scattering spectra before and after

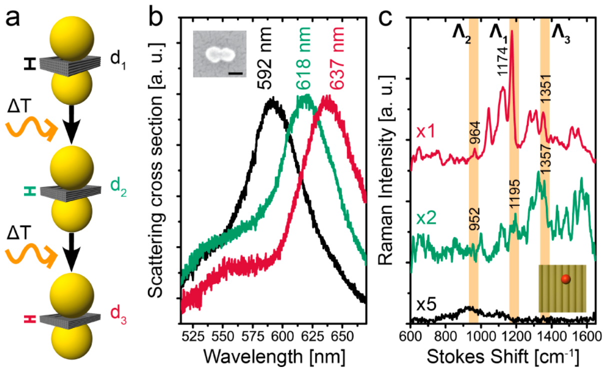

**Figure 2. Laser-induced gap size shrinkage. (a) Schematic representation of the experimental procedure. Representative Rayleigh (b) and Raman (c) scattering spectra of an individual dimer structure modified with a single Cy3.5 molecule placed at the hot spot before (black) and after a first (green) and a second (red) round of 10 s laser excitation (612 nm, ~60 kW/cm$^2$). The intensities of the Raman scattering spectra have been scaled as indicated. The recorded Raman scattering signals showed the characteristic spectral fluctuations associated with single-molecule SERS.[40] Inset in (b): Corresponding SEM image of the dimer structure. Scale bar 40 nm.**

the Raman measurement were taken to ensure that the laser illumination during the Raman measurement did not cause any change or deterioration of the sample. In the next step, the same dimer structure was irradiated with a four times higher laser power density (60 kW/cm$^2$) for 10 s. After the first of such a heating step, the scattering peak displayed a red shift from 592 to 618 nm (Figure 2b, green line), indicative of a reduction of the nanoparticle gap and increased plasmonic coupling. When repeating the Raman measurement, peaks for the single Cy3.5 dye (952, 1195, 1357 cm$^{-1}$) were now observed in the spectrum (Figure 2c, green line). The intensities of these Raman peaks improved further after repeating the heating step for a second time. Also the scattering peak of the gold dimer structure was red-shifted again by about 30 nm from 618 to 637 nm (Figure 2b, red line), indicating even stronger plasmonic coupling. In addition, the emergence of a smaller peak at ~555 nm was observed, corresponding to the transverse plasmon mode along the short axis of the dimer structure. The new Raman spectrum again displayed a strong increase of the peak intensities as a result of the much stronger field enhancement in the nanoparticle gap (Figure 2c, red line).

The detected Raman signals were stable, limited only by bleaching of the dye. The recorded Raman scattering signals showed the characteristic spectral fluctuations associated with single-molecule SERS.[40] Cy3.5 is a Raman analyte with many characteristic fingerprints. We identified typical Cy3.5 vibrational modes located at approximately 960, 1180, 1280, 1315, 1350, 1390, 1430, 1470, 1520, 1550, 1590, 1600, and 1620 cm$^{-1}$ for gap sizes smaller than 2.5 nm. Peaks can be attributed as follows: 960 cm$^{-1}$, vibrational modes of the central $\pi$-conjugated chain;[41] 1280 cm$^{-1}$, motions of the ethyl groups attached to the aromatic moiety;[42] 1350 cm$^{-1}$, methine chain motions;[42,43] and 1390 and 1470 cm$^{-1}$, symmetric and asymmetric deformation modes of $CH_3$, respectively.[42,43] Features between 1550 and 1590 cm$^{-1}$ are attributed to the $N^+{=}C$ stretching motion[42−44] and those at 1600 and 1620 cm$^{-1}$ to the $C{=}C$ stretching mode.[44] We also observed some peaks related to the vibrational modes of DNA at approximately 760, 1030, and 1580 cm$^{-1}$.[45,46] The peaks located at 760 and 1030 cm$^{-1}$ are attributed to ring breathing[47] and a methyl rocking vibration of the thymine nucleotide,[48] respectively. The peak at 1580 cm$^{-1}$ corresponds to the ring stretching of adenine nucleotides as well as the $N6H_2$ deformation.[47] The peak at 1090 cm$^{-1}$ corresponds to the vibrational mode originated from the symmetric stretching vibration of the phosphodioxy-($PO_2^-$) DNA backbone.[45,46,49]

We inferred the gap sizes for individual DNA AuNP dimers from their Rayleigh scattering spectra using Mie theory.[50,51] According to the data shown in Figure 2b and our numerical simulations, the gap size was reduced from ~3.3 to 1.9 nm and from ~1.9 to 1.3 nm in the first and second round of laser heating, respectively. We did not observe any melting or reshaping of the gold particles after laser treatment, as verified by SEM and TEM measurements. The observed red shift of the plasmon resonance can therefore be attributed solely to the irreversible reduction of the nanoparticle gap by optothermally-induced shrinking of the DNA template. The structural stability of the DNA origami template depends on temperature. For temperatures beyond 200 °C, thermally-induced structural changes are reflected in a change of the AuNP dimer gap size. However, the extent of the plasmonic shift and gap size reduction varies between 20% and 40% from dimer to dimer, as confirmed by Rayleigh scattering spectroscopy and TEM imaging (see Figure S4). Yet, a gradual red-shift of the scattering peak due to a reduction of the nanoparticle gap, as schematically depicted in Figure 2a, was observed for all samples.

We performed numerical simulations to estimate the increase in temperature of the nanoparticle dimer (see Methods section and Figure S5). The maximum temperature of the structure for the radiant flux density of ~14 kW/cm$^2$ (used for Raman measurements) is lower than 200 °C, independent of the initial position of the longitudinal plasmonic mode. For an excitation intensity of ~60 kW/cm$^2$, however, the AuNP dimers reach temperatures well beyond 200 °C, at which point the reduction in the thickness of the DNA origami template is expected.[36] This is consistent with our observation of significant gap closure at the higher excitation intensity only.

**Mapping the Gap-Dependent SERS Signal at the Single-Molecule Level.** Nanoscale control of the dimer gap size and the Raman-analyte position is critical for quantitative single-molecule SERS. To further understand the relationship between interparticle distance and SERS intensity, we plotted the correlation between those two (see Figure 3). We used the strong SERS signals of the distinctive Raman peak located at 1180 cm$^{-1}$ as the standard peak. This Raman peak is thought to arise from the polyene C−C−H deformation vibrational mode.[44] Figure 3 displays the experimental data set of SERS signals (red squares) corresponding to either the dimer structures with one dye (a and b) or four dyes (c and d) normalized to the maximum intensity. The data points were derived from measurements of individual DNA origami dimers whose gap sizes were gradually tuned using the previously described plasmonic heating protocol.

For small vibrational frequencies, the Raman-scattering enhancement scales roughly with the fourth power of the electric-field enhancement. Specifically, it is possible to calculate the enhancement factor ($E^4$) as[24]

$$E^4 = |E(\omega_{\mathrm{exc}})|^2 |E(\omega_{\mathrm{R}})|^2 \qquad (1)$$

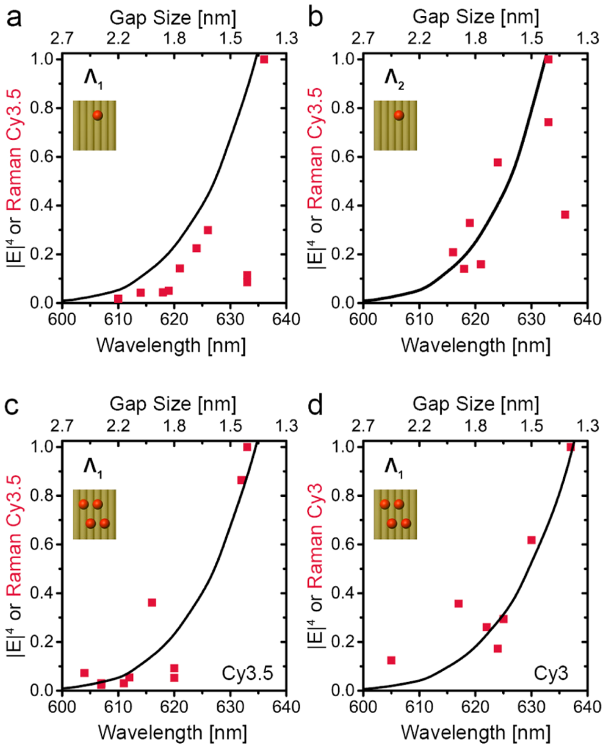

**Figure 3. Mapping the gap-dependent SERS signal. Normalized Raman scattering intensities (red squares) of the vibrational modes of Cy3.5 (a−c) and Cy3 (d) located at $\Lambda_1$ (~1180 cm$^{-1}$) (a, c, and d) and $\Lambda_2$ (~960 cm$^{-1}$) (b) as a function of the peak wavelength of the longitudinal plasmonic mode, which is related to the gap size of the DNA origami AuNP dimer. The theoretical Raman-scattering enhancement is plotted as black lines and normalized with respect to the gap size for which the highest Raman signal was observed. The data points correspond to a collection of individual DNA origami dimers whose gap sizes were gradually tuned using the plasmonic heating protocol.**

where $E(\omega_{\text{exc}})$ and $E(\omega_{\text{R}})$ corresponds to electrical field at the excitation and the particular vibrational shifted frequencies of the Raman signal. We used the generalized Mie theory to analytically calculate the electromagnetic-field enhancement factors generated by the AuNP dimer structure as a function of the gap size. The enhancement factors are extremely sensitive to the specific position of the molecule in the structure. The DNA origami template was designed to either hold one single molecule or four molecules around the geometrical center of the dimer structure. Therefore, to obtain the theoretical SERS enhancements, we calculated the enhancements field directly at the dimer center. The black lines in Figure 3 correspond to the normalized results of this theoretical calculation.

The comparison between the experimental SERS data and the classical electromagnetic theory indicates that the observed enhancement is dominated by the pure electromagnetic effect and that there is no contribution of chemical enhancement, as expected (the dyes are not in direct contact with the AuNP surface). We observed approximately 2 orders of magnitude enhancement in the Raman scattering signal of the single molecules placed in the dimer hot spot when reducing the dimer gap size from ~2.5 to 1.4 nm. The results of multiple DNA origami AuNP dimer structures with different type and amount of dyes located in the hot spot and the different vibrational modes presented in Figures 3 and S6 validate our findings. For the one-dye Cy3.5 dimer structure, we monitored the fingerprints peaks of ~960, 1180, and 1350 cm$^{-1}$ highlighted by orange lines in Figure 2. Independent of the chosen vibrational mode (see Figures 3a,b and S6) or the Raman reporter molecule (see Figure 3c,d), the correlation between Raman scattering intensity signals and dimer gap size are in good agreement.

We finally used fluorescence microscopy techniques to prove that our DNA origami AuNP dimers have indeed exactly one or four dyes incorporated in their structures. We measured temporal sequences of fluorescence images for the one- and four-dye-modified DNA origami structures using total internal reflection (TIR) illumination. We imaged the DNA origami structures prior to AuNP assembly to avoid quenching of the fluorescence signal of the dyes due to energy-transfer processes from the molecule to the metallic particle.[S2] Figure 4 displays two representative fluorescence time traces of single DNA origami structures modified with either one (green line) or four (red line) Cy3.5 molecules. The one and four photobleaching steps of the emission traces confirm the number of dyes located in the nanoparticle hot spot.

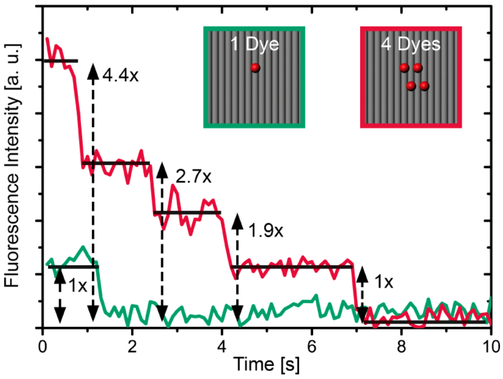

**Figure 4. Single-molecule positioning validated by fluorescence microscopy. Fluorescence intensity trajectories of single DNA origami templates modified with either one (green line) or four (red line) Cy3.5 molecules localized around the geometrical center of the structure. The inset shows a zoom in top view schematic representation of the dye-modified DNA origami designs.**

## CONCLUSIONS

We have devised a reliable approach to produce highly sensitive SERS active materials that enable quantitative single-molecule detection. Plasmonic heating offers the potential of producing highly reproducible nanodimers with tailored plasmonic properties. The optothermal or purely thermal effect is of general nature and can be transferred to other DNA origami-based plasmonic assemblies where small gap sizes are desirable. Our approach combined with the nanometer-precise localization of individual molecules offered by the DNA origami technology is key to outline the gap size dependence of the enhanced electrical field inside the hot spot. We endorse our results by mapping the effect of the enhanced near-field on nanosized hybrids with different numbers of dyes and different Raman reporter molecules.

## METHODS

**Dye Labeling of Oligonucleotides.** For the functionalization of single-stranded DNA oligonucleotides with either Cy3-Azide or Cy3.5-Azide dyes (Baseclick, Germany), the DNA staples were 5′ alkyne modified (Baseclick, Germany). Here we dye labeled directly four different DNA staple sequences, which are part of the DNA origami structure. The subsequent click chemistry labeling of the alkyne-modified oligonucleotides was done *via* the Baseclick Oligo-Click-M (Baseclick, Germany) set. A detailed description can be found in the Oligo-Click-M user manual. After functionalization of the DNA staple strand with the corresponding dye, 3 washing/DNA precipitation steps with 3 M NaOAc and EtOH were performed to remove excess unbound dyes. The concentration of the modified DNA oligonucleotide was determined *via* UV−vis absorption spectroscopy (Nanodrop).

**DNA Origami Folding.** To fold the DNA origami template structure, 10 nM of p7249 scaffold was mixed with 200 nM of each unmodified staple oligonucleotide, 10 mM Tris, 1 mM EDTA (pH 8), and 16 mM $MgCl_2$. The dye-modified staple strands were added to the folding solution in a concentration of 400 nM to ensure incorporation into the origami structure during the folding process. Next, the folding solution was heated up to 65 °C for 20 min to denature all DNA strands and then slowly cooled down to 20 °C over a period of 1.5 days (1 °C per 45 min). For each structure investigated here, a different batch of folding solution was prepared, *e.g.*, for the structure with only one dye-modified staple strand incorporated in the design, the other three possible strands were used in their unmodified version. After folding the DNA origami template structures, they were purified from excess unbound staple strands *via* gel electrophoresis (1.0% agarose gel in 1× TAE buffer (40 mM Tris, 40 mM acetic acid, 1 mM EDTA, pH 8) with 11 mM $MgCl_2$). The bands containing the well-folded structures were cut out of the gel, and the structures recovered by squeezing the cut-out gel piece.

**Concentration and Conjugation with DNA of AuNP.** The as-bought 40 nm AuNP (BBI Solutions, 20 mL) were first concentrated and then functionalized with thiol-modified DNA according to the protocol of Schreiber *et al.*[7] In short, to the AuNP BSPP (bis(*p*-sulfonatophenyl)phenylphosphine dihydrate dipotassium salt, Sigma-Aldrich) was added (8 mg) and stirred for 3 days. Then the AuNP were concentrated by adding sodium chloride (5 M) until the color of the solution turned bluish. Afterward the solution was centrifuged (1600 rcf, 30 min). The supernatant was removed, and a washing step with 2.5 mM BSPP and methanol was performed. After a second centrifugation step, the supernatant was discarded again, and the concentration of the AuNP was determined *via* UV−vis spectroscopy (Nanodrop). In the next step the AuNPs were functionalized with thiolated single-stranded DNA (ssDNA) (thiol-T19, Biomers, Germany). This step has two functions. Fist, the DNA functionalized AuNPs are stabilized against high $MgCl_2$ concentrations, which are used within the DNA origami folding process, and second, the sequence is used for the hybridization to the DNA origami template, which allows a site-specific binding of the AuNP to the template structure. A ratio of ssDNA:AuNP of 4800:1 was used in 1× TAE buffer. The mixture was stirred 3 days on a shaker for incubation. The unbound excess of ssDNA was then removed by centrifugation of the solution with 100 kDa MWCO centrifugal filters (Amicon Ultra, Millipore, 5 min, 9500 rcf, 400 μL 1× TAE buffer). This procedure was repeated eight times to make sure no unbound ssDNA strands are left. To reach a high yield of attached AuNP to the DNA origami, this purification step for the AuNP from unbound ssDNA was done directly before adding the AuNP to the DNA template structure. This way the attachment points (handles) on the template structure are not blocked by unbound ssDNA.

**Functionalization of DNA Origami Template Structure with AuNP.** To functionalize the template DNA origami structure at the designed attachment sites with AuNP, a ration of (DNA-modified AuNP:attachment site) of 4:1 was used. The solution was left for incubation on a shaker over 12 h at 22 °C. As a last step, the solution was gel purified from excess AuNP and eventually occurring agglomerates (0.7% agarose gel in 1× TAE buffer with 11 mM $MgCl_2$) to obtain the final self-assembled dimer AuNP DNA origami structure. The structures were extracted from the gel by cutting out the corresponding gel band and squeezing it while recovering the liquid.

**TEM.** To control the assembly yield, the gel-purified structures were immobilized on a carbon-Formvar-coated TEM grid (Ted Pella) and stained with 1% uranyl acetate for 15 s. To monitor a change in the dimer gap size, nonstained samples were prepared. Therefore, the grids were flushed with 1× TAE $MgCl_2$ instead of uranyl acetate. The TEM measurements were performed with a JEOL JEM-1100 electron microscope at 80 kV. For the gap size monitoring experiments (see Figure S4c), first TEM images of individual structures were taken, then the grids were heated in an oven to 200 °C, and afterward the same structures were imaged again with the TEM.

**Raman and Rayleigh Scattering Microscopy and Spectroscopy.** To perform the dark-field scattering spectroscopy and SERS measurements, the structures were diluted to ∼5 pM in 1× TAE and 11 mM $MgCl_2$ buffer and immobilized on a glass slide, which was then water flushed and nitrogen dried. Single-point Raman and Rayleigh scattering spectra were acquired in an upright Zeiss Axio Scope A1 (Zeiss) microscope equipped with an oil immersion condenser (Zeiss Axiotech 100, NA 1.2−1.4) and using an Acton SP2500 spectrometer (Princeton Instruments). For illumination, a 100 W halogen lamp (Zeiss) was used. The microscope was adapted for Raman experiments by coupling a 612 nm CW randomly polarized laser beam (Carl Zeiss Jena, LGK7411) and using a cleanup 610 ± 10 nm bandpass filter (Laser Components) and 630 nm long pass edge filter (Laser Components, LC-630LP-25) that transmits the Raman-Stokes signal and blocks the resonant scattered laser light. An Epiplan-Neofluar 100× air objective (NA = 0.9, Zeiss) was used to collect the Raman and Rayleigh scattered light and to focus the excitation laser. The acquisition time for the Raman scattering spectra measurements was 100 s per measurement, and the laser power after the objective was measured to be 150 μW, yielding a power density at the focal position of ∼14 kW/cm$^2$. Plasmonic heating of the DNA origami AuNPs dimers was possible by increasing the power density at the focal position to 60 kW/cm$^2$ and irradiating the structure for 10 s. A cross scratch was marked on the top surface of the coverslip to assist subsequent location of the AuNP DNA origami dimers in the SEM. Dark-field imaging was recorded using a digital SLR Canon EOS 550D camera (Canon) with a resolution of 5184 × 3456 using the same objective.

**SEM.** AuNP DNA origami dimers immobilized on the surface of a glass coverslip were imaged in an ULTRA Series Zeiss microscope (Zeiss). Prior to SEM imaging, a 2 nm gold−palladium layer was sputtered on the sample (20 s, 30 mA, 5 cm working distance). Imaging was performed in SE2 and InLens modes at an electron acceleration voltage of 2 kV with a working distance of ∼3 mm.

**Heating (see Figure S4d).** Rayleigh scattering spectra or TEM images of AuNP DNA origami dimers deposited on the surface of a glass coverslip or a TEM grid, respectively, were acquired before and after heating. A programmable hot plate (MR Hei-Tec, Heidolph Instruments) was used to heat the samples at 200 °C for 5 min.

**Fluorescence Microscopy.** Total internal reflection fluorescence (TIRF) imaging experiments were conducted in borosilicate chambers with 0.6 cm$^2$ well area (sticky-Slide VI, Ibidi) with an Olympus IX81 (Olympus) microscope. A solution of ∼40 pM DNA origami structures (functionalized with one, two, three, or four Cy3.5 dyes) was loaded into the microscope chambers immediately after flushing it with 1× TAE buffer (containing 11 mM $MgCl_2$). Cy3.5 fluorophores were excited with a CW TEM$_{00}$ 561 nm laser (Cobolt Jive, Cobolt AB) coupled and collimated into the microscope. A beam splitter CMR-U-M3TIR-405-488-561 (AHF) was used to reflect the excitation light into the oil immersion TIRF objective (100×, NA1.45, Olympus, Plan APO). The fluorescent signal was passed through a 600 nm long pass filter (Thorlabs) and collected with an iXon Ultra 897 EM-CCD (Andor) with 512 × 512 pixels of 16 μm × 16 μm size, operated at 100 ms per frame. Fluorescence intensity temporal time traces of single DNA origami structures were obtained with a homemade MATLAB routine.[53]

DOI: 10.1021/acsnano.6b05276
ACS Nano 2016, 10, 9809−9815

**Numerical Simulations.** Optical properties of AuNP dimers were calculated with numerical solvers of the generalized Mie-Theory, implemented in Fortran.[50,51] Two spheres with a diameter of 40 nm were placed with variable distance in a surrounding medium. The refractive index of the two particles was interpolated values of the data set obtained by Johnson and Christy.[54] For the surrounding medium, an effective medium approach was used by matching the transverse plasmon mode, which is not dependent on the gap size, to the simulated plasmon peak. A value of $n = 1.4$ matched the experimental values best. The electric field was evaluated in the center between the two spheres. All simulations were averaged over both excitation parallel and perpendicular to the dimer axis. For calculating the heat profile of the dimers, the absorbed laser power was calculated with homemade Mathematica scripts from the absorption cross-section obtained from the previous simulations. The steady-state temperature of the dimers upon laser illumination was simulated with the COMSOL Multiphysics 5.2 Heat Transfer Module.

## ASSOCIATED CONTENT

### Ⓢ Supporting Information

The Supporting Information is available free of charge on the ACS Publications website at DOI: 10.1021/acsnano.6b05276.

Experimental details and data (PDF)

## AUTHOR INFORMATION

### Corresponding Authors

*E-mail: tim.liedl@physik.lmu.de.
*E-mail: t.lohmueller@lmu.de.

### Author Contributions

T.L. and T.L. conceived the idea and contributed to the design of the experiments. T.L, S.S., and E.M.R. cowrote the manuscript. A.J.T. and R.S. designed the DNA origami structure. E.M.R. designed and synthesized all the AuNP DNA origami dimer structures and conducted the TEM and SEM characterization. S.S. and P.U. performed the microscopy and spectroscopy experiments and analyzed the data. P.U. performed the numerical simulations.

### Author Contributions

⊥These authors contributed equally.

### Notes

The authors declare no competing financial interest.

## ACKNOWLEDGMENTS

This work has been supported by the Volkswagen Foundation, the ERC through the Advanced Investigator Grant "HYMEM" and the Starting Grant "ORCA" and the DFG through the SFB 1032 project A6 and A8. We acknowledge Prof. Jochen Feldmann, Paul Kühler, and Arzhang Ardavan for helpful discussions.

## REFERENCES

(1) Rothemund, P. W. K. Folding DNA to Create Nanoscale Shapes and Patterns. *Nature* **2006**, *440*, 297−302.

(2) Douglas, S. M.; Dietz, H.; Liedl, T.; Hogberg, B.; Graf, F.; Shih, W. M. Self-Assembly of DNA into Nanoscale Three-Dimensional Shapes. *Nature* **2009**, *459*, 414−418.

(3) Hung, A. M.; Micheel, C. M.; Bozano, L. D.; Osterbur, L. W.; Wallraff, G. M.; Cha, J. N. Large-Area Spatially Ordered Arrays of Gold Nanoparticles Directed by Lithographically Confined DNA Origami. *Nat. Nanotechnol.* **2010**, *5*, 121−126.

(4) Bui, H.; Onodera, C.; Kidwell, C.; Tan, Y.; Graugnard, E.; Kuang, W.; Lee, J.; Knowlton, W. B.; Yurke, B.; Hughes, W. L. Programmable Periodicity of Quantum Dot Arrays with DNA Origami Nanotubes. *Nano Lett.* **2010**, *10*, 3367−3372.

(5) Maune, H. T.; Han, S.-p.; Barish, R. D.; Bockrath, M.; Goddard, W. A., III; Rothemund, P. W. K.; Winfree, E. Self-Assembly of Carbon Nanotubes into Two-Dimensional Geometries Using DNA Origami Templates. *Nat. Nanotechnol.* **2010**, *5*, 61−66.

(6) Kuzyk, A.; Laitinen, K. T.; Törmä, P. DNA Origami as a Nanoscale Template for Protein Assembly. *Nanotechnology* **2009**, *20*, 235305.

(7) Schreiber, R.; Do, J.; Roller, E.-M.; Zhang, T.; Schuller, V. J.; Nickels, P. C.; Feldmann, J.; Liedl, T. Hierarchical Assembly of Metal Nanoparticles, Quantum Dots and Organic Dyes Using DNA Origami Scaffolds. *Nat. Nanotechnol.* **2014**, *9*, 74−78.

(8) Bell, N. A. W.; Engst, C. R.; Ablay, M.; Divitini, G.; Ducati, C.; Liedl, T.; Keyser, U. F. DNA Origami Nanopores. *Nano Lett.* **2012**, *12*, 512−517.

(9) Wei, R.; Martin, T. G.; Rant, U.; Dietz, H. DNA Origami Gatekeepers for Solid-State Nanopores. *Angew. Chem., Int. Ed.* **2012**, *51*, 4864−4867.

(10) Ke, Y.; Lindsay, S.; Chang, Y.; Liu, Y.; Yan, H. Self-Assembled Water-Soluble Nucleic Acid Probe Tiles for Label-Free Rna Hybridization Assays. *Science* **2008**, *319*, 180−183.

(11) Linko, V.; Eerikainen, M.; Kostiainen, M. A. A Modular DNA Origami-Based Enzyme Cascade Nanoreactor. *Chem. Commun.* **2015**, *51*, 5351−5354.

(12) Surana, S.; Shenoy, A. R.; Krishnan, Y. Designing DNA Nanodevices for Compatibility with the Immune System of Higher Organisms. *Nat. Nanotechnol.* **2015**, *10*, 741−747.

(13) Smith, D.; Schüller, V.; Engst, C.; Rädler, J.; Liedl, T. Nucleic Acid Nanostructures for Biomedical Applications. *Nanomedicine* **2013**, *8*, 105−121.

(14) Zhao, Y.-X.; Shaw, A.; Zeng, X.; Benson, E.; Nyström, A. M.; Högberg, B. DNA Origami Delivery System for Cancer Therapy with Tunable Release Properties. *ACS Nano* **2012**, *6*, 8684−8691.

(15) Schüller, V. J.; Heidegger, S.; Sandholzer, N.; Nickels, P. C.; Suhartha, N. A.; Endres, S.; Bourquin, C.; Liedl, T. Cellular Immunostimulation by Cpg-Sequence-Coated DNA Origami Structures. *ACS Nano* **2011**, *5*, 9696−9702.

(16) Jungmann, R.; Avendano, M. S.; Woehrstein, J. B.; Dai, M.; Shih, W. M.; Yin, P. Multiplexed 3d Cellular Super-Resolution Imaging with DNA-Paint and Exchange-Paint. *Nat. Methods* **2014**, *11*, 313−318.

(17) Steinhauer, C.; Jungmann, R.; Sobey, T. L.; Simmel, F. C.; Tinnefeld, P. DNA Origami as a Nanoscopic Ruler for Super-Resolution Microscopy. *Angew. Chem., Int. Ed.* **2009**, *48*, 8870−8873.

(18) Roller, E.-M.; Khorashad, L. K.; Fedoruk, M.; Schreiber, R.; Govorov, A. O.; Liedl, T. DNA-Assembled Nanoparticle Rings Exhibit Electric and Magnetic Resonances at Visible Frequencies. *Nano Lett.* **2015**, *15*, 1368−1373.

(19) Kuzyk, A.; Schreiber, R.; Fan, Z.; Pardatscher, G.; Roller, E.-M.; Hogele, A.; Simmel, F. C.; Govorov, A. O.; Liedl, T. DNA-Based Self-Assembly of Chiral Plasmonic Nanostructures with Tailored Optical Response. *Nature* **2012**, *483*, 311−314.

(20) Kuzyk, A.; Schreiber, R.; Zhang, H.; Govorov, A. O.; Liedl, T.; Liu, N. Reconfigurable 3d Plasmonic Metamolecules. *Nat. Mater.* **2014**, *13*, 862−866.

(21) Acuna, G. P.; Möller, F. M.; Holzmeister, P.; Beater, S.; Lalkens, B.; Tinnefeld, P. Fluorescence Enhancement at Docking Sites of DNA-Directed Self-Assembled Nanoantennas. *Science* **2012**, *338*, 506−510.

(22) Giannini, V.; Fernández-Domínguez, A. I.; Heck, S. C.; Maier, S. A. Plasmonic Nanoantennas: Fundamentals and Their Use in Controlling the Radiative Properties of Nanoemitters. *Chem. Rev.* **2011**, *111*, 3888−3912.

(23) Jiang; Bosnick, K.; Maillard, M.; Brus, L. Single Molecule Raman Spectroscopy at the Junctions of Large Ag Nanocrystals. *J. Phys. Chem. B* **2003**, *107*, 9964−9972.

(24) Novotny, L.; Hecht, B. *Principles of Nano-Optics*; Cambridge University Press: Cambridge, U.K., 2012.

(25) Prinz, J.; Schreiber, B.; Olejko, L.; Oertel, J.; Rackwitz, J.; Keller, A.; Bald, I. DNA Origami Substrates for Highly Sensitive Surface-Enhanced Raman Scattering. *J. Phys. Chem. Lett.* **2013**, *4*, 4140−4145.

(26) Kühler, P.; Roller, E.-M.; Schreiber, R.; Liedl, T.; Lohmüller, T.; Feldmann, J. Plasmonic DNA-Origami Nanoantennas for Surface-Enhanced Raman Spectroscopy. *Nano Lett.* **2014**, *14*, 2914−2919.

(27) Pilo-Pais, M.; Watson, A.; Demers, S.; LaBean, T. H.; Finkelstein, G. Surface-Enhanced Raman Scattering Plasmonic Enhancement Using DNA Origami-Based Complex Metallic Nano-structures. *Nano Lett.* **2014**, *14*, 2099−2104.

(28) Thacker, V. V.; Herrmann, L. O.; Sigle, D. O.; Zhang, T.; Liedl, T.; Baumberg, J. J.; Keyser, U. F. DNA Origami Based Assembly of Gold Nanoparticle Dimers for Surface-Enhanced Raman Scattering. *Nat. Commun.* **2014**, *5*, 3448.

(29) Maier, S. A. *Plasmonics: Fundamentals and Applications*. Springer Science & Business Media: New York, 2007.

(30) Wang, Y.; Irudayaraj, J. Surface-Enhanced Raman Spectroscopy at Single-Molecule Scale and Its Implications in Biology. *Philos. Trans. R. Soc., B* **2013**, *368*, 20120026.

(31) Lim, D.-K.; Jeon, K.-S.; Kim, H. M.; Nam, J.-M.; Suh, Y. D. Nanogap-Engineerable Raman-Active Nanodumbbells for Single-Molecule Detection. *Nat. Mater.* **2010**, *9*, 60−67.

(32) Lee, H.; Lee, J.-H.; Jin, S. M.; Suh, Y. D.; Nam, J.-M. Single-Molecule and Single-Particle-Based Correlation Studies between Localized Surface Plasmons of Dimeric Nanostructures with ∼ 1 Nm Gap and Surface-Enhanced Raman Scattering. *Nano Lett.* **2013**, *13*, 6113−6121.

(33) Lee, J.-H.; You, M.-H.; Kim, G.-H.; Nam, J.-M. Plasmonic Nanosnowmen with a Conductive Junction as Highly Tunable Nanoantenna Structures and Sensitive, Quantitative and Multiplexable Surface-Enhanced Raman Scattering Probes. *Nano Lett.* **2014**, *14*, 6217−6225.

(34) Prinz, J.; Heck, C.; Ellerik, L.; Merk, V.; Bald, I. DNA Origami Based Au-Ag-Core-Shell Nanoparticle Dimers with Single-Molecule Sers Sensitivity. *Nanoscale* **2016**, *8*, 5612−5620.

(35) Urban, A. S.; Fedoruk, M.; Nedev, S.; Lutich, A.; Lohmueller, T.; Feldmann, J. Shrink-to-Fit Plasmonic Nanostructures. *Adv. Opt. Mater.* **2013**, *1*, 123−127.

(36) Pillers, M. A.; Lieberman, M. Thermal Stability of DNA Origami on Mica. *J. Vac. Sci. Technol., B* **2014**, *32*, 040602.

(37) Kim, H.; Surwade, S. P.; Powell, A.; O'Donnell, C.; Liu, H. Stability of DNA Origami Nanostructure under Diverse Chemical Environments. *Chem. Mater.* **2014**, *26*, 5265−5273.

(38) Baffou, G.; Quidant, R. Thermo-Plasmonics: Using Metallic Nanostructures as Nano-Sources of Heat. *Laser Photonics Rev.* **2013**, *7*, 171−187.

(39) Govorov, A. O.; Richardson, H. H. Generating Heat with Metal Nanoparticles. *Nano Today* **2007**, *2*, 30−38.

(40) Etchegoin, P. G.; Le Ru, E. C. Resolving Single Molecules in Surface-Enhanced Raman Scattering within the Inhomogeneous Broadening of Raman Peaks. *Anal. Chem.* **2010**, *82*, 2888−2892.

(41) Yu, N.-T.; Nie, S.; Lipscomb, L. A. Surface-Enhanced Hyper-Raman Spectroscopy with a Picosecond Laser. New Vibrational Information for Non-Centrosymmetric Carbocyanine Molecules Adsorbed on Colloidal Silver. *J. Raman Spectrosc.* **1990**, *21*, 797−802.

(42) Yang, J. P.; Callender, R. H. The Resonance Raman Spectra of Some Cyanine Dyes. *J. Raman Spectrosc.* **1985**, *16*, 319−321.

(43) Sato, H.; Kawasaki, M.; Kasatani, K.; Katsumata, M.-a. Raman Spectra of Some Indo-, Thia- and Selena-Carbocyanine Dyes. *J. Raman Spectrosc.* **1988**, *19*, 129−132.

(44) Lednev, I. K.; Fomina, M. V.; Gromov, S. P.; Stanislavsky, O. B.; Alfimov, M. V.; Moore, J. N.; Hester, R. E. A Raman Spectroscopic Study of Indolinium Steryl Dyes. *Spectrochim. Acta, Part A* **1992**, *48*, 931−937.

(45) Movileanu, L.; Benevides, J. M.; Thomas, G. J. Temperature Dependence of the Raman Spectrum of DNA. Ii. Raman Signatures of Premelting and Melting Transitions of Poly(Da)·Poly(Dt) and Comparison with Poly(Da-Dt)·Poly(Da-Dt)*. *Biopolymers* **2002**, *63*, 181−194.

(46) Barhoumi, A.; Zhang, D.; Tam, F.; Halas, N. J. Surface-Enhanced Raman Spectroscopy of DNA. *J. Am. Chem. Soc.* **2008**, *130*, 5523−5529.

(47) Treffer, R.; Lin, X.; Bailo, E.; Deckert-Gaudig, T.; Deckert, V. Distinction of Nucleobases − a Tip-Enhanced Raman Approach. *Beilstein J. Nanotechnol.* **2011**, *2*, 628−637.

(48) Chandra, A. K.; Nguyen, M. T.; Zeegers-Huyskens, T. Theoretical Study of the Interaction between Thymine and Water. Protonation and Deprotonation Enthalpies and Comparison with Uracil. *J. Phys. Chem. A* **1998**, *102*, 6010−6016.

(49) Xu, L.-J.; Lei, Z.-C.; Li, J.; Zong, C.; Yang, C. J.; Ren, B. Label-Free Surface-Enhanced Raman Spectroscopy Detection of DNA with Single-Base Sensitivity. *J. Am. Chem. Soc.* **2015**, *137*, 5149−5154.

(50) Ringler, M.; Schwemer, A.; Wunderlich, M.; Nichtl, A.; Kürzinger, K.; Klar, T. A.; Feldmann, J. Shaping Emission Spectra of Fluorescent Molecules with Single Plasmonic Nanoresonators. *Phys. Rev. Lett.* **2008**, *100*, 203002.

(51) Xu, Y.-l.; Wang, R. T. Electromagnetic Scattering by an Aggregate of Spheres: Theoretical and Experimental Study of the Amplitude Scattering Matrix. *Phys. Rev. E: Stat. Phys., Plasmas, Fluids, Relat. Interdiscip. Top.* **1998**, *58*, 3931−3948.

(52) Anger, P.; Bharadwaj, P.; Novotny, L. Enhancement and Quenching of Single-Molecule Fluorescence. *Phys. Rev. Lett.* **2006**, *96*, 113002.

(53) Simoncelli, S.; Roberti, M. J.; Araoz, B.; Bossi, M. L.; Aramendía, P. F. Mapping the Fluorescence Performance of a Photochromic−Fluorescent System Coupled with Gold Nanoparticles at the Single-Molecule−Single-Particle Level. *J. Am. Chem. Soc.* **2014**, *136*, 6878−6880.

(54) Johnson, P. B.; Christy, R. W. Optical Constants of the Noble Metals. *Phys. Rev. B* **1972**, *6*, 4370−4379.

DOI: 10.1021/acsnano.6b05276
*ACS Nano* 2016, 10, 9809−9815

# B. Appendix

## B.1. Supporting Information for P1

### DNA-Assembled Nanoparticle Rings Exhibit Electric and Magnetic Resonances at Visible Frequencies

by

Eva-Maria Roller, Larousse Khosravi Khorashad, Michael Fedoruk, Robert Schreiber, Alexander O. Govorov, and Tim Liedl

published in Nano Letters, 15, 1368 - 1373 (2015).

## Supporting Information

# DNA-assembled nanoparticle rings exhibit electric and magnetic resonances at visible frequencies

*Eva-Maria Roller*[1], *Larousse Khosravi Khorashad*[2], *Michael Fedoruk*[1], *Robert Schreiber*[3], *Alexander O. Govorov*[2] *and Tim Liedl*[1*]

[1]Fakultät für Physik and Center for Nanoscience, Ludwig-Maximilians-Universität München,

Geschwister-Scholl-Platz 1, 80539 Munich, Germany

[2]Department of Physics and Astronomy, Ohio University, Athens, Ohio 45701, USA

[3]Clarendon Laboratory, Department of Physics, University of Oxford, Parks Road,

Oxford OX1 3PU, UK

## Materials and Methods:

### Supplementary Note S1. Assembly of plasmonic ring structures.

*DNA origami folding.* For the DNA origami ring template structure 10 nM of p8634 scaffold, 100 nM of each staple, 10 mM Tris, 1 mM EDTA (pH 8) and 16 mM $MgCl_2$ were mixed together. This solution was then heated up to 65 °C for 20 min to denature all DNA strands and afterwards slowly cooled down to 25 °C over the course of 40 hours (1 °C per 1 hour). According to the desired design, various sets of elongated handle strands were chosen for nanoparticle attachment (see table 1). After folding, the DNA origami template structures were purified from the excess staple strands by running the samples on a 1.0 % agarose gel in 0.5x TBE buffer with 11 mM $MgCl_2$. The bands containing the structures were excised with a razor blade from the gel and then centrifuged with Freeze 'N Squeeze spin columns (BioRad) at 2.600 rcf for 8 min.

*Concentration of AuNPs.* For the functionalization of the DNA-modified AuNPs (10, 20, 30 and 40 nm, 20 ml, BBI Solutions) with single-stranded DNA sequences, the protocol of Schreiber *et al*.[1] was used with minor changes: First the AuNPs were stirred for three days after adding 8 mg of BSPP (Bis(*p*-sulfonatophenyl)phenylphosphine dihydrate dipotassium salt, Sigma-Aldrich). To concentrate the particles, sodium chloride (5 M) was added until the color of the solution changed from red to bluish. Afterwards the solution was centrifugated at 1,600 rcf for 30 min and the supernatant was removed. After dissolving the AuNPs again in BSPP solution (0.8 ml, 2.5 mM in $H_2O$) and an equal amount of methanol, the mixtures was centrifugated one more time (1.600 rcf, 30 min). The supernatant was removed and the concentrated AuNPs were dissolved in BSPP solution (0.25 ml, 2.5 mM in $H_2O$). An absorption measurement via UV-Vis spectroscopy (Nanodrop) at a wavelength of 530 nm was performed to determine the concentration of the particles ($c = absorbance/(\varepsilon * d)$, with the molar extinction coefficient for 40 nm AuNP $\varepsilon = 8.42 * 10^9$ and path length $d$).

*AuNP-DNA conjugation.* To stabilize the AuNPs against high $MgCl_2$ concentration that are needed during the DNA origami folding process and to cover the AuNPs with DNA strands for the hybridization to the DNA origami template, the particles were conjugated with thiolated single-stranded DNA (ssDNA) strands (biomers.net, HPLC purified). To reduce possible disulfide bonds, the thiolated ssDNA was incubated with TCEP (Tris(2-carboxyethyl)phosphine hydrochloride), Sigma-Aldrich; 20 mM final concentration) for 30 min. AuNPs and thiolated oligonucleotides were mixed together in 0.5x TBE buffer at a ratio of DNA:AuNP = 4800:1 for 40 nm AuNPs and stirred over 3 days on a shaker. To get rid of the excess of unbound ssDNA strands the mixture was centrifugated with 100 kDa MWCO centrifugal filters (Amicon Ultra, Millipore, 10 min, 8,000 rcf) followed by 8 additional spinning steps with 400 µl of 0.5x TBE buffer added to the filter before each centrifugation step. The centrifugation was done directly before adding the AuNPs to the DNA origami structures so that the least possible amount of unbound oligonucleotides – which can block the attachment sites on the DNA origami structure – are present during the conjugation.

*AgNP-DNA conjugation.* The preparation of silver nanoparticle (AgNP) followed with minor changes the protocol of Pal et al.[2, 3] The AgNP (20 nm, BBI Solutions) were concentrated by centrifugation with 100 kDa MWCO centrifugal filter (8,000 rcf, 5 min). Thiolated DNA (biomers.net, HPLC purified) was added in a ratio of DNA:AgNP = 1200:1 and the solution was incubated on a shaker over night. Then the pH was lowered to pH 3 by adding citrate-HCl buffer to a final concentration of 10 mM. After 30 min of incubation, NaCl was added to a final concentration of 30 mM. Then the pH was raised again by adding 10x the sample volume of 0.5x TBE buffer. The excess of unbound DNA strands was removed by 8 times centrifugation of the mixture with 100 kDa MWCO centrifugal filters (Amicon Ultra, Millipore, 10 min 8,000 rcf).

*Functionalization of DNA origami structures with AuNPs (AgNPs).* The stability of the DNA conjugated AuNPs was tested by adding a droplet of AuNPs to a solution containing 20 mM of $MgCl_2$. If no color change is observed, the particles are fully covered with DNA and ready for the DNA origami structure functionalization. The DNA-covered AuNPs (AgNPs) were mixed together with the purified DNA origami template structure in a ratio of 3 AuNPs (AgNPs) per attachment site on the DNA origami structure. A four particle ring structure, for example, offers 4 attachment sites and thus the ratio of AuNPs:DNAorigami is 12:1. This excess of NPs is necessary to avoid cross-linking of different DNA origami structures. The solution was kept on a shaker over 24 h at 22 °C. After attachment of the AuNPs (AgNPs) to the DNA origami structures the assembled plasmonic ring structures were purified from excess of unbound AuNPs (AgNPs) via 0.7 % agarose gel in 0.5x TBE buffer with 11 mM $MgCl_2$. The structures were extracted from the gel by excising the bands and centrifuging the gel pieces with Freeze ‘N Squeeze spin columns (BioRad) at 2.600 rcf for 8 min.

*Transmission electron microscopy (TEM) grid preparation, dark-field scattering spectroscopy and scanning electron microscopy (SEM).* The gel-purified structures were immobilized on a carbon-formvar-coated grid and stained with 1 % uranyl acetate for 20 seconds. The TEM measurements were performed using a JEOL JEM-1100 electron microscope at 80 kV. For dark-field scattering spectroscopy the gel-purified structures were 100x diluted with 0.5x TBE buffer and 11 mM $MgCl_2$ and deposited on a glass slide. First, scattering spectroscopy was performed in liquid in a dark field configuration using an oil immersion dark field condenser with NA=1.2 (Zeiss) and Achroplan 100x water objective (NA=1.0, Zeiss). After drying the samples with a nitrogen flow, the samples were further studied with an Epiplan-Neofular 100x air objective (NA=0.9, Zeiss). The illumination source was a 100 W halogen lamp (Zeiss) and the spectra were detected with an Acton SP2500 spectrometer (Princeton Instruments). Subsequently the glass slides were carbon sputtered and SEM images were taken with a Gemini Ultra Plus SEM (Zeiss). The absorption spectrum of the gel-purified structures in solution was taken with a Jasco V-650 spectrometer.

**Supplementary Note S2. CaDNAno[4] image of the DNA origami ring structure.** The scaffold path (blue), the staple oligonucleotides (grey), the connection staples to close the ring (turquoise) and the attachment sites (red and orange, encircled in red) are shown in this schematic picture. The folded ring template structure has a diameter of around 60 nm and offers 14 attachment sites for AuNPs or AgNPs, each site consisting of 5 single stranded 15 nucleotide (nt) long extensions on the 3' end of the origami staples. The AuNPs are bound via hybridization to the DNA origami template by covering them with ssDNA of complementary sequence to the attachment sites. To specifically attach AuNPs of different sizes as shown in Fig 1b of the manuscript, different DNA extension sequences were used for the attachment sites as well as for covering the nanoparticles.

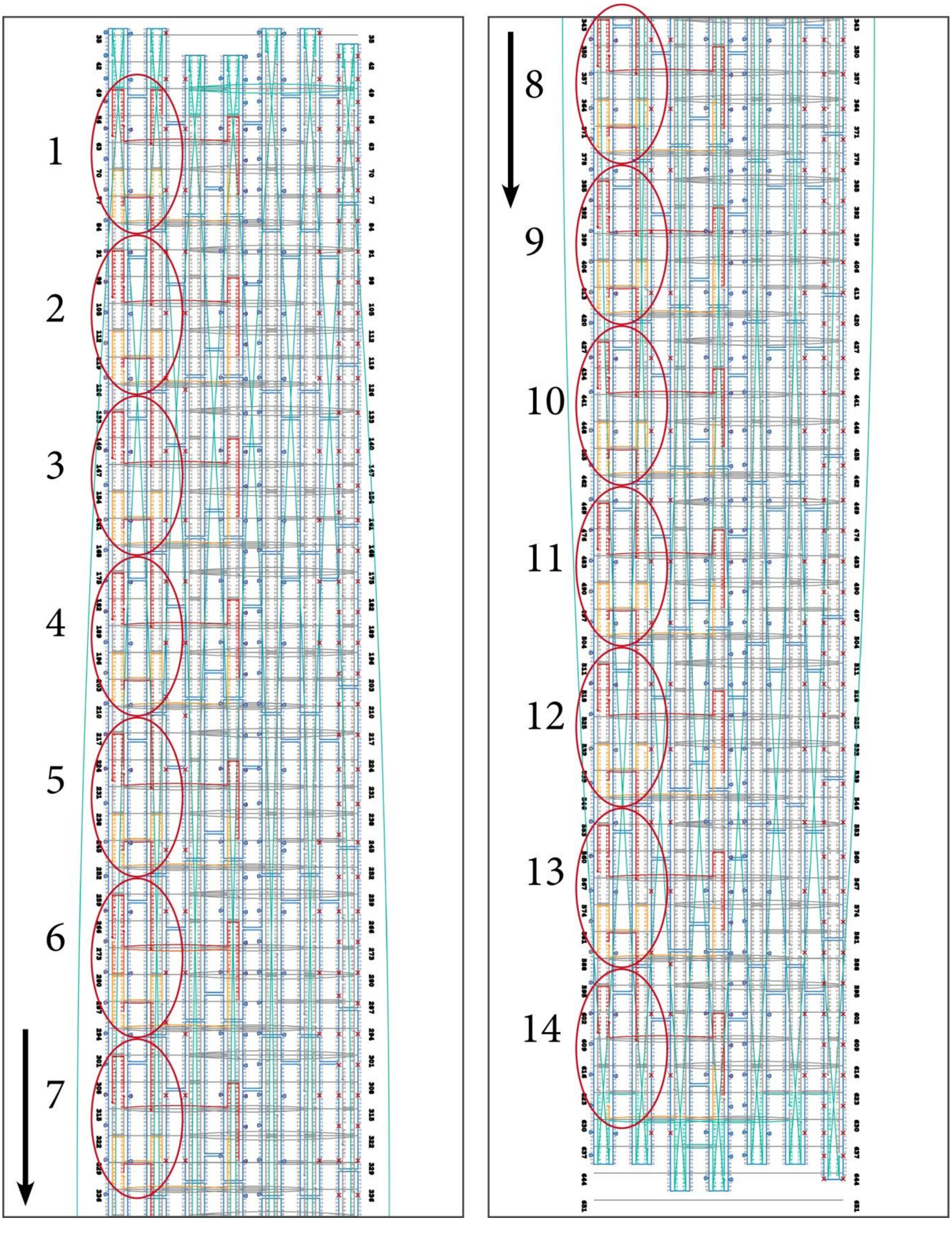

**Supplementary Note S3. Activated attachment sites on the DNA origami template for different plasmonic ring structures.** The number of the attachment sites and the colors correspond to the definition given in S2. All red attachment sites consist of 3 elongated ssDNA strands; all orange attachment sites consist of 2 elongated ssDNA strands (this is due to design and space considerations). All in all the structure offers specific addressable attachment sites every 21 base pairs.

| **Attachment site #** | **SRR** | **8x AuNP Dimer** | **8 AuNP ring** | **6 AuNP ring** | **5 AuNP ring** | **4 AuNP ring** |
|---|---|---|---|---|---|---|
| **1** | | | **orange** | **orange** | **red**<br>**orange** | **orange** |
| **2** | | **red**<br>**orange** | **red** | **red** | | **red**<br>**orange** |
| **3** | **red**<br>**orange** | **red**<br>**orange** | **orange** | | | |
| **4** | **red**<br>**orange** | | | **red**<br>**orange** | **red**<br>**orange** | |
| **5** | **red**<br>**orange** | **orange** | **red**<br>**orange** | | | **red**<br>**orange** |
| **6** | **red**<br>**orange** | **red**<br>**orange** | | **orange** | | **red** |
| **7** | **red**<br>**orange** | **red** | **red** | **red** | **red** | |
| **8** | **red**<br>**orange** | | **orange** | | | |
| **9** | **red**<br>**orange** | **red**<br>**orange** | **red** | **red** | | **red**<br>**orange** |
| **10** | **red**<br>**orange** | **red**<br>**orange** | **red** | | **red** | |
| **11** | **red**<br>**orange** | | | **red**<br>**orange** | | |
| **12** | **red**<br>**orange** | **orange** | **red**<br>**orange** | | **orange** | **orange** |
| **13** | | **red**<br>**orange** | | **orange** | **red** | **red**<br>**orange** |
| **14** | | **red** | **red** | **red** | | |

**Supplementary Note S4. CaDNAno image of the DNA origami ring structure with four attachment sites for (metal) nanoparticles.** The attachment sites used for a ring structure consisting of four metal nanoparticles are shown (red and orange, encircled in red).

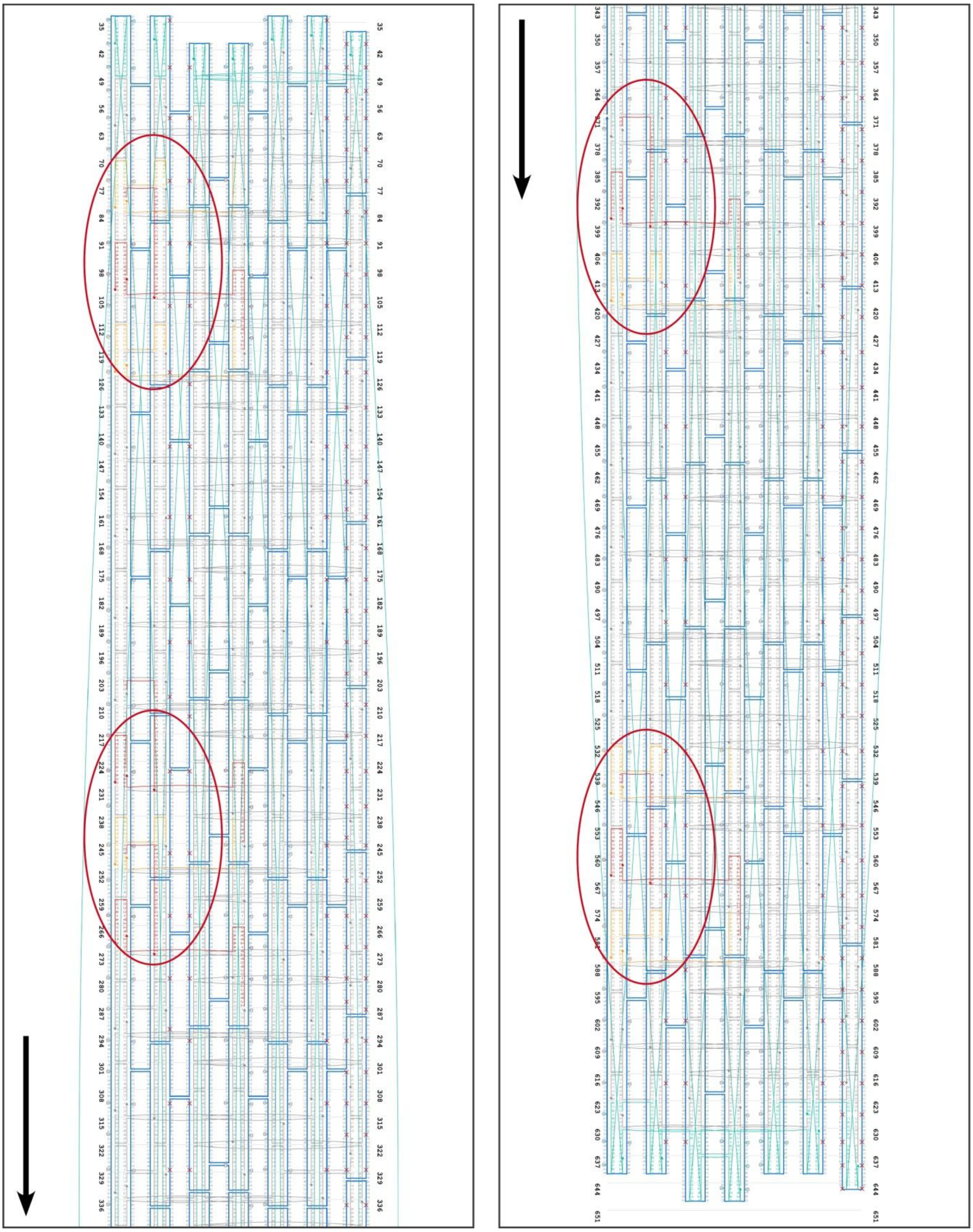

**Supplementary Note S5. a,** Purification of the plasmonic ring structures by gel electrophoresis from free AuNPs and smaller aggregates. **b,** Wide field TEM image of plasmonic ring structures with four 40 nm AuNPs attached. Scale bar 500 nm.

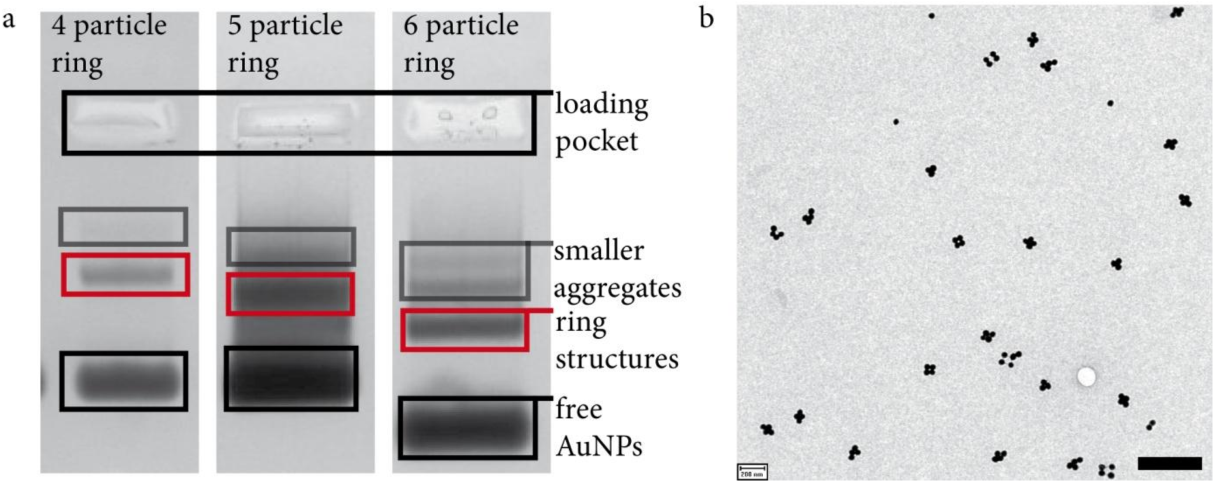

**Supplementary Note S6. a,** Wide field TEM images of plasmonic ring structures with four 40 nm AuNPs attached. **b,** Statistics of the number of bound AuNPs per four-particle-ring-structure after gel purification. The four ring assembly yield was determined by electron microscopy analysis. Out of the analyzed structures up to 68 % were assembled with four particles attached, 10 % of the structures are consisting out of five and more particles or smaller aggregates and 22 % have only three or two particles attached.

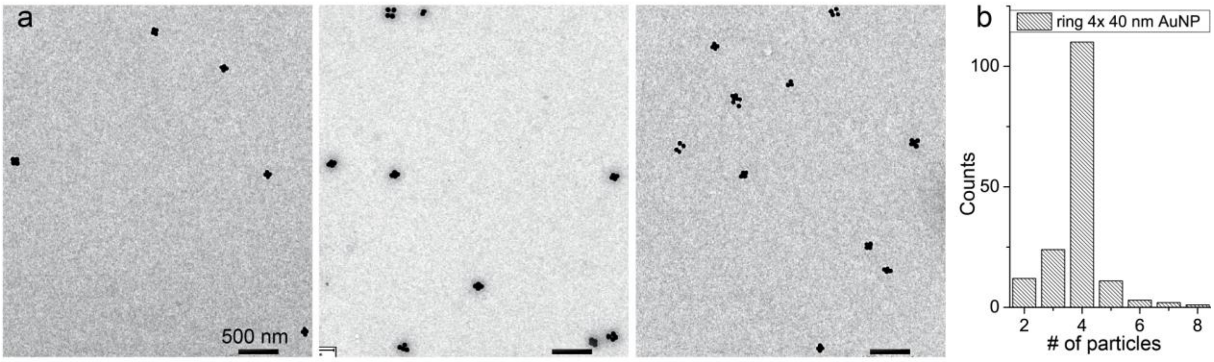

**Supplementary Note S7. a,** Additional TEM images of ring structures with four 40 nm AuNPs attached. **b,** The gap size (surface-to-surface distances) of 256 neighbouring AuNPs was measured, the median value is 1.7 nm, the mean value 2.4 nm (±1.9 nm SD). Structures where the AuNPs are arranged on the outside of the DNA origami were excluded from the measurements (15 %). Two of such structures are shown in the lower right part of panel a. The larger gap sizes (more than 4 nm) appear in structures which were immobilized on the TEM grid in a slightly asymmetric arrangement due to the distortion during the adsorption and drying process on the TEM grids (*cf.* the two examples in the lower of panel a).

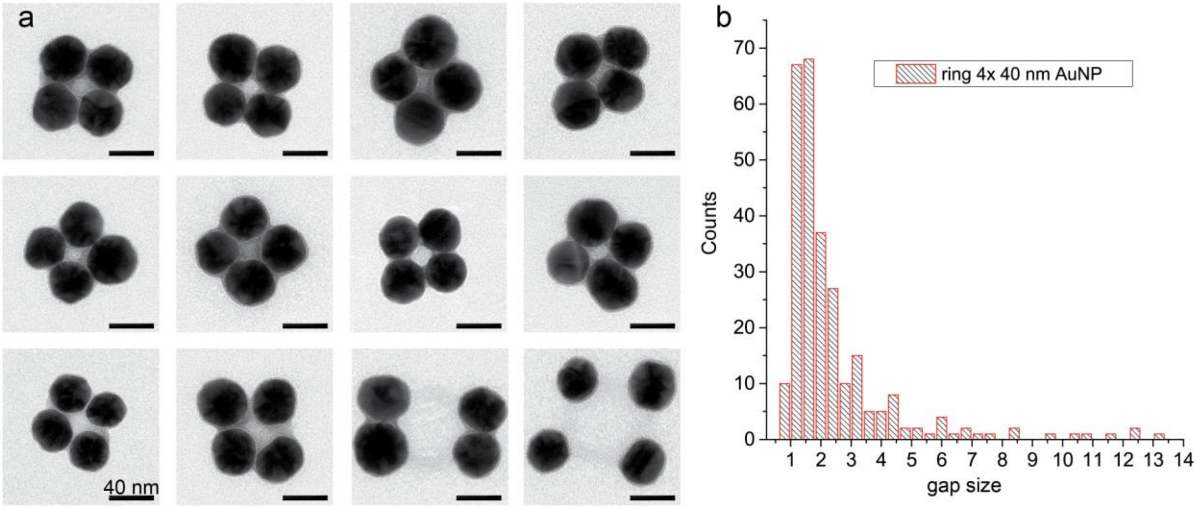

**Supplementary Note S8.** Wide field TEM and zoom in images of plasmonic ring structures with **a,** five 30 nm AuNPs and **b,** six 30 nm AuNPs attached. **c,** The assembly yield was determined by electron microscopy for five bound 30 nm AuNPs to 73 % and for six bound 30 nm AuNPs to 65 %. Structures with a distorted geometry, which can occur during the adsorption and drying process on the TEM grids, are shown in the lower right of **a** and **b**.

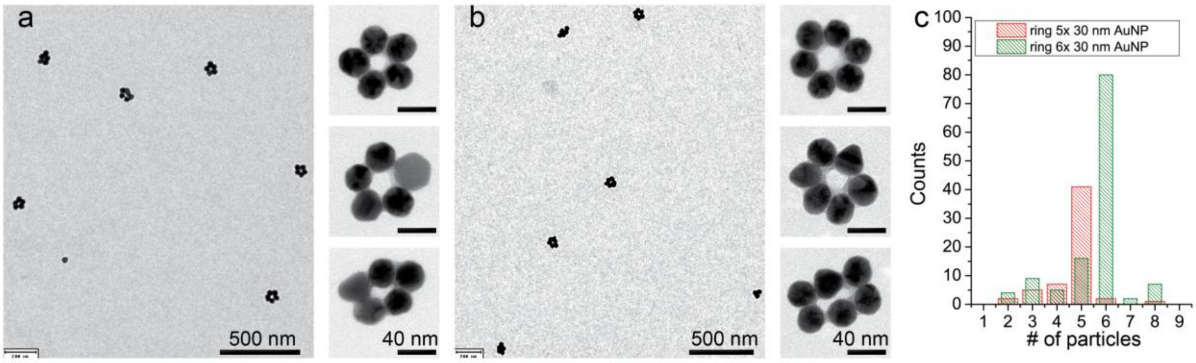

**Supplementary Note S9.** Wide field TEM images of a rings with eight 10 nm AuNPs attached, **b,** rings with 10 nm AuNPs attached in a SRR conformation, **c,** rings with eight 10 nm AuNPs attached in pairs of two and **d,** additional images of asymmetric ring structures with three 40 nm AuNPs and one 20 nm AgNP, **e,** five 20 nm AuNPs and one 30 nm AuNP. Note that for the latter two particle arrangements the concentrations were too low to find more than one structure per wide field image.

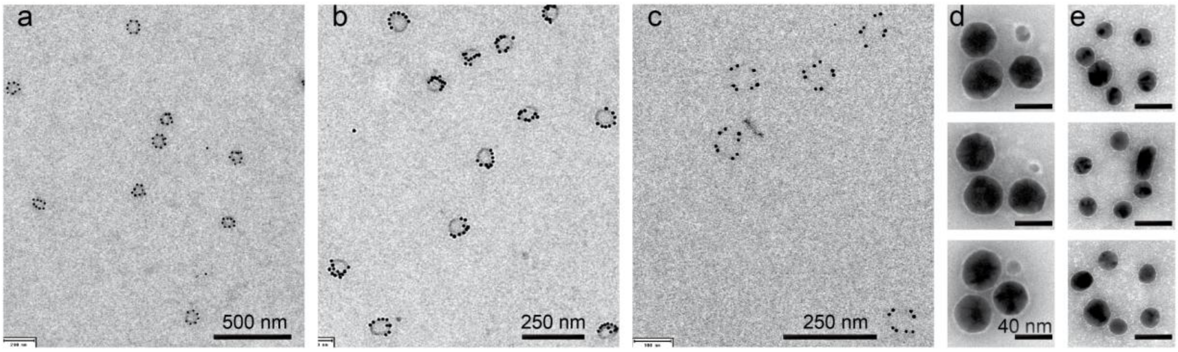

**Supplementary Note S10. Additional dark-field scattering spectra and corresponding simulations.** Scattering spectra of single structures immobilized on glass substrate (**a, d**) and corresponding simulation (**b, e**). The simulation of the surface charge distribution for all peaks as well as the electric and magnetic field distribution (**c, f**) reveals the origin of the peaks at dipole, multi-polar and magnetic interaction.

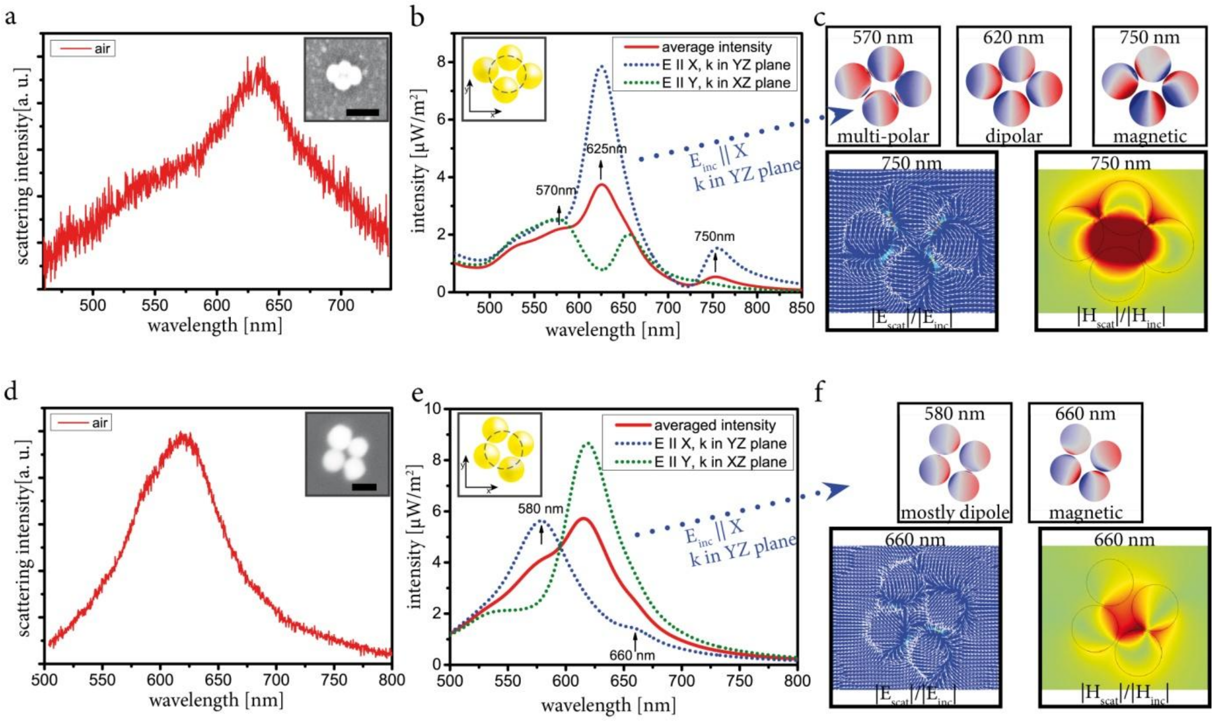

**Supplementary Note S11. a, Dark-field scattering spectra of individual ring structures consisting of four, five and six AuNPs.** Ring of four 40 nm AuNP diameter, ring of five 40 nm AuNPs and ring of six 30 nm AuNPs. The corresponding SEM images are shown in the right panel. Scale bars: 50 nm. **b, Scattering intensity as a function of the angle of the incident electric field.** The simulation of the peak intensities of the structure in S10a as a function of the angle of the incident light illustrates the anisotropic response of a not perfectly symmetric ring structure.

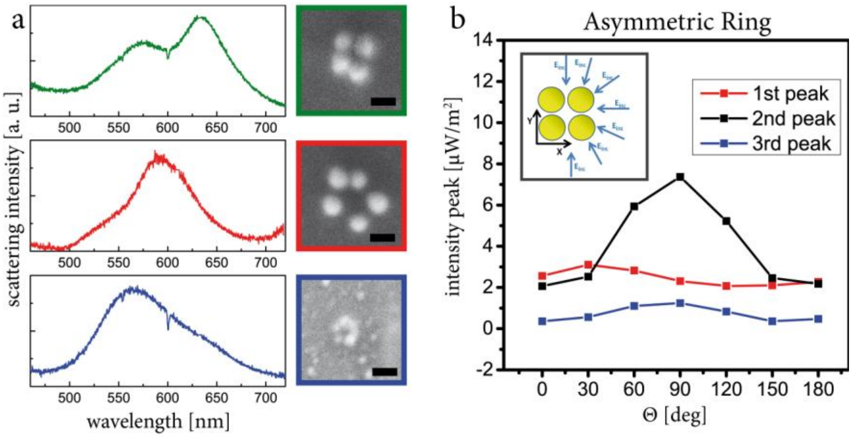

**Supplementary Note S12. FDTD simulation.** FDTD simulations of AuNP ring structures in solution (particle diameter 40 nm, gap size 10 nm) were performed using Lumerical FDTD solutions (Lumerical Solutions, Canada). Linear polarized light was injected from all three directions with a total-field scattered-field source and the calculated absorption cross sections were averaged to reproduce the experimentally measured bulk absorption measurement. Convergence was reached with a mesh size of 0.4 nm.

**Supplementary Note S13. Comsol simulation.** To simulate the dark-field scattering spectra Comsol Multiphysics (www.comsol.com) was used. The permittivity of the matrix regarding the simulation of samples in air, dried on a glass plate has been modified to ε = 1.75 regarding to samples in solution on a glass plate to ε = 2.15.

## References:

(1) Schreiber, R.; Do, J.; Roller, E.-M.; Zhang, T.; Schuller, V. J.; Nickels, P. C.; Feldmann, J.; Liedl, T. *Nat. Nanotechnol.* **2014,** 9, 74-78.
(2) Zhang, X.; Servos, M. R.; Liu, J. *Chem. Commun.* **2012,** 48, 10114-10116.
(3) Pal, S.; Deng, Z.; Ding, B.; Yan, H.; Liu, Y. *Angew. Chem. Int. Ed.* **2010,** 49, 2700-2704.
(4) Douglas, S. M.; Marblestone, A. H.; Teerapittayanon, S.; Vazquez, A.; Church, G. M.; Shih, W. M. *Nucleic Acids Res.* **2009,** 37, 5001-5006.

## B.2. Supporting Information for P2

### Plasmon-Exciton Coupling Using DNA Templates

by

Eva-Maria Roller, Christos Argyropoulos, Alexander Högele, Tim Liedl, and
Mauricio Pilo-Pais

published in Nano Letters, 16, 5962 - 5966 (2016).

# Supporting Information

# Plasmon-Exciton Coupling Using DNA Templates

Eva-Maria Roller,[†] Christos Argyropoulos,[‡] Alexander Högele,[†] Tim Liedl,[†] and
Mauricio Pilo-Pais[*,†]

†*Faculty of Physics and Center for NanoScience (CeNS), Ludwig-Maximilians-Universität (LMU), Munich 80539, Germany*

‡*Department of Electrical and Computer Engineering, University of Nebraska-Lincoln, Lincoln, Nebraska 68588, USA*

E-mail: m.pilopais@lmu.de

## Supporting Note 1. Assembly of dimer structures and characterization

### DNA origami design:

DNA-origami design was made using CaDNAno[1] and is based on a rectangular design consisting of two layers - 2LS (2 layer sheet). The folded structure has dimensions of 60 $nm$ length, 40 $nm$ width and 5 $nm$ height. It offers two attachment sites for nanoparticles each consisting out of twelve 15 nucleotides long 3' extensions of the staple strands. These extensions have a complementary sequence (15x A) to the DNA modified AuNPs which are bounded via hybridization. Supporting Fig. S1 shows the scaffold marked in blue, the staples in grey, and the elongated attachment staple strands in red and green.

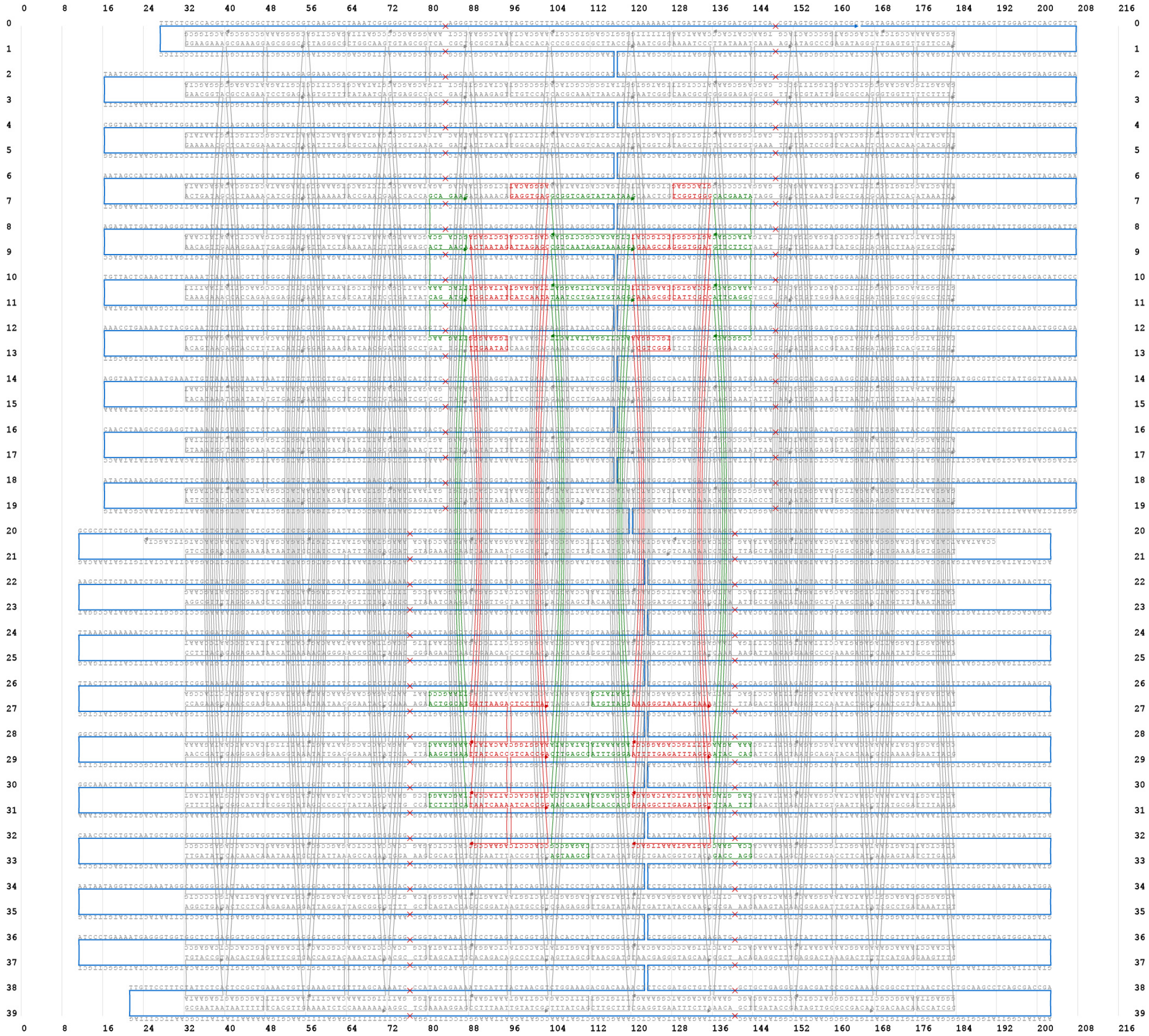

Figure S1: **2LS DNA origami design.** Scaffold (blue), staples (grey), and elongated attachment staple strands (red and green).

## DNA Origami folding:

Unmodified DNA sequences were purchased from Eurofins Genomics (Germany). The DNA origami structure was folded by annealing p7560 scaffold (10 nM, vector derived from the single-stranded M13-bacteriophage genome, 7, 560 bases) and staples (100 nM, ∼ 40 nts), in a 1x TE (40 mM Tris, 1 mM EDTA, pH 8), buffer and 12 mM $MgCl_2$. The solution was heated to 65° C, ramping down to 20 ° C over the course of 24 hours. The folded DNA origami structures were purified from excess staples strands by gel electrophoresis using a

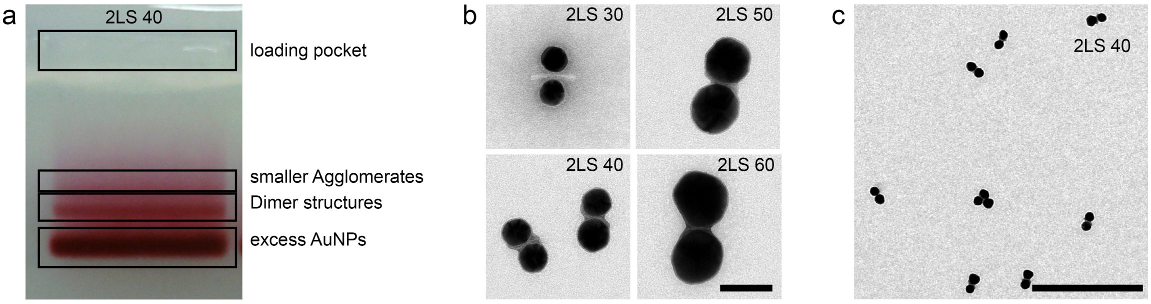

Figure S2: **Structure purification.** **(a)** Agarose gel purification of dimer structures with two attached AuNPs from excess unbound AuNPs. **(b)** TEM images of dimer structures. NPs sizes are $30\,nm$, $40\,nm$, $50\,nm$, and $60\,nm$. Scale bar $60\,nm$. **(c)** Wide field TEM image of dimer structures with $40\,nm$ AuNPs. Scale bar $500\,nm$.

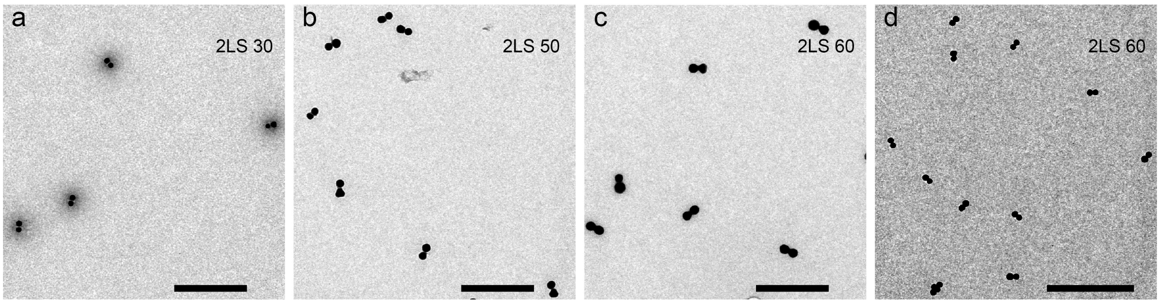

Figure S3: **Wide field TEM images.** Wide field TEM images of dimer structures with **(a)** $30\,nm$, **(b)** $50\,nm$, **c** $60\,nm$ AuNPs. Scale bar $500\,nm$. **d** TEM image of dimer structures with $60\,nm$ AuNPs showing a dimer yield above 75%. Scale bar $1000\,nm$.

1.0 % agarose gel in 1x TAE buffer (40 mM Tris, 40 mM Acetic Acid, 1 mM EDTA, pH 8) with 11 mM $MgCl_2$ and running for 2.5 hours at 4 V/cm. To extract the DNA origami structures from the gel, the appropriate band was cut out and squeezed from the gel using cover slips wrapped with parafilm. The concentration of the remaining solution was determined via UV-Vis absorption spectroscopy (Nanodrop).

## Gold Nanoparticle DNA concentration and conjugation:

Thiolated DNA was purchased from Biomers.net GmbH (Germany). Gold Nanoparticles (AuNPs) (BBI solutions) were concentrated using a BSPP protocol.[2] Functionalization with thiol-modified DNA strands (19x T sequence, 5'thiol) was performed following the protocol from Schreiber et al.[3] (see the reference supporting information section) and from Loweth et al.[4] AuNP-DNA conjugates were purified by centrifugation at $10,000\,\mathrm{rcf}$, removal of supernatant, and resuspension in 1x TAE buffer. This step was repeated eight times. The concentration of the thiol functionalized AuNPs was determined using UV-Vis absorption spectroscopy (Nanodrop).

## Conjugation of DNA origami structures with AuNPs:

To hybridize the DNA modified AuNPs to the origami structures an excess of four AuNPs per binding site on the structures was used. The AuNPs origami mixture was incubated overnight on a shaker at 22 ° C. The assembled dimer structures were then ran over a 0.7 % agarose gel in 1x TAE buffer with 11 mM $MgCl_2$ to purify them from excess unbound AuNPs. The band containing correctly formed dimers was extracted as described before.

## Dimer structures and J-aggregate deposition on glass slides:

The gel extracted dimer structures were diluted with 1x TAE buffer and 11 mM $MgCl_2$, to a concentration of 50 pM and deposited onto oxygen plasma cleaned glass slide substrates. After 5 mins incubation, the slides were rinsed with water and nitrogen dried. Subsequently, the samples were placed into a bath solution containing 50 mM J-aggregates (5,6-Dichloro-2-[[5,6-dichloro-1-ethyl-3-(4-sulfobutyl)-benzimidazol-2-ylidene]-propenyl]-1- ethyl-3-(4-sulfobutyl)-benzimidazolium hydroxide, inner salt, sodium salt, CAS# 18462-64-1, FEW Chemicals GmbH) and incubated overnight. Samples were removed and dried by nitrogen blow. In the aggregated form this dye displays a narrow absorption maximum at $584\,nm$ ($2.12\,eV$) and full width half maxima (FWHM) linewidth of $30\,meV$. When absorbed to glass slides, the J-aggregates exhibited a small blue-shifting with scattering peak at $580\,nm$ ($2.14\,eV$).

### SEM and TEM measurements:

Scanning electron microscopy (SEM) images were taken with a Gemini Ultra Plus field emission scanning electron microscope (Zeiss). To avoid charging, the glass slides were sputtered with a gold-palladium layer. Transmission electron microscope (TEM) images were taken with a JEOL JEM 1100 electron microscope at 80 kV. For TEM grid preparation, the gel purified structures were immobilized onto a formvar/carbon copper grid (300 mesh, TedPella Inc.) and stained with 1 % uranyl acetate for 15 seconds.

## Supporting Note 2: Dark-field Measurements

Assemblies were characterized using a home-built darkfield microscope (Olympus BX51 microscope, Princeton Instruments SP2300i Acton Standard Spectrograph, Princeton Instruments PIXIS 256E CCD detector). All measurements were taken using a 100 W halogen lamp with an oil condenser (Olympus U-DCW NA 1.4), a MPLFLN-BD 100x/N.A. 0.9 Olympus objective, and a grating of 300 g/mm 500-nm blaze. Spectra were acquired using the full CCD mode without pre-defining regions of interest and post-analyzed using Origin (Origin Labs). In short, a uniform background was subtracted from the raw signal, and normalized using a Lambert white scatterer. The full CCD mode measurement-scheme was crucial to guarantee an adequate background subtraction during signal analysis, and therefore to obtain reliable data, as the substrate could contain pockets of residual dye which if subtracted from the scattering spectra, would introduce artificial dips (Supporting Fig. S4). For each individual measurement the selection of adjacent pixels was carefully screened for uniformity. This ensures that no over-subtraction was made. In fact, our displayed spectra are likely to underestimate the dip transparency due to scattering of J-aggregates located in the vicinity of the “hot spot” which do not couple to the plasmon but rather act as “spectators”. We found our approach to provide more reliable results as opposed to those obtained from spin coating where we obtained a less uniform substrate background. We acquired polarized spectra of the 40 $nm$ dimer structure with J-aggregate as shown in Supporting Fig. S5a.

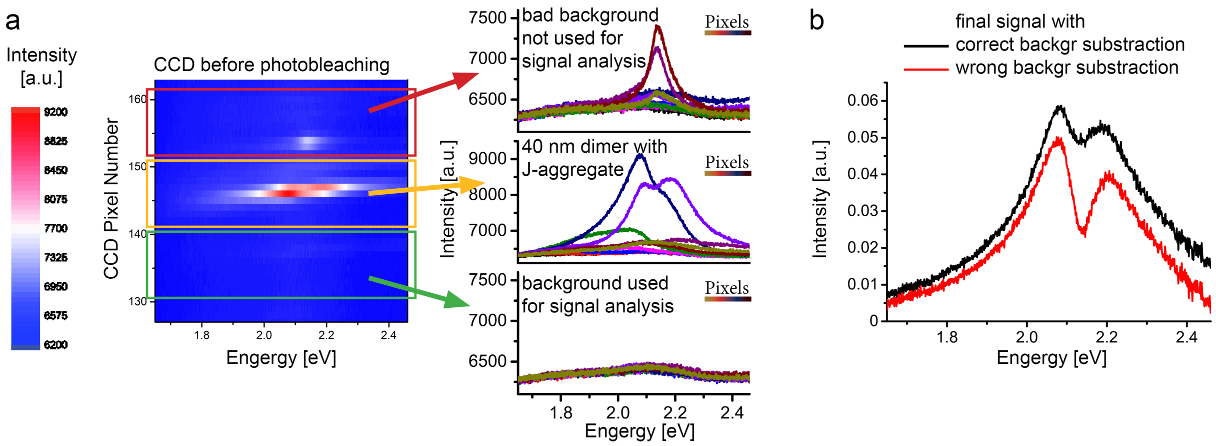

Figure S4: **Full CCD mode used during Darkfield measurements.** Careful analysis of single pixels ensures no over subtraction is performed, which otherwise would artificially enhance the dip of the spectra.

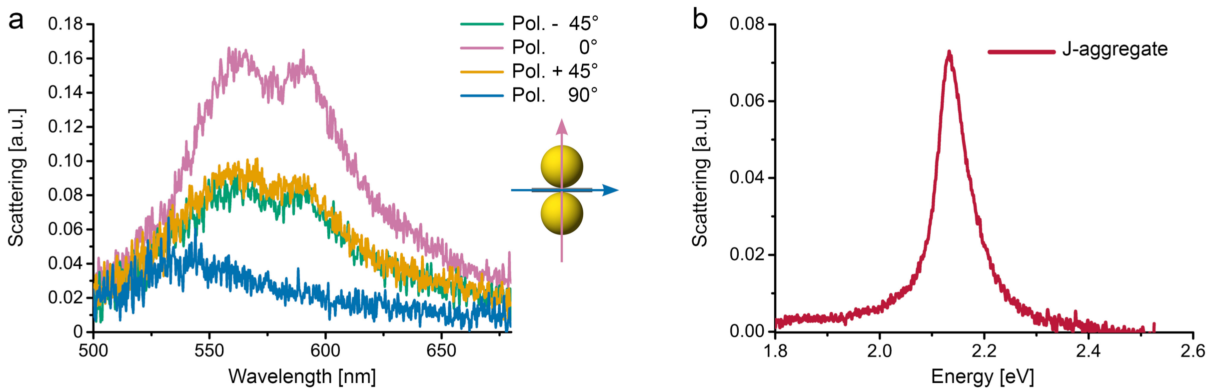

Figure S5: **Polarization dependent measurements and J-aggregate scattering spectrum.** **(a)** Polarized spectra of a 40 $nm$ dimer structure with J-aggregates show that the longitudinal mode is responsible for the coupling. **(b)** Scattering of J-aggregate residual on glass slide with energy $2.14\,eV$.

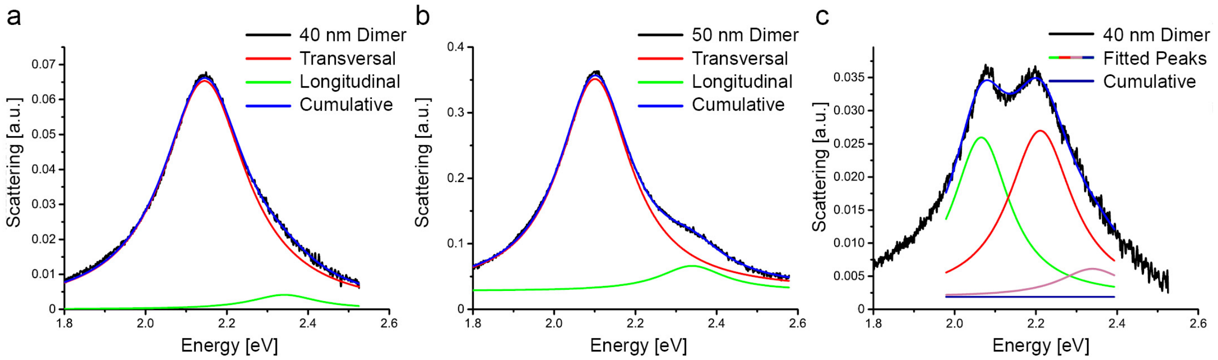

Figure S6: **Data extraction from scattering spectra.** On-axis mode energy and full width half maxima are found by deconvolution of transversal and longitudinal plasmon modes. The transversal mode is less prominent in smaller particles as shown on **(a)** 40 $nm$ than on **(b)** 50 $nm$ dimers. **(c)** Peak deconvolution of hybrid modes.

# Supporting Note 3: Data Analysis

The position of the plasmon ($\omega_p$) and FWHM ($\Gamma_p$) were extracted from deconvoluting the transversal and longitudinal modes of the bleached spectra (Supporting Fig. S6a-b). The position of the hybrid modes was obtained by peak deconvolution on the unbleached spectra of the two hybrid modes and the non-contributing transversal mode (Supporting Fig. S6c). Fitting was performed using a two coupled harmonic oscillator model with Hamiltonian,

$$\hat{\mathcal{H}} = \begin{pmatrix} \tilde{\omega}_p & g \\ g & \tilde{\omega}_{qe} \end{pmatrix} \tag{1}$$

which results in the complex eigenvalues,

$$\tilde{\omega}_\pm = \frac{\tilde{\omega}_p + \tilde{\omega}_{qe}}{2} \pm \sqrt{g^2 + \frac{1}{4}\left((\omega_p - \omega_{qe}) + \imath \frac{\Gamma_p - \Gamma_{qe}}{2}\right)^2} \tag{2}$$

We fitted the real component of the eigenvalue, namely,

$$\omega_\pm = \frac{\omega_p + \omega_{qe}}{2} \pm \frac{1}{2}\sqrt[4]{(\omega_p - \omega_{qe})^2(\Gamma_p - \Gamma_{qe})^2 + \left(4g^2 + (\omega_p - \omega_{qe})^2 - \frac{(\Gamma_p - \Gamma_{qe})^2}{4}\right)^2} \tag{3}$$

which readily reduces to the expression of Ref. Gomez et al.[5] when $\omega_p = \omega_{qe}$,

$$\Delta\omega = 2\sqrt{g^2 - \frac{1}{16}(\Gamma_p - \Gamma_{qe})^2} \tag{4}$$

or to the expression of Ref. Zengin et al.[6] when $\Gamma_p = \Gamma_{qe} = 0$,

$$\omega_\pm = \frac{\omega_p + \omega_{qe}}{2} \pm \frac{1}{2}\sqrt{4g^2 + (\omega_p - \omega_{qe})^2} \tag{5}$$

Fitting Fig. 3a on the main text was performed using an average plasmon width $\Gamma_{p,avg} = 230\, meV$. Importantly, the fitting is very robust when using this average plasmon width value ($\Gamma_{p,avg}$), as we obtained similar Rabi values when using either boundary for plasmon widths between $215\, meV < \Gamma_p < 320\, meV$. For Fig 3b, the fitting was performed using $g = a * R^n$, while the parameters $\Gamma_{p\,(R)}$ and $\omega_{p\,(R)})$ are functions of the radius $R$ extracted from the corresponding experimental data. The coupling constant $g$ for individual structures was extracted using equation 3, where $\omega_{qe} = 2.14\ eV$ and $\Gamma_{qe} = 30\ meV$, and $\Gamma_p$, $\Delta\omega$, and $\omega_p$ were obtained from experimental values, as described above. As an example, taking a $R = 20\, nm$ dimer size structure with $\omega_p = 2.15\, eV$, $\Gamma_p = 250\, meV$, $\omega_+ = 2.21\, eV$, and $\omega_- = 2.07\, eV$ we obtain a coupling constant of $g = 91\, meV$, a splitting energy of $\Delta\omega = 145\, meV$, and a lower bound for strong coupling of $\sqrt{\Gamma_p^2 + \Gamma_{qe}^2}/4 = 63\, meV$. Fitting the data of Fig. 3c using $g = a{*}R^n$ we extracted the radial dependence of the coupling constant of $g \sim 1/\, R^n$ with $n = 0.63{\pm}0.08$. Analysis was performed using the commercial software Origin software (OriginLab Corporation, OriginPro 2016G) and Mathematica (Wolfram Research, Inc., Mathematica 10.3).

## Supporting Note 4: Simulations

Full-wave simulations of the four different spherical nanodimers with diameters $D = 30\, nm$, $40\, nm$, $50\, nm$, and $60\, nm$ were performed with the commercial finite-element simulation

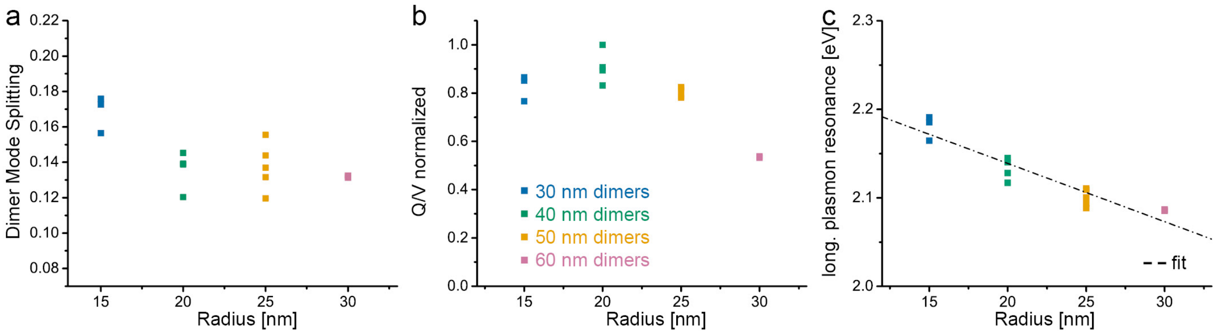

Figure S7: **Normal mode splitting, Purcell factor and Longitudinal plasmon resonance (a)** Normal mode splitting for individual structures obtained from experimental data. These values along with their correspondent $\Gamma_p$, $\Delta\omega$, and $\omega_p$ were used to calculate individual coupling constants $g$ using equation 2. Dimers composed of smaller NP sizes display a greater normal mode splittings $\Delta\omega$ as well as coupling constant $g$. **(b)** The Purcell Factor $\propto Q/V$ is also greater for smaller NPs. **(c)** Longitudinal mode plasmon resonance of varying NP sizes with fixed gap distance $d = 5\,nm$.

software COMSOL Multiphysics. The nanodimers are surrounded by a spherical domain, which is terminated by scattering boundary conditions to mimic an open boundary. Their dimensions are changed to match the dimensions of the experimental nanodimers. The scattering was computed based on the scattered-field formulation, in which we obtain the scattered fields by subtracting them from the analytical solution of an incident plane wave in the absence of the nanodimers (background field). The permittivity of gold was modeled based on the dispersive parameters obtained by experimental data.[7] The DNA template was simulated as a rectangular dielectric slab with refractive index $n = 2$ placed at the center of the nanodimerâĂŹs gap similar to Fig. 1a. The DNA slab thickness is equal to the nanodimerâĂŹs gap thickness ($\ell = 5\,nm$) and both of its sides are equal to the diameter $D$ of the spheres composing the nanodimer. The J-aggregate material was also placed at the center of the nanodimerâĂŹs gap inside the DNA slab. It has a rectangular shape with thickness $1\,nm$, one side equal to $D/8$ and the other side equal to $D/2$. The Lorentz permittivity model was used to approximate the dispersion of the J-aggregate.[6] Hence, the J-aggregate permittivity was given from the formula: $\epsilon_{qe} = \epsilon_{\infty} - \frac{f\omega_{qe}^2}{\left(\omega^2 - \omega_{qe}^2 - \imath\Gamma_{qe}\omega\right)}$, where $\epsilon_{\infty} = 1.6$, $\omega_{qe} = 2.14\,eV$ and $\Gamma_{qe} = 30\,meV$.[8] The reduced oscillator length is given by the parameter f in the Lorentz model. In all our simulations, this parameter was set equal to $f = 0.04$ in order to match the simulation results with the experimental spectra. After incorporating all the dispersive materials in the numerical modeling, the simulations exhibits excellent agreement with the experimental results, as it is shown in Fig. 2b.

# References

(1) Douglas, S. M.; Marblestone, A. H.; Teerapittayanon, S.; Vazquez, A.; Church, G. M.; Shih, W. M. *Nucleic Acids Res.* **2009**, *37*, 5001–6.

(2) Kuzyk, A.; Schreiber, R.; Fan, Z.; Pardatscher, G.; Roller, E.-M.; Högele, A.; Simmel, F. C.; Govorov, A. O.; Liedl, T. *Nature* **2012**, *483*, 311–4.

(3) Schreiber, R.; Do, J.; Roller, E.-M.; Zhang, T.; Schüller, V. J.; Nickels, P. C.; Feldmann, J.; Liedl, T. *Nat. Nanotechnol.* **2014**, *9*, 74–8.

(4) Loweth, C. J.; Caldwell, W. B.; Peng, X.; Alivisatos, A. P.; Schultz, P. G. *Angew. Chemie* **1999**, *38*, 1808–1812.

(5) Gómez, D. E.; Giessen, H.; Davis, T. J. *J. Phys. Chem. C* **2014**, *118*, 23963–23969.

(6) Zengin, G.; Wersäll, M.; Nilsson, S.; Antosiewicz, T. J.; Käll, M.; Shegai, T. *Phys. Rev. Lett.* **2015**, *114*, 157401.

(7) Palik, E. D., Ed. *Handbook of Optical Constants of Solids*; Academic Press: Burlington, 2002; pp 319–325.

(8) Pirotta, S.; Patrini, M.; Liscidini, M.; Galli, M.; Dacarro, G.; Canazza, G.; Guizzetti, G.; Comoretto, D.; Bajoni, D. *Appl. Phys. Lett.* **2014**, *104*, 051111.

## B.3. Supporting Information for P3

### Plasmonic Focus Point Analysis of Chiral Molecules

by

Luisa M. Kneer*, Eva-Maria Roller*, Robert Schreiber, Alexander O. Govorov,
and Tim Liedl
*equal contribution

Manuscript in preparation (2016).

# Supporting Information

# Plasmonic Focus Point Analysis of Chiral Molecules

*Luisa M. Kneer[1†], Eva-Maria Roller[1†], Robert Schreiber[2], Alexander O. Govorov[3] and Tim Liedl[1*]*

[1]Fakultät für Physik and Center for Nanoscience, Ludwig-Maximilians-Universität München, Geschwister-Scholl-Platz 1, 80539 Munich, Germany

[2]Clarendon Laboratory, Department of Physics, University of Oxford, Parks Road, Oxford OX1 3PU, UK

[3]Department of Physics and Astronomy, Ohio University, Athens, Ohio 45701, USA

†These authors contributed equally to this work.

## Supplementary Note S1: DNA origami structures

*DNA origami design and binding sites for nanoparticles.* The DNA origami structure was designed using the software caDNAno.[1] The rectangular shaped structure consists of 2 layers of DNA with dimensions of roughly 57 nm x 52 nm x 5 nm (2 layer sheet, 2LS). The structure offers 2 binding sites for nanoparticles, each consisting of twelve staple strands extended by 15 nucleotides (anchors). The binding sites are placed in the middle of the flat side of the structure facing each other. Figure S1 shows the caDNAno design of the 2LS, anchor strands are marked with red and turquoise color. The locations of the binding sites on the DNA origami structure are chosen such that all twelve anchors are spread over an area of 13 nm x 17 nm. This compact distribution of the anchors allows a very robust binding of bigger gold nanoparticles (AuNPs) and triggers the gold nanorods (AuNRs) to attach upright on the origami instead of lying parallel on it.

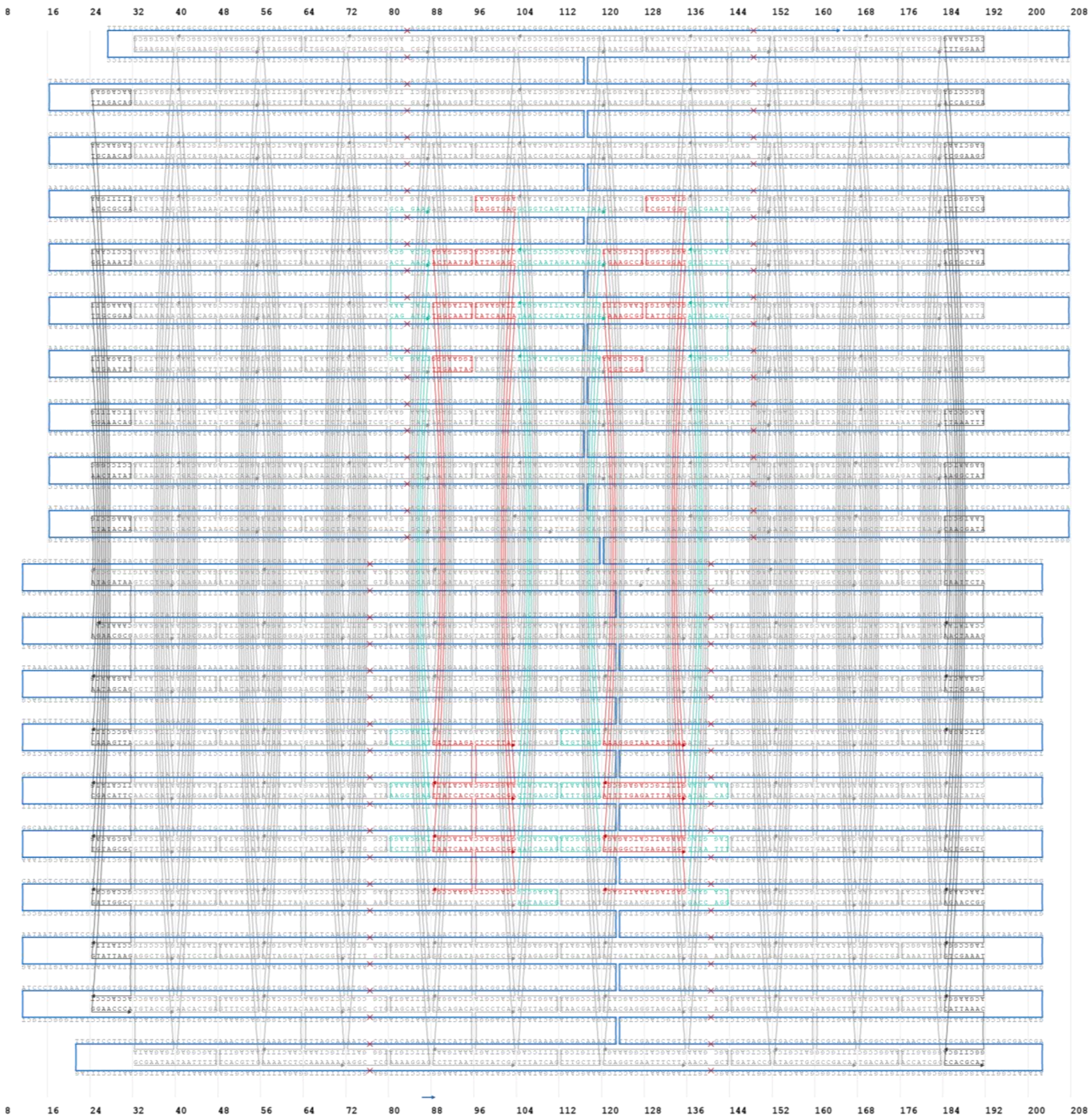

**Figure S1 |** CaDNAno[1] image of the 2LS design. Staples which were used as attachment points for nanoparticles are marked in red and turquoise.

*DNA origami folding and purification.* For the DNA origami folding 10 nM of scaffold p7560, 100 nM of each staple strand, 200 nM of each anchor strand, 10 mM Tris, 1 mM EDTA (pH 8) and 12 mM MgCl$_2$ were mixed together. The mixture was heated up to 65 °C for 2 min and slowly cooled down to 25 °C over 25 hours. The folded DNA origami structures were purified from excess staple strands by gel electrophoresis. The samples were running over a 1.0 % agarose gel in 1x TAE buffer with 11 mM MgCl$_2$. After staining with ethidium bromide the band containing the correct folded structures was retrieved by cutting it out and squeezing the chopped gel with a glass slide. The concentration of the DNA origami structures was determined by UV-Vis spectroscopy (*Nanodrop*) at a wavelength of 260 nm.

## Supplementary Note S2: Nanoparticle functionalization with DNA

*Gold nanoparticle (AuNP) concentration.* The protocol used follows Schreiber *et al.*[2] with minor changes. To concentrate the AuNPs, 8 mg of BSPP (Bis(p-sulfonatophenyl)phenylphosphine dehydrate dipotassium salt, Sigma-Aldrich) were added to the unmodified AuNPs (40 nm, BBI Solutions, 20 ml). The mixture was then stirred for three days. Afterwards, sodium chloride (5 M) was added until a color change from red to bluish was observed and the solution was centrifuged at 1,600 rcf for 30 min. The supernatant was discarded and the AuNPs were dissolved in equal amounts of a 2.5 mM BSPP solution and 0.8 mL methanol. After mixing, the solution was centrifuged again (1,600 rcf, 30 min), the supernatant was discarded and the AuNPs were dissolved in BSPP (0.2 mL, 2.5 mM). To determine the final AuNP concentration UV-Vis spectroscopy (Nanodrop) at a wavelength of 530 nm was performed (molar extinction coefficient for 40 nm AuNP $\varepsilon = 8.42 * 10^9$).

*Functionalization of AuNPs with DNA.* In order to hybridize the AuNPs to DNA origami structures, they must be functionalized with single stranded DNA complementary to the anchor sequence used on the DNA origami structures. Further, the AuNPs must be stabilized against high $MgCl_2$ concentrations, which are used during the DNA origami folding process. Therefore the concentrated AuNPs were conjugated with thiolated single stranded DNA (ssDNA) strands (HPLC purified, biomers.net). First, thiolated ssDNA was incubated with TCEP (Tris(2-carboxyethyl)phosphine hydrochloride, Sigma-Aldrich, 20 mM final concentration) for at least 30 min. Then the AuNPs and the thiolated ssDNA were mixed in 0.5x TBE buffer with a ratio of DNA:AuNP = 6,000:1. The solution was incubated on a shaker for 3 days. Finally, to prevent blocking of the nanoparticle binding sites on the DNA origami by unbound excess thiolated ssDNA the AuNP solution was purified by using 100 kDa MWCO centrifugal filters (Amicon Ultra, Millipore, 3 min, 10,000 rcf). This step was repeated 8 times with 400 µl 0.5x TBE buffer added before each centrifugation step. It is important to perform this purification step directly before attaching the AuNPs to the DNA origami structures to get high yields of bound AuNPs. The concentration was determined by UV-Vis absorption spectroscopy at 530 nm (Nanodrop).

*Functionalization of AuNRs with DNA.* The AuNR functionalization follows mainly the protocol from Kuzyk *et al.*[3]. First, the thiolated ssDNA strands were incubated for at least 30 min with TCEP (20 mM final concentration) to reduce the disulfide bonds. Then 1 mL stock solution of AuNRs (700 nm and 800 nm absorption, negatively charged, 1.4 nM stock concentration, Alfa Aesar), a final concentration of 0.05 % SDS (Sodium dodecyl sulfate), 1x TBE (pH 8) buffer and the thiolated ssDNA were added. The ratio was AuNRs:ssDNA = 1:3,000. To this mixture 1 M HCl was added to lower the pH between 2 to 3. After 1 hour of incubation on the shaker, NaCl was added to a final concentration of 0.5 M and the solution was again gently shaken for incubation during 3 hours. Then the pH was adjusted back to 8 by adding 500 µl of 0.5x TBE with 0.03% SDS. Again, the mixture was kept for incubation on the shaker overnight. Just before attaching the AuNRs to the DNA origami, the AuNRs solution was purified from unbound excess thiolated ssDNA. This step is important to prevent blocking of the complementary anchor DNA sequences on the DNA origami structure by free thiolated ssDNA. To purify the AuNR mixture, it was centrifuged for 20 min at 6,000 rcf at 4°C. After each centrifugation step, the supernatant was discarded and 2 ml of 0.5x TBE with 0.03% SDS was added. After 4 washing steps, the purified AuNRs were finally dissolved in 20 µL 0.5x TBE. The concentration was determined by UV-Vis absorption spectroscopy at the longitudinal resonance frequency of the AuNRs (here 680 nm and 780 nm). The extinction coefficients were taken from Orendorff *et al.*[4].Link *et al.*.[5]

## Supplementary Note S3: Assembly of nanoparticle DNA dimer structures

The purified AuNPs respectively AuNRs were added to the gel purified DNA origami structures. To achieve a high attachment yield we added an excess of 5 times more nanoparticles per binding site on the DNA origami structure. The mixture was kept at room temperature on a shaker overnight for incubation. A second agarose gel purification (0.7% agarose gel in 1x TAE buffer with 11 mM $MgCl_2$) was performed to get rid of the excess unbound nanoparticles and to separate the well formed dimer structures from smaller agglomerates with more than two bound particles per structure. The band containing the nanoparticle DNA dimer structures was cut out of the gel and the final solution of chirality sensors was recovered by squeezing out this gel band. Figure S2 shows the purification agarose gel.

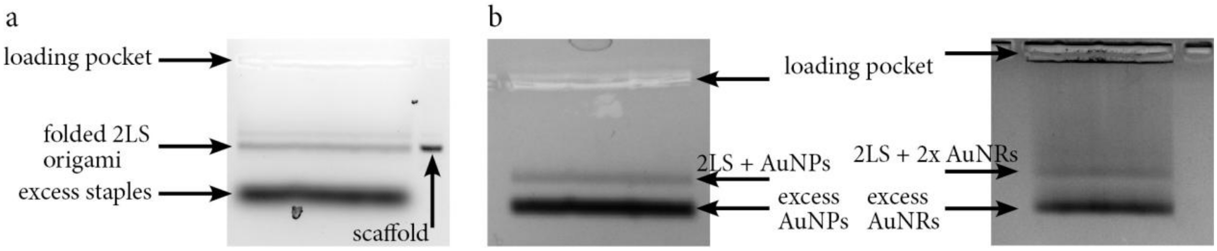

**Figure S2 |** Purification of the nanoconstructs by gel electrophoresis. **a,** Image of the folded 2LS origami structures. **b,** Image of the purification gel of the origami structures with attached AuNPs (left) or attached AuNRs (right).

## Supplementary Note S4: TEM homogeneity analysis of the CD-sensors

After immobilization the gel purified dimer structures on a carbon/formvar-coated grid (Plano GmbH, Germany) they were stained with 1% uranyl acetate for 15 seconds. The TEM measurements were taken with a JEOL JEM-1100 electron microscope at 80 kV acceleration voltage. Figure S3 shows assembled dimer structures. Since the homogeneity of the structures is crucial for CD measurements, analysis of the attachment yield of nanoparticles per DNA origami structure were performed. A statistic is shown in Figure S4 – S6. The yield of correct assembled CD-sensors is determined to be 75% for the AuNP sensors.

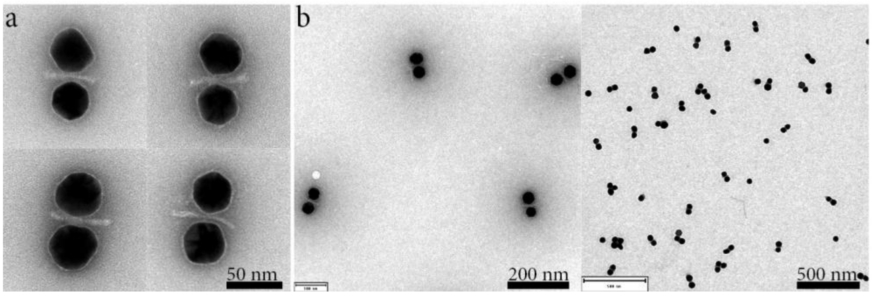

**Figure S4 |** TEM images of the dimer structures consisting out of two 40 nm AuNPs bound to a 2LS origami structure. **a,** Representativ TEM images of the dimer structure. **b,** Wide field TEM images.

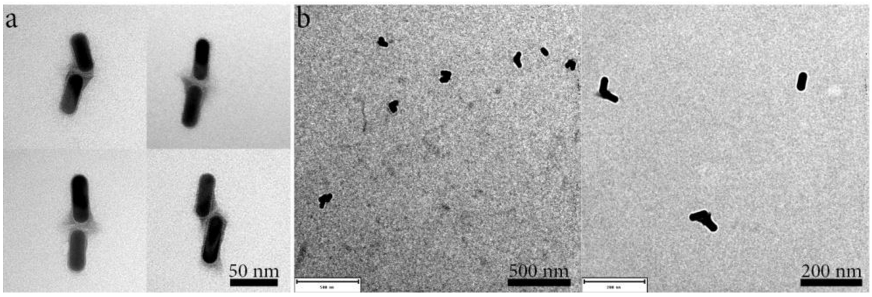

**Figure S5 |** TEM images of the dimer structures consisting out of two 40 nm AuNRs bound to a 2LS origami structure. **a,** Representativ TEM images of the dimer structure. **b,** Wide field TEM images.

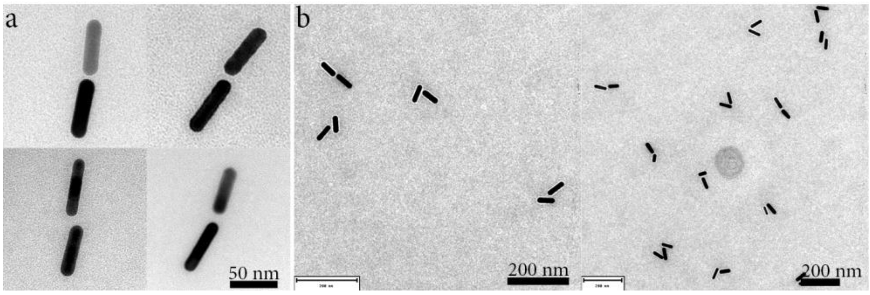

**Figure S6 |** TEM images of the dimer structures consisting out of two 40 nm AuNRs (longitudinal resonance 800 nm) bound to a 2LS origami structure. **a,** Representativ TEM images of the dimer structure. **b,** Wide field TEM images.

## Supplementary Note S5: CD measurements

CD measurements were performed with an Applied Photophysics Chirascan-plus CD Spectrometer (UK). The used Quartz SUPRASIL cuvette (Hellma Analytics, Germany) had a light path of 3 mm. The scanning speed was set to 0.5 s with a step size of 1.0 nm. Each measurement curve represents an average over 5 runs.

## Supplementary Note S6: Silver enhanced dimer structures

Since silver nanoparticles have a higher plasmonic enhancement factor than gold nanoparticles[6], we also assembled the 2LS dimer structure with two AuNPs with a diameter of 10 nm attached (identical functionalization protocol as for 40 nm AuNPs). The 10 nm AuNPs bound to the DNA origami structures were then enhanced to a diameter of 40 nm with silver. Here, we used a commercially available silver enhancement kit (HQ Silver, Nanoprobes, USA). To 20 µl of sample volume (2 nM) we added 7 µl of the premixed solutions of A, B and C of the enhancement kit. CD measurements of those silver enhanced CD sensor structures show a much stronger signal compared to CD sensors with 40 nm AuNPs. Nevertheless, we want to point out, that the enhancement process does not yield as uniform dimer structures as those described in the main text.

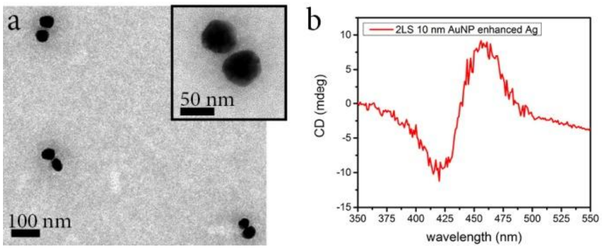

**Figure S7 |** Subsequently silver enhanced dimer structures consisting out of two 10 nm AuNPs bound to the origami 2LS structure. **a,** TEM images of the silver enhanced dimers. **b,** CD measurement of the silver enhanced structures.

1. Douglas, S. M.; Marblestone, A. H.; Teerapittayanon, S.; Vazquez, A.; Church, G. M.; Shih, W. M., Rapid Prototyping of 3d DNA-Origami Shapes with Cadnano. *Nucleic Acids Res.* **2009,** *37*, 5001-5006.
2. Schreiber, R.; Do, J.; Roller, E.-M.; Zhang, T.; Schuller, V. J.; Nickels, P. C.; Feldmann, J.; Liedl, T., Hierarchical Assembly of Metal Nanoparticles, Quantum Dots and Organic Dyes Using DNA Origami Scaffolds. *Nat. Nanotechnol.* **2014,** *9*, 74-78.
3. Kuzyk, A.; Schreiber, R.; Zhang, H.; Govorov, A. O.; Liedl, T.; Liu, N., Reconfigurable 3d Plasmonic Metamolecules. *Nat. Mater.* **2014,** *13*, 862-866.
4. Orendorff, C. J.; Murphy, C. J., Quantitation of Metal Content in the Silver-Assisted Growth of Gold Nanorods. *J. Phys. Chem. B* **2006,** *110*, 3990-3994.
5. Link, S.; Mohamed, M. B.; El-Sayed, M. A., Simulation of the Optical Absorption Spectra of Gold Nanorods as a Function of Their Aspect Ratio and the Effect of the Medium Dielectric Constant. *J. Phys. Chem. B* **1999,** *103*, 3073-3077.
6. Govorov, A. O.; Gun'ko, Y. K.; Slocik, J. M.; Gerard, V. A.; Fan, Z.; Naik, R. R., Chiral Nanoparticle Assemblies: Circular Dichroism, Plasmonic Interactions, and Exciton Effects. *J. Mater. Chem.* **2011,** *21*, 16806-16818.

# B.4. Supporting Information for P4

## Hot spot-mediated non-dissipative and ultrafast plasmon passage

by

Eva-Maria Roller, Lucas V. Besteiro, Claudia Pupp, Larousse Khosravi Khorashad, Alexander O. Govorov, and Tim Liedl

submitted (2016).

## Supplementary Information

# Hot spot-mediated non-dissipative and ultrafast plasmon passage

Eva-Maria Roller[1], Lucas V. Besteiro[2], Claudia Pupp[1], Larousse Khosravi Khorashad[2], Alexander O. Govorov[2†], Tim Liedl[1†]

[1] *Physics Department and CeNS, Ludwig-Maximilians-Universität München, 80539 Munich, Germany*

[2] *Department of Physics and Astronomy, Ohio University, Athens, Ohio 45701, USA*

[†] govorov@helios.phy.ohiou.edu; tim.liedl@lmu.de;

## Materials and Methods:

### Supplementary Note S1. Assembly of heterogeneous particle trime structures.

*DNA origami folding.* In DNA origami, a ~ 8000 nucleotide long viral single-stranded DNA (ssDNA) scaffold is folded into a programmed shape with the help of ~ 200 short, synthetic ssDNA staple strands. Due to the sequence-defined assembly of the DNA structure the location of each staple strand and each DNA base within the structure is exactly defined. By extending a selected subset of the staple strands with tailored anchor sequences, the folded DNA origami structure can be employed as a breadboard exhibiting unique and sequence-specific binding sites for DNA-modified metal nanoparticles. Our DNA origami structure offers two outer attachment sites with the same DNA anchor sequence and a middle site with an orthogonal sequence. The DNA origami 14 helix bundle (14hB) was folded using 10 nM of the scaffold p8634, 100 nM of each staple strand, 10 mM Tris, 1 mM EDTA (pH 8) and 16 mM $MgCl_2$. This mixture was heated to 65 °C for 20 min and then slowly cooled down to 20 °C over a period of 40 hours. Specific staple strands at the attachment site were elongated by either 15 x A bases for AuNP attachment or by the sequence ATG TAG GTG GTA GAG AA for AgNP attachment. Thus each attachment site consists of five single-stranded extensions of staples whose ends are located close to each other on the surface of the origami structure. The extended staple strands are labeled in Figure S1 with red colour. All the staples for nanoparticle attachment *via* DNA hybridization were already included into the folding solution. After folding the structures, a purification step with a 1 % agarose gel in 1 x TAE (40 mM Tris, 40 mM Acetic Acid, 1 mM EDTA, pH 8) containing 11 mM $MgCl_2$ was performed. The band containing the structures was cut out from the gel with a razor blade. The DNA origami structures were recovered with a pipette while squeezing the gel band between two glass slides. The concentration of the 14-helix bundle after purification was determined via UV-Vis spectroscopy (Nanodrop).

*Concentration of AuNPs and conjugation with DNA.* First, 40 nm AuNPs (BBI Solutions, 20 ml) were concentrated using the protocol of Schreiber *et al*.:[1] The AuNPs were mixed with 8 mg BSPP (Bis(*p*-sulfonatophenyl)phenylphosphine dihydrate dipotassium salt, Sigma-Aldrich) and shaken for 3 days. Afterwards NaCl was added till a colour change to blue was observed. Then the solution was centrifuged at 1,600 rcf for 30 min and the supernatant discarded. Next, 1 ml of 2.5 mM BSPP in H2O and 1 ml Methanol was added. After vortexing, the solution was centrifuged again at 1,600 rcf for 30 min and the supernatant was discarded. The concentrated AuNPs were redissolved in 200 µl 2.5 mM BSPP and their concentration was determined *via* UV-Vis spectroscopy (Nanodrop). The following functionalization of the AuNPs with 5' thiol-modified ssDNA strands (Biomers.net, 19 x T bases) has two goals: First, the DNA coverage of the AuNPs renders them stable against high $MgCl_2$ concentrations as they are used within the DNA origami folding process. Second, the sequence of the thiol modified ssDNA strands is chosen to be complementary to the single-stranded extensions of the staple strands that together form the AuNP attachment sites on the 14-helix bundle structure. Thus the AuNPs can hybridize to the predesigned sites on the DNA origami structure. For the functionalization a ratio of AuNPs:thiol ssDNA of 1:5,000 was used. 0.5 x TBE buffer was added to the AuNPs and the ssDNA and the solution was kept on a shaker for 3 days. Afterwards a purification step was performed to get rid of the unbound ssDNA strands. For that the AuNPs were run over a 100 kDa MWCO centrifugal filter (Amicon Ultra, Millipore, 5 min, 8,000 rcf) followed by additional 8 centrifugation steps with a filter exchange after 4 steps. This purification from unbound ssDNA strands is crucial to avoid blocking of the attachment sites on the DNA origami structure by free complementary ssDNA strands. Best yields of AuNPs-to-DNA-origami-binding can be achieved if the last centrifugation steps are performed directly before mixing the AuNPs with the DNA origami structures.

*AgNPs functionalization with DNA.* For the functionalization of AgNPs with ssDNA a 5' thiol-modified sequence TTC TCT ACC ACC TAC AT (biomers.net) was used. A functionalization sequence that is different to the AuNP sequence guarantees that the attachment of AuNPs and AgNPs to the 14-helix bundle is specific. First, the as-purchased AgNPs (Cytodiagnostics, 50 nm, 1 ml) were mixed with the sequence (40 µl, 100 µM stock concentration) and 1 x TE buffer. This solution was kept protected from light on a shaker for one week. Afterwards NaCl aging was performed by slowly raising the NaCl concentration to 100 mM over the course of one day. Then short 5'thiol-modified ssDNA (5x T, MWG eurofines, 20 µl, 1 mM stock concentration) were added. This short DNA strand is used as "back filler" to assure high $MgCl_2$ stability of the AgNPs while it is too short to hybridize to the DNA origami structure. The solution was left again over night for incubation. Then the NaCl concentration was raised to a final concentration of 500 mM over the course of 6 hours. As the last step, the DNA-functionalized AgNPs were purified from excess unbound ssDNA strands by using 100 kDa MWCO centrifugal filters as described in the AuNPs procedure.

*Functionalization of DNA origami 14-helix bundle structure with AuNPs and AgNPs.* After determining the concentration of the DNA-modified AgNPs and AuNPs *via* UV-Vis spectroscopy, they were mixed together with the purified DNA origami 14-helix bundle template. This structure offers two attachment sites for AuNPs and one attachment site for AgNPs. Each attachment site consists of five elongated staple strands offering the complementary sequence to the corresponding metal nanoparticle. The DNA origami structure and the metal nanoparticles were mixed in a ratio attachment site:AuNP/AgNP of 1:4. The excess of metal nanoparticles over attachment sites ensures high binding yields and prevents crosslinking of origami structures mediated by nanoparticles. After overnight incubation of the solution, a 0.7% agarose gel electrophoresis in 1 x TAE and 11 mM $MgCl_2$ buffer was run to separate the desired heterogeneous trimer structures from excess, unbound metal nanoparticles and from aggregates. The band containing the trimer structures was excised from the gel and the nanostructures extracted by squeezing the cut gel band between two glass slides. The solution received in a pipette contained the purified final trimer structures.

## Supplementary Note S2. Characterization of heterogenous particle trimer structures.

*Transmission electron microscopy (TEM).* TEM was used to control the correct assembly of the particle trimer nanostructures. A droplet of the solution containing the purified structures was deposited on a plasma-exposed carbon-formvar-coated TEM grid (Ted Pella) and then dabbed off after 3 minutes. The grid was stained with 1% uranyl formate for 15 seconds. Imaging was performed with a JEOL JEM-1100 at an acceleration voltage of 80 kV.

*Dark-field scattering spectroscopy.* In order to take scattering spectra of single trimer structures the purified trimer solution was diluted 20 x in 1 x TAE buffer containing 11 mM $MgCl_2$ and immobilized on cleaned glass cover slides. Therefor, a droplet of the diluted solution was deposited for 5 min onto the glass slides, and then ddH2O was rinsed over the slide to wash away salt residues. To avoid denaturation of the DNA structures, the slides were dried with a nitrogen flush immediately. The dark-field scattering spectra were collected with a home-build dark-field set up in transmission mode using a 100x air objective (Olympus) and an oil condenser (Olympus NA 1.4) with a 100 W halogen bulb as illumination source coupled to an Acton SP2300 spectrometer (Princeton Instruments). Polarization-resolved scattering spectra were taken by exciting the system with unpolarized incident light and detecting the scattered light through a rotatable polarizer.

*Scanning electron microscopy (SEM).* The single structures characterized in the dark-field set-up were further analyzed by SEM. Therefor, the glass slides were subsequently sputtered with a 3 nm gold palladium layer and imaged using a Gemini Ultra Plus field emission SEM (Zeiss). The images were taken using the in-lens detector and an electron acceleration voltage of 2 kV at a working distance of 3.0 mm.

## Supplementary Note S3. Theoretical Modelling of trimer plasmonic bus structures.

*Classical theoretical simulations.* Theoretical computations of the NP chains were performed using classical electrodynamics with Comsol Multiphysics with the standard boundary conditions and with local dielectric functions for the gold sphere[2] and the silver sphere.[3] The optical dielectric constant of the matrix was taken as an average between water and glass ($\varepsilon = 2.25$). The trimer particle chain was simulated with the following parameters: diameter of Au sphere 40 nm, diameter of the silver sphere 30 nm and gap size in between the spheres 4 nm. The scattering intensities were simulated with light approaching the plane of the trimer at an angle of 20 ° and the elastic scattering was collected computationally on the vertical axis. Calculations were done for the incident beams with two orthogonal polarizations and the resulting scattering spectra were averaged over the incident polarizations.

The local dissipation spectra and maps in Figure 2c in the main text were computed from the standard equation for the local rate of losses:

$$Q_{abs,local} = \langle \mathbf{j} \cdot \mathbf{E} \rangle_{time} = \mathrm{Im}(\varepsilon_{metal}) \frac{\omega}{8\pi} \mathbf{E}_{\omega} \cdot \mathbf{E}_{\omega}^{*},$$

where $\mathbf{E}_{\omega}$ and $\varepsilon_{metal}$ are the complex field amplitude and dielectric constant, respectively.

Another important parameter of our trimer system is the splitting between the wavelengths of the symmetric (bright) and antisymmetric (dark) modes. The experimental and theoretical data in the figures in the main text reveal only the optically-allowed, symmetric modes, since the system is relatively small and the incident plane wave is able to excite predominantly the symmetric modes. In theory, we can now excite the system with two dipoles that have opposite phases (Supplementary Figure S1). In this way, we create an antisymmetric driving field for the system and, therefore, the dark modes should become active in the extinction and absorption spectra. Then, we see now clearly the splitting between the symmetric (optically bright) mode and the antisymmetric (optically dark) mode in Figure SI theory dipoles. Using this splitting, we can estimate the characteristic transfer time in our trimer system. The splitting between the peaks for the two modes is equal to 0.22eV in the energy units. We now assume that, using an ultra-short pulse, we excite only NP1. This thought experiment can be realized using an exciting plasmonic tip that is placed near NP1. Then, NP1 becomes predominantly excited in the first moment. Another words, the ultra-short localized pulse sets up the initial conditions at $t=0$ for the motion of the dipoles of the two Au NPs: $P_{NP1}(t=0)=P_0$ and $P_{NP2}(t=0)=0$, where $P_{NP1}(t)$ and $P_{NP2}(t)$ are the polarizations of the NP1 and NP2, correspondingly. In this simplified approach, we can ignore the Ag NP, which plays a role of a transmitter, and consider only Au NPs regarding them as NP1 and NP2. The time dynamics of a harmonic system with two modes is the following and the appropriate initial conditions:

$$P_{NP1}(t)=\frac{P_0}{2}\left(\cos[\omega_1 t]+\cos[\omega_2 t]\right)=P_0\cos[\frac{\omega_1+\omega_2}{2}t]\cdot\cos[\frac{\omega_1-\omega_2}{2}t],$$
$$P_{NP2}(t)=\frac{P_0}{2}\left(\cos[\omega_1 t]-\cos[\omega_2 t]\right)=-P_0\sin[\frac{\omega_1+\omega_2}{2}t]\cdot\sin[\frac{\omega_1-\omega_2}{2}t].$$

The polarizations have the fast and slow components and the slow component oscillates with the circular frequency $(\omega_1-\omega_2)/2=\Delta_{splitt}/2$. Since the energy of a NP is proportional to the square of the polarization, the slow components give the evolution of the energies stored on the NPs in the system:

$$E_{NP1}(t)\propto\cos^2[\frac{\omega_1-\omega_2}{2}t],$$
$$E_{NP2}(t)\propto\sin^2[\frac{\omega_1-\omega_2}{2}t].$$

The characteristic transfer time can be estimated as the time when NP2 receives a half of the initial energy from NP1. It happens when $\frac{\omega_1-\omega_2}{2}t=\frac{\pi}{4}$. This equation sets up the transfer time $t_{transfer}=\frac{\pi}{2(\omega_1-\omega_2)}$ which is used in the main text.

*Quantum theoretical calculations:* As described in the main text, we can model our nanoparticles as three-dimensional quantum oscillators (Figure 4a). To develop such a model, we first write down the Hamiltonian in the coordinate representation and then we turn this Hamiltonian into the plasmonic second-quantization representation, which will correspond to a quantum picture of plasmons. The Hamiltonian of our system involving the dipole-dipole couplings between the NPs has the form:

$$\hat{H} = \sum_{\substack{\alpha=(i,\gamma) \\ i=1,2,3 \\ \gamma=x,y,z}} \frac{\hat{p}_\alpha^2}{2m_{eff,i}} + \frac{k_i x_\alpha^2}{2} + \frac{1}{\varepsilon_{eff}} \sum_{i>j} \frac{\mathbf{d}_i \cdot \mathbf{d}_j - 3(\mathbf{d}_i \cdot \hat{z})(\mathbf{d}_j \cdot \hat{z})}{R_{ij}^3}, \qquad \text{(S1)}$$

$$\mathbf{d}_i = e_{eff,i}\mathbf{r}_i \ ,$$

where $\hat{p}_\alpha$ is the momentum operator for the oscillator $\alpha = (i,\gamma)$, where the index $i$ is the NP number ($i = 1,2,3$) and $\gamma$ indicates the direction of the oscillation ($\gamma = x, y, z$); $R_{ij}$ is the NP-NP distance, and $e_{eff,i}$ is the effective plasmonic change of the i-NP. In our system, we have two Au NPs ($i = 1,2$) and one Ag NP ($i = 3$) and, correspondingly, $e_{eff,1} = e_{eff,2} = e_{Au}$ and $e_{eff,3} = e_{Ag}$. The coefficient $\varepsilon_{ff}$ is an effective dielectric constant of the matrix. In this model, three quantum plasmonic oscillators are embedded into an effective medium and coupled via the Coulomb dipole-dipole interaction. The first two terms are just the internal energy of the oscillators with the following frequencies:

$$\omega_{p,Au} = \omega_1 = \omega_2 = \sqrt{\frac{k_{Au}}{m_{eff,Au}}} \ , \ \omega_{p,Ag} = \omega_3 = \sqrt{\frac{k_{Ag}}{m_{eff,Ag}}} \ . \qquad \text{(S2)}$$

These oscillator frequencies should be matched with the plasmon energies of the isolated Au and Ag NPs: $\hbar\omega_{p,Au} = 2.29eV$ and $\hbar\omega_{p,Ag} = 2.8eV$. We now can quantize the oscillations by introducing the corresponding creation and annihilation operators of plasmons:[4]

$$x_\alpha = \sqrt{\frac{\hbar}{2m_{eff,\alpha}}}\left(\hat{c}_\alpha + \hat{c}_\alpha^+\right), \quad \hat{p}_\alpha = i\sqrt{\frac{m_{eff,\alpha}\hbar\omega_{p,\alpha}}{2}}\left(\hat{c}_\alpha^+ - \hat{c}_\alpha\right).$$

These operators diagonalize the first two terms in Eq. S1 and give the energy operator for the non-interacting system of plasmons,

$$\hat{H}_0 = \sum_\alpha \hbar\omega_{p,\alpha}\left(\hat{c}_\alpha^+\hat{c}_\alpha + \frac{1}{2}\right),$$

with the corresponding frequencies of the plasmonic excitations. Then, the total Hamiltonian of the coupled NPs reads:

$$\hat{H} = \hat{H}_0 + \hat{H}_{\text{int}},$$

$$\begin{aligned}
\hat{H}_{\text{int}} &= \frac{1}{\varepsilon_{eff}} \sum_{i>j} \frac{\mathbf{d}_i \cdot \mathbf{d}_j - 3(\mathbf{d}_i \cdot \hat{z})(\mathbf{d}_j \cdot \hat{z})}{R_{ij}^3} = \sum_{\substack{\alpha=(i,\gamma),\\ \beta=(j.\gamma')\\ i>j}} w_{\alpha\beta} \hat{c}_\alpha^+ \hat{c}_\beta + v_{\alpha\beta} \hat{c}_\alpha^+ \hat{c}_\beta^+ + h.c., \\
w_{(i,x),(j,x)} &= w_{(i,y),(j,y)} = \sqrt{\frac{\hbar}{2m_{eff,i}}} \sqrt{\frac{\hbar}{2m_{eff,i}}} \frac{\left(e_{eff,i} e_{eff,j}\right)}{\varepsilon_{ff} R_{ij}^2}, \\
w_{(i,z),(j,z)} &= -2\sqrt{\frac{\hbar}{2m_{eff,i}}} \sqrt{\frac{\hbar}{2m_{eff,i}}} \frac{\left(e_{eff,i} e_{eff,j}\right)}{\varepsilon_{ff} R_{ij}^2}, \\
v_{(i,x),(j,x)} &= v_{(i,y),(j,y)} = \sqrt{\frac{\hbar}{2m_{eff,i}}} \sqrt{\frac{\hbar}{2m_{eff,i}}} \frac{\left(e_{eff,i} e_{eff,j}\right)}{\varepsilon_{ff} R_{ij}^2}, \\
v_{(i,z),(j,z)} &= -2\sqrt{\frac{\hbar}{2m_{eff,i}}} \sqrt{\frac{\hbar}{2m_{eff,i}}} \frac{\left(e_{eff,i} e_{eff,j}\right)}{\varepsilon_{ff} R_{ij}^2}.
\end{aligned} \qquad \text{(S3)}$$

The above operator includes the Coulomb-interaction terms between all three plasmonic quantum oscillations. The easiest way to proceed with the Hamiltonians (S1) and (S3) is to write down the equations of motion in the presence of a monochromatic external field $\mathbf{E} = \mathbf{E}_0 \cos[\omega t]$ for the average velocities and coordinates of the oscillators:

$$\overline{v}_\alpha = \left\langle \Psi(t) \right| \frac{\hat{p}_\alpha}{m} \left| \Psi(t) \right\rangle, \ \overline{x}_\alpha = \left\langle \Psi(t) \right| x_\alpha \left| \Psi(t) \right\rangle.$$

Then, by calculating at the eigen-frequencies of the system, we find the energies of the coupled plasmonic modes. Since the Hamiltonian is quadratic, the equations of motion for our system are simple and have the classical-mechanics form:

$$\begin{aligned}
m_\alpha \frac{dv_\alpha}{dt} &= -k_\alpha x_\alpha + e_{eff,\alpha} E_{on\,\alpha} - m_\alpha \Gamma v_\alpha, \\
E_{on\,\alpha} &= E_{0,\gamma}(t) + \sum_{\beta \neq \alpha} E_{\beta\to\alpha}(t),
\end{aligned} \qquad \text{(S4)}$$

where $E_{on\,\alpha} = E_0(t) + \sum\limits_{\beta \neq \alpha} E_{\beta\to\alpha}(t)$ is the total dynamic field acting on the $\alpha$-oscillator, $E_{\beta\to\alpha}(t)$ is the electric field created by the $\beta$-oscillator and acting on the $\alpha$-oscillator; the rate $\Gamma = 1/\tau$ describes slow energy dissipation in the system. The equations are easy to solve using the symmetry of the system and the standard approach of complex variables. First, consider the incident field in the z-direction (the molecular axis), $\mathbf{E}_0 = \hat{z} \operatorname{Re} E_0 e^{-i\omega t}$. Then, the velocities have only z-components and should be found in the form of $\mathrm{Re}[v_{iz,\omega}e^{-i\omega t}]$. The system of equations for the complex amplitudes of the velocity follows from Eq. S4:

$$\begin{cases} (\omega^2-\omega_{p,Au}^2+i\omega\Gamma)v_{1z,\omega}+\Omega_{Au-Au}^2 v_{2z,\omega}+\Omega_{Au-Ag,a}^2 v_{3z,\omega}=\dfrac{\omega e_{eff,Au}}{m_{eff,Au}}iE_0 \\ \Omega_{Au-Au}^2 v_{1z,\omega}+(\omega^2-\omega_{p,Au}^2+i\omega\Gamma)v_{2z,\omega}+\Omega_{Au-Ag,a}^2 v_{3z,\omega}=\dfrac{\omega e_{eff,Au}}{m_{eff,Au}}iE_0 \\ \Omega_{Au-Ag,b}^2 v_{1z,\omega}+\Omega_{Au-Ag,b}^2 v_{2z,\omega}+(\omega^2-\omega_{p,Ag}^2+i\omega\Gamma)v_{3z,\omega}=\dfrac{\omega e_{eff,Ag}}{m_{eff,Ag}}iE_0 \end{cases}, \quad \text{(S5)}$$

where the key interaction parameters are given by

$$\Omega_{Au-Au}^2=\frac{2e_{eff,Au}^2}{\varepsilon_{eff}m_{eff,Au}R_{12}^3},\quad \Omega_{Au-Ag,a}^2=\frac{2e_{eff,Au}e_{eff,Ag}}{\varepsilon_{eff}m_{eff,Au}R_{13}^3},\quad \Omega_{Au-Ag,b}^2=\frac{2e_{eff,Au}e_{eff,Ag}}{\varepsilon_{eff}m_{eff,Ag}R_{13}^3}.$$

Equation S5 determines the frequencies of plasmonic excitations in the coupled system of three oscillators. In the limit of small dissipation ($\Gamma\to 0$), the eigen-frequencies of the system are given by

$$\det\begin{Bmatrix} \omega^2-\omega_{p,Au}^2 & \Omega_{Au-Au}^2 & \Omega_{Au-Ag,a}^2 \\ \Omega_{Au-Au}^2 & \omega^2-\omega_{p,Au}^2 & \Omega_{Au-Ag,a}^2 \\ \Omega_{Au-Ag,b}^2 & \Omega_{Au-Ag,b}^2 & \omega^2-\omega_{p,Au}^2 \end{Bmatrix}=0\,.$$

This equation has three positive solutions that correspond to the three longitudinal plasmons (L-modes) in our system:

$$\omega_{LD,Au-like}=\sqrt{\omega_{p,Au}^2+\Omega_{Au-Au}^2},$$

$$\omega_{LB,Ag-like}=\sqrt{\frac{\omega_{p,Au}^2+\omega_{p,Ag}^2-\Omega_{Au-Au}^2}{2}+\frac{1}{2}\sqrt{\left(\omega_{p,Ag}^2-\omega_{p,Au}^2\right)^2+8\Omega_{Au-Ag,a}^2\Omega_{Au-Ag,b}^2+\Omega_{Au-Au}^4+2\Omega_{Au-Au}^2\omega_{p,Ag}^2-2\Omega_{Au-Au}^2\omega_{p,Au}^2}},$$

$$\omega_{LB,Au-like}=\sqrt{\frac{\omega_{p,Au}^2+\omega_{p,Ag}^2-\Omega_{Au-Au}^2}{2}-\frac{1}{2}\sqrt{\left(\omega_{p,Ag}^2-\omega_{p,Au}^2\right)^2+8\Omega_{Au-Ag,a}^2\Omega_{Au-Ag,b}^2+\Omega_{Au-Au}^4+2\Omega_{Au-Au}^2\omega_{p,Ag}^2-2\Omega_{Au-Au}^2\omega_{p,Au}^2}}.$$

Two of the L-modes are bright (LB-modes) and one L-mode is dark (LD-mode). In this model, the Ag-like LB-mode experiences a blue shift, and the main Au-like LB-mode shows the red shift. The Au-like LD-mode, that is not active in our experiments, has the blue shift. In a similar way, we can solve the geometry with the T-modes when $\mathbf{E}_0 \parallel \hat{y}$ or $\mathbf{E}_0 \parallel \hat{x}$. The results for these configurations can be obtained from the above equations using the following formal equations for the interaction parameters:

$$\Omega^2_{Au-Au} = -\frac{e^2_{eff,Au}}{\varepsilon_{eff} m_{eff,Au} R^3_{12}}, \quad \Omega^2_{Au-Ag,a} = -\frac{e_{eff,Au} e_{eff,Ag}}{\varepsilon_{eff} m_{eff,Au} R^3_{13}}, \quad \Omega^2_{Au-Ag,b} = -\frac{e_{eff,Au} e_{eff,Ag}}{\varepsilon_{eff} m_{eff,Ag} R^3_{13}}.$$

Figure 4 of the main text summarizes results obtained from the above quantum model. Here we list the model parameters used in our quantum calculations:

(1) Radii of the particles: $R_{Au} = 20nm$ and $R_{Ag} = 15nm$;

(2) Effective optical dielectric constant of the medium: $\varepsilon_{eff} = 2.25$;

(3) Effective charges and effect masses of the electrons in the NPs: $e_{eff,Au} = e \cdot N_{e,Au}$, $e_{eff,Ag} = e \cdot N_{e,Ag}$, $m_{eff,Au} = m_0 \cdot N_{e,Au}$ and $m_{eff,Ag} = m_0 \cdot N_{e,Ag}$.

(4) Effective numbers of free carriers in the NPs: $N_{e,Au} = 1.5 \cdot 10^6$ and $N_{e,Ag} = 0.6 \cdot 10^6$.

We note that the chosen numbers for $N_{e,Au}$ and $N_{e,Ag}$ are of the same order of magnitude as the calculated numbers of free electrons in the Au and Ag NPs. By taking such numbers, we obtain a reasonable agreement with the experiment (Figure 4). This is another supporting argument towards our simplified quantum model of plasmons.

Finally, we should note again that our quantum model is simplified and qualitative, but nevertheless describing the main effects. Three things omitted in our quantum model are: (1) The dielectric screening of the Ag-plasmons due to the core dielectric constant of the Au particles, (2) the interband transitions in gold, and (3) the multipole plasmon-plasmon interactions.

**Supplementary Figure S1. Theory dipoles.** Calculations for the Au-Ag-Au trimer excited with two time-dependent dipoles placed on the left- and right-hand sides of our system. The panels show the field maps and the optical cross sections of our system under **a,** the symmetric and **b,** anti-symmetric local excitations.

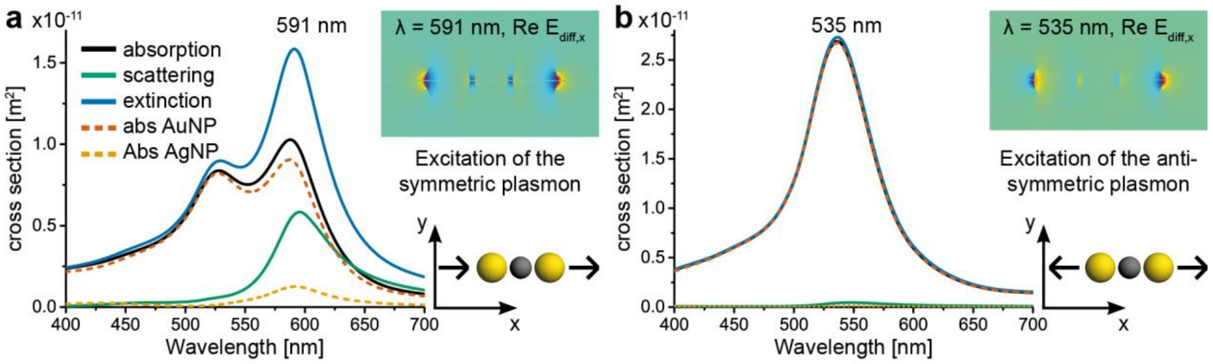

**Supplementary Figure S2. Design of 14hB DNA origami template structure.** The template structure consists of a 200 nm long 14 helix bundle. The scaffold path (blue), the staple oligonucleotides (grey) and the elongated staple oligonucleotides at the nanoparticle attachment sites (red for AuNPs and green for AgNP) are displayed. The metal nanoparticle attachment is done *via* DNA hybridization of the functionalized AuNPs/AgNPs. The difference in the DNA sequence of the attachment site elongations as well as the complementary nanoparticle functionalizations guarantee site specific binding.

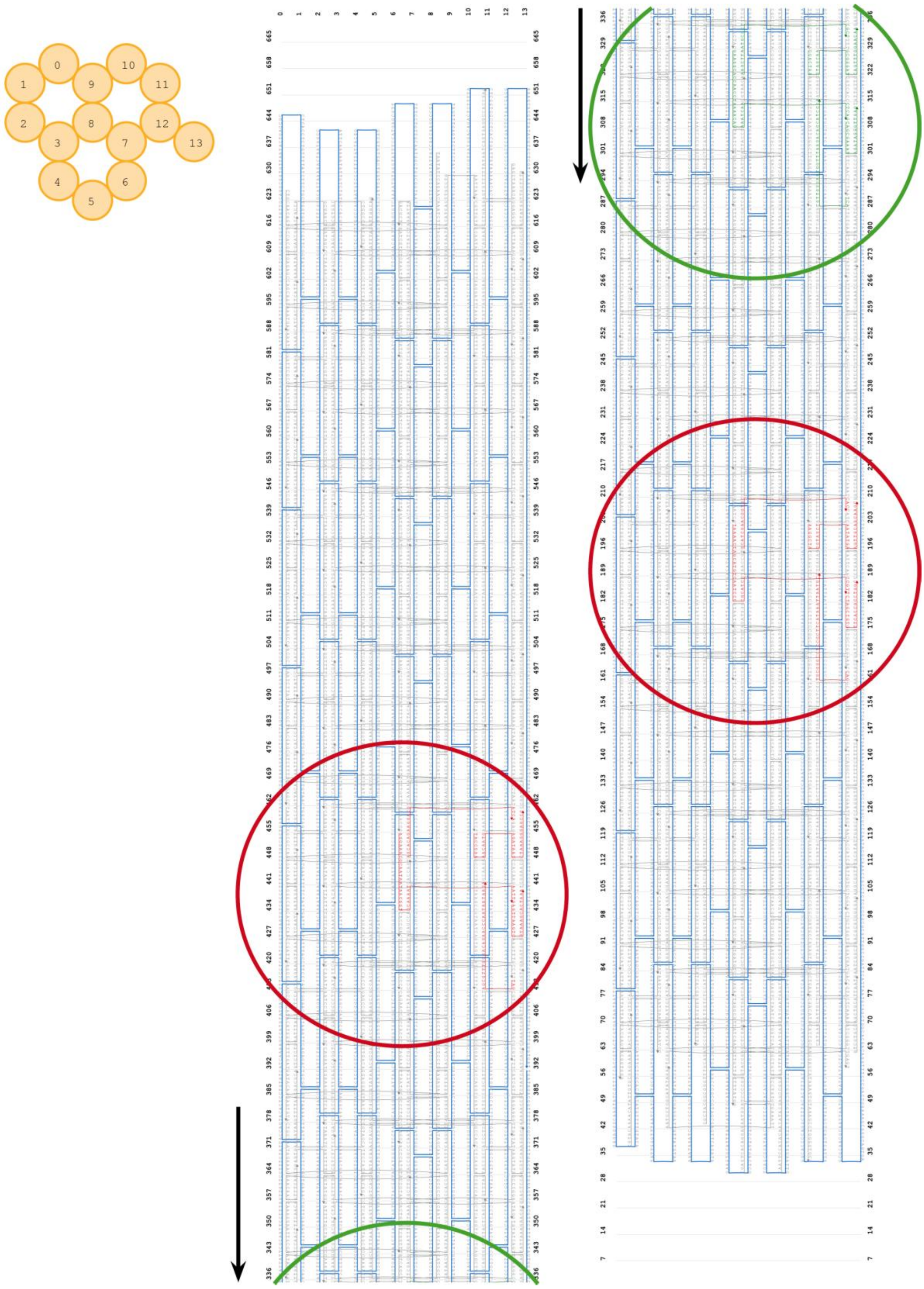

**Supplementary Figure S3. Gel purification of the nanoparticle-functionalized DNA origami structures. a,** Agarose gel purification of the trimer structure with two 40 nm AuNPs and one 30 nm AgNP attached to the DNA origami. **b,** gel purification of the dimer structure with two 40 nm AuNPs attached to the DNA origami.

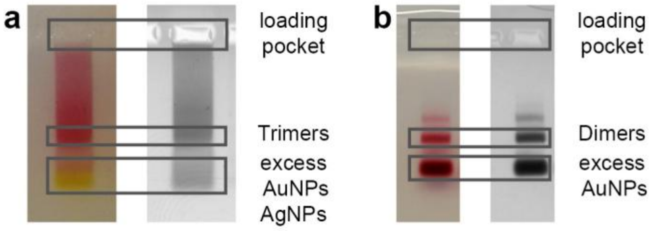

**Supplementary Figure S4. Polarization dependent data of the dimer structure. a,** Polarization resolved scattering spectra of a single AuNP dimer structure and **b,** corresponding simulations. Only a small peak shift between the longitudinal mode and the transversal mode is observed, indicating that the AuNPs are far apart from each other so that they only couple slightly.

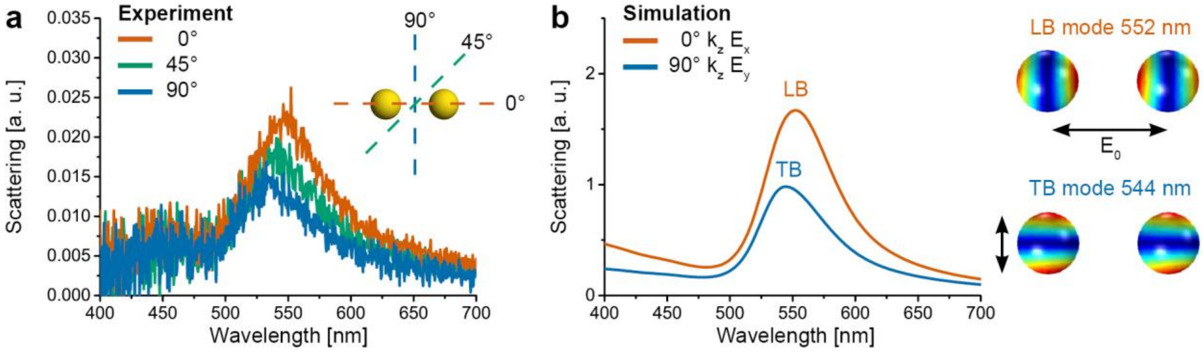

**References:**

1 Schreiber, R. *et al.* Hierarchical assembly of metal nanoparticles, quantum dots and organic dyes using DNA origami scaffolds. *Nat. Nano* **9**, 74-78 (2014).
2 Johnson, P. B. & Christy, R. W. Optical Constants of the Noble Metals. *Phys. Rev. B* **6**, 4370-4379 (1972).
3 Palik, E. D. *Handbook of optical constants of solids*. Vol. 3 (Academic press, 1998).
4 Mahan, G. D. *Many-particle physics*. (Kluwer Academic/ Plenum Publisher, New York, 2000).

# B.5. Supporting Information for P5

## Quantitative single molecule surface-enhanced Raman Scattering by optothermal tuning of DNA origami assembled pasmonic nanoantennas

by

Sabrina Simoncelli*, Eva-Maria Roller*, Patrick Urban, Robert Schreiber,
Andrew J. Turberfield, Tim Liedl, and Theobald Lohmüller
*equal contribution

published in ACS Nano, 10, 9809 - 9815 (2016).

# Supporting Information

# Quantitative Single Molecule Surface-Enhanced Raman Scattering by Optothermal Tuning of DNA Origami-Assembled Plasmonic Nanoantennas

*Sabrina Simoncelli*[1‡], *Eva-Maria Roller*[2‡], *Patrick Urban*[1], *Robert Schreiber*[4], *Andrew J. Turberfield*[4], *Tim Liedl*[2,3*] *and Theobald Lohmüller*[1,3*]

[1]Photonics and Optoelectronics Group, Department of Physics and Center for Nanoscience (CeNS), Ludwig-Maximilians-Universität München, Amalienstraße 54, Munich, 80799, Germany

[2]Department of Physics and Center for Nanoscience (CeNS), Ludwig-Maximilians-Universität München, Geschwister-Scholl-Platz 1, Munich, 80539, Germany

[3]Nanosystems Initiative Munich (NIM), Schellingstraße 4, 80539 Munich, Germany

[4]Clarendon Laboratory, Department of Physics, University of Oxford, Parks Road, Oxford OX1 3PU, United Kingdom

[‡]These authors contributed equally to this work

tim.liedl@physik.lmu.de, t.lohmueller@lmu.de

**Supporting Figure S1:**

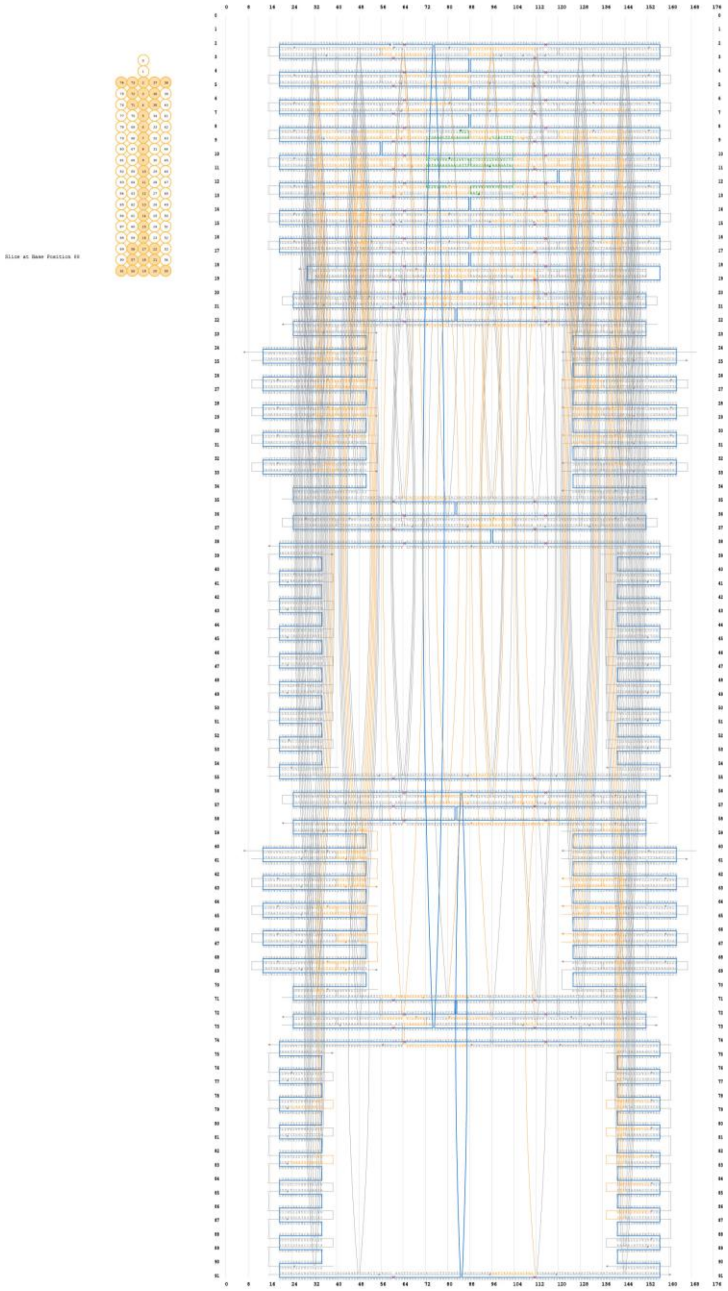

**Figure S1. DNA origami design.** CaDNAno[1] image of the DNA origami template structure. In the schematic picture the scaffold path (blue), the staple oligonucleotides (grey), the attachment sites (orange) for AuNPs and the four potential dyes modified staple oligonucleotides (green) are displayed. The design of the DNA origami is performed to encompass the AuNPs slightly into the structure. This design ensures a rigid dimer conformation with fixed AuNPs positions. The DNA origami has dimensions of ~ 47 nm x 44 nm and consists in the center only of a one layer DNA structure (thickness in solution 2.5 nm). Two DNA modified AuNPs can be attached to the structure via DNA hybridization with 10xA nucleotide long extensions on the 3' end of the orange origami staples. The dye modified staples strands are directly incorporated into the structure whereas the dye modification is performed on the 5' end. The staples used this dye modification are shown in green. Here we used up to four dye modified staples strands so that the total amount of dyes per dimer structure can be varied from 1 to 4 depending on the folding stock solution.

## Supporting Figure S2:

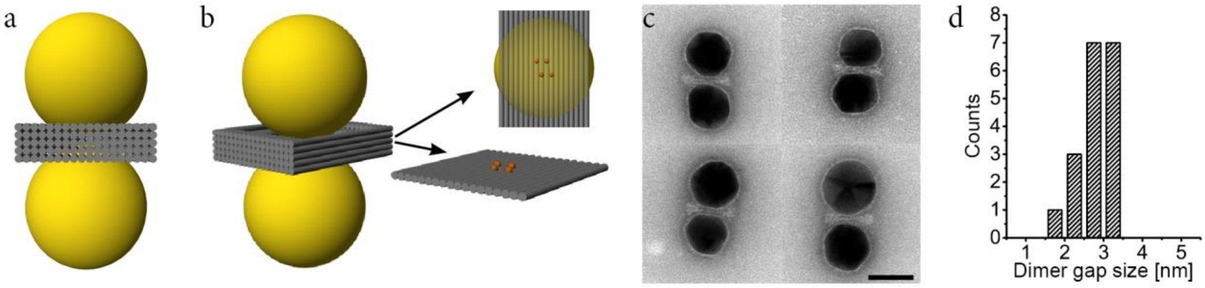

**Figure S2. Dimer structure.** Schematic image of the dimer structure**. (a)** Front view displaying the partial encompassment of the AuNPs into the DNA origami structure. **(b)** Perspective view of the dimer structure design and the position of the four dye modified staples strands in the middle layer of the DNA origami. **(c)** TEM images of the dimer structure. Scale bar 40 nm. TEM images of stained dimer samples revealed an average gap size of ~ 3.1±1.5 nm. **(d)** Histogram of the AuNP gap size determined from the longitudinal plasmon resonance of the dimer structures of Figure 2 and Figure 3 before plasmonic heating.

## Supporting Figure S3:

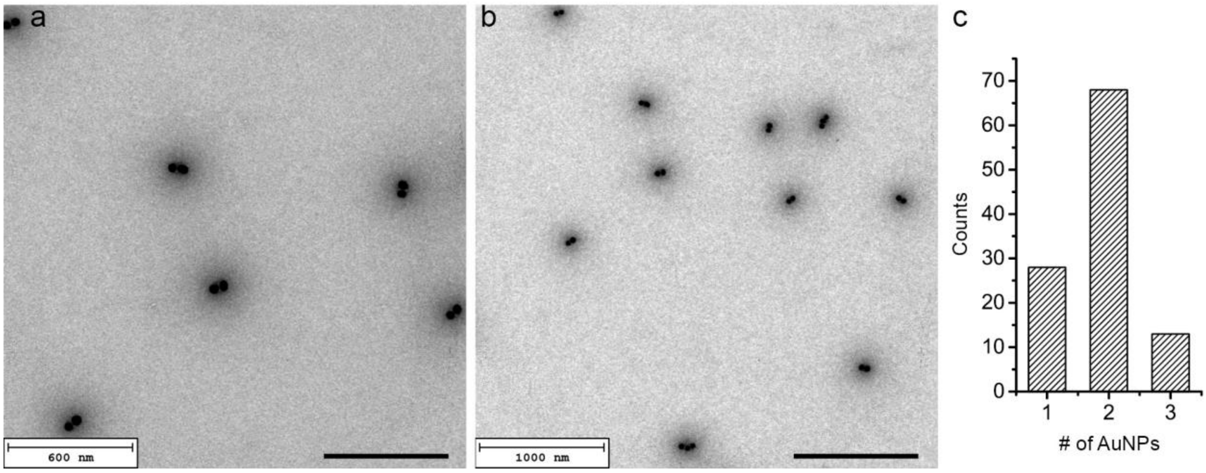

**Figure S3. TEM analysis of the dimer yield. (a)** and **(b)** Wide-field TEM images of dimer structures. **(c)** Histogram of attached AuNPs per DNA origami structure. The synthetic yield of the DNA origami gold dimers is 62 % as verified by TEM images.

**Supporting Figure S4:**

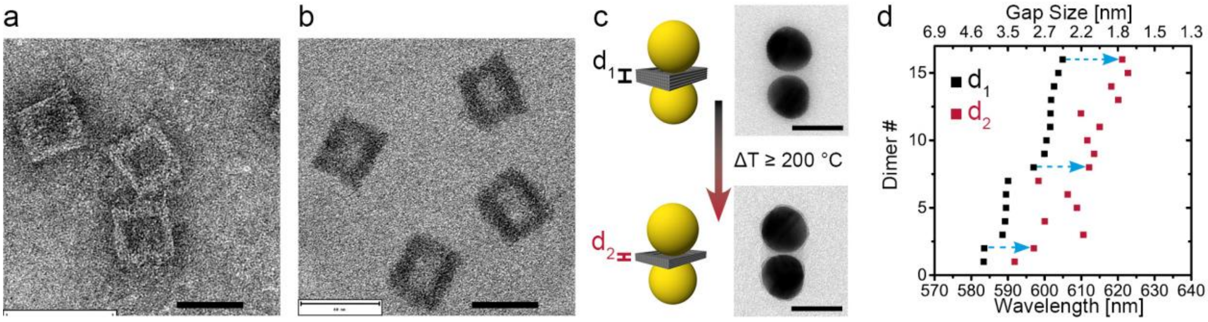

**Figure S4. Thermal heating of the dimer structure.** TEM **image**s of DNA origami structures **(a)** not heated and **(b)** after heating the TEM grid up to 200°C for 5 min. Scale bars 50 nm. **(c)** Schematic diagram and representative TEM images of the plasmonic dimer nanoantenna before and after heating the TEM grid at 200 °C for 5 min. Scale bar, 40 nm. **(d)** Comparison of the dimer plasmon resonance peak measured by single particle Rayleigh scattering spectroscopy of structures before (black) and after (red) thermal treatment (200 °C, 5 min) and corresponding calculated dimer gap size. The nanoparticle gap size shrinked by thermal heating the dried DNA origami dimer nanoparticle structure.

**Supporting Figure S5:**

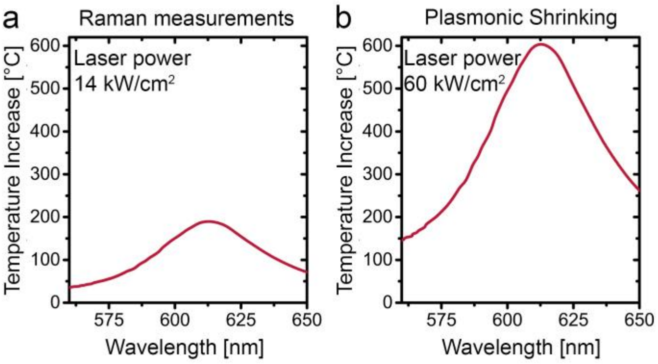

**Figure S5. Temperature simulations.** Numerical simulations of the maximum increase in temperature around an AuNP dimer in air while irradiating the nanostructure with a 612 nm light source at ~ 14 kW/cm$^2$ **(a)** or 60 kW/cm$^2$ **(b)**.

**Supporting Figure S6:**

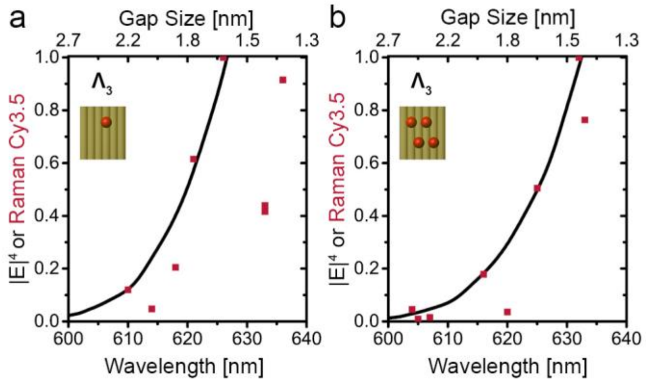

**Figure S6. Additional gap-dependent SERS signal mapping.** Raman scattering intensities (red squares) of the vibrational modes of Cy3.5 located at $\Lambda_3$ (~ 1352 $cm^{-1}$) for the one dye **(a)** and the four dyes dimers structures **(b)**. The data is plotted as a function of the longitudinal plasmon resonance or gap size of the DNA origami AuNPs dimer. The theoretical Raman-scattering enhancement is plotted as black lines and normalized with respect to the gap size for which the highest Raman signal was observed.

## References:

1. Douglas, S. M.; Marblestone, A. H.; Teerapittayanon, S.; Vazquez, A.; Church, G. M.; Shih, W. M., Rapid Prototyping of 3d DNA-Origami Shapes with Cadnano. Nucleic Acids Res. **2009**, 37, 5001-5006.

# List of Figures

# Bibliography

[1] Masciangioli, T. and Zhang, W.X., Peer reviewed: Environmental technologies at the nanoscale, *Environ. Sci. Technol.* **37**, 102A–108A (2003).

[2] Jain, P.K., Huang, X., El-Sayed, I.H., and El-Sayed, M.A., Noble metals on the nanoscale: Optical and photothermal properties and some applications in imaging, sensing, biology, and medicine, *Acc. Chem. Res.* **41**, 1578–1586 (2008).

[3] Mie, G., Beiträge zur Optik trüber Medien, speziell kolloidaler Metallösungen, *Ann. Phys.* **330**, 377–445 (1908).

[4] Lorenz, L., Lysbevægelsen i og uden for en af plane Lysbølger belyst Kugle, vol. 6, (Det Kongelige Danske Videnskabernes Selskabs Skrifter 1890).

[5] Bohm, D. and Pines, D., A collective description of electron interactions: III. Coulomb interactions in a degenerate electron gas, *Phys. Rev.* **92**, 609–625 (1953).

[6] Sau, T.K. and Murphy, C.J., Room temperature, high-yield synthesis of multiple shapes of gold nanoparticles in aqueous solution, *J. Am. Chem. Soc.* **126**, 8648–8649 (2004).

[7] Grzelczak, M., Perez-Juste, J., Mulvaney, P., and Liz-Marzan, L.M., Shape control in gold nanoparticle synthesis, *Chem. Soc. Rev.* **37**, 1783–1791 (2008).

[8] Murphy, C.J., Sau, T.K., Gole, A.M., Orendorff, C.J., Gao, J., Gou, L., Hunyadi, S.E., and Li, T., Anisotropic metal nanoparticles: Synthesis, assembly, and optical applications, *J. Phys. Chem. B* **109**, 13857–13870 (2005).

[9] Mody, V.V., Siwale, R., Singh, A., Mody, H.R. *et al.*, Introduction to metallic nanoparticles, *J. Pharm. BioAllied Sci.* **2**, 282 (2010).

[10] Biswas, A., Bayer, I.S., Biris, A.S., Wang, T., Dervishi, E., and Faupel, F., Advances in top–down and bottom–up surface nanofabrication: Techniques, applications & future prospects, *Adv. Colloid Interface Sci.* **170**, 2 – 27 (2012).

[11] Ventra, M., Evoy, S., and Heflin, J.R., Introduction to nanoscale science and technology, (Springer Science & Business Media 2006).

[12] Mijatovic, D., Eijkel, J.C.T., and van den Berg, A., Technologies for nanofluidic systems: top-down vs. bottom-up-a review, *Lab Chip* **5**, 492–

500 (2005).

[13] Henzie, J., Lee, J., Lee, M.H., Hasan, W., and Odom, T.W., Nanofabrication of plasmonic structures, *Annu. Rev. Phys. Chem.* **60**, 147–165 (2009).

[14] Ozbay, E., Plasmonics: Merging photonics and electronics at nanoscale dimensions, *Science* **311**, 189–193 (2006).

[15] Grzelczak, M., Vermant, J., Furst, E.M., and Liz-Marzán, L.M., Directed self-assembly of nanoparticles, *ACS Nano* **4**, 3591–3605 (2010).

[16] Zhihong Nie, Alla Petukhova, E.K., Properties and emerging applications of self-assembled structures made from inorganic nanoparticles, *Nat. Nanotechnol.* **5**, 15 – 25 (2010).

[17] Rothemund, P.W.K., Folding DNA to create nanoscale shapes and patterns, *Nature* **440**, 297–302 (2006).

[18] Douglas, S.M., Dietz, H., Liedl, T., Hogberg, B., Graf, F., and Shih, W.M., Self-assembly of DNA into nanoscale three-dimensional shapes, *Nature* **459**, 414–418 (2009).

[19] Dietz, H., Douglas, S.M., and Shih, W.M., Folding DNA into twisted and curved nanoscale shapes, *Science* **325**, 725–730 (2009).

[20] Kuzyk, A., Schreiber, R., Fan, Z., Pardatscher, G., Roller, E.M., Högele, A., Simmel, F.C., Govorov, A.O., and Liedl, T., DNA-based self-assembly of chiral plasmonic nanostructures with tailored optical response, *Nature* **483**, 311–314 (2012).

[21] Acuna, G.P., Möller, F.M., Holzmeister, P., Beater, S., Lalkens, B., and Tinnefeld, P., Fluorescence enhancement at docking sites of DNA-directed self-assembled nanoantennas, *Science* **338**, 506–510 (2012).

[22] Friedrich, M., Ueber die chemische Zusammensetzung der Eiterzellen, *Medicinisch-chemische Untersuchungen* **4**, 441–460 (1871).

[23] Levene, P.A., The structure of yeast nucleic acid, *J. Biol. Chem.* **40**, 415–424 (1919).

[24] Hershey, A.D. and Chase, M., Inedpendent functions of viral protein and nucleic acid in growth of bacteriophage, *J. Gen. Physiol.* **36**, 39–56 (1952).

[25] Watson, J. and Crick, F., Molecular Structure of Nucleic Acids: A Structure for Deoxyribose Nucleic Acid, *Nature* **171**, 737–738 (1953).

[26] Wissmann, J., Calladine, C., Drew, H., Luisi, B., and Travers, A., DNA: Das Molekül und seine Funktionsweise, (Spektrum Akademischer Verlag 2005).

[27] John SantaLucia, J., Allawi, H.T., and Seneviratne, P.A., Improved nearest-neighbor parameters for predicting dna duplex stability, *Biochemistry* **35**, 3555–3562 (1996).

[28] Yakovchuk, P., Protozanova, E., and Frank-Kamenetskii, M.D., Base-stacking and base-pairing contributions into thermal stability of the dna

double helix, *Nucleic Acids Res.* **34**, 564–574 (2006).

[29] Egli, M. and Saenger, W., Principles of nucleic acid structure, (Springer Science & Business Media 2013).

[30] Wing, R., Drew, H., Takano, T., Broka, C., Tanaka, S., Itakura, K., and Dickerson, R.E., Crystal structure analysis of a complete turn of B-DNA, *Nature* **287**, 755 – 758 (1980).

[31] Dickerson, R., Drew, H., Conner, B., Wing, R., Fratini, A., and Kopka, M., The anatomy of A-, B-, and Z-DNA, *Science* **216**, 475–485 (1982).

[32] Seeman, N.C., Nucleic acid junctions and lattices, *J. Theor. Biol.* **99**, 237 – 247 (1982).

[33] Pinheiro, A.V., Han, D., Shih, W.M., and Yan, H., Challenges and opportunities for structural DNA nanotechnology, *Nat. Nanotechnol.* **6**, 763–772 (2011).

[34] Seeman, N.C., An overview of structural DNA nanotechnology, *Mol. Biotechnol.* **37**, 246–257 (2007).

[35] Seeman, N.C., Nanomaterials based on DNA, *Annu. Rev. Biochem.* **79**, 65–87 (2010).

[36] Hagerman, P.J., Flexibility of DNA, *Annu. Rev. Biophys. Biophys. Chem.* **17**, 265–286 (1988).

[37] Taylor, W.H. and Hagerman, P.J., Application of the method of phage T4 DNA ligase-catalyzed ring-closure to the study of DNA structure: Ii. NaCl-dependence of DNA flexibility and helical repeat, *J. Mol. Biol.* **212**, 363–376 (1990).

[38] Bustamante, C., Marko, J., Siggia, E., and Smith, S., Entropic elasticity of lambda-phage DNA, *Science* **265**, 1599–1600 (1994).

[39] Holliday, R., A mechanism for gene conversion in fungi, *Genet. Res.* **5**, 282–304 (1964).

[40] Lilley, D.M. and Clegg, R.M., The structure of the four-way junction in DNA, *Annu. Rev. Biophys. Biomol. Struct.* **22**, 299–328 (1993).

[41] Chen, J. and Seeman, N.C., Synthesis from DNA of a molecule with the connectivity of a cube, *Nature* **350**, 631–633 (1991).

[42] Shih, W.M., Quispe, J.D., and Joyce, G.F., A 1.7-kilobase single-stranded DNA that folds into a nanoscale octahedron, *Nature* **427**, 618–621 (2004).

[43] Winfree, E., Liu, F., Wenzler, L.A., and Seeman, N.C., Design and self-assembly of two-dimensional DNA crystals, *Nature* **394**, 539–544 (1998).

[44] Andersen, E.S., Dong, M., Nielsen, M.M., Jahn, K., Subramani, R., Mamdouh, W., Golas, M.M., Sander, B., Stark, H., Oliveira, C.L. *et al.*, Self-assembly of a nanoscale DNA box with a controllable lid, *Nature* **459**, 73–76 (2009).

[45] Ke, Y., Sharma, J., Liu, M., Jahn, K., Liu, Y., and Yan, H., Scaffolded DNA origami of a DNA tetrahedron molecular container, *Nano Lett.* **9**, 2445–2447 (2009).

[46] Ding, B., Deng, Z., Yan, H., Cabrini, S., Zuckermann, R.N., and Bokor, J., Gold nanoparticle self-similar chain structure organized by DNA origami, *J. Am. Chem. Soc.* **132**, 3248–3249, pMID: 20163139 (2010).

[47] Zhao, Y.X., Shaw, A., Zeng, X., Benson, E., Nyström, A.M., and Högberg, B., DNA origami delivery system for cancer therapy with tunable release properties, *ACS nano* **6**, 8684–8691 (2012).

[48] Smith, D., Schüller, V., Engst, C., Rädler, J., and Liedl, T., Nucleic acid nanostructures for biomedical applications, *Nanomedicine* **8**, 105–121 (2013).

[49] Schüller, V.J., Heidegger, S., Sandholzer, N., Nickels, P.C., Suhartha, N.A., Endres, S., Bourquin, C., and Liedl, T., Cellular immunostimulation by CpG-sequence-coated DNA origami structures, *ACS Nano* **5**, 9696–9702 (2011).

[50] Steinhauer, C., Jungmann, R., Sobey, T., Simmel, F., and Tinnefeld, P., DNA origami as a nanoscopic ruler for super-resolution microscopy, *Angew. Chem., Int. Ed.* **48**, 8870–8873 (2009).

[51] Jungmann, R., Steinhauer, C., Scheible, M., Kuzyk, A., Tinnefeld, P., and Simmel, F.C., Single-molecule kinetics and super-resolution microscopy by fluorescence imaging of transient binding on DNA origami, *Nano Lett.* **10**, 4756–4761 (2010).

[52] Jungmann, R., Avendano, M.S., Woehrstein, J.B., Dai, M., Shih, W.M., and Yin, P., Multiplexed 3D cellular super-resolution imaging with DNA-PAINT and Exchange-PAINT, *Nat. Methods* **11**, 313–318 (2014).

[53] Pal, S., Deng, Z., Ding, B., Yan, H., and Liu, Y., DNA-origami-directed self-assembly of discrete silver-nanoparticle architectures, *Angew. Chem.* **122**, 2760–2764 (2010).

[54] Sharma, J., Ke, Y., Lin, C., Chhabra, R., Wang, Q., Nangreave, J., Liu, Y., and Yan, H., DNA-tile-directed self-assembly of quantum dots into two-dimensional nanopatterns, *Angew. Chem., Int. Ed.* **47**, 5157–5159 (2008).

[55] Bui, H., Onodera, C., Kidwell, C., Tan, Y., Graugnard, E., Kuang, W., Lee, J., Knowlton, W.B., Yurke, B., and Hughes, W.L., Programmable periodicity of quantum dot arrays with DNA origami nanotubes, *Nano Lett.* **10**, 3367–3372 (2010).

[56] Schreiber, R., Do, J., Roller, E.M., Zhang, T., Schüller, V.J., Nickels, P.C., Feldmann, J., and Liedl, T., Hierarchical assembly of metal nanoparticles, quantum dots and organic dyes using DNA origami scaffolds, *Nat. Nanotechnol.* **9**, 74–78 (2014).

[57] Kuzyk, A., Schreiber, R., Zhang, H., Govorov, A.O., Liedl, T., and Liu, N., Reconfigurable 3D plasmonic metamolecules, *Nat. Mater.* **13**, 862–866 (2014).

[58] Saha, K., Agasti, S.S., Kim, C., Li, X., and Rotello, V.M., Gold nanoparticles in chemical and biological sensing, *Chemical reviews* **112**, 2739–2779 (2012).

[59] Barnes, W.L., Dereux, A., and Ebbesen, T.W., Surface plasmon subwavelength optics, *Nature* **424**, 824–830 (2003).

[60] Westphalen, M., Kreibig, U., Rostalski, J., Lüth, H., and Meissner, D., Metal cluster enhanced organic solar cells, *Solar Energy Materials and Solar Cells* **61**, 97–105 (2000).

[61] Maier, S.A., Plasmonics: fundamentals and applications, (Springer Science & Business Media 2007).

[62] Maradudin, A.A., Sambles, J.R., and Barnes, W.L., Modern Plasmonics, vol. 4, (Elsevier 2014).

[63] Uwe Kreibig, M.V., Optical Properties of Metal Clusters, vol. 25, (Springer Series in Materials Science 1995).

[64] Quinten, M., Optical properties of nanoparticle systems: Mie and beyond, (John Wiley & Sons 2010).

[65] Zeman, E.J. and Schatz, G.C., An accurate electromagnetic theory study of surface enhancement factors for silver, gold, copper, lithium, sodium, aluminum, gallium, indium, zinc, and cadmium, *J. Phys. Chem. C* **91**, 634–643 (1987).

[66] Johnson, P.B. and Christy, R.W., Optical constants of the noble metals, *Phys. Rev. B* **6**, 4370–4379 (1972).

[67] Palik, E.D., Handbook of optical constants of solids, vol. 3, (Academic press 1998).

[68] Jackson, J.D., Classical electrodynamics, (Wiley 1999).

[69] Tipler, P.A., Physik, (Spektrum Akademischer Verlag 1994).

[70] Craig F. Bohren, D.R.H., Absorption and Scattering of Light by Small Particles, (Wiley-VCH Verlag GmbH & co. KGaA, Weinheim 2004).

[71] Nordlander, P., Oubre, C., Prodan, E., Li, K., , and Stockman, M.I., Plasmon hybridization in nanoparticle dimers, *Nano Lett.* **4**, 899–903 (2004).

[72] Sheikholeslami, S., wook Jun, Y., Jain, P.K., and Alivisatos, A.P., Coupling of optical resonances in a compositionally asymmetric plasmonic nanoparticle dimer, *Nano Lett.* **10**, 2655–2660 (2010).

[73] Jain, P.K. and El-Sayed, M.A., Plasmonic coupling in noble metal nanostructures, *Chem. Phys. Lett.* **487**, 153 – 164 (2010).

[74] Jain, P.K., Eustis, S., and El-Sayed, M.A., Plasmon coupling in nanorod assemblies: Optical absorption, discrete dipole approximation simulation,

and exciton-coupling model, *J. Phys. Chem. B* **110**, 18243–18253 (2006).

[75] Govorov, A.O. and Richardson, H.H., Generating heat with metal nanoparticles, *Nano Today* **2**, 30 – 38 (2007).

[76] von Cube, F., Irsen, S., Diehl, R., Niegemann, J., Busch, K., and Linden, S., From isolated metaatoms to photonic metamaterials: Evolution of the plasmonic near-field, *Nano Lett.* **13**, 703–708 (2013).

[77] Pendry, J., Holden, A., Robbins, D., and Stewart, W., Magnetism from conductors and enhanced nonlinear phenomena, *IEEE Trans. Microwave Theory Tech.* **47**, 2075 – 2084 (1999).

[78] Maxwell, J.C., A dynamical theory of the electromagnetic field, *Philos. Trans. R. Soc. London* **155**, 459–512 (1865).

[79] Shelby, R.A., Smith, D.R., and Schultz, S., Experimental verification of a negative index of refraction, *Science* **292**, 77–79 (2001).

[80] Gwinner, M.C., Koroknay, E., Fu, L., Patoka, P., Kandulski, W., Giersig, M., and Giessen, H., Periodic large-area metallic split-ring resonator metamaterial fabrication based on shadow nanosphere lithography, *Small* **5**, 400–406 (2009).

[81] Zhou, J., Koschny, T., Kafesaki, M., Economou, E.N., Pendry, J.B., and Soukoulis, C.M., Saturation of the magnetic response of split-ring resonators at optical frequencies, *Phys. Rev. Lett.* **95**, 223902 (2005).

[82] Klein, M.W., Enkrich, C., Wegener, M., Soukoulis, C.M., and Linden, S., Single-slit split-ring resonators at optical frequencies: limits of size scaling, *Opt. Lett.* **31**, 1259–1261 (2006).

[83] O'Brien, S., McPeake, D., Ramakrishna, S.A., and Pendry, J.B., Near-infrared photonic band gaps and nonlinear effects in negative magnetic metamaterials, *Phys. Rev. B* **69**, 241101 (2004).

[84] Zhang, S., Fan, W., Panoiu, N.C., Malloy, K.J., Osgood, R.M., and Brueck, S.R.J., Experimental Demonstration of Near-Infrared Negative-Index Metamaterials, *Phys. Rev. Lett.* **95**, 137404 (2005).

[85] Lahiri, B., McMeekin, S.G., Khokhar, A.Z., Rue, R.M.D.L., and Johnson, N.P., Magnetic response of split ring resonators (SRRs) at visible frequencies, *Opt. Express* **18**, 3210–3218 (2010).

[86] Mary, A., Rodrigo, S.G., Garcia-Vidal, F.J., and Martin-Moreno, L., Theory of negative-refractive-index response of double-fishnet structures, *Phys. Rev. Lett.* **101**, 103902 (2008).

[87] Kafesaki, M., Tsiapa, I., Katsarakis, N., Koschny, T., Soukoulis, C.M., and Economou, E.N., Left-handed metamaterials: The fishnet structure and its variations, *Phys. Rev. B* **75**, 235114 (2007).

[88] Valentine, J., Zhang, S., Zentgraf, T., Ulin-Avila, E., Genov, D.A., Bartal, G., and Zhang, X., Three-dimensional optical metamaterial with a negative

refractive index, *Nature* **455**, 376–379 (2008).

[89] Ni, X., Emani, N.K., Kildishev, A.V., Boltasseva, A., and Shalaev, V.M., Broadband light bending with plasmonic nanoantennas, *Science* **335**, 427–427 (2012).

[90] Yang, S., Ni, X., Yin, X., Kante, B., Zhang, P., Zhu, J., Wang, Y., and Zhang, X., Feedback-driven self-assembly of symmetry-breaking optical metamaterials in solution, *Nat. Nanotechnol.* **9**, 1002–1006 (2014).

[91] Kante, B., O'Brien, K., Niv, A., Yin, X., and Zhang, X., Proposed isotropic negative index in three-dimensional optical metamaterials, *Phys. Rev. B* **85**, 041103 (2012).

[92] Pendry, J.B., A Chiral Route to Negative Refraction, *Science* **306**, 1353–1355 (2004).

[93] Alù, A., Salandrino, A., and Engheta, N., Negative effective permeability and left-handed materials at optical frequencies, *Opt. Express* **14**, 1557–1567 (2006).

[94] Alù, A. and Engheta, N., Dynamical theory of artificial optical magnetism produced by rings of plasmonic nanoparticles, *Phys. Rev. B* **78**, 085112 (2008).

[95] Alu, A. and Engheta, N., The quest for magnetic plasmons at optical frequencies, *Opt. Express* **17**, 5723–5730 (2009).

[96] Shafiei, F., Monticone, F., Le, K.Q., Liu, X.X., Hartsfield, T., Alu, A., and Li, X., A subwavelength plasmonic metamolecule exhibiting magnetic-based optical fano resonance, *Nat. Nanotechnol.* **8**, 95–99 (2013).

[97] Roller, E.M., Khorashad, L.K., Fedoruk, M., Schreiber, R., Govorov, A.O., and Liedl, T., DNA-assembled nanoparticle rings exhibit electric and magnetic resonances at visible frequencies, *Nano Lett.* **15**, 1368–1373, pMID: 25611357 (2015).

[98] Wang, P., Gaitanaros, S., Lee, S., Bathe, M., Shih, W.M., and Ke, Y., Programming self-assembly of DNA origami honeycomb two-dimensional lattices and plasmonic metamaterials, *J. Am. Chem. Soc.* **138**, 7733–7740 (2016).

[99] Tame, M.S., McEnery, K.R., Özdemir, .K., Lee, J., Maier, S.a., and Kim, M.S., Quantum plasmonics, *Nat. Phys.* **9**, 329–340 (2013).

[100] Gonzalez-Ballestero, C., Feist, J., Moreno, E., and Garcia-Vidal, F.J., Harvesting excitons through plasmonic strong coupling, *Phys. Rev. B* **92**, 121402 (2015).

[101] Tam, J.M.S.F., Halas, N.J., and Naik, R.R., Peptide-assembled optically responsive nanoparticle complexes, *Nano Lett.* **7**, 1054–1058 (2007).

[102] Törmä, P. and Barnes, W.L., Strong coupling between surface plasmon polaritons and emitters: A review, *Rep. Prog. Phys.* **78**, 013901 (2015).

[103] Thompson, R.J., Rempe, G., and Kimble, H.J., Observation of normal-mode splitting for an atom in an optical cavity, *Phys. Rev. Lett.* **68**, 1132–1135 (1992).

[104] Gröblacher, S., Hammerer, K., Vanner, M.R., and Aspelmeyer, M., Observation of strong coupling between a micromechanical resonator and an optical cavity fiel, *Nature* **460**, 724–727 (2009).

[105] Yoshie, T., Scherer, A., Hendrickson, J., Khitrova, G., Gibbs, H.M., Rupper, G., Ell, C., Shchekin, O.B., and Deppe, D.G., Vacuum rabi splitting with a single quantum dot in a photonic crystal nanocavity, *Nature* **432**, 200–203 (2004).

[106] Purcell, E.M., Spontaneous emission probabilities at radio frequencies, *Phys. Rev.* **69**, 681 (1946).

[107] Kleppner, D., Inhibited spontaneous emission, *Phys. Rev. Lett.* **47**, 233–236 (1981).

[108] Manjavacas, A., de Abajo, F.J.G., and Nordlander, P., Quantum plexcitonics: Strongly interacting plasmons and excitons, *Nano Lett.* **11**, 2318–2323 (2011).

[109] Antosiewicz, T.J., Apell, S.P., and Shegai, T., Plasmon-exciton interactions in a core-shell geometry: From enhanced absorption to strong coupling, *ACS Photonics* **1**, 454–463 (2014).

[110] Gómez, D.E., Giessen, H., and Davis, T.J., Semiclassical plexcitonics: Simple approach for designing plexcitonic nanostructures, *J. Phys. Chem. C* **118**, 23963–23969 (2014).

[111] Bellessa, J., Bonnand, C., Plenet, J.C., and Mugnier, J., Strong coupling between surface plasmons and excitons in an organic semiconductor, *Phys. Rev. Lett.* **93**, 036404 (2004).

[112] Bellessa, J., Symonds, C., Vynck, K., Lemaitre, A., Brioude, A., Beaur, L., Plenet, J.C., Viste, P., Felbacq, D., Cambril, E., and Valvin, P., Giant Rabi splitting between localized mixed plasmon-exciton states in a two-dimensional array of nanosize metallic disks in an organic semiconductor, *Phys. Rev. B* **80**, 033303 (2009).

[113] Zengin, G., Johansson, G., Johansson, P., Antosiewicz, T.J., Käll, M., and Shegai, T., Approaching the strong coupling limit in single plasmonic nanorods interacting with J-aggregates., *Sci. Rep.* **3**, 3074 (2013).

[114] Schlather, A.E., Large, N., Urban, A.S., Nordlander, P., and Halas, N.J., Near-field mediated plexcitonic coupling and giant Rabi splitting in individual metallic dimers, *Nano Lett.* **13**, 3281–3286 (2013).

[115] Fofang, N.T., Grady, N.K., Fan, Z., Govorov, A.O., and Halas, N.J., Plexciton dynamics: Exciton-plasmon coupling in a J-aggregate-Au nanoshell complex provides a mechanism for nonlinearity, *Nano Lett.* **11**, 1556–1560

(2011).

[116] Zengin, G., Wersäll, M., Nilsson, S., Antosiewicz, T.J., Käll, M., and Shegai, T., Realizing strong light-matter interactions between single-nanoparticle plasmons and molecular excitons at ambient conditions, *Phys. Rev. Lett.* **114**, 157401 (2015).

[117] DeLacy, B.G., Miller, O.D., Hsu, C.W., Zander, Z., Lacey, S., Yagloski, R., Fountain, A.W., Valdes, E., Anquillare, E., Soljačić, M., Johnson, S.G., and Joannopoulos, J.D., Coherent plasmon-exciton coupling in silver platelet-J-aggregate nanocomposites, *Nano Lett.* **15**, 2588–2593 (2015).

[118] Chikkaraddy, R., de Nijs, B., Benz, F., Barrow, S.J., Scherman, O.A., Rosta, E., Demetriadou, A., Fox, P., Hess, O., and Baumberg, J.J., Single-molecule strong coupling at room temperature in plasmonic nanocavities, *Nature* **535**, 127–130 (2016).

[119] Santhosh, K., Bitton, O., Chuntonov, L., and Haran, G., Vacuum Rabi splitting in a plasmonic cavity at the single quantum emitter limit, *Nat. Commun.* **7**, ncomms11823 (2016).

[120] Roller, E.M., Argyropoulos, C., Högele, A., Liedl, T., and Pilo-Pais, M., Plasmon-exciton coupling using DNA templates, *Nano Lett.* **16**, 5962–5966 (2016).

[121] Lekeufack, D.D., Brioude, A., Coleman, A.W., Miele, P., Bellessa, J., De Zeng, L., and Stadelmann, P., Core-shell gold J-aggregate nanoparticles for highly efficient strong coupling applications, *Appl. Phys. Lett.* **96**, 253107 (2010).

[122] Savage, K.J., Hawkeye, M.M., Esteban, R., Borisov, A.G., Aizpurua, J., and Baumberg, J.J., Revealing the quantum regime in tunnelling plasmonics, *Nature* **491**, 574–577 (2012).

[123] Lewis, D.G. and Johnson, W.C., Circular dichroism of dna in the vacuum ultraviolet, *J. Mol. Biol.* **86**, 91–96 (1974).

[124] Baumruk, V. and Keiderling, T.A., Vibrational circular dichroism of proteins in water solution, *J. Am. Chem. Soc.* **115**, 6939–6942 (1993).

[125] Berova, N. and Nakanishi, K., Circular dichroism: principles and applications, (John Wiley & Sons 2000).

[126] Woody, R.W., [4] circular dichroism, in Biochemical Spectroscopy, *Methods in Enzymology*, vol. 246, 34 – 71, (Academic Press1995).

[127] Kypr, J., Kejnovská, I., Renciuk, D., and Vorlícková, M., Circular dichroism and conformational polymorphism of dna, *Nucleic Acids Res.* **37**, 1713–1725 (2009).

[128] Kelly, S.M. and Price, N.C., The use of circular dichroism in the investigation of protein structure and function, *Curr. Protein Pept. Sci.* **1**, 349–384 (2000).

[129] Anker, J.N., Hall, W.P., Lyandres, O., Shah, N.C., Zhao, J., and Van Duyne, R.P., Biosensing with plasmonic nanosensors, *Nat. Mater.* **7**, 442–453 (2008).

[130] Govorov, A.O., Fan, Z., Hernandez, P., Slocik, J.M., and Naik, R.R., Theory of circular dichroism of nanomaterials comprising chiral molecules and nanocrystals: Plasmon enhancement, dipole interactions, and dielectric effects, *Nano Lett.* **10**, 1374–1382 (2010).

[131] Eyring, H., Liu, H.C., and Caldwell, D., Optical rotatory dispersion and circular dichroism, *Chem. Rev.* **68**, 525–540 (1968).

[132] Rosenfeld, L., Quantenmechanische Theorie der natürlichen optischen Aktivität von Flüssigkeiten und Gasen, *Zeitschrift für Physik* **52**, 161–174 (1928).

[133] Zhang, H. and Govorov, A.O., Giant circular dichroism of a molecule in a region of strong plasmon resonances between two neighboring gold nanocrystals, *Phys. Rev. B* **87**, 075410 (2013).

[134] Gérard, V.A., Gun'ko, Y.K., Defrancq, E., and Govorov, A.O., Plasmon-induced cd response of oligonucleotide-conjugated metal nanoparticles, *Chem. Commun.* **47**, 7383–7385 (2011).

[135] Maoz, B.M., Chaikin, Y., Tesler, A.B., Elli, O.B., Fan, Z., Govorov, A.O., and Markovich, G., Amplification of chiroptical activity of chiral biomolecules by surface plasmons, *Nano Lett.* **13**, 1203–1209 (2013).

[136] Slocik, J.M., Govorov, A.O., and Naik, R.R., Plasmonic circular dichroism of peptide-functionalized gold nanoparticles, *Nano Lett.* **11**, 701–705 (2011).

[137] Shukla, N., Bartel, M.A., and Gellman, A.J., Enantioselective separation on chiral Au nanoparticles, *J. Am. Chem. Soc.* **132**, 8575–8580 (2010).

[138] Han, B., Zhu, Z., Li, Z., Zhang, W., and Tang, Z., Conformation modulated optical activity enhancement in chiral cysteine and au nanorod assemblies, *Journal of the American Chemical Society* **136**, 16104–16107 (2014).

[139] Shemer, G., Krichevski, O., Markovich, G., Molotsky, T., Lubitz, I., and Kotlyar, A.B., Chirality of silver nanoparticles synthesized on DNA, *J. Am. Chem. Soc.* **128**, 11006–11007 (2006).

[140] Rao, C., Wang, Z.G., Li, N., Zhang, W., Xu, X., and Ding, B., Tunable optical activity of plasmonic dimers assembled by dna origami, *Nanoscale* **7**, 9147–9152 (2015).

[141] Scholes, G.D., Fleming, G.R., Olaya-Castro, A., and van Grondelle, R., Lessons from nature about solar light harvesting, *Nat. Chem.* **3**, 763–774 (2011).

[142] Green, M.A., Third generation photovoltaics: solar cells for 2020 and beyond, *Phys. E* **14**, 65–70 (2002).

[143] Forster, T., Disc, *Faraday Soc.* **27** (1959).

[144] Dexter, D.L., A theory of sensitized luminescence in solids, *J. Chem. Phys* **21**, 836–850 (1953).

[145] Vitanov, N.V., Halfmann, T., Shore, B.W., and Bergmann, K., Laser-induced population transfer by adiabatic passage techniques, *Annu. Rev. Phys. Chem.* **52**, 763–809 (2001).

[146] Bergmann, K., Theuer, H., and Shore, B., Coherent population transfer among quantum states of atoms and molecules, *Rev. Mod. Phys.* **70**, 1003 (1998).

[147] Gaubatz, U., Rudecki, P., Schiemann, S., and Bergmann, K., Population transfer between molecular vibrational levels by stimulated Raman scattering with partially overlapping laser fields. A new concept and experimental results, *J. Chem. Phys.* **92**, 5363–5376 (1990).

[148] Greentree, A.D., Cole, J.H., Hamilton, A., and Hollenberg, L.C., Coherent electronic transfer in quantum dot systems using adiabatic passage, *Phys. Rev. B* **70**, 235317 (2004).

[149] Eckert, K., Lewenstein, M., Corbalán, R., Birkl, G., Ertmer, W., and Mompart, J., Three-level atom optics via the tunneling interaction, *Phys. Rev. A* **70**, 023606 (2004).

[150] Longhi, S., Della Valle, G., Ornigotti, M., and Laporta, P., Coherent tunneling by adiabatic passage in an optical waveguide system, *Phys. Rev. B* **76**, 201101 (2007).

[151] Longhi, S., Transfer of light waves in optical waveguides via a continuum, *Phys. Rev. A* **78**, 013815 (2008).

[152] Ornigotti, M., Della Valle, G., Fernandez, T.T., Coppa, A., Foglietti, V., Laporta, P., and Longhi, S., Visualization of two-photon Rabi oscillations in evanescently coupled optical waveguides, *J. Phys. B: At., Mol. Opt. Phys.* **41**, 085402 (2008).

[153] Shegai, T., Chen, S., Miljkovic, V.D., Zengin, G., Johansson, P., and Kall, M., A bimetallic nanoantenna for directional colour routing, *Nat. Commun.* **2**, 481 (2011).

[154] Xu, L., Tan, L.S., and Hong, M.H., Tuning of localized surface plasmon resonance of well-ordered Ag/Au bimetallic nanodot arrays by laser interference lithography and thermal annealing, *Appl. Opt.* **50**, G74–G79 (2011).

[155] Lee, J.H., Kim, G.H., and Nam, J.M., Directional synthesis and assembly of bimetallic nanosnowmen with DNA, *J. Am. Chem. Soc.* **134**, 5456–5459 (2012).

[156] Lee, J.H., You, M.H., Kim, G.H., and Nam, J.M., Plasmonic nanosnowmen with a conductive junction as highly tunable nanoantenna structures and sensitive, quantitative and multiplexable surface-enhanced Raman scatter-

ing probes, *Nano Lett.* **14**, 6217–6225 (2014).

[157] Weller, L., Thacker, V.V., Herrmann, L.O., Hemmig, E.A., Lombardi, A., Keyser, U.F., and Baumberg, J.J., Gap-dependent coupling of Ag-Au nanoparticle heterodimers using DNA origami-based self-assembly, *ACS Photonics* **0**, null (2016).

[158] Raman, C.V. and Krishnan, K.S., A new type of secondary radiation, *Nature* **121**, 501–502 (1928).

[159] Landsberg, G., Eine neue Erscheinung bei der Lichtzerstreuung in Krystallen, *Naturwissenschaften* **16**, 558 (1928).

[160] Smekal, A., Zur Quantentheorie der Dispersion, *Naturwissenschaften* **11**, 873–875 (1923).

[161] Banwell, C.N., McCash, E.M. *et al.*, Fundamentals of molecular spectroscopy, (McGraw-Hill London 1972).

[162] Colthup, N., Introduction to infrared and Raman spectroscopy, (Elsevier 2012).

[163] Stiles, P.L., Dieringer, J.A., Shah, N.C., and Van Duyne, R.P., Surface-enhanced Raman spectroscopy, *Annu. Rev. Anal. Chem.* **1**, 601–626 (2008).

[164] McFarland, A.D., Young, M.A., Dieringer, J.A., and Van Duyne, R.P., Wavelength-scanned surface-enhanced Raman excitation spectroscopy, *J. Phys. Chem. B* **109**, 11279–11285 (2005).

[165] Jeanmaire, D.L. and Duyne, R.P.V., Surface Raman spectroelectrochemistry, *J. Electroanal. Chem. Interfacial Electrochem.* **84**, 1 – 20 (1977).

[166] Nie, S. and Emory, S.R., Probing single molecules and single nanoparticles by surface-enhanced Raman scattering, *Science* **275**, 1102–1106 (1997).

[167] Kneipp, K., Wang, Y., Kneipp, H., Perelman, L.T., Itzkan, I., Dasari, R.R., and Feld, M.S., Single molecule detection using surface-enhanced Raman scattering (SERS), *Phys. Rev. Lett.* **78**, 1667 (1997).

[168] Moskovits, M., Surface-enhanced Raman spectroscopy: a brief retrospective, *J. Raman Spectrosc.* **36**, 485–496 (2005).

[169] Le Ru, E., Blackie, E., Meyer, M., and Etchegoin, P.G., Surface enhanced Raman scattering enhancement factors: a comprehensive study, *J. Phys. Chem. C* **111**, 13794–13803 (2007).

[170] Graham, D., Thompson, D.G., Smith, W.E., and Faulds, K., Control of enhanced Raman scattering using a DNA-based assembly process of dye-coded nanoparticles, *Nat. Nanotechnol.* **3**, 548–551 (2008).

[171] Lim, D.K., Jeon, K.S., Kim, H.M., Nam, J.M., and Suh, Y.D., Nanogap-engineerable Raman-active nanodumbbells for single-molecule detection, *Nat. Mater.* **9**, 60–67 (2010).

[172] Kühler, P., Roller, E.M., Schreiber, R., Liedl, T., Lohmüller, T., and Feldmann, J., Plasmonic DNA-origami nanoantennas for surface-enhanced

Raman spectroscopy, *Nano Lett.* **14**, 2914–2919 (2014).

[173] Thacker, V.V., Herrmann, L.O., Sigle, D.O., Zhang, T., Liedl, T., Baumberg, J.J., and Keyser, U.F., DNA origami based assembly of gold nanoparticle dimers for surface-enhanced Raman scattering, *Nat. Commun.* **5**, 10.1038/ncomms4448 (2014).

[174] Pilo-Pais, M., Watson, A., Demers, S., LaBean, T., and Finkelstein, G., Surface-enhanced Raman scattering plasmonic enhancement using DNA origami-based complex metallic nanostructures, *Nano Lett.* **14**, 2099–2104 (2014).

[175] Prinz, J., Schreiber, B., Olejko, L., Oertel, J., Rackwitz, J., Keller, A., and Bald, I., DNA origami substrates for highly sensitive surface-enhanced Raman scattering, *J. Phys. Chem. Lett.* **4**, 4140–4145 (2013).

[176] Stein, I.H., Schüller, V., Böhm, P., Tinnefeld, P., and Liedl, T., Single-molecule FRET ruler based on rigid DNA origami blocks, *ChemPhysChem* **12**, 689–695 (2011).

[177] Su, K.H., Wei, Q.H., Zhang, X., Mock, J.J., Smith, D.R., and Schultz, S., Interparticle coupling effects on plasmon resonances of nanogold particles, *Nano Lett.* **3**, 1087–1090 (2003).

[178] Lee, H., Lee, J.H., Jin, S.M., Suh, Y.D., and Nam, J.M., Single-molecule and single-particle-based correlation studies between localized surface plasmons of dimeric nanostructures with 1 nm gap and surface-enhanced Raman scattering, *Nano Lett.* **13**, 6113–6121 (2013).

[179] Prinz, J., Heck, C., Ellerik, L., Merk, V., and Bald, I., Dna origami based Au–Ag-core–shell nanoparticle dimers with single-molecule SERS sensitivity, *Nanoscale* **8**, 5612–5620 (2016).

[180] Simoncelli, S., Roller, E.M., Urban, P., Schreiber, R., Turberfield, A.J., Liedl, T., and Lohmüller, T., Quantitative single molecule surface-enhanced Raman scattering by optothermal tuning of DNA origami-assembled plasmonic nanoantennas, *ACS Nano* **10**, 9809–9815 (2016).

[181] Pillers, M.A. and Lieberman, M., Thermal stability of DNA origami on mica, *J. Vac. Sci. Technol., B* **32**, 040602 (2014).

[182] Kim, H., Surwade, S.P., Powell, A., O'Donnell, C., and Liu, H., Stability of DNA origami nanostructure under diverse chemical environments, *Chem. Mater.* **26**, 5265–5273 (2014).

# Vielen Dank...

- **Prof. Tim Liedl** für die Möglichkeit, meine Doktorarbeit in seiner Gruppe schreiben zu dürfen, für die von großer Unterstützung, Vertrauen und Freiräumen geprägte Betreuung, für die vielfältigen Gelegenheiten, auf Konferenzen und Aufenthalten in Boise und Santa Barbara die (Wissenschafts-) Welt kennenzulernen, und für die immer offen stehende Türe bei Fragen. Es waren großartige und lehrreiche Jahre, die ich nicht missen möchte.
- special thanks to **Prof. Alexander O. Govorov, Lucas V. Besteiro and Larousse Khosravi Khorashad** for great co-operations and sharing lots of knowledge and experience in theoretical physics.
- special thanks to **Mauricio Pilo-Pais, Prof. Christos Argyropoulos and Prof. Alexander Högele** for the co-operation and support.
- **Dr. Theobald Lohmüller, Sabrina Simoncelli, Michael Fedoruk und Patrick Urban** für die hervorragende Zusammenarbeit.
- **Susanne Kempter** für perfekte Unterstützung im Labor, Hilfe bei zahlreichen Fragen und für das offene Ohr.
- **Robert Schreiber** für vielerlei Anregungen und motivierende Worte.
- **den aktuellen und ehemaligen Mitgliedern der Arbeitsgruppe Liedl** für die einmalig gute Atmosphäre und Stimmung innerhalb und außerhalb des Labores. Vielen Dank Alex, Amelie, Andrea, Caro, Claudia, Daniel, Dave, Francesca, Iain, Kevin, Linh, Luisa, Marina, Marlene, Mauricio, Michael, Philipp, Robert, Samet, Steffi, Susi, Tao, Thomas, Timon, Verena, Wooli, Yongzheng.
- **Prof. Joachim O. Rädler und den Mitgliedern seines Lehrstuhls** für die freundliche Aufnahme an den Lehrstuhl und die Unterstützung bei meiner Arbeit.
- **den Verantwortlichen des Lehrstuhls Prof. Feldmann** für die Erlaubnis, Teile meiner Experimente in den Räumlichkeiten des Lehrstuhls durchführen zu dürfen.
- **Prof. Wan Kuang and William Klein** for the great time in Boise.
- **meinen Bürokollegen** Rafał, Christian, Farzad und Alexandra für eine wunderbare und unvergessliche Zeit in toller Bürogemeinschaft.
- **meiner Familie** für die jederzeitige und vielfältige Unterstützung.
- **Alex** für sein Verständnis und seine Geduld.